(1) ANISOTROPY AND CRYSTAL STRUCTURE OF FERROMAGNETIC THIN FILMS.

(2) INVESTIGATIONS INTO MAGNETIC MICROSTRUCTURE BY LORENTZ MICROSCOPY.

Thesis by

Takao Suzuki

In Partial Fulfillment of the Requirements
For the Degree of
Doctor of Philosophy

California Institute of Technology

Pasadena, California

1969

(Submitted May14, 1969)

To my parents.

Acknowledgements

The author wishes to most sincerely express gratitude to Professor C. H. Wilts and Professor F. B. Humphrey for their enthusiastic interest, encouragement and helpful guidance through the present work. To work with them has been a privilege and a pleasure. The author also wishes to gratefully acknowledge Dr. C. E. Patton, Dr. H. Hoffmann, Professor P. Duwez and Mr. T. C. McGill for their very valuable and stimulating discussions. Helpful discussions and correspondence with Dr. D. Wohlleben, Dr. M. S. Cohen, and Professor S. Chikazumi are also acknowledged.

Financial support for this work was derived, in part, from the research budget of the magnetics group of the Electrical Engineering Department and from research grants from the Jet Propulsion Laboratory. The author also acknowledges Burroughs Corporation for the use of the electron microscope, which is one of the most essential apparatuses in the present work.

During the course of this work, the author was the grateful recipient of graduate research assistantships from the Institute, Ford Foundation Fellowships and General Telephone Fellowship. The author is also grateful to the Fulbright Commission (Department of State, U.S.A.) for financial support and for making his stay in this country possible.

Last, but not least, the secretarial services of Miss C. Elsbree and Mrs. S. DeWitt are acknowledged in the preparation of the final manuscript of this dissertation.

ABSTRACT

The induced magnetic uniaxial anisotropy of Ni-Fe alloy films has been shown to be related to the crystal structure of the film. By use of electron diffraction, the crystal structure of vacuum-deposited films was determined over the composition range 5% to 85% Ni, with substrate temperature during deposition at various temperatures in the range 25° to 500°C. The phase diagram determined in this way has boundaries which are in fair agreement with the equilibrium boundaries for bulk material above 400°C. The ($\alpha + \gamma$) mixture phase disappears below 100°C.

The measurement of uniaxial anisotropy field for 25% Ni-Fe alloy films deposited at temperatures in the range -80°C to 375°C has been carried out. Comparison of the crystal structure phase diagram with the present data and those published by Wilts indicates that the anisotropy is strongly sensitive to crystal structure. Others have proposed pair ordering as an important source of anisotropy because of an apparent peak in the anisotropy energy at about 50% Ni composition. The present work shows no such peak, and leads to the conclusion that pair ordering cannot be a dominant contributor.

Width of the 180° domain wall in 76% Ni-Fe alloy films as a function of film thickness up to 1800 Å was measured using the defocused mode of Lorentz microscopy. For the thinner films, the measured wall widths are in good agreement with earlier data obtained by Fuchs. For films thicker than 800 Å, the wall width increases with film thickness to about 9000 Å at 1800 Å film thickness. Similar measurements for polycrystalline Co films with thickness from 200 to 1500 Å have been

made. The wall width increases from 3000 Å at 400 Å film thickness to about 6000 Å at 1500 Å film thickness. The wall widths for Ni-Fe and Co films are much greater than predicted by present theories. The validity of the classical determination of wall width is discussed, and the comparison of the present data with theoretical results is given.

Finally, an experimental study of ripple by Lorentz microscopy in Ni-Fe alloy films has been carried out. The following should be noted: (1) the only practical way to determine experimentally a meaningful wavelength is to find a well-defined ripple periodicity by visual inspection of a photomicrograph. (2) The average wavelength is of the order of 1μ. This value is in reasonable agreement with the main wavelength predicted by the theories developed by others. The dependence of wavelength on substrate deposition temperature, alloy composition and the external magnetic field has been also studied and the results are compared with theoretical predictions. (3) The experimental fact that the ripple structure could not be observed in completely epitaxial films gives confirmation that the ripple results from the randomness of crystallite orientation. Furthermore, the experimental observation that the ripple disappeared in the range 71 and 75% Ni supports the theory that the ripple amplitude is directly dependent on the crystalline anisotropy. An attempt to experimentally determine the order of magnitude of the ripple angle was carried out. The measured angle was about 0.02 rad. The discrepancy between the experimental data and the theoretical prediction is serious. The accurate experimental determination of ripple angle is an unsolved problem.

Table of Contents

Chapter 1 Introduction

The study of matter in the thin film state has fascinated many investigators, and a voluminous experimental and theoretical literature has been built up. Although the magnetic properties of thin films had occasionally come under consideration, the emphasis had distinctly been on other physical properties, particularly the crystal growth mechanism. In the last fifteen years, however, magnetic studies in thin films have received considerable attention. This interest promises to continue as the magnetic properties of thin films have not only intrinsic scientific interest, but also emerging technological significance for digital computer components. The general purpose of this thesis is to describe investigations into three topics which appear to be important in understanding magnetism in evaporated thin films. The thesis consists of three main parts: 1) Induced uniaxial anisotropy and its correlation with crystal structure (Chapters 2 and 3), 2) Domain wall structure (Chapter 4), and 3) Magnetization ripple structure (Chapter 5).

The shape of a thin film provides a strong anisotropy which usually constrains the magnetization to lie in the film plane. This geometry is expected to make the film normal a direction of hard magnetization and all directions in the film plane equally easy. However, actual polycrystalline ferromagnetic thin films almost invariably show uniaxial anisotropy in the film plane. Also additional contributions to anisotropy in the normal direction may arise from the physical state of the film. This case, however, is not discussed in the present thesis. A considerable amount of study on magnetic anisotropy in thin metallic films has

been carried out, but little systematic information is available except for the Ni-Fe system and the origin of the anisotropy is not wholly understood yet. The first part of this thesis is concerned with the uniaxial anisotropy in thin polycrystalline metal alloy films (Chapter 2). First, the origin of the uniaxial anisotropy in thin films will be discussed on the basis of the mechanisms put forward by others. Second new experimental data for the anisotropy in Ni-Fe alloy films will be presented and discussed with earlier data from the crystallographical point of view. This discussion is based on new results for the crystal structure which are given in Chapter 3. Since the basic knowledge of film structure is required in understanding the magnetic properties of thin films, such studies were carried out by electron microscopy. The crystal structure, crystallite size and lattice parameters as a function of composition and deposition condition will be summarized in Chapter 3.

Lorentz microscopy, Kerr magneto optics and Bitter technique reveal the ferromagnetic domain structure in thin films. The knowledge of the domain wall structure (magnetization spin distribution across walls and accordingly wall width) is necessary to understand the dynamical process of flux reversal by wall motion. However, the wall structure in thin films, which is rather different from that in bulk materials, has not been well understood. The only calculations to date are based on simple wall models, and no experimental studies have been carried out systematically. The purpose of Chapter 4 is to describe first the present status of wall energy and wall thickness calculations. Secondly the experimental technique and new wall width measurements obtained by Lorentz microscopy will be given for Ni-Fe

alloy and Co films.

Localized stresses and imperfections extending over small regions in thin films may give rise to localized anisotropy of magnetization. Furthermore, since the individual crystallites are randomly oriented in a polycrystalline film, the crystalline anisotropy, which is dependent on the crystallographical orientations of a crystallite, varies from one crystallite to another. Thus such local variation of anisotropy should give rise to local variation of magnetization direction with respect to the over-all mean magnetization direction. This local variation of magnetization is called ripple. Lorentz microscopy reveals such a ripple structure. In Chapter 5, the investigation of ripple as a function of film composition, substrate deposition temperature and the applied field will be summarized and discussed in conjunction with the theories presented by others.

Much of this work has been published in the technical literature:

Chapters 2 and 3:

T. Suzuki and C. H. Wilts, J.A.P. 38, 1356 (1967)

T. Suzuki and C. H. Wilts, J.A.P. 39, 6110 (1968)

Chapter 4:

T. Suzuki, C. H. Wilts and C. E. Patton, J.A.P. 39, 1983 (1968)

T. Suzuki and C. H. Wilts, J.A.P. 40, to be published (1969)

Chapter 5:

T. Suzuki and C. H. Wilts, J.A.P. 39, 1151 (1968)

Chapter 2

Magnetic Uniaxial Anisotropy

2.1. Introduction

It was predicted many years ago and verified experimentally that the shape demagnetizing fields would constrain the magnetization to lie in the plane of most thin film ferromagnets. It was not expected that there would be an anisotropy in the plane of the film. However, it is an experimental fact that most ferromagnetic thin films have a particular direction along which the mean magnetization lies in the absence of an applied field. This direction is called the easy axis, and the perpendicular direction (in the film plane) is called the hard axis. The existence of a preferred direction implies that energy must be supplied to orient the magnetization in another direction. The maximum energy required for orientation along the hard axis is called the anisotropy energy. The direction of the easy axis can be selected by applying a magnetic field in this direction during fabrication of the film.

The uniaxial anisotropy is usually approximated by

$$E_u = K_u \sin^2\theta \qquad (2.1)$$

where K_u is the uniaxial anisotropy constant and φ is the angle between the magnetization direction in the film plane and the easy axis. It is easily shown from Eq.(2.1)that a field in the hard axis direction produces a component of $\bar{M}$ directly proportional to the field up

to a critical value that makes the component of $\overline{M}$ equal to the saturation magnetization value. This critical value of H is called the anisotropy field H_k and is given by the equation

$$H_k = 2K_u/M_s \tag{2.2}$$

where M_s is the saturation magnetization of the film. The anisotropy field H_k may be measured in several ways. Four commonly used methods are: (1) the hard axis hysteresis loop, (2) use of the hysteresis looper with a method described first by Kobelev (1962), (3) the torque magnetometer and (4) ferromagnetic resonance. Since the first three have been used experimentally in this research to measure the uniaxial anisotropy, these methods are described in detail in Appendix 2.

One of the most intriguing and interesting aspects of ferromagnetic thin films is the origin of the magnetic uniaxial anisotropy. In the case of vacuum evaporation, it is known to have a strong dependence on the alloy composition and the substrate temperature during deposition. It also has an unusual dependence on the angle of the incident vapor atoms with respect to the substrate surface. This appears to be due to the development of structural defects which are difficult to measure and analyze. As a result, most work is done with normal incidence beams in order to obtain reproducible characteristics. All work reported in this thesis was done in this way. Surprisingly, the anisotropy shows little dependence on other deposition parameters, such as slight impurities, rate of deposition, degree of vacuum and substrate material provided the surface is sufficiently smooth.

It is the purpose of this chapter, first to discuss the mechanisms which have been proposed to explain these observed facts about the magnetic uniaxial anisotropy in ferromagnetic thin films. Second, new experimental data for the magnetic uniaxial anisotropy of 25% Ni-75% Fe alloy as a function of substrate deposition temperature will be presented along with other data previously reported by Wilts (1966) for Ni-Fe alloy films. Third, it will be pointed out that no combination of the mechanisms discussed earlier will satisfactorily explain the experimental results in thin films. In addition, a correlation will be pointed out between anisotropy variations and a crystal structure transition in the Ni-Fe alloy.

2.2. Magnetic Uniaxial Anisotropy

2.2.1. Pair Ordering Mechanism

As a possible mechanism to account for induced uniaxial anisotropy in ferromagnetic binary alloys, such as Ni-Fe alloys, the pair ordering model is the first which has been proposed by Néel (1953, 1954) and Taniguchi (1955). Consider an alloy of two components with A and B atoms randomly distributed over the lattice points, both having magnetic moments which are constrained to be parallel to each other. The dipole-dipole interaction energy of neighboring A and B atoms is

$$E_p = \ell_{ab}(r)\,(\cos^2\varphi - 1/3) \qquad (2.3a)$$

$$\ell_{ab}(r) = -3M_a M_b / r^3 \tag{2.3b}$$

where M_a and M_b are the magnetic moments of the A and B atoms respectively, r is the distance between the two atoms and φ is the angle between the magnetization direction and the line joining the two atoms. Only nearest neighbor interactions will be considered since the interaction falls off rapidly with the distance r. Thus, the energy due to the random distribution of three possible kinds of atom pairs over differently oriented pair directions is

$$E_p = \sum_i \left(N_{aa_i} \ell_{aa} + N_{bb_i} \ell_{bb} + N_{ab_i} \ell_{ab}\right) \left(\cos^2 \varphi_i - 1/3\right) \tag{2.4}$$

where N_{aa_i}, N_{bb_i} and N_{ab_i} are the number of the A-A, B-B and A-B pairs directed parallel to the $i^{\underline{th}}$ direction respectively, φ_i is the angle between the magnetization direction and the $i^{\underline{th}}$ direction and ℓ_{aa}, ℓ_{bb} and ℓ_{ab} denote the dipole coupling coefficients given in Eq.(2.3b). It should be noted that N_{aa_i}, N_{bb_i} and N_{ab_i} are not independent of each other. For example, an increase by unity in the number of B-B atom pairs in one of the nearest-neighbor directions through any interchange between A and B atoms results in an increase by unity in the number of A-A pairs and a decrease by two in the number of A-B pairs in the same direction. It follows that the change in the energy of the dipole coupling due to an interchange between A and B atoms may be expressed as $\ell_o \left(\cos^2 \varphi_i - 1/3\right)$ where

$$\ell_o = \ell_{aa} + \ell_{bb} - 2\ell_{ab} \tag{2.5}$$

Therefore, the total energy change in the sample can be expressed in terms of the anisotropic distribution of B-B atom pairs.

$$E_u = \sum_i N_{bb_i} \ell_o (\cos^2 \varphi_i - 1/3) \qquad (2.6)$$

These equations indicate that if the energy of the dipole-dipole interaction is different between the different kinds of atom pairs, namely between A-A, A-B and B-B pairs and if the atoms are arranged in the directionally ordered way, then one can expect the total array of dipole-dipole pairs to give rise to a non-zero anisotropy. For quantitative estimates it is necessary to have a calculated magnitude of ℓ_o for a typical material such as Ni-Fe alloy. For simplicity, the Bohr magneton numbers for Ni and Fe atoms are assumed to be the same as they are in the pure metals, 0.6 for Ni and 2.2 for Fe. Using Eq.(2.3) and the known lattice parameter for the alloy, one finds that

$$\ell_{Ni\text{-}Ni} = -0.56 \cdot 10^{-17} \text{ erg.}$$
$$\ell_{Fe\text{-}Fe} = -0.77 \cdot 10^{-16} \text{ erg.}$$
$$\ell_{Ni\text{-}Fe} = -0.20 \cdot 10^{-16} \text{ erg.}$$

Thus,

$$\ell_o = -0.43 \cdot 10^{-16} \text{ erg.} \qquad (2.7)$$

During anneal at a high temperature T' in the presence of a strong magnetic field, diffusion of the atoms in the lattice takes place and the B-B pairs, for instance, may tend to align themselves parallel to the direction of magnetization, provided the sign of ℓ_o is negative as in the case of Ni-Fe alloys. If all the Fe-Fe pairs in

a Ni-Fe alloy, for example, were aligned (10^{22} pairs/cc), then the maximum uniaxial anisotropy energy E_u predicted would be of the order of 10^6 erg./cc. However, as will be seen, thermal disorder reduces the fractional excess alignment of pairs in the low energy orientation to about 10^{-3}.

In estimating the anisotropy energy it is assumed that the number of B-B pairs found in the $i^{\underline{th}}$ bond direction is in thermal equilibrium governed by the Boltzmann factor. That is

$$N_{bb_i} = N_{bb} e^{-\ell_o' \cos^2 \varphi_i / kT'} \Big/ \sum_i e^{-\ell_o' \cos^2 \varphi_i / kT'}$$

where N_{bb} is the most probable number of B-B pairs (assuming $C_b \ll 1$). The exponentials can be approximated by the first two terms of the power series expansion since (ℓ_o'/kT') is of the order of 10^{-3} at the temperatures of interest here. Also since ℓ_o is a function of the distance between the two atoms, ℓ_o may be dependent on the temperature. Thus, ℓ_o' is the value of ℓ_o at $T'^{\circ}K$.

If the sample is rapidly cooled down to the lower temperature $T^{\circ}K$ at which measurement is to be made, no further diffusion of atoms can be expected and the anisotropic arrangement of B-B atom pairs is conserved (quenched). For such a quenched state, Néel (1953 and 1954) has used the above considerations to derive the anisotropy energy of dipole-dipole interaction for isotropic polycrystalline materials,

$$E_p = -nN(1/15kT') \, C_a^2 \, C_b^2 \, \ell_o \ell_o' \cos^2 \varphi \qquad (2.8)$$

where N is the number of atoms per unit volume, n is the number of the nearest neighboring atoms, C_a and C_b are the concentrations of A and B atoms, respectively. The angle between the magnetic field direction applied at T' and the magnetization direction at T is given by φ.

The expression of Eq.(2.8)can be compared with the anisotropy energy expression of Eq.(2.1)and one can define K_u for the pair ordering model to be

$$K_p = (1/15)nN\ell_o\ell_o'C_a^2C_b^2/kT' \qquad (2.9)$$

This equation illustrates the dependence of magnetic induced uniaxial anisotropy on the alloy composition, i.e., the anisotropy is proportional to $C_a^2C_b^2 = C_b^2(1 - C_b)^2$. For 50 % Ni-Fe alloys, the predicted value of K_u is about $2\cdot10^2$ erg/cc for T' = 300°C, assuming $\ell_o = \ell_o'$.

The attempt to experimentally verify the mechanism of the pair ordering model was first made by Chikazumi and Oomura (1955). They carried out the magnetic annealing of Ni-Fe bulk materials (rod shape) from 60% to 100% Ni content using various cooling rates from 600°C to room temperature. Even though the anisotropy was found to depend on the cooling rate, the anisotropy energy constant K_u varied as a function of Ni content in a manner similar to that expressed by Eq.(2.9). However, the magnitude of K_u extrapolated to 50 % Ni-Fe composition was about $5\cdot10^3$ erg/cc which is larger than that expected from theory by a factor of 30. The composition dependence of uniaxial anisotropy has also been measured by Ferguson (1958) in bulk materials with Ni composition above 50%. The value of the anisotropy K_u obtained at

50% Ni content is about $3 \cdot 10^3$ erg/cc which is in reasonable agreement with the results of Chikazumi and Oomura. Ferguson also found that the anisotropy is proportional to $(T_c - T')c_b^2 c_a^2$, where T_c is the Curie temperature and T' is the anneal temperature. The experimental dependence of K_u on composition is similar to the magnetic anisotropy induced by mechanical rolling as shown by Rathenau and Snoek as early as in 1941. However, the value of the anisotropy K_u produced by the mechanical rolling was about $2 \cdot 10^5$ erg/cc which is still larger by a factor of about 40 than that obtained by Chikazumi and Oomura for annealing of bulk alloys. Since the rolling process is not likely to produce pair ordering, evidently other mechanisms exist which give the same directional dependence.

Even though it is not clear that the anisotropy due to rolling may or may not have the same origin as that of the magnetic annealing, the discrepancy between the measured values and the theory prediction is serious. It leads clearly to the conclusion that the pair ordering model based on the classical magnetic dipole-dipole coupling does not explain the induced uniaxial anisotropy in bulk ferromagnetic binary alloys.

Néel and Taniguchi have been aware of this discrepancy and suggested that the interaction energy between atoms, whose origin is probably related to the spin-orbit coupling, must be treated quantum mechanically. The quantum mechanical origin of this coupling is believed to be due to the combined effects of spin-orbit interaction and the un-quenching of the orbital angular momentum by inhomogeneous

crystalline fields and by orbital exchange interaction with neighboring atoms. To be more explicit, the spin and orbital angular momentum interact with each other via spin-orbit coupling, and orbital motion is in turn influenced by the crystalline field and overlapping wave functions associated with the neighboring atoms of the crystal lattice. However, the quantum mechanical origin and its magnitude are controversial yet today and no quantitative discussion has been given in the literature.

In the case of thin films, the experimental situation is quite different. The pure metal films, such as Ni, Fe and Co are known to have large values of uniaxial anisotropy instead of zero. In these cases, the pair ordering mechanism can have no part in producing the anisotropy. In addition, the composition dependence of uniaxial anisotropy for the alloys of these metals has been found to be much more complicated than that predicted by Eq.(2.9). (Robinson (1961), Takahashi (1962), West (1964), Wilts (1966), and Wilts and Humphrey (1968)). This will be discussed in detail in the following sections. In the light of the experimental situation, Robinson and West have suggested an additional mechanism to account for a part of the uniaxial anisotropy in thin films. This mechanism, dependent on stress and magnetostriction, is discussed in the next section.

2.2.2 Stress Mechanism

The anisotropy predicted by the pair order model cannot be used to explain the total anisotropy of thin films. This model predicts no anisotropy for pure single element films, while experimentally such films are found to have a substantial anisotropy. In an effort to explain the experimental data for Ni-Fe alloy films, Robinson (1962) suggested an additional mechanism caused by magnetostriction and anisotropic stresses associated with the tight adherence of the film to the substrate. In other words, he proposed that the origin of the uniaxial anisotropy energy in thin films is due to two mechanisms--the Néel-Taniguchi pair order mechanism and a stress mechanism.

The additional mechanism proposed by Robinson can be described as follows: When the film is deposited in a magnetized condition at a substrate deposition temperature T', the film is spontaneously strained in the direction of the applied field. At the time the film is formed, the atoms of the film are considered to be sufficiently mobile to relieve any anisotropic stress in the film. Thus the state of the film after evaporation in an applied field may be considered as one in which the film is free from anisotropic stress but strained magnetostrictively by an amount of $\lambda_{s'}$ where $\lambda_{s'}$ is the longitudinal saturation magnetostriction constant at temperature T'. When the film is cooled to room temperature, the magnetization remains in the same direction as the applied field direction, that is along the easy axis. If the magnetization is now rotated to another direction by applying a suitable magnetic field, the substrate prevents any change in the strain in the film, so that a magnetostrictive stress is produced. Based on this idea,

Robinson derived an expression for an additional uniaxial anisotropy energy E_λ of the form

$$E_\lambda = K_\lambda \sin^2\theta = \frac{3}{2} \lambda_s \lambda_s' G \sin^2\theta \tag{2.10}$$

and

$$K_\lambda = \frac{3}{2} \lambda_s \lambda_s' G \tag{2.11}$$

where K_λ is a uniaxial anisotropy constant due to stress, λ_s is the longitudinal saturation magnetostriction constant at temperature T where the measurement is to be made, G is Young's modulus, and θ is the angle between the direction of the stress in the film and the magnetization direction. Robinson suggested that the total uniaxial anisotropy of thin films results from a simple summation of terms due to the pair order (K_p) and this stress mechanism (K_λ);

$$K_u = K_p + K_\lambda \tag{2.12}$$

West (1964), however, pointed out that Robinson's calculation was fundamentally incorrect and calculated the sum of the magneto-elastic and elastic energies for each crystallite, and then averaged the energy over the randomly oriented array of crystallites. The result obtained for materials with cubic symmetry is

$$K_\lambda = \frac{9}{10}[(C_{11} - C_{12})\lambda_{100}\lambda'_{100} + 3C_{44}\lambda_{111}\lambda'_{111}] \tag{2.13}$$

where C_{11}, C_{12} and C_{44} are the standard elastic constants at temperature T, and λ and λ' are longitudinal magnetostrictions at temperature T and T' respectively. As before, T' is a substrate deposition temperature.

It is worth comparing these two results with the experimental data. First, one is interested in knowing the values for pure elements such as Ni, Fe and Co. This comparison is made in Table 2-1. The theoretical values were computed by West using magnetostrictive and elastic data referenced in his paper. The difference between the results of West and Robinson is very small in the case of Ni, where λ_{111} and λ_{100} are of same sign so that λ_s has the same order of magnitude as the simple crystal constants. The experimental results by Wilts are in good agreement with both values. However, in the case of Fe, where λ_{100} and λ_{111} are nearly equal but of opposite sign, the difference becomes significant. Robinson's result predicts a much smaller value for K_u than the corresponding calculation by West. The reason for this is as follows. Robinson's result was based on the average change in dimension of an unstressed film. If λ_{111} and λ_{100} are opposite sign and approximately in the ratio of 2 to 3, then the value of λ_s becomes very small and the energy according to Eq. (2.11) becomes also small. On the other hand, West considered the equilibrium strain and the corresponding total of magnetoelastic and elastic energies in each crystallite based on the larger (and more nearly correct) single crystal constants. Then he averaged the energy over the randomly distributed crystallites obtaining an average energy much larger than that predicted by Robinson. As shown in Table 2.1, the value for Fe obtained in this way by West is in excellent agreement with the measured value by Wilts. On the other hand, the value by Robinson is smaller than these by an order of magnitude. In the case of Co, because of the hexagonal symmetry the expression of anisotropy is different than that of Eq. (2.13). The detailed calculation by West is not of primary interest here, but the result is important. As shown in Table 2.1, the

Table 2-1

COMPARISON OF THEORETICAL AND EXPERIMENTAL VALUES OF UNIAXIAL ANISOTROPY FOR SINGLE ELEMENT FILMS

All data are for films deposited at 25°C and measured at 25°C. Values are given in units of 10^3 ergs/cc.

	Ni	Fe	Co
Robinson (Eq. 2.11)	3.5	0.2	30
West (Eq. 2.13)	4.1	1.8	42
Wilts (Experimental)	3.6	1.6	20

difference between the results by Robinson and West is not significant ($30 \cdot 10^3$ erg/cc and $42 \cdot 10^3$ erg/cc respectively). The measured value of Co films evaporated at 25°C is about $20 \cdot 10^3$ erg/cc (Wilts, 1968), which disagrees with the calculated values by a factor of about 2. At the present time, the reason for this discrepancy is not clear. If the experimental value were too large, one could postulate another anisotropy source to explain the difference. However, in this case the experimental value is low. It should be mentioned that the phase transformation between ϵ and γ in Co films with changing substrate deposition temperature is gradual, as will be discussed in section (3.2.3). Even though the electron diffraction photograph in Fig. 3.7 indicates primarily hexagonal structure at 25°C, one can see a diffuse line which may correspond to $(200)_{f.c.c.}$ in the photograph. This implies that the films evaporated at 25°C may contain a very small amount of f.c.c. structure. Accordingly the anisotropy could be different from that based on the theory for h.c.p. structure. It is also possible that the single crystal magnetostriction constants for hexagonal cobalt are in error. In any case the discrepancy though substantial is not unreasonably large.

As discussed, the measured uniaxial anisotropy for pure Ni, Fe and Co films are in reasonable agreement with those predicted by the stress mechanism. However, there still remain some difficulties with this mechanism. Before discussing this matter, it is worth pointing out that there is good agreement between the experimental data and the prediction by a combination of stress and pair order over a limited range of alloy composition in Ni-Fe films. As mentioned before, in an attempt to explain the observed anisotropy Robinson and West proposed a combination of stress mechanism with no adjustable parameters

(Eqs. (2.11) and (2.13)) and the pair order mechanism with an empirical coupling constant ℓ_o (Eq. (2.9)). The dependence of K_λ on Ni composition in Ni-Fe alloy films, as expressed by Eqs. (2.11) and (2.13), is plotted in Fig. 2.1 for the composition range between 35 and 100% Ni, and for deposition temperature 25 °C (after the paper of West, 1964). The difference between the two curves is little for Ni content greater than 70%. However, for composition below this value, the difference becomes significant; the prediction by West is much larger than that by Robinson. The adjustable constant for the pair order model was empirically determined from the measured anisotropy at about 80% Ni where the stress part of uniaxial anisotropy is expected to be negligible since the magnetostriction constants are nearly zero. The resulting anisotropy, consisting of the stress and pair order parts, is plotted in Fig. 2.2 as a function of Ni composition in the range 35% to 100% Ni. In the figure, experimental data for films deposited at 25 °C are also shown for comparison (Wilts, 1966). On the whole, the agreement is reasonable between the data and the predictions of the theories. However in view of the high curvature near 50% Ni and the very sharp decrease below 40% Ni, it would be desirable to obtain more experimental points in this region. New experimental data to clarify this matter are given in section (2.3.2).

For further check of the theories, one should look at other alloys with zero magnetostrictive compositions ($\lambda_s = 0$). Two examples are Ni-Co and Ni-Fe alloys. The recent study of Ni-Co alloys by Brownlow and Wilts (1968) indicates that there is no minimum in the anisotropy at the composition where λ_s is zero. Clearly Robinson's model fails here and the agreement with West's model is poor.

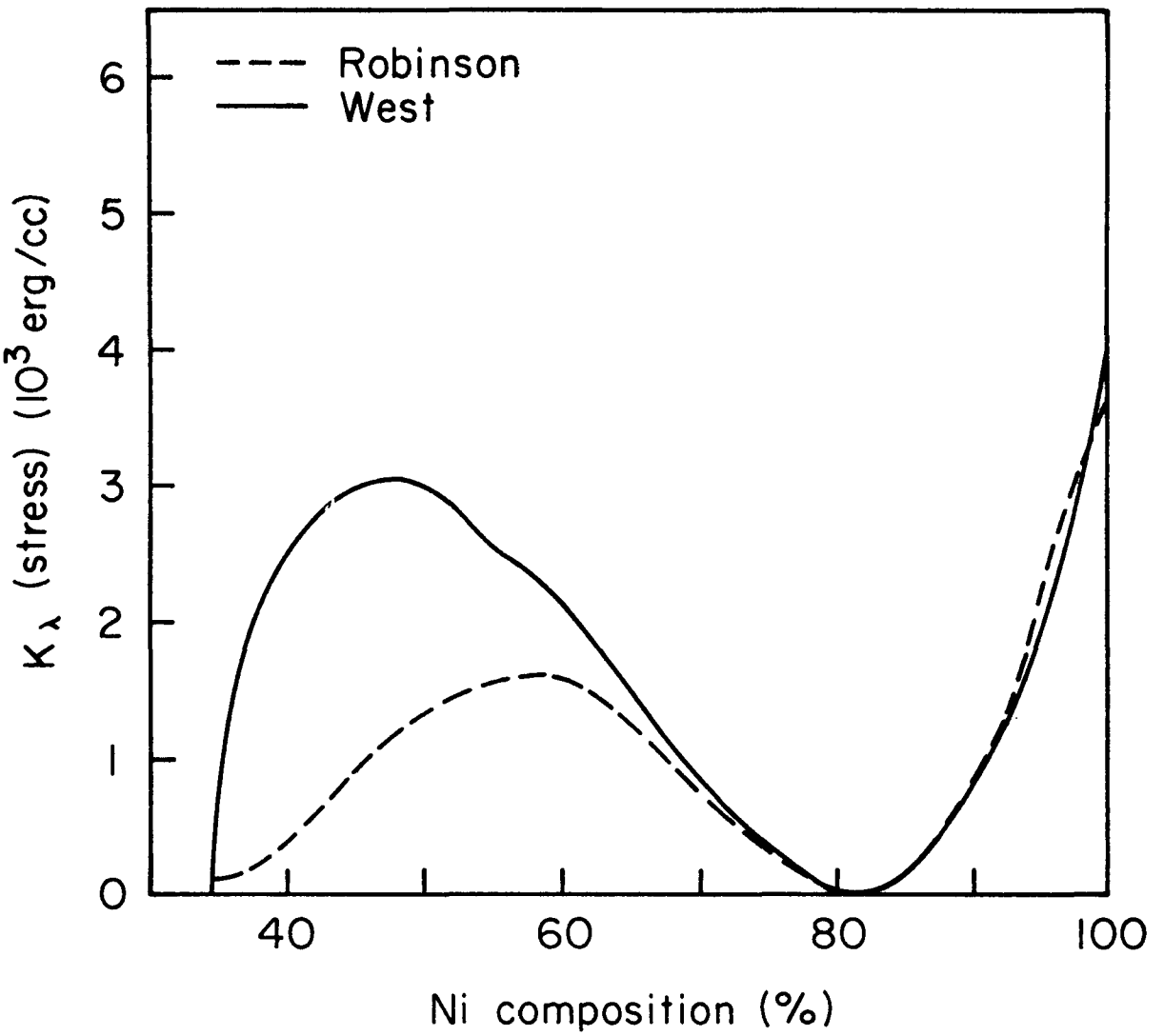

Fig.2-1 Uniaxial anisotropy due to stresses as a function of Ni composition in Ni-Fe alloy films. The dashed line is based on the model by Robinson(1964) and the solid line is based on the model by West(1964). The figure is reproduced from the paper by West (1964). $T=T'=25^{\circ}C$.

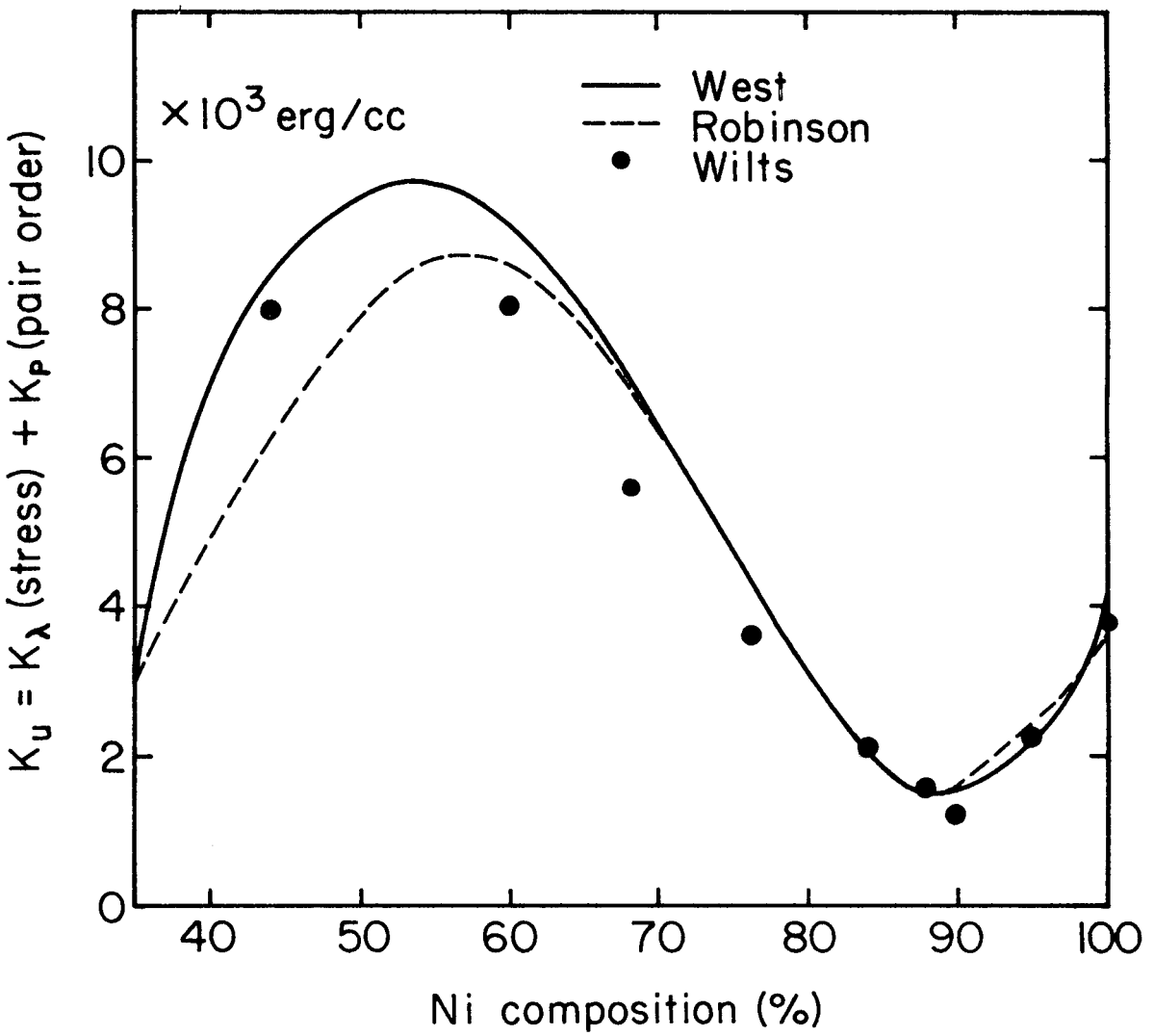

Fig.2-2 Total uniaxial anisotropy K_u as a function of Ni composition in Ni-Fe alloy films. The solid dots are the experimental values by Wilts (1966) for films evaporated at room temperature. Also shown are the theoretical predictions by Robinson(1962) and by West (1964). $T=T' = 25^{\circ}C$.

Since the stress mechanism is based on the stress due to the adherence of the film to the substrate, one might expect the stress part of the total anisotropy to disappear after removing a film from the substrate. However, Pugh and coworkers (1960) have found that the uniaxial anisotropy in Fe films deposited on NaCl substrate was about the same after removal as before. They concluded that the stress mechanism could not account for any significant part of the uniaxial anisotropy. A similar result has also been reported by Wako and his coworkers (1963) for Ni films. On the other hand, Krukover (1968) has recently reported a result contrary to that of Wako et al. The anisotropy of Ni evaporated at 100 ^{o}C was found to be $3.5 \cdot 10^{3}$ erg/cc, which is in good agreement with the theoretical values of Robinson and West and the experimental value of Wilts. However, he found that the anisotropy decreased to zero after removal from the substrate. He inferred from this that the magnetostrictive stress mechanism is mainly responsible for induced anisotropy in the case of Ni films. The anisotropy of Co films, on the contrary, was found to decrease very little, from $15 \cdot 10^{3}$ erg/cc to $13.5 \cdot 10^{3}$ erg/cc. From this he concluded that only 10% of the total anisotropy could be attributed to the stress mechanism, even though West's calculation predicted a value of $40 \cdot 10^{3}$ erg/cc based on this mechanism. In addition, for Fe films, he found little change in anisotropy after separating the films from the substrates, concluding that the stress mechanism contributed less than 10% of the measured anisotropy even though West's calculation agreed very well with the experimental value. In the light of this chaotic situation, a systematic study of this matter is needed.

In an attempt to explain anisotropy in thin films, some workers have discussed the importance of lattice defects and impurities (Bozorth (1957), Anderson (1961), Takahashi (1962) and Purtton (1963)). It was proposed that structural defects such as vacancies, dislocations and impurities might contribute to the anisotropy, if an alignment of these defects occurs during deposition. However, this is not plausible in the case of impurities since the magnetic uniaxial anisotropy observed does not seem to depend on residual gas in the vaccuum system over a relatively wide range of vacuum (10^{-5} to 10^{-7} mm Hg) or on small amount of impurities in the melt, but it does vary widely with composition, substrate deposition, and measuring temperatures over a range of at least 20 to 1. The same argument may not apply to vacancies, dislocations and other defects, but in any case, no meaningful quantitative predictions have been advanced.

As seen so far, the origin of the uniaxial anisotropy is not satisfactorily understood, and the experimental results of the magnetic uniaxial anisotropy cannot be explained fully in terms of the mechanisms discussed earlier. Therefore, it is worthwhile to consider whether relevant information can be obtained from investigating variation of anisotropy with crystallographic structure of thin films. Such investigations were made in Ni-Fe alloy films, and the results and discussion will be given in the following sections.

2.3 Measurement of Magnetic Uniaxial Anisotropy and Correlation with Crystal Structure

2.3.1 Introduction

In the previous section, the pair ordering and the magnetostriction stress mechanisms for induced magnetic uniaxial anisotropy have been discussed and it was pointed out that neither mechanism nor a combination of them fully explains the experimental results. In the light of this discrepancy, it seems plausible that some significant factors which contribute to the uniaxial anisotropy energy have been overlooked, and the origin of the uniaxial anisotropy should be reconsidered. In this section, an experimental investigation of the correlation between crystal structure and anisotropy in Ni-Fe alloy films is presented.

The motivation for this study was initiated by Wilts (1966) who first suggested a correlation between the uniaxial anisotropy and the crystal structure in ferromagnetic thin films on the basis of the measurement of anisotropy made on the 19% Ni-Fe alloy. To confirm his results, the same measurements were repeated for the 25% Ni-Fe alloy, a slightly different composition from that which he used. At the same time, crystal structure determination was carried out by electron diffraction for compositions ranging from 5% to 80% Ni content and over a wide range of substrate deposition temperature. This experimental crystal structure work is discussed in detail in a later section.

2.3.2 Measurement of the Uniaxial Anisotropy of Ni-Fe Alloy Films

The experimental values of uniaxial anisotropy obtained by many workers over the last decade show common trends even though the specific numerical values show a large variation from one laboratory to another. The most striking systematic variations are the dependence of uniaxial anisotropy on alloy composition and on the substrate deposition temperature. The first of these has been commonly used by many workers to check the validity of the theories put forward, but the latter dependence has not been given much attention. This is mainly because of two reasons. First the pair ordering indicates directly the compositional dependence but not the temperature dependence of induced uniaxial anisotropy. Specifically the temperature dependence of the number of pairs and the parameter ℓ'_o in Eq. (2.9) is not known. Second, the stress mechanism predicts that the other component of anisotropy depends on the elastic and magnetostriction constants whose composition dependence has been determined experimentally at room temperature, but whose temperature dependence is unknown. Accordingly, the dependence of anisotropy on substrate deposition temperature was thought not to provide any significant information to test directly the theories.

However, this view is not necessarily true. If the uniaxial anisotropy is closely related to crystal structure in Ni-Fe alloy films, this correlation between them might suggest sources which were overlooked in the previous considerations of the origin of anisotropy, or might shed some light on the mechanism of pair formation. Since the crystal structure depends on deposition temperature as well as composition, a corresponding variation of anisotropy would demonstrate the significance of structure.

It is experimentally difficult to measure the dependence of uniaxial anisotropy on substrate deposition temperature in the desired composition range near 30% Ni content. Since the suspected correlation is based on a single measurement of this type by Wilts, it was felt desirable to first verify his previous work. Consequently, an additional measurement was made of the uniaxial anisotropy as a function of deposition temperature. The film composition 25% Ni was chosen since the alloy with this composition is known to have a crystal structure transition at about 250 ^{o}C (see Fig. 3-1 in the next chapter). This temperature is significantly different than the corresponding temperature for the alloy used by Wilts, but is still within the range of interest. In order to obtain this film composition a melt composition of 45% Ni was used. The deposition condition and the procedures are described fully in Appendix 1.

The induced uniaxial anisotropy constant K_u or anisotropy field H_k may be measured by several methods, 1) use of a hard axis hysteresis loop, 2) the same instrument but using a procedure first described by Kobelev (1962), and 3) use of a high field torque magnetometer (Humphrey, 1967). These procedures are described in Appendix 2. Of these, the hard axis hysteresis method is the most common for measuring the uniaxial anisotropy. However, in practice, this method frequently fails to give a meaningful value for the uniaxial anisotropy. In some cases, the M-H characteristic opens up into a loop without well defined shape, and for other films the characteristic remains nearly single valued, but has a slope which depends on the amplitude of the applied field. For example, characteristics such as these are almost always found in the so-called inverted films in which H_c is greater than the anisotropy field H_k. They also occur in situations

where the dispersion and ripple amplitude are very large.

Almost all of the films investigated in the present work with 25% Ni content showed a slightly opened loop for a low field applied in the hard axis direction so that an accurate measurement was impossible by this method. However, both the Kobelev method and the high field torque magnetometer gave reasonably consistent and apparently meaningful values for the anisotropy field. Both of these were used in the present study.

The uniaxial anisotropy field H_k determined by the torque magnetometer as a function of substrate deposition temperature T' is shown in Fig. 2.3. It is seen that the uniaxial anisotropy field H_k slowly decreases with substrate deposition temperature from the value of about 9 oe. at -80°C to 6 oe at 250 °C, and then rapidly decreases to zero at about 420 °C. This indicates that some transition in the behavior of H_k as a function of T' takes place at about 250 °C. The uniaxial anisotropy field H_k determined by Kobelev's method is shown in Fig. 2.4. As can be seen by comparing the two figures, the values measured by Kobelev's method are generally smaller than those obtained by the torque magnetometer by about 15%. However, the trend of anisotropy as a function of substrate deposition temperature is the same. Again, a distinct abrupt change in slope occurs at about 250°C substrate deposition temperature. Evidently this result is not influenced by the method used for measuring the uniaxial anisotropy.

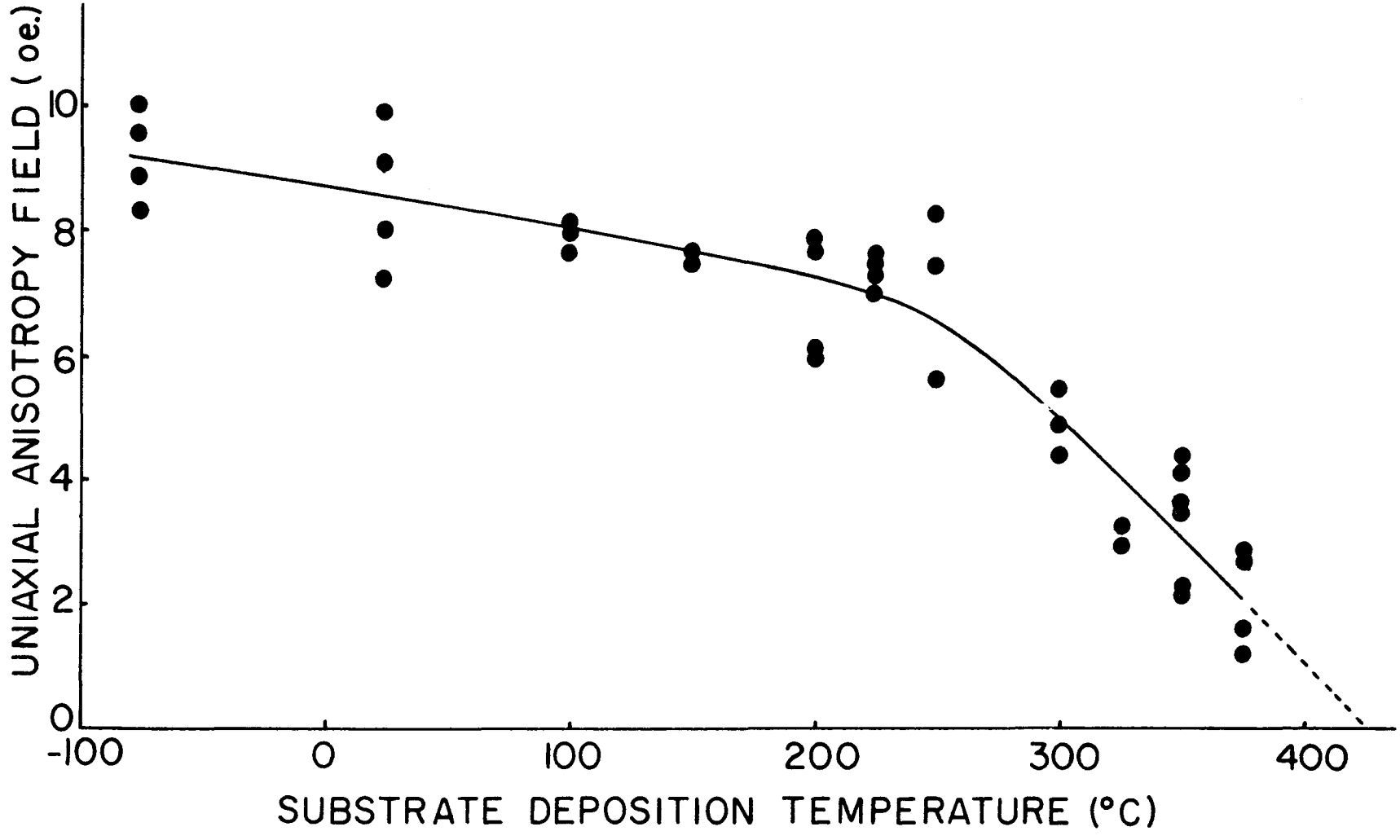

Fig.2-3 Uniaxial anisotropy field H_k measured by torque magnetometer as a function of substrate deposition temperature for 25%Ni-Fe alloy films.

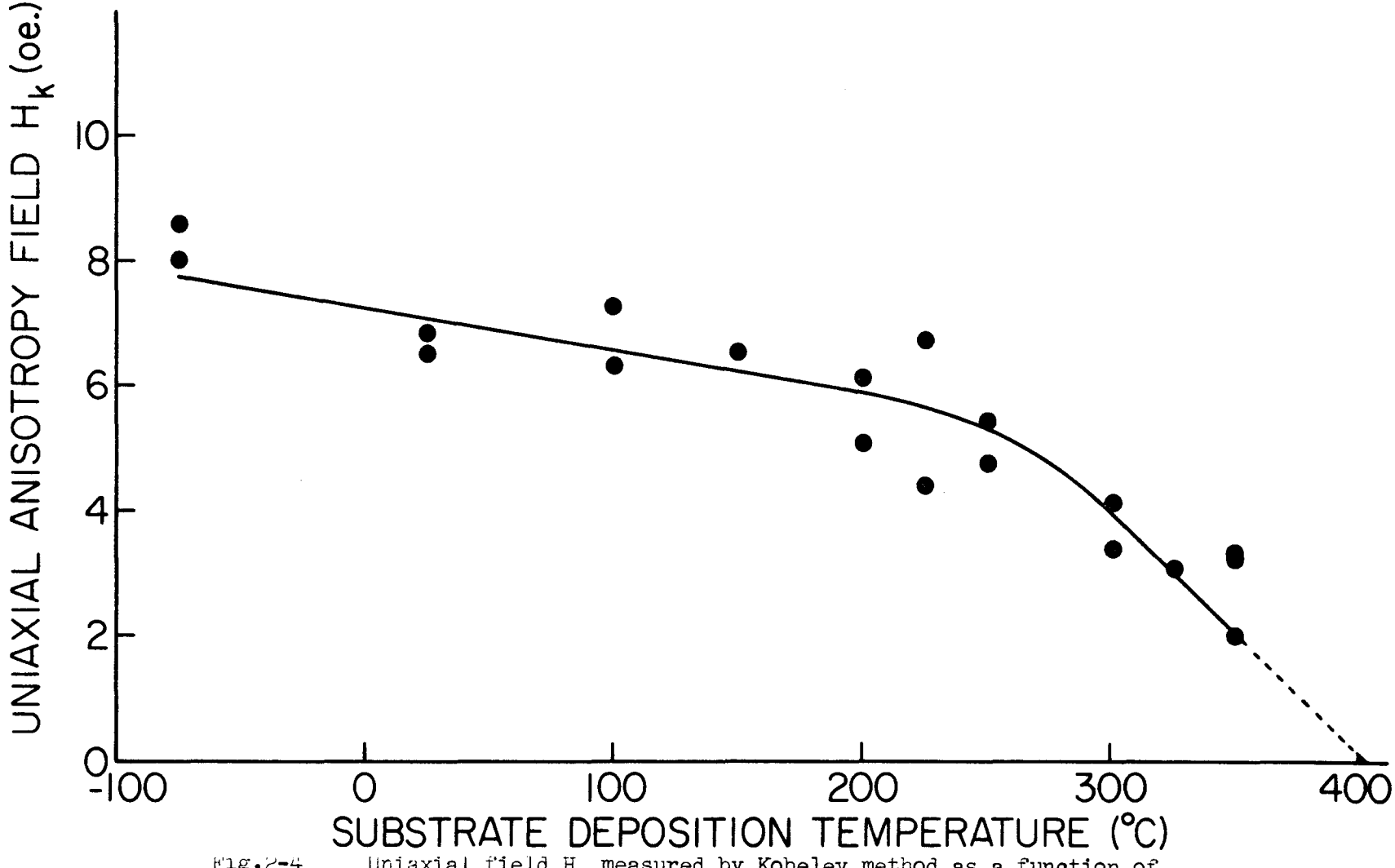

Fig.2-4 Uniaxial field H_k measured by Kobelev method as a function of substrate deposition temperature for 25%Ni-Fe alloy films. The figure should be compared to Fig.2-3.

2.3.3 Correlation of Uniaxial Anisotropy with Crystal Structure

In Fig. 2.5, values of H_k as a function of T' for 44%, 19%, 11% and 0% Ni compositions in Ni-Fe alloy films are reproduced from the data by Wilts (1966), along with the present data for 25% Ni composition. The curves for 44%, 11% and 0% Ni composiition show a smooth variation with no rapid change in slope. On the other hand, the curves for 25% and 19% Ni compositions show definite break points at about 250 ^{o} and 330 ^{o}C, respectively. As will be seen in a later section, these temperatures lie within the transition range from b.c.c (α) to f.c.c (γ) crystal structure. For ease of comparison, the arrows in Fig. 2.5 indicate the temperatures at which the transition from α to γ phase is about 25% complete for the two compositions of interest. These temperatures were obtained from Fig. 3.1 which will be discussed in detail in a later section. Since the data on crystal structure is only semi-quantitative, the correlation between the two sets of data seems very good.

It can also be observed in Fig. 3.1 that no phase transition takes place in the temperature range from 0^{o} to 500 ^{o}C for films with 0% and 44% Ni compositions. Correspondingly, there are no breaks in the data in Fig. 2.5 for these compositions. On the other hand, Fig. 3.1 shows a definite phase transition just above 400 ^{o}C for the 11% Ni alloy films. Accordingly, a break in the curve of H_k vs T' would be expected at a temperature in the range 400 ^{o}C to 425 ^{o}C. However, the anisotropy field H_k has been measured only up to 400 ^{o}C, so it is not known whether the correlation holds for this composition. One may

conclude that the experimental evidence indicates a definite correlation between the crystal structure transition and the abrupt change in the behavior of uniaxial anisotropy as a function of substrate deposition temperature in Ni-Fe alloy films. If this correlation is found in Ni-Fe alloys, then it also should be observed in other alloy systems. One such study has been recently carried out by Brownlow and Wilts (1968). Again, there appears to be a correlation between the crystal structure transition and the anisotropy in Ni-Co alloy films.

The variation of anisotropy with composition has been used to test theories of the origin of anisotropy. This is customarily done for films made at an elevated temperature of about 300 ^{o}C. Inspection of Fig. 5 in the paper by Wilts (1966) shows that the varying Curie temperature makes the comparison very questionable. Values extrapolated to a low temperature, or the value at some fraction of the Curie temperature or alternatively the slope of the curve at the Curie temperature would appear to be more suitable. Since the Curie temperature and data near the Curie temperature are not known for all compositions, in what follows all comparisons will be made by extrapolation to 0 ^{o}K.

From Figs. 2.5 and 3.1, it is plausible that those parts of the curves for 19% and 25% Ni compositions which lie below the break points in temperature correspond to the anisotropy in the α phase. Similarly, the other portions at high temperature above the break indicates the anisotropy in the γ phase. In order to estimate the uniaxial anisotropy at 0 ^{o}K for the γ phase it is necessary to make an extreme extrapolation of the curves at high temperatures to the lower temperature region. In this way one can estimate and compare the uniaxial anisotropy as a function of alloy composition for both α and γ phases in the composition

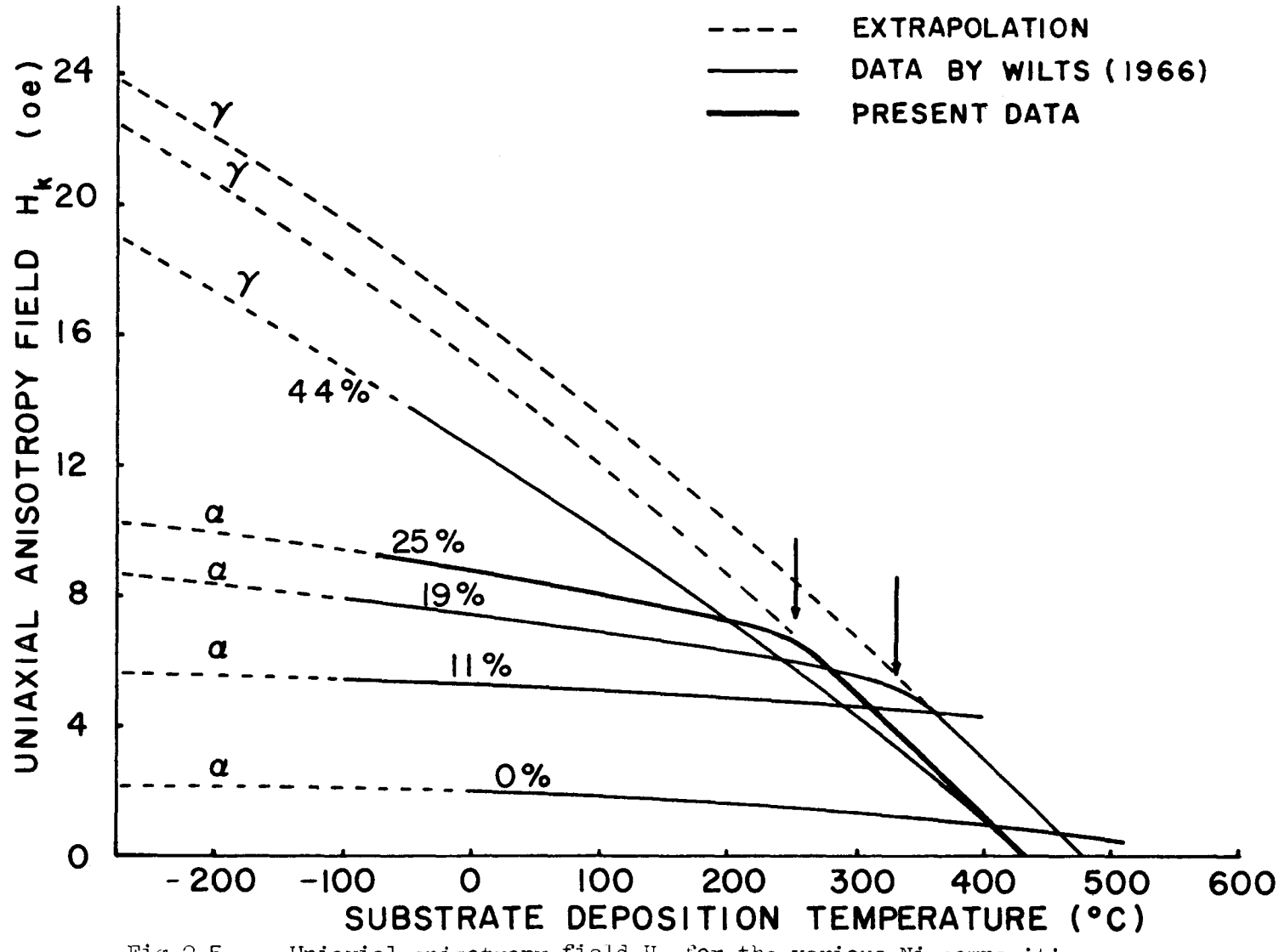

Fig.2-5 Uniaxial anisotropy field H_k for the various Ni compositions as a function of substrate deposition temperature. The experimental data by Wilts (1966) are also shown.

range where both phases are present at different temperatures. The data obtained by such an extrapolation are shown in Fig. 2.6. In this figure, the anisotropy energy rather than the anisotropy field is given. This is obtained from the equation $K_u = (1/2)H_k M_s$, where M_s is the saturation magnetization. It is seen in Fig. 2.6 that the uniaxial anisotropy for the γ phase decreases with increasing Ni content from about $20 \cdot 10^3$ erg/cc at 19% Ni to $2 \cdot 10^3$ erg/cc at 90% Ni, and then increases to the values $5 \cdot 10^3$ erg/cc at 100% Ni content. Further, it should be noted that the uniaxial anisotropy for the γ phase is much larger than that for the α phase at 20 to 25% Ni composition where the anisotropy can be measured for both structures. For direct comparison with West's and Robinson's theories, similar data for room temperature (25°C) are shown in Fig. 2.7. For the Ni rich composition range, the anisotropy shown in Fig. 2.7 is in reasonable agreement with the prediction by Robinson and West. However, for the Fe rich compositions, the discrepancy becomes very large. The anisotropy for the γ phase in Fig. 2.7 does not show a peak near 50% composition nor much curvature. Even qualitatively, the present data show that the model put forward by Robinson and West is not satisfactory to account for the observed uniaxial anisotropy. For the α phase, theoretical calculations are not possible because the necessary magnetostriction data are not available.

2.4 Summary

This section on magnetic uniaxial anisotropy in thin films first discussed the theories which have been advanced to explain the origin of magnetic uniaxial anisotropy. To provide additional experimental

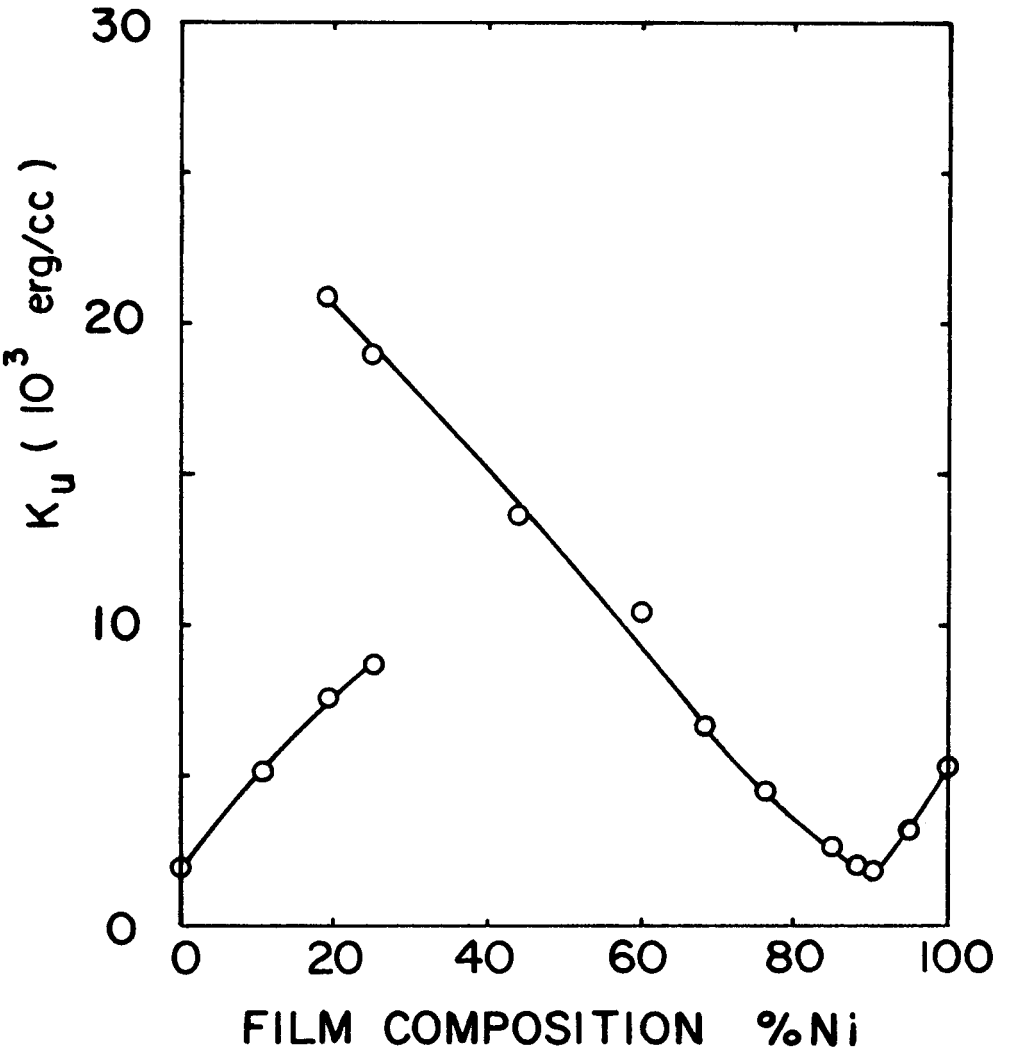

Fig.2-6 Uniaxial anisotropy constant K_u at $0^{\circ}K$ obtained by extraporation, on the basis of the data given in Fig.2-5.

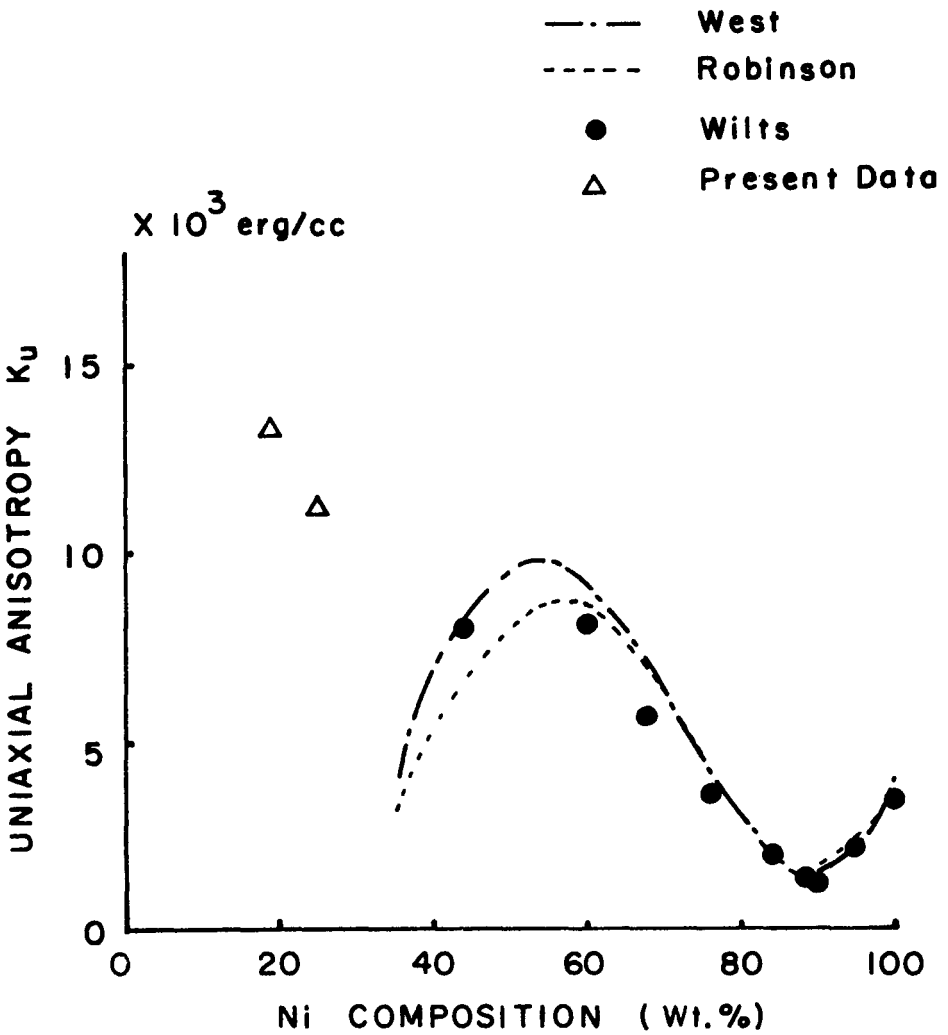

Fig.2-7 Uniaxial anisotropy K_u as a function of Ni composition in Ni-Fe alloy films. The anisotropy energy constant K_u is for γ phase at room temperature. The solid dots are the values published by Wilts (1966) and the theoretical predictions by Robinson and West are also shown by the dotted lines.
The present data for 25%Ni and 19%Ni are shown by the empty triangles. The figure should be compared with Fig.2-2.

data, the measurement of uniaxial anisotropy for 25% Ni-Fe alloy films was carried out as a function of substrate deposition temperature. The uniaxial anisotropy field H_k was measured by the Kobelev method and the high field torque magnetometer. The results obtained by both methods were in good agreement, and furthermore agreed well with measurements by Wilts on the 19% Ni-Fe alloy. These data were compared with the results of the crystal structure study which is given in the next chapter. It was found that a break point in the curve of anisotropy vs. deposition temperature corresponded to the phase transition between the α and γ phases. For compositions which do not have a crystal structure transition over the temperature under consideration, the anisotropy data showed no such breaks. This indicates that the uniaxial anisotropy in thin films is strongly sensitive to crystal structure.

The uniaxial anisotropy for the γ phase was found to be much larger than that for the α phase at 20 to 25% Ni composition where the anisotropy can be measured for both structures. Furthermore, the dependence of anisotropy as a function of composition was found to be very different from that predicted by the pair ordering mechanism and therefore, the pair ordering mechanism does not make a major contribution to the magnetic uniaxial anisotropy in this composition range.

Chapter 3

Structure Study of Ni-Fe and Ni-Co Alloy Films by Electron Optics

3.1. Introduction

It is commonly known that the magnetic properties of bulk materials are influenced by the type of crystal structure, the crystalline state (i.e., polycrystalline, single crystal or amorphous), and by the presence of defects, impurities and so forth. Thus, it is a reasonable assumption that an understanding of the magnetic properties of thin films will require information about the crystallographic properties of such films. For example it was pointed out in Chapter 2 that the uniaxial anisotropy in Ni-Fe alloy films appears to be dependent on the crystal structure. Little is known about the anisotropy of other ferromagnetic alloys, but on the basis of fragmentary data it appears likely that a similar dependence may exist for the binary alloys of Ni-Co and Fe-Co. For this reason it is important to make a systematic study of the crystal structure of ferromagnetic alloy films to look for a similar dependence on crystal structure.

In the present study, the determination of crystal structure in Ni-Fe and Ni-Co films was carried out by electron diffraction. The result for Ni-Fe alloy films has been referenced in the previous chapter and discussed in connection with magnetic uniaxial anisotropy. In addition, the lattice parameter in Ni-Fe alloy films has been carefully measured. Finally, the mean crystallite size has been obtained, since

such information is important in the discussion of magnetization ripple which will be given in Chapter 5.

3.2. Crystal Structure Study

3.2.1. Crystal Structure of Ni-Fe Alloy Thin Films

It is well known in Ni-Fe bulk alloys that the exact placing of the equilibrium phase boundaries has met with great experimental difficulties due to the formation of metastable structural states which vary widely according to the composition and heat treatment and due to the extreme sluggishness of diffusion at temperatures below 500°C. Particularly at low temperature, the published data of the phase transformation between α(b.c.c) and γ(f.c.c) may represent a metastable state rather than the equilibrium state. (See for example, Owen and Sully (1939), Owen and Liu (1949), Pickles and Sucksmith (1940) and Hoselitz and Sucksmith (1943).) The transition between the α and γ phases in bulk Ni-Fe alloys is shown in Fig. 3-1 by the dotted lines. This transition has been measured both by x-ray method (Owen and Liu (1949) and by magnetic method (Hoselitz and Sucksmith (1943)). The boundaries were determined for alloys subjected to very long periods of annealing. For example, Owen and Liu annealed the bulk alloys for more than one year to obtain the data for 300 and 350°C. However, the figure shows that even after long periods of anneal, the transition boundaries between the α and γ phase vary from one experiment to another, especially in the temperature range 300 to 450°C.

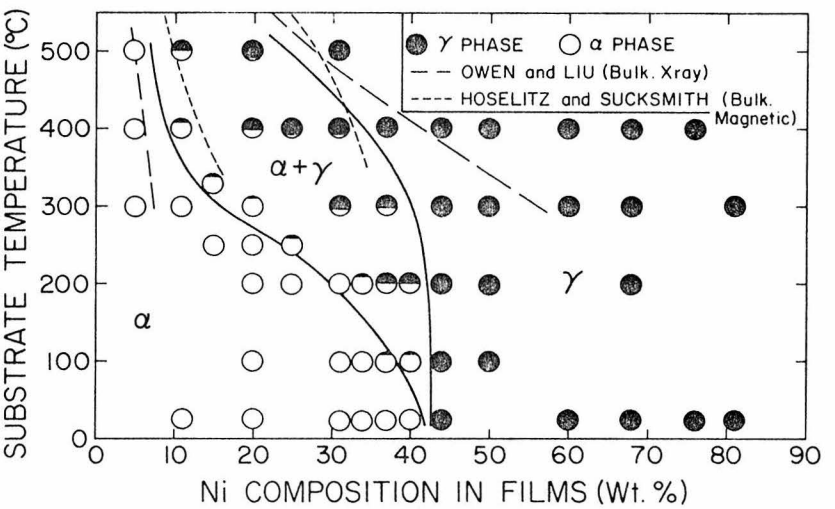

Fig.3-1. Dependence of crystal structure of evaporated Ni-Fe alloy films on composition and substrate deposition temperature. The dotted lines indicate the bulk phase diagram after E.A.Owen and Y.H.Liu (1949) and K.Hoselitz and W.Sucksmith (1943).

It is worth mentioning that the existence of metastable conditions is evidenced by the fact that the transformation between the α and γ phases is effected with a temperature hysteresis that increases with increasing Ni-content. The transformation temperature on heating is typically a few hundred degrees higher than that on cooling, and the temperatures of the transformation are quite independent of the rate of change of temperature between 2 and 150°C/min. (Jones and Pumphrey (1949)). It is also believed that the transformation between the α and γ on continuous heating and cooling has the features of a diffusion-less, martensitic transformation. The α phase formed on continuous cooling is usually called the α_2 phase, and gives broad lines in the x-ray diffraction because of the lattice distortion in the crystal. The martensitic transformation has been the subject of numerous studies so far, but the phenomena observed are not yet fully understood.

The present study concerns the crystal structure of Ni-Fe alloy films as a function of substrate deposition temperature and alloy composition. All electron diffraction was performed at room temperature. The films examined were evaporated onto cleaved NaCl single crystal substrates as described in detail in Appendix 1. Vacuum during deposition was about 10^{-7} Torr, evaporation rate was about 10 Å/sec, and cooling rate after deposition was about 40°C/min. The film thickness was about 500 Å. The samples were floated off the substrate in water and left in the water for about three minutes so that all NaCl from the substrate was completely dissolved. Then, the sample was picked up on an electron microscope grid for examination in the electron

microscope. The transmission electron diffraction was carried out in the RCA EMU 2 and 3 electron microscopes, operated at 50 kV and 100 kV, respectively. Crystal structure was determined by examining the rings or spots in the diffraction photograph. In the case of mixture phases, the relative volume of the two phases was estimated from the relative intensity of the rings or spots. The alloy composition was varied from 5% to 100% Ni and the substrate deposition temperature from 25 to 500°C. The other evaporation parameters, such as degree of vacuum, evaporation speed, cooling rate after deposition and substrate surface condition, were kept as constant as possible, and the present results are believed not to be influenced significantly by fluctuations in these parameters.

The resulting phase diagram is shown in Fig. 3-1. In this figure, the crystal structure measured at room temperature is indicated as a function of substrate deposition temperature and alloy composition. The α phases are shown by an open circle, the γ phases by a shaded circle and a mixture phase of the two by a partially shaded circle in which the degree of shading gives a rough estimate of the ratio of the α and γ phases. In comparing the data with the phase diagram of bulk alloys, it should be remembered that for thin films the ordinate represents the deposition temperature while for bulk materials the ordinate represents the temperature at which the crystal structure was determined. In the present results, the α structure is found at all temperatures for Fe rich composition, while the γ structure is found for Ni rich composition. The mixture of α and γ phases is found between 5% and 45% Ni, with its exact location varying greatly with substrate

deposition temperature. The diffraction photos in Fig. 3-2 show the gradual change of phase for films with 30% Ni content as the substrate deposition temperature is varied from 25 to 500°C. At room temperature only the α phase is found. At higher temperature, the γ phase appears, and the α phase decreases with increasing temperature, disappearing at substrate deposition temperatures above 400°C.

Approximate boundaries between the single and the mixture phases are shown by the solid lines in Fig. 3-1. These boundaries correspond to about 10% transformation. The important result which can be seen in this figure is that the phase diagram of thin films is in good agreement with that for bulk materials at temperatures above 400°C. It should be recalled that the ordinate in the figure for bulk phase diagram does not have the same meaning as that for thin films. However, the two phase diagrams are in good agreement. This close agreement suggests the following argument. The crystal structure determined at room temperature in a thin film is very close to the structure at time of deposition since the phase transformation rate is very slow compared to the cooling rate after formation of the film. If the film is formed in the equilibrium structure for that temperature then the diagram of Figure 3-1 would represent a true equilibrium diagram.

For thin films the boundaries between the mixture and the single phases shift toward each other at temperatures below 300°C, and the mixture phase essentially disappears at temperatures below 100°C, as shown in Fig. 3-1. No corresponding behavior is seen in the

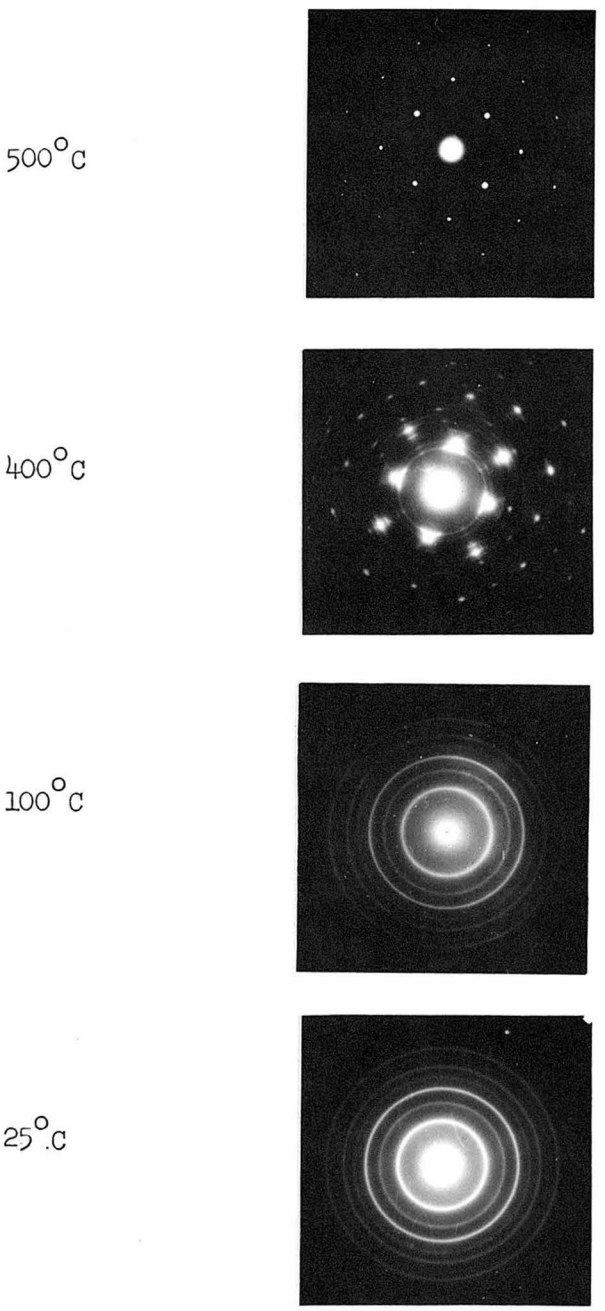

Fig. 3-2. Diffraction photographs of 30%Ni-Fe alloy films evaporated onto NaCl substrates, taken at 50 kV.

equilibrium phase diagram for bulk alloys. This does not support the suggestion in the previous paragraph that the thin film data might also represent the bulk equilibrium situation. Certainly the data by Owen and Liu do not appear to support this statement, although as discussed earlier their data may not represent a true equilibrium state. The data of Hoselitz and Sucksmith do not deviate from the present results by a significant amount, but their data do not extend to temperatures low enough to establish or even indicate the disappearance of the mixture phase.

It should also be noted that although epitaxial growth is found at temperatures above 300 to 400°C, the existence or absence of epitaxy seems to have no significant effect on the type of crystal structure. Examples of epitaxial growth are shown in Figs. 3-3 a and b. Both the f.c.c and b.c.c films have the epitaxial orientation of $(100)_{Ni\text{-}Fe} \parallel (100)_{NaCl}$. The additional satellite spots near those corresponding to the basic (100) epitaxial orientations may be due to double diffraction (Burbank and Heidenreich (1960)) or different epitaxial orientations (Ogawa, Watanabe and Fujita (1955)). The film of Fig. 3.3 b shows the partial epitaxial growth for the b.c.c struture. In general, the epitaxial growth temperature for the b.c.c(α) structure was found to be higher than that for the f.c.c(γ) structure.

In summary, through use of electron diffraction, the crystal structure of vacuum deposited films was determined over the composition range 5% to 80% Ni, with substrate temperature during deposition varied throughout the range 25 to 500°C. The phase diagram determined

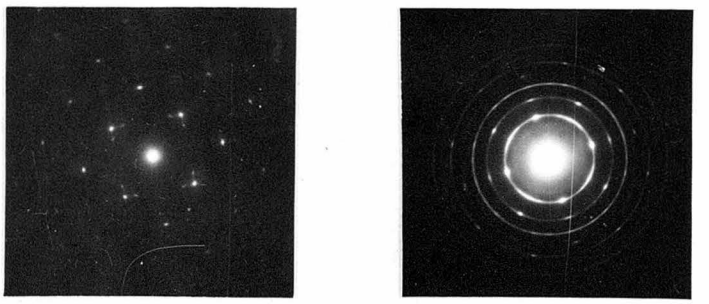

(a) 60%Ni-Fe (b) 5%Ni-Fe

Fig. 3-3. Diffraction photographs, exhibiting the epitaxial growth for the f.c.c structure (a) of the 60%Ni-Fe alloy film and for the b.c.c structure (b) of the 5%Ni-Fe alloy film, deposited onto NaCl substrates at 400°C. The photographs were taken at 50 kV.

in this way has boundaries which are in good agreement with the equilibrium boundaries for bulk materials above 400°C. It is suggested that even though there is no data available on the phase diagram of bulk materials at temperatures below 300°C, the equilibrium boundaries of bulk materials may be indicated by the present results for thin films. The ($\alpha + \gamma$) mixture phase disappears below 100°C. Although epitaxial growth occurs at high temperatures, the existence or absence of epitaxy has no significant effects on the type of crystal structure.

3.2.2. Lattice Parameter of Ni-Fe Alloy Evaporated Thin Films

The lattice parameter of a solid solution binary alloy is often found to vary approximately linearly with composition, except in a two phase region where the lattice parameters remain constant. This rule of behavior, called Vegard's Law, is expected to be followed if the two phases represent the true equilibrium structure. The question has been raised in the literature (Nagakura et al. (1963)) whether the lattice constant of evaporated thin films varies in this way, but no systematic study has been reported. The present section is concerned with an investigation of the lattice parameter of Ni-Fe alloy films. The results will be discussed in connection with the phase diagram of Ni-Fe films previously discussed in the Section 3.2.1.

Alloys of nickel and iron were evaporated in a vacuum of about 10^{-7} Torr onto cleaved NaCl single crystal substrates. The evaporation speed was about 10 Å/sec. After evaporation, the films were cooled as rapidly as possible without admitting gas to the vacuum system. The cooling rate was about 40°C/min. The film composition was varied

from 0% Ni to 100% Ni as determined by X-ray fluorescence, and the substrate deposition temperature was varied from room temperature to 500°C. The film thickness was between 200 Å and 700 Å. Transmission electron diffraction was performed in an RCA EMU-3 electron microscope at 50 and 100 kV. For calibration purpose, evaporated thin films of gold 400 Å in thickness were used. The lattice parameter for the gold films was assumed to be the same as bulk material and the most probable value was taken to be 4.0783 Å (Wyckoff (1948)). There is however a possible uncertainty of almost 0.2%, since a recent publication (Otooni (1968)) reports a lattice parameter of 4.071 Å perpendicular to the plane of the film when still adhering to the substrate. Except for this uncertainty, the probable error in lattice constant determination is estimated to be about 0.2%.

It is seen in Fig. 3-1 that the phase diagram has boundaries which are in fair agreement with the published equilibrium boundaries for bulk materials only above 400°C. The (α = γ) mixture phase disappears below 100°C. For the γ phase, the measured values of lattice parameter for bulk materials are shown in Fig. 3-4. In the figure, the data corresponding to different substrate deposition temperatures are designated by different symbols. The measured lattice parameter a_o increases with decreasing Ni composition from a_o = 3.527 Å at 100% Ni to a_o = 3.591 Å at 42% Ni. For composition below 42% Ni, the measured lattice parameter is essentially constant at about 3.590 Å. Within the small scatter of the experimental data, it was found that the measured lattice parameter did not depend on substrate deposition

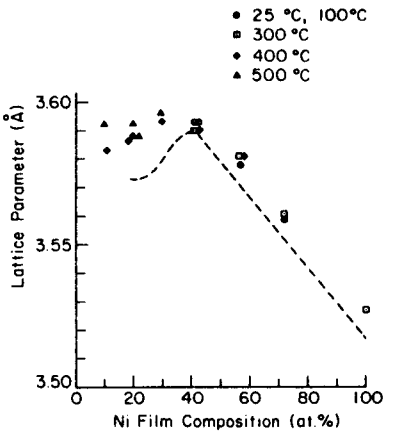

Fig.3-4. Lattice parameter of the γ phase as a function of Ni composition for films deposited at various temperatures. The dotted line indicates the lattice parameter for bulk material after Bozorth (1951).

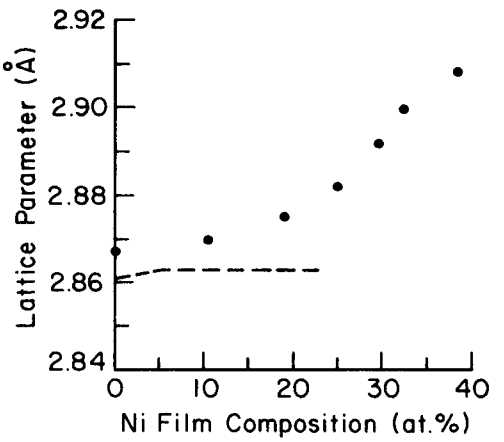

Fig.3-5. Lattice parameter of the α phase as a function of Ni composition for films deposited at 25° C. The dotted line indicates the lattice parameter for bulk material after Bozorth (1951).

temperature. For comparison, the dotted line shows the value of the lattice parameter for bulk material at 25°C determined by X-ray diffraction (Bozorth (1951), Owen (1937)). For bulk alloys the lattice parameter increases linearly with decreasing Ni to 40% Ni composition; below 40% Ni, the lattice parameter decreases with decreasing Ni composition. Above 40% Ni, the present data are systematically about 0.2% larger than the lattice parameter of bulk alloys. Below 40% Ni, the difference becomes larger. In particular, the change in lattice parameter for bulk alloys between 20 and 40% Ni does not seem to be present in the case of evaporated films.

It should be mentioned that Nagakura and co-workers (1963) measured the lattice parameter of the γ phase of evaporated Ni-Fe alloy films with composition range between 18 and 23% Ni. The mean measured value of the lattice constant was 3.591 Å, in good agreement with the present data in this composition range.

For the α phase, it was found that the lattice parameter a_o for films deposited at 400°C does not depend on the Ni composition between 5% and 30% Ni. The lattice parameter had an average value of 2.874 Å with mean deviation 0.3%. However, for films deposited at room temperature, the lattice parameter does depend on Ni content. As shown in Fig. 3-5, the lattice parameter increases with increasing Ni composition from a_o = 2.866 Å at 0% Ni to a_o = 2.910 Å at 41% Ni. The dotted line in Fig. 3-5 indicates the published lattice parameter for bulk material at 25°C, determined by X-ray diffraction (Owen, Yates and Sully (1937)). The bulk lattice parameter increases slightly

with Ni composition from $a_o = 2.861$ Å at 0% Ni up to $a_o = 2.863$ Å at about 5% Ni and then remains constant up to 23% Ni composition. The present data are in reasonable agreement with those for bulk material only in the composition range 0% to 10% Ni. The sharp increase in the lattice parameter with Ni composition beyond 20% Ni would not be predicted from the bulk material data.

The most important question raised by the data of Fig. 3-1 is whether the crystallites of the two phases have equilibrium composition corresponding to the temperature at time of deposition. This would be a reasonable supposition since the films are formed rather slowly (3 atomic layers per second), the crystallites are small (about 100 Å), and the films are quenched rapidly to room temperature. Since this would also imply that the boundaries in the diagram are equilibrium ones, the question could be answered in part by comparison with bulk equilibrium phase boundaries. However, as can be seen in Fig. 3-1, there are no such data available below 300^o, and data for bulk material from different laboratories are in substantial disagreement in the range from 300^o to 400^o. Another way to test the hypothesis is by comparison of the measured lattice parameters with predictions based on empirical rules such as Vegard's Law.

At first glance the data of Fig. 3-4 for the γ-phase appear to satisfy this rule with the break in slope occuring in the region 40 to 45% Ni, in good agreement with the low temperature Y-phase boundary of Fig. 3-1. However all data in Fig. 3-4 below 41% Ni correspond to high substrate temperatures. Fig. 3-1 shows that the lattice

parameter for temperatures of 400° and 500° should show a break in slope at 35 and 25% Ni (rather than 45% Ni) and therefore mixture phase lattice constants of 3.606 and 3.619 Å, respectively. In other words, the high temperature data of Fig. 3-4 are inconsistent with Vegard's Law and the γ-phase boundary shown in Fig. 3-1.

Data for the α-phase are in qualitative agreement with Vegard's Law. According to the phase diagram in Fig. 3-1, two phases are present at 400°C throughout the composition range used. This then is consistent with the observed constant lattice parameter. At room temperature only one phase is present and variation of lattice constant is to be expected. However, the measured lattice constant of Fig. 3-5 does not increase linearly with composition.

In summary, the following points should be emphasized:

(1) For films deposited at 25°C, only α-phase crystallites are present from 0 to 40% Ni, and only γ-phase crystallites from 45 to 100% Ni. For 25°C films, the measured lattice parameter from the γ-phase is about 0.2% above that of bulk materials. The same is true of the α-phase only in the composition range 0 to 10% Ni.

(2) From 10% Ni to 40% Ni the lattice parameter of the α-phase increases much more rapidly than would be expected from published bulk material data.

(3) Whether Fig. 3-1 represents an equilibrium diagram cannot be answered with certainty from consideration of Vegard's Law since deviations from this law appear to be too large.

3.2.3. Crystal Structure of Ni-Co Alloy Thin Films

It is known that Co-Ni alloys form a continuous series of solid solutions in the γ-phase (f.c.c) at temperatures above 500°C. At lower temperatures the ε-phase (h.c.p) is found for the high cobalt alloys. The structures of the γ- and ε-phases were first confirmed by X-ray diffraction by Masumoto (1926) and Osawa (1930). The hysteresis of the transformation temperature between the ε and γ was also determined by measuring changes in properties on heating and cooling (Masumoto (1926), Hashimoto (1937) and Broniewski and Pietrik (1935)). The hysteresis of the transformation is roughly constant independent of composition, and the separation of the two temperatures is 70 to 100°C as shown by the dashed lines in Fig. 3-6. In the bulk alloy, it is believed that the transformation between ε and γ is diffusionless and takes place slowly, just as in the case of Ni-Fe alloys.

The crystal structure in Ni-Co alloy films has been studied by electron diffraction. This investigation was originally motivated by the knowledge that this alloy has a phase transition between ε- and γ-phases, and some corresponding change in magnetic properties might be found as was the case with Ni-Fe alloys. The Ni-Co alloy films were evaporated in vacuum onto NaCl crystals as explained in detail in Appendix 1. The two phases observed are the ε (h.c.p) and the γ (f.c.c). Diffraction photographs of Co films deposited at 25 , 200, 300, and 350°C are shown in Fig. 3-7. For the ε-phase it was found that the ratio of c/a is 1.622, which is not far from the ideal ratio for hexagonal closest packing (c/a = 1.633). For bulk

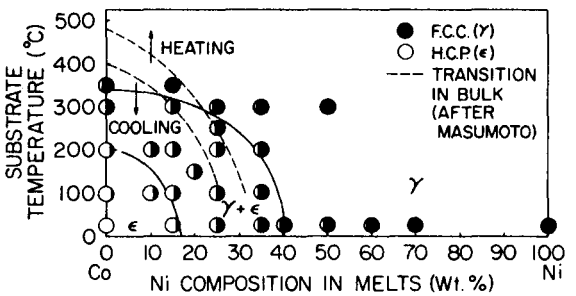

Fig.3-6. Dependence of crystal structure of evaporated Ni-Co alloy films on composition and substrate deposition temperature. The dotted lines indicate the hysteresis of the transformation after Bozorth (1951).

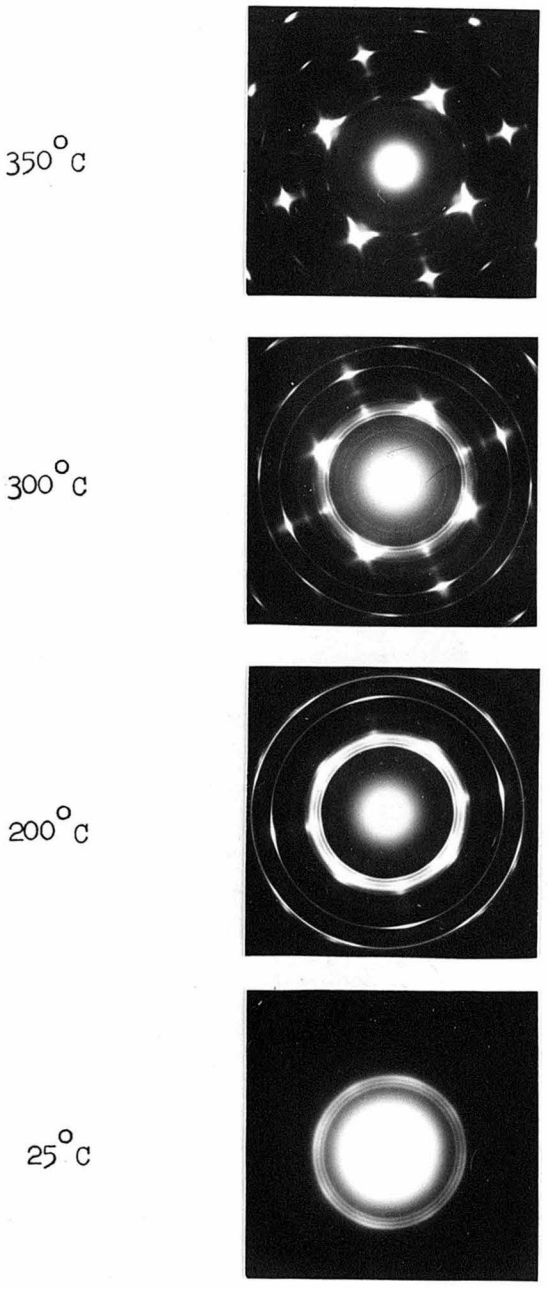

Fig.3-7. Electron diffraction photographs of Co films for various deposition temperatures. The films were deposited onto NaCl substrates. The photographs were taken at 100 kV.

materials, the ratio of 1.62 has been reported (Bozorth, "Ferromagnetism"). It can be seen in Fig. 3-7 that epitaxial growth occurs at quite low temperatures. Even at room temperature a very weak partial epitaxy is found. This was not observed at such low temperatures in Ni-Fe alloy films.

The observed phase diagram is shown in Fig. 3-6. The ratio of the two phases in the mixture region was determined by the relative intensity of the spots or rings, mainly of the $(100)_{h.c.p}$ and $(200)_{f.c.c.}$ which are not coincident with or close to corresponding diffraction features from the other structure. One can see that the phase transition between ε and γ takes place very gradually over a wide range of composition and substrate deposition temperature. This may be because the crystallographical similarity between h.c.p and f.c.c structures gives nearly equal energy for the two structures. For ease of comparison with the bulk transition boundaries, solid lines are used in Fig. 3-6 to show approximate boundaries for 70% transformation. Unlike the phase diagram for Ni-Fe alloy films, the mixture phase ($\varepsilon + \gamma$) remains at low temperature. On the other hand, for substrate deposition temperature above 350°C, the mixture phase vanishes and only the γ phase is found over the entire composition range. It would be surprising that the mixture range in thin films be so wide if the diagram in any way represents the equilibrium situation. In this respect the data for Ni-Fe and Ni-Co thin films appear to be at variance. Since no data on the range of the mixture phase in bulk materials have been

reported, it is not possible to compare directly the thin film results with that for bulk materials.

3.3. Crystallite Size in Thin Films as a Function of Substrate Deposition Temperature

It is quite plausible that crystallographic microstructures, such as crystallites, may have an influence on the local distribution of magnetization, called ripple structure. Indeed, the accepted theories of magnetization ripple predict a structure which is related to the mean size of the crystallites. Thus, the crystallite size must be known to discuss the ripple theories in a quantitative way. No comprehensive study of crystallite size in ferromagnetic thin films is available and only a few experimental measurements have been published (Wiedenmann and Hoffmann (1964)). In order to support the research on ripple structure discussed in the next chapter, it was felt necessary to make additional independent measurements. The present section concerns especially the crystallite size in Ni-Fe and Co films, as a function of substrate deposition temperature.

The films were prepared by vacuum deposition onto cleaved NaCl single crystal substrates in vacuum of about 10^{-7} Torr. Details of the deposition procedure are described in Appendix 1. The films were stripped from the substrates in water and mounted on microscope grids. Observation was made by means of high resolution transmission electron microscopy using an accelerating voltage of 100 kV. The films examined in the present study had thickness of 100 to 400 Å.

Typical transmission electron microscope photographs for Ni-Fe alloy films are shown in Fig. 3-8. The increase in size of crystallites with increasing substrate deposition temperature is clearly evident in the photographs. Electron micrographs of Co films are shown in Fig. 3-9. The average crystallite size is very nearly the same as that for Ni-Fe alloy films deposited at the corresponding substrate deposition temperature. Since there is little difference in crystallite size between Ni-Fe and Co films, data for both materials were averaged. The average crystallite size is shown in Fig. 3-10 as a function of substrate deposition temperature. The bar indicates the range of scatter in the data. The crystallite size increases with temperature from a mean value of about 100 Å at 25°C to about 600 Å at 500°C. It should be recalled, as mentioned in the previous section, that epitaxial growth is found above 350°C in Ni-Fe alloy films evaporated onto NaCl substrates. However, the occurence of epitaxy does not seem to influence the size of the crystallites. In Fig. 3-10 the size increases monotonically with temperature and the curve does not indicate any change with the onset of epitaxy. Thus, it may be inferred that films evaporated onto glass substrates (without epitaxy at any temperature) should consist of crystallites with approximately the same size as indicated in the figure. These results may be compared with the data by Wiedenmann and Hoffmann (1964). They examined surface replicas of Ni-Fe alloy films evaporated onto glass substrates, inferring crystallite size from surface features. Transmission micrographs of selected thin samples were used to confirm the validity of

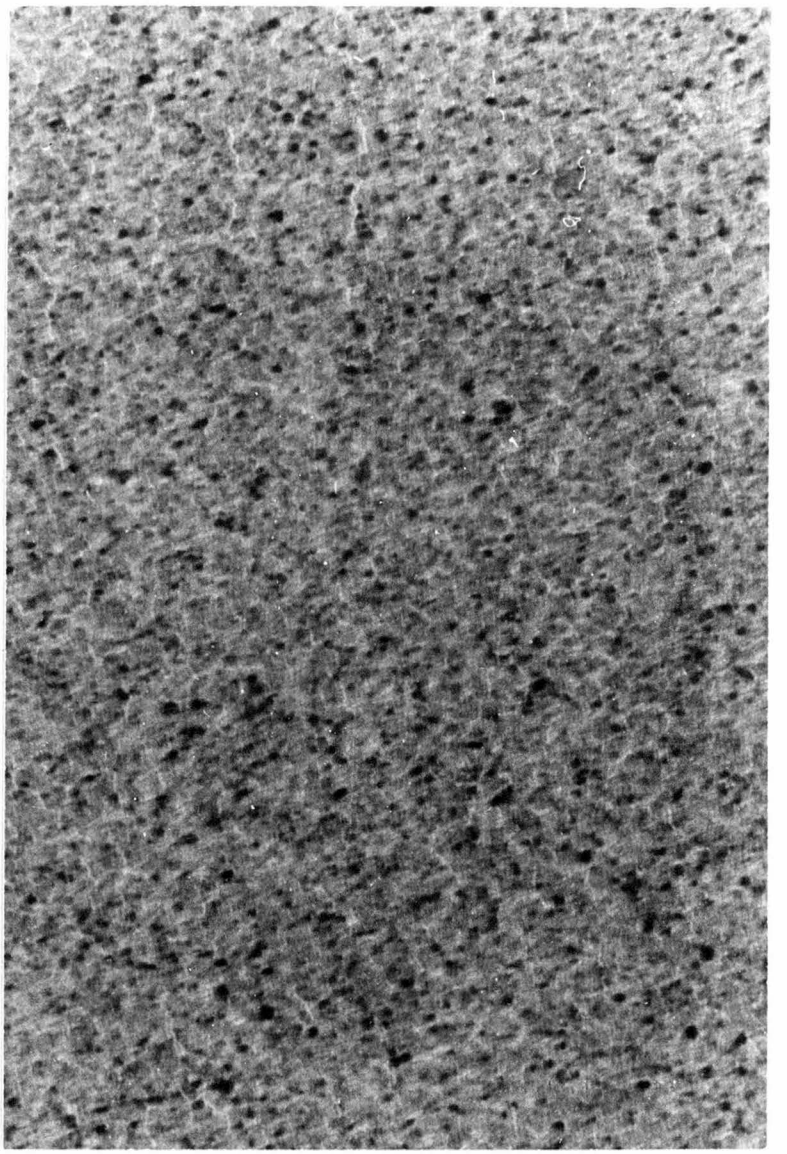

Fig. 3-8a Electron transmission micrograph of a 76%Ni-Fe alloy film. The substrate deposition temperature is 25°C. The photograph was taken at 100 kV.

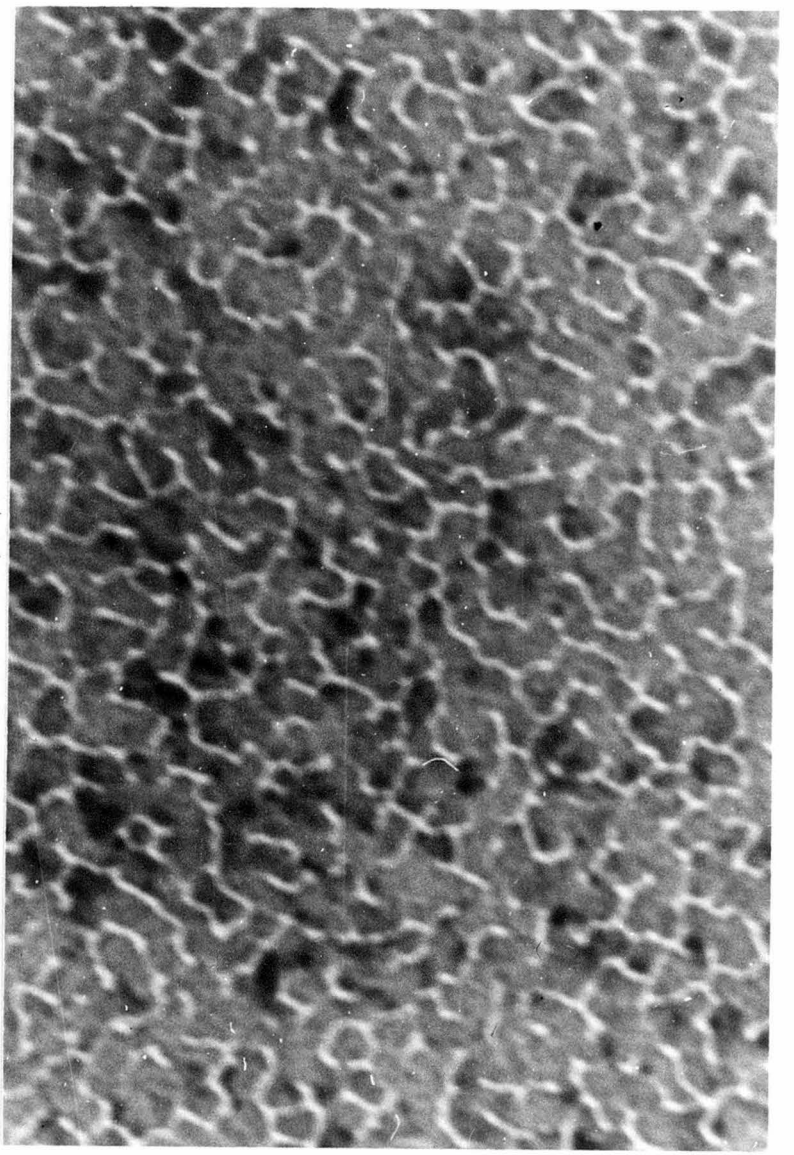

Fig.3-8 b Electron transmission micrograph of a 76%Ni-Fe alloy film. The substrate deposition temperature is 300°C. The photograph was taken at 100 kV.

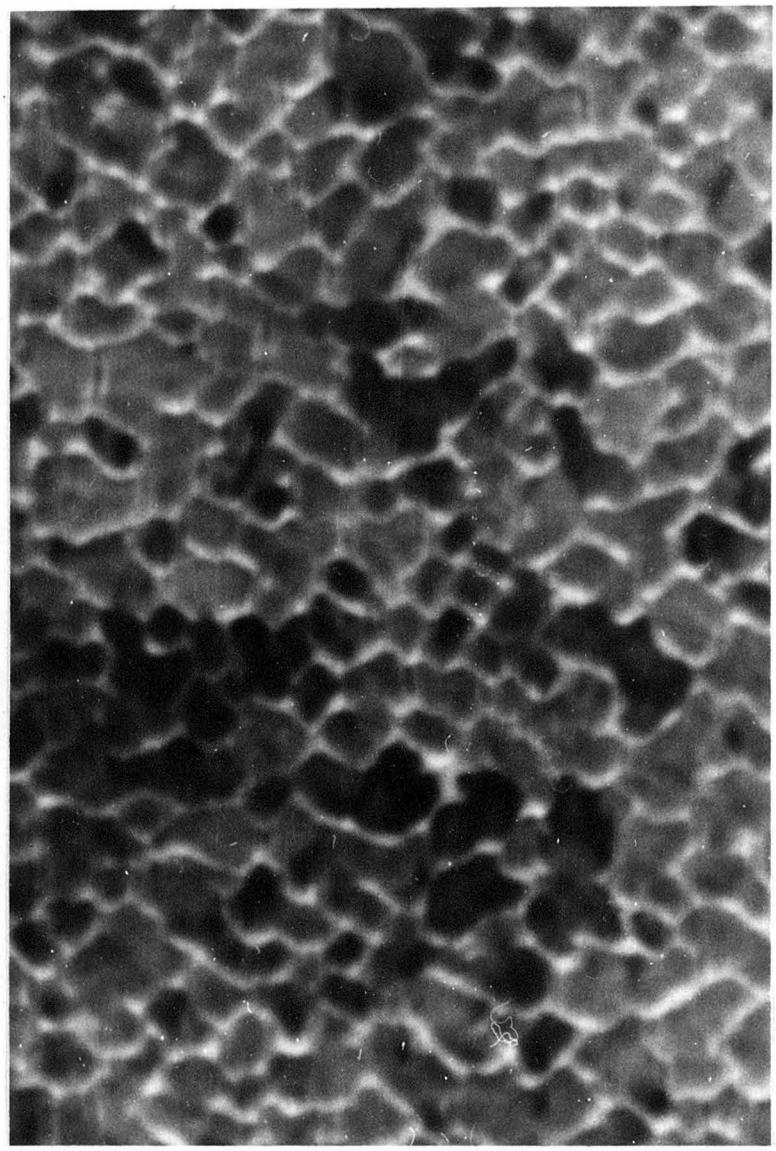

Fig.3-8c Electron transmission micrograph of a 76%Ni-Fe alloy film. The substrate deposition temperature is 400°C. The photograph was taken at 100kV.

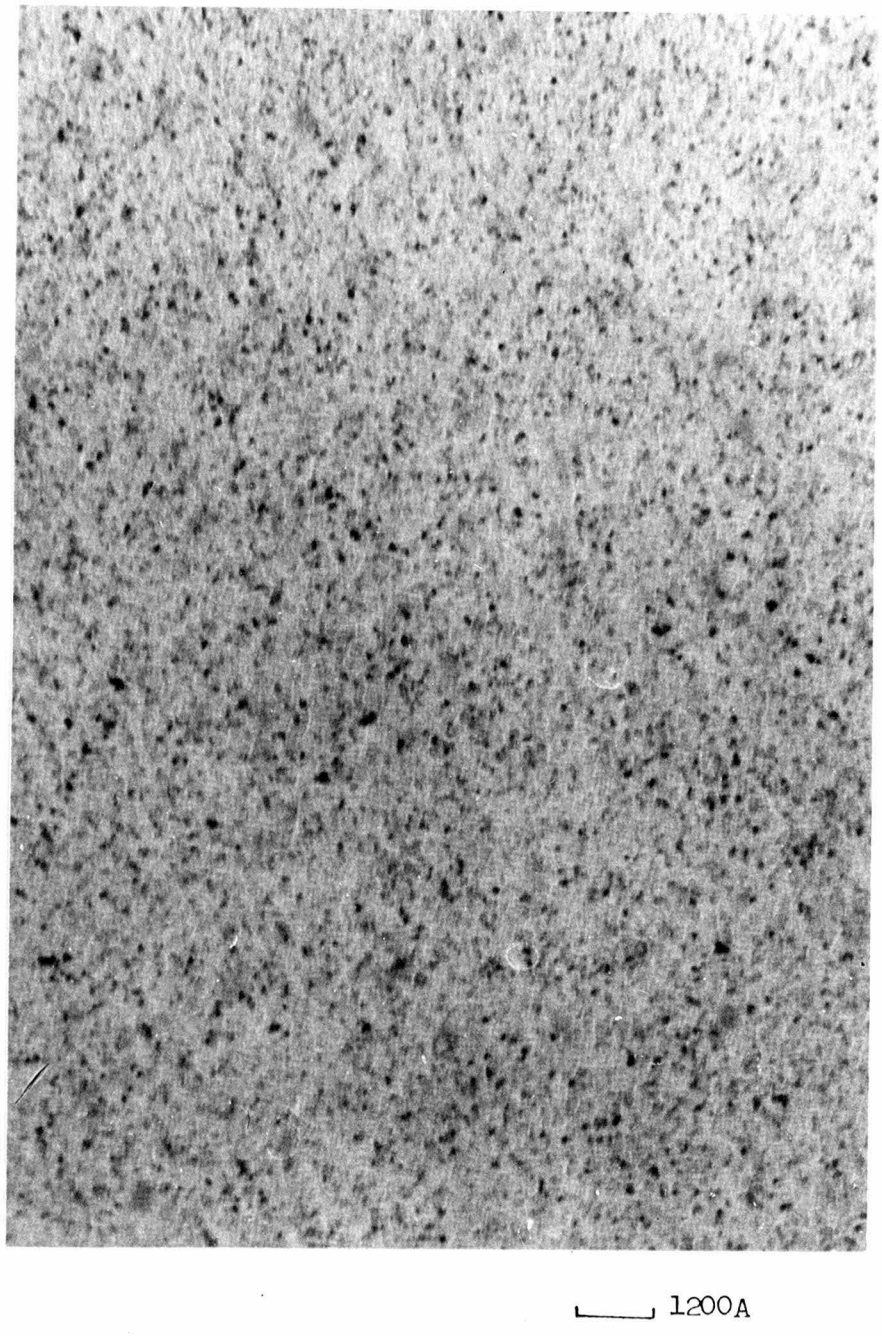

Fig.3-9 a Electron transmission micrograph of a Co film. The substrate deposition temperature is 25°C. The photograph was taken at 100 kV.

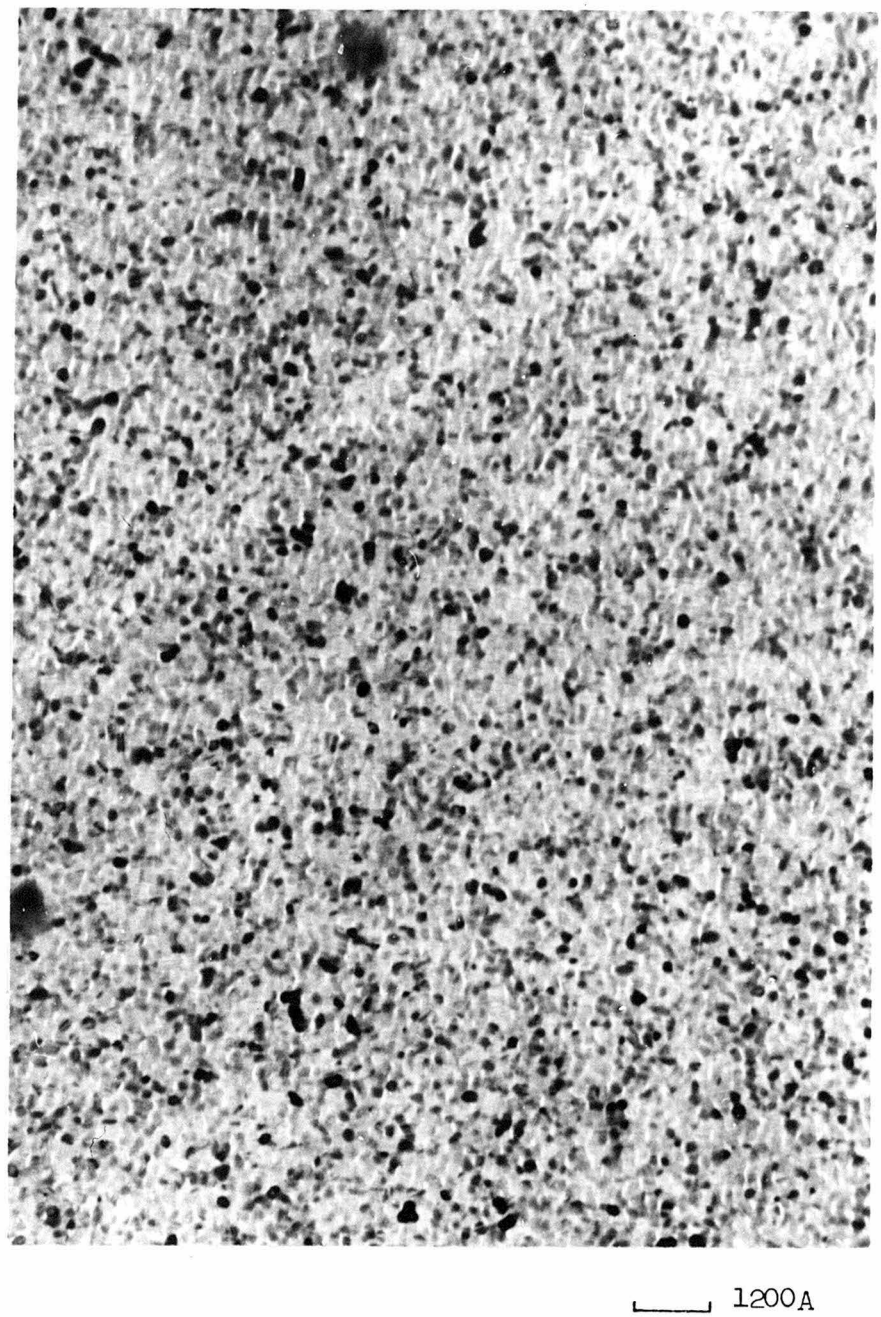

Fig.3-9b Electron transmission micrograph of a Co film. The substrate deposition temperature is 200°C. The photograph was taken at 100 kV.

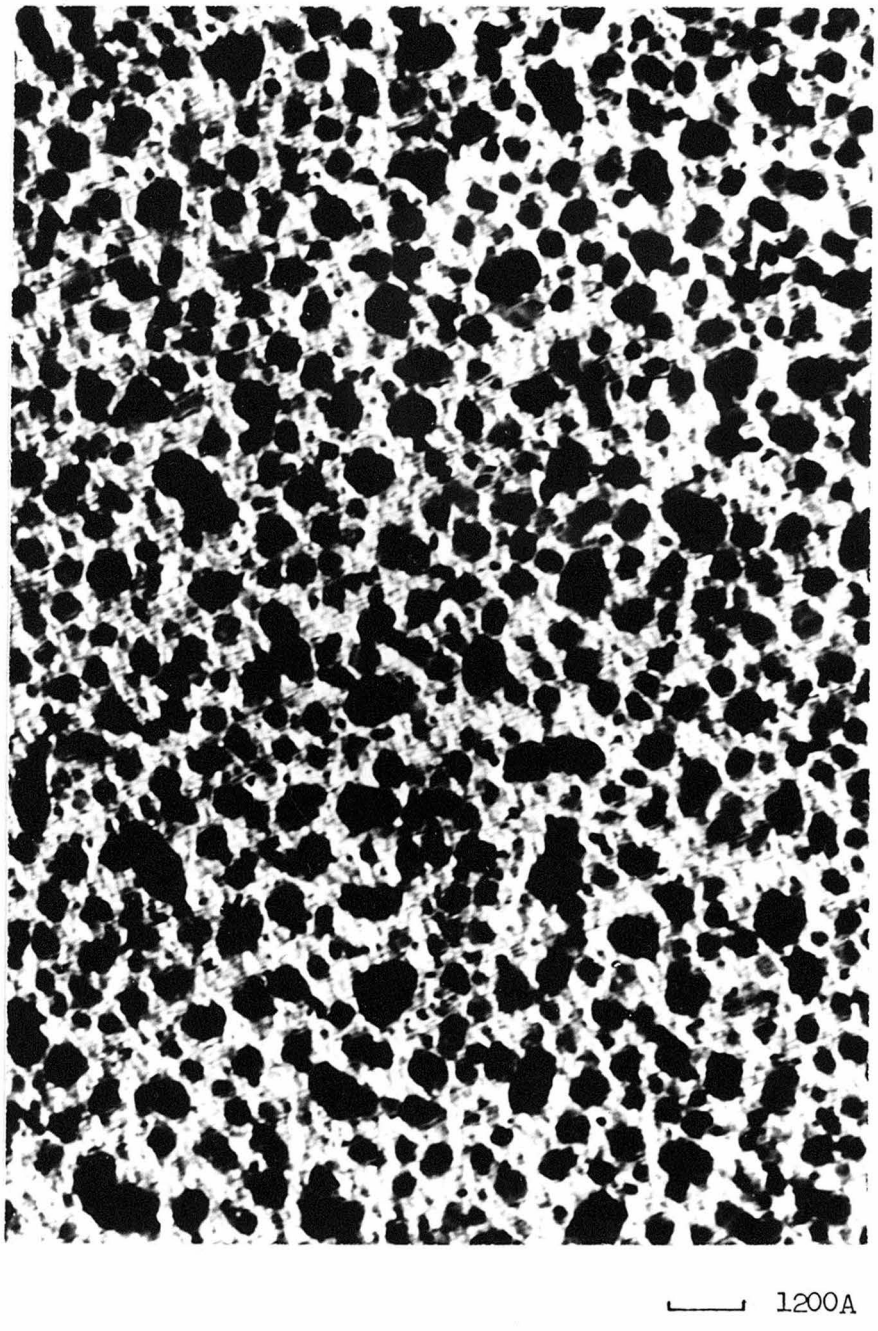

Fig.3-9c Electron transmission micrograph of a Co film. The substrate deposition temperature is 400°C. The photograph was taken at 100 kV.

the method. Their data for Ni-Fe films about 300 Å thick, and evaporated at 1 Å/sec are shown by the dotted line in Fig. 3-10. The agreement between the two sets of data is quite good. Also shown in the figure, by a triangle, is the value obtained by Baltz and Doyle (1964) for a single film deposited at 25°C onto NaCl substrate. This value is also in good agreement with the other data. The film thickness used by them is not given, but it is presumed to be in the thickness range of the present study since the film was also examined by transmission electron microscopy.

The data by Wiedenmann and Hoffmann also show the dependence of crystallite size on film thickness between 100 Å and 1000 Å. The crystallite size was found to increase slightly with film thickness, typically about 50% increase between 100 and 1000 Å. However, the increase was generally less at low temperatures (25°C) and somewhat larger at high temperature (400°C). At the present time, no data by transmission microscopy have been reported on this thickness dependence. However, as discussed earlier, the agreement between the two methods for thin films (100 to 400 Å) suggests that the surface features seen on replica examination correctly indicate crystallite size not only for this thickness range but for thicker films also.

In summary, the crystallite size in Ni-Fe and Co films was examined by high resolution transmission electron microscopy. It was found that the average crystallite size differs very little between Ni-Fe and Co films. The average crystallite size increases with

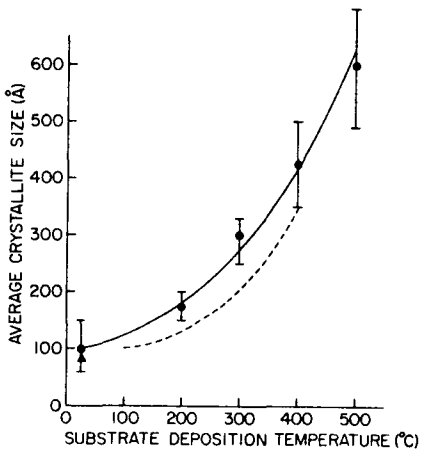

Fig.3-10 The average crystallite size as a function of substrate deposition temperature in Ni-Fe alloy and Co films evaporated onto NaCl substrates. The solid line indicates the present result and the dotted line the data by Wiedenmann and Hoffmann (1965). The triangle point is after Baltz and Doyle (1964).

substrate deposition temperature from about 100 Å at 25°C to 600 Å at 500°C. The present data are in good agreement with the other data reported previously.

3.4. Summary

To understand the magnetic properties of thin films requires knowledge of fundamental, crystallographic properties. However, no systematic study of such properties is found in the literature. Therefore, in the present chapter, the results of a careful study of structural features of Ni-Fe and Ni-Co alloy films has been presented. The crystal structure of Ni-Fe alloy films has been already referred to in the previous chapter in connection with magnetic uniaxial anisotropy.

The phase diagram determined in Ni-Fe alloy films has boundaries which are in fair agreement with the equilibrium boundaries for bulk materials above 400°C and which deviate markedly below 300°C. Although epitaxial growth occurs at high temperature, the existence or absence of epitaxy has no significant effects on the type of crystal structure.

The careful study of lattice parameter of Ni-Fe alloy films was performed by electron diffraction. The following points were emphasized. (1) For 25°C films, the measured lattice parameter for the γ-phase is about 0.2% above that of bulk materials. The same is true of the α-phase only in the composition range 0 to 10% Ni. (2) From 10% Ni to 40% Ni the lattice parameter of the α-phase increases much more rapidly than would be expected from published bulk material data.

The crystal structure study of Ni-Co alloy films indicates the gradual transition between the γ- and ε-phases over a wide range of composition and substrate deposition temperature. Unlike the phase diagram for Ni-Fe alloy films, the mixture phase remains at low temperature. On the other hand, for substrate deposition temperature above 350°C, the mixture phase vanishes and only the γ-phase is found over the entire composition range.

Finally, the average crystallite size in Ni-Fe and Co films was examined by high resolution transmission electron microscopy. It was found that the average crystallite size differs very little between Ni-Fe and Co films. The average size increases with substrate deposition temperature from about 100 Å at 25°C to 600 Å at 500°C. Epitaxy is found in varying degrees at high temperatures, but the existence or absence of epitaxy does not seem to have any effect on the crystallite size.

Chapter 4

Domain Wall Structure

4.1 Introduction

The existence of domains in ferromagnetic materials was first postulated by Weiss (1907). His hypotheses were: 1) A ferromagnetic specimen of macroscopic dimensions contains in general a number of small regions (domains) which are spontaneously magnetized and the net magnetization of the specimen is determined by the vector sum of the magnetic moments of the individual domains. 2) Within each domain the spontaneous magnetization is due to the existence of a "molecular field," which tends to produce a parallel alignment of the atomic dipoles. The explanation of the molecular field in terms of exchange forces was contributed by Heisenberg in 1928, and an explanation of the origin of domains in terms of magnetic field energy was given by Landau and Lifshitz in 1935. The existence of domains may be inferred from the character of the magnetization curve itself. However, by far the most direct and cogent evidence of domain structure is furnished by microphotographs of domain boundaries obtained using the technique of magnetic powder patterns introduced by Bitter, (1931). This is the first method which provided convincing proof that domains exist in a ferromagnetic material, although since that time magneto-optics and Lorentz microscopy have also been used to demonstrate their existence.

Bloch (1932) was the first to study the nature of the transition region or domain wall which separates adjacent domains magnetized in different directions. Bloch's essential idea is that the magnetic dipole direction in going from one domain to another does not change abruptly across one atomic layer, but gradually in a manner determined by the balance between exchange and anisotropy and any other torques.

The exchange energy between two adjacent dipoles is proportional to $(1-\cos\theta)$ and hence for small angles to θ^2 where θ is the angle between the directions of the dipoles. In the absence of other energy sources this would give an infinite width to a domain wall. On the other hand, since the dipoles within the wall are directed away from the direction of minimum anisotropy energy one expects an increase in anisotropy energy which is roughly proportional to the thickness of the wall, thus favoring a wall of zero width. In bulk materials it can be shown that the magnetostatic stray field energy may be neglected. In this case if magnetostrictive effects are ignored the actual wall width as well as its shape can be found by a variational calculation which minimizes the total energy consisting of exchange and anisotropy components.

In thin films, however, the domain wall situation is quite different. As will be discussed in detail in later sections, the magnetostatic stray field energy is no longer negligible and plays an important role in determining the shape of the wall. Néel (1955) was the first to point out the importance of the magnetostatic field of a wall in thin films, and proposed a different type of wall structure from that predicted by Bloch for bulk materials. Since then, attempts to calculate the stray field energy of a wall in thin films have been made on the basis of simple wall models by a number of workers including Middlehoek (1961), Dietz and Thomas (1961), Collette (1964), Brown and LaBonte (1965), Aharoni (1967) and Kirchner and Döring (1968). On the other hand, very little has been accomplished in experimental measurements of domain wall structure in both bulk materials and thin films, and accordingly no meaningful, systematic comparison between the theoretical

predictions and the experimental observations has been possible.

Fuller and Hale (1960) first suggested a method to measure wall width in thin films by a special mode of operation of the electron microscope called Lorentz microscopy. Fuchs (1962) was the first to attempt a systematic measurement of the wall width of Ni-Fe alloy thin films using this method. The results obtained by Fuchs indicated that except for very thin films (of the order of 100Å thickness) the wall widths were much larger than those calculated with the simple wall models of Néel and others. Also, based on an entirely different kind of evidence, Patton and Humphrey (1966) suggested that the actual wall width in thin films is much wider than that calculated from the simple wall models. Therefore, there is some doubt about the validity of the models postulated for the wall structure, and a more systematic investigation of wall width has been urged.

The primary concern in this section is to present new experimental measurements of wall width obtained by Lorentz microscopy in Ni-Fe alloy and Co films, and to discuss the results in conjunction with the theoretical predictions. Furthermore, the validity of the present technique of Lorentz microscopy is a matter of obvious importance, and this will be discussed in detail. Before presenting the experimental results, it is worth discussing briefly the fundamental problem of calculating wall width in thin films and the current wall models based on a one dimensional magnetization rotation. This will be given in the next section.

4.2 Theoretical considerations of domain wall structure

The first studies of the transition layer between two adjacent domains in bulk materials were made by Bloch in 1932. For this reason such domain walls are usually called Bloch walls. The main concept associated with Bloch's model of the transition region is that the change in dipole moment orientation does not occur suddenly across one atomic plane, but gradually over many planes. A Bloch wall is defined as one in which the orientation of a dipole moment changes from that in a given domain to that in a neighboring domain by rotating about an axis normal to the plane of the wall. This is shown schematically in Fig. 4-1(a) for the special case of a 180° wall in a thin film. The x and y axes represent the hard and easy axes in the film plane, and the z axis is the normal to the film plane. The magnetization rotates in the y-z plane.

The magnetostatic stray field term can be calculated from a hypothetical magnetic charge density defined by $\rho_m = -\nabla\cdot\vec{M}$. For a Bloch wall, the divergence of $\overline{M}$ is zero everywhere except where the wall intersects the surface of the material. Therefore, magnetic free charges ρ_m occur only on the intersection surface. If θ_s is the angle between the magnetization direction and the normal to the upper surface of the sample, the magnetostatic charge density at the upper surface σ_m is equal to $M\cos\theta_s$, and the charge density at the opposite lower surface is equal to $-M\cos\theta_s$. The magnetostatic stray field H_s can be thought to arise from these charges. The stray field energy density associated with a wall is given by

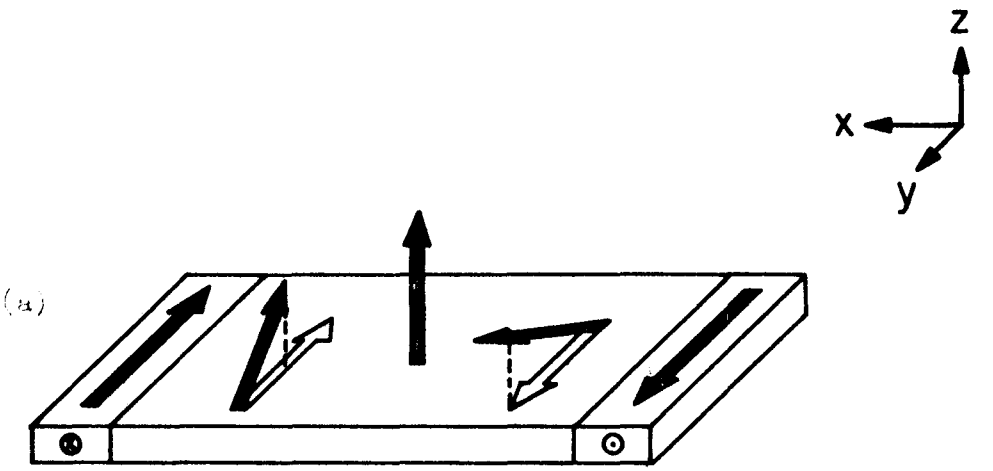

Bloch Wall

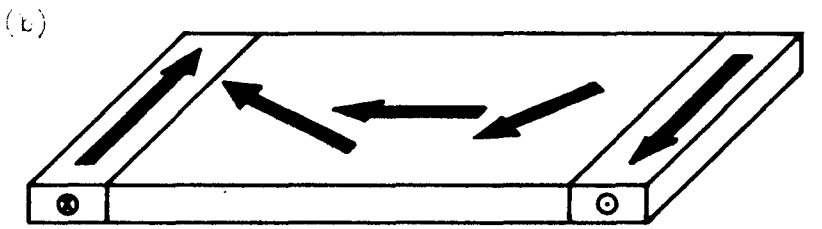

Néel Wall

Fig.4-1 Schematical illustration of magnetization direction in Bloch and Néel walls.

$$E_s = -1/2\ \vec{M} \cdot \vec{H}_s \qquad (4.1)$$

In bulk materials, the positive and negative charges are very far apart in comparison to the wall width, so that throughout most of the wall the field H_s is small and the stray field energy density is likewise small and can be neglected in comparison with the anisotropy and exchange energies.

A one dimensional 180° Bloch wall is one in which the magnetization vector lies in the y-z plane and the angle θ between the magnetization $\vec{M}$ and the y-axis is dependent only on the x-coordinate. For such a wall, exchange energy density is very well approximated by the simple function

$$E_e = \text{exchange energy density} = A\ (d\theta/dx)^2 \quad .$$

In thin films we are primarily interested in the case of uniaxial anisotropy given by the equation

$$E_u = \text{uniaxial anisotropy energy density} = K_u \sin^2\theta \ .$$

In these equations A is the exchange constant and K_u is the uniaxial anisotropy constant as defined by Eq. (2.1). Thus the total wall energy per unit area of wall for a bulk material with ideal uniaxial anisotropy is given by

$$\gamma = \int_{-\infty}^{\infty} \left[K_u \sin^2 \theta + A(d\theta/dx)^2\right] dx \qquad (4.2)$$

The stable magnetization configuration within the wall can be obtained by minimizing the total wall energy with the boundary condition that

$(d\theta/dx)_{x=\pm\infty} = 0$. The result of such a variational problem is

$$\theta = \theta(x) = -\cot^{-1}(\sinh x/\delta_o) \tag{4.3}$$

where $\delta_o = (A/K_u)^{1/2}$.

This is the exact result for the magnetization variation in a domain wall in bulk material with uniaxial anisotropy where no stray field energy and no magnetostriction effects are considered and where the magnetization is considered to be continuously distributed instead of consisting of localized dipoles at atomic sites. The orientation θ of the magnetization expressed by Eq. (4.3) is shown by the solid line in Fig. 4.2(a). For this magnetization distribution the wall width for a 180^o wall has been customarily defined as the product of the total rotation π and the reciprocal of the slope of the magnetization rotation at the center of the wall. In this case, the wall width a_o is expressed by

$$a_o = \pi(d\theta/dx)^{-1}_{x=o} = \pi\delta_o = \pi(A/K_u)^{1/2} \tag{4.4}$$

However, it should be emphasized that this definition of wall width is slightly different from that used in this thesis. For reasons discussed in detail elsewhere, the wall width in the present thesis is defined to be

$$\underline{a(180^o \text{ wall}) = (2)^{1/2}\,\pi(d\theta/dx)^{-1}_{x=o}}$$

so that the wall width in the case of no demagnetizing field becomes $a = \sqrt{2}a_o$. The minimum wall energy per unit area γ_o corresponding to the magnetization rotation expressed by Eq. (4.3) is

$$r_o = 4(AK_u)^{1/2} \tag{4.5}$$

In thin films, the domain wall situation is quite different from this. The free poles at the surface of a Bloch wall are separated by a distance equal to the film thickness, and yield relatively large stray fields and stray field energy which cannot be a priori neglected in comparison with the exchange and the anisotropy energies. In fact, Bloch wall energy density approaches the large value $2\pi M_s^2$ in the limit of zero film thickness. On the other hand, if the magnetization remains in the plane of the film as it rotates from one domain to the other, then the energy density approaches zero in this same limit. It follows that in the limit of zero thickness, the magnetization in a domain wall rotates about an axis perpendicular to the plane of the film instead of about an axis in the plane of the film. Néel first demonstrated (1955) in an approximate calculation that there is a definite range of thickness above zero in which the energy of such a wall is less than that of a Bloch wall. This type of wall, called a Néel wall, is schematically shown in Fig. 4.1(b). The magnetization turns around an axis normal to the film plane (parallel to the z-axis). For this magnetization configuration, there appears no magnetostatic surface charge associated with the wall intersection at the film surface since $M_z = 0$ and $\partial M_z/\partial z = 0$. However, since M_x and $\partial M_x/\partial x$ are non-zero, a magnetostatic volume charge occurs inside the wall, and this in turn produces a magnetostatic stray field.

The wall width calculation in films of finite thickness was first carried out by Néel (1955). For purposes of calculating the magneto-

static field energy, the wall was approximated by a cylinder with an elliptical cross section, while for the calculation of the anisotropy and exchange energies, a linear rotation of the magnetization inside the wall was assumed. The width of the cylinder and the region of linear rotation are both taken to have the width a. Néel further assumed the saturation magnetization M_s itself for the effective magnetization of the cylinder. Middlehoek (1961) has also treated the one dimensional ellipsoidal model for the stray field energy calculation for the wall. However, he used the value $(2)^{-1/2} M_s$ as the effective magnetization of the cylinder in order to get agreement with the exact calculation for the magnetostatic energy in limiting cases. For Middlehoek's model, the total wall energy per unit area γ_B for a Bloch wall is approximated by

$$\gamma_B = \int_{-a/2}^{a/2} (E_s + E_e + E_u)dx$$

$$= \pi a^2 M_s^2/(a+d) + A\pi^2/a + (1/2)aK_u \qquad (4.6)$$

and for a Néel wall,

$$\gamma_N = \pi ad M_s^2/(a+d) + A\pi^2/a + (1/2)aK_u \qquad (4.7)$$

where a is the wall width, d is the film thickness, and E_s, E_e and E_u are the stray field energy, the exchange energy and the uniaxial anisotropy energy densities respectively. Minimizing γ_B and γ_N with respect to the parameter a gives an approximate value for the wall width and energy of Bloch and Néel walls. Such values of wall width and wall energy as a function of film thickness are given by the solid lines in Figs. 4-3 and 4-4. The exchange constant, the saturation mag-

netization and the uniaxial anisotropy constant are taken to have the values $A = 10^{-6}$ erg/cm , $M_s = 800$ oe , $K_u = 10^3$ erg/cc respectively. These values are typical for Ni-Fe alloy films with composition about 80% Ni deposited on substrates at 300°C, and will be used in all cases where various theoretical predictions are compared. However, it should be noted that these values are not appropriate for the material used for the actual wall width measurements discussed in a later section. For practical reasons (namely to avoid epitaxy on NaCl substrates) these films were deposited at room temperature and have a correspondingly higher value of anisotropy energy, $K_u = 3.5 \times 10^3$ ergs/cc.

The calculated wall energy per unit area for a Bloch wall decreases with increasing film thickness, while the wall energy per unit area for a Néel wall increases with increasing film thickness. It is important to note that in the limit of infinite thickness for a Bloch wall and of zero thickness for a Néel wall, the magnetostatic stray field energy terms in Eqs. (4-6) and (4-7) vanish, and one obtains the wall energy per unit area to be

$$\lim_{d\to\infty} \gamma_B = \lim_{d\to o} \gamma_N = \gamma_o = (2)^{1/2}\pi(AK_u)^{1/2} \tag{4.8}$$

and the corresponding wall width a to be

$$a = (2)^{1/2}\pi(A/K_u)^{1/2} = (2)^{1/2}a_o \tag{4.9}$$

The linear wall shape for the limiting cases is shown in Fig. 4-2(a) for ease of comparison with the exact solution.

The wall energy per unit area γ_o for the limiting case of the linear wall model, Eq. (4.8), differs from that expressed by Eq. (4.5)

for the exact model by only 10%. However, the wall width defined by Eq. (4.9) for the linear model differs by a factor of $(2)^{1/2}$ from that given by Eq. (4.4). Though this difference is not large, it is desirable to have the same wall width value for both models at infinite film thickness and at zero film thickness where the effect of the demagnetizing field vanishes. In the light of this, the wall width except for the linear rotation model is defined to be larger than the customary definition by a factor of $(2)^{1/2}$

$$a = (2)^{1/2}\pi(d\theta/dx)^{-1}_{x=o} \tag{4.10}$$

instead of the value given by Eq. (4.4). Comparison of the two wall shapes in Fig. 4-2(a) shows the latter definition to be quite reasonable from the physical standpoint.

It is an unsolved problem whether the linear rotation ellipsoidal magnetization model for wall structure gives accurate width and energy for real films which have neither zero nor infinite thickness, or whether a more sophisticated assumption of the magnetization configuration could lead to a more accurate structure and lower energy. In an attempt to clarify this point, several workers have made calculations on the basis of more complicated one-dimensional wall models (Dietz and Thomas (1961), Collette (1964), Brown and LaBonte (1965), Oredson and Torok (1967) and Kirchner and Döring (1968)). More recently Aharoni (1967) completed a calculation for a two-dimensional wall model.

Dietz and Thomas used a simple function for the distribution of magnetization in a one-dimensional wall model, and computed all energy terms (exchange, anisotropy and stray field) corresponding to this

assumed distribution function. The assumed functional form is

$$\sin \theta = \left[1 + (x/b)^2\right]^{-1} \quad 0 < \theta < \pi \tag{4.11}$$

where θ is the angle between the magnetization direction and the easy direction in the film plane. Wall width and energy were obtained by minimizing the total energy with respect to the parameter b, which is directly related to the wall width.

Since the shape is quite similar to that of the exact solution for zero or infinite thickness, it is not surprising that the predicted wall width agrees quite well with the exact calculation for these limiting cases. Comparison of shape and size is shown in Fig. 4.2(b). In their published work, Dietz and Thomas defined the wall width to be 2b, which is of course different from the other definitions discussed above. For consistency it is necessary to convert their results to conform to the definition given in Eq. (4.10).* The wall widths obtained in this way are shown in Fig. 4-3. These values are in good agreement with those obtained by Middlehoek for both Bloch and Néel walls. The wall energies per unit area are shown in Fig. 4-4(a) and (b) for Bloch and Néel walls respectively. The wall energy does not differ significantly from those obtained by Middlehoek either.

In the above discussions, the wall shapes assumed by Middlehoek and by Dietz and Thomas were considered to be unchanged with film thickness. It is quite reasonable to surmise that the wall shape would vary with thickness, depending on the relative importance of the magnetostatic stray field. Therefore, it is open to question whether

*It is necessary to multiply the Dietz and Thomas wall width by the factor $\pi/2$ to give the wall width expressed by Eq. (4.10).

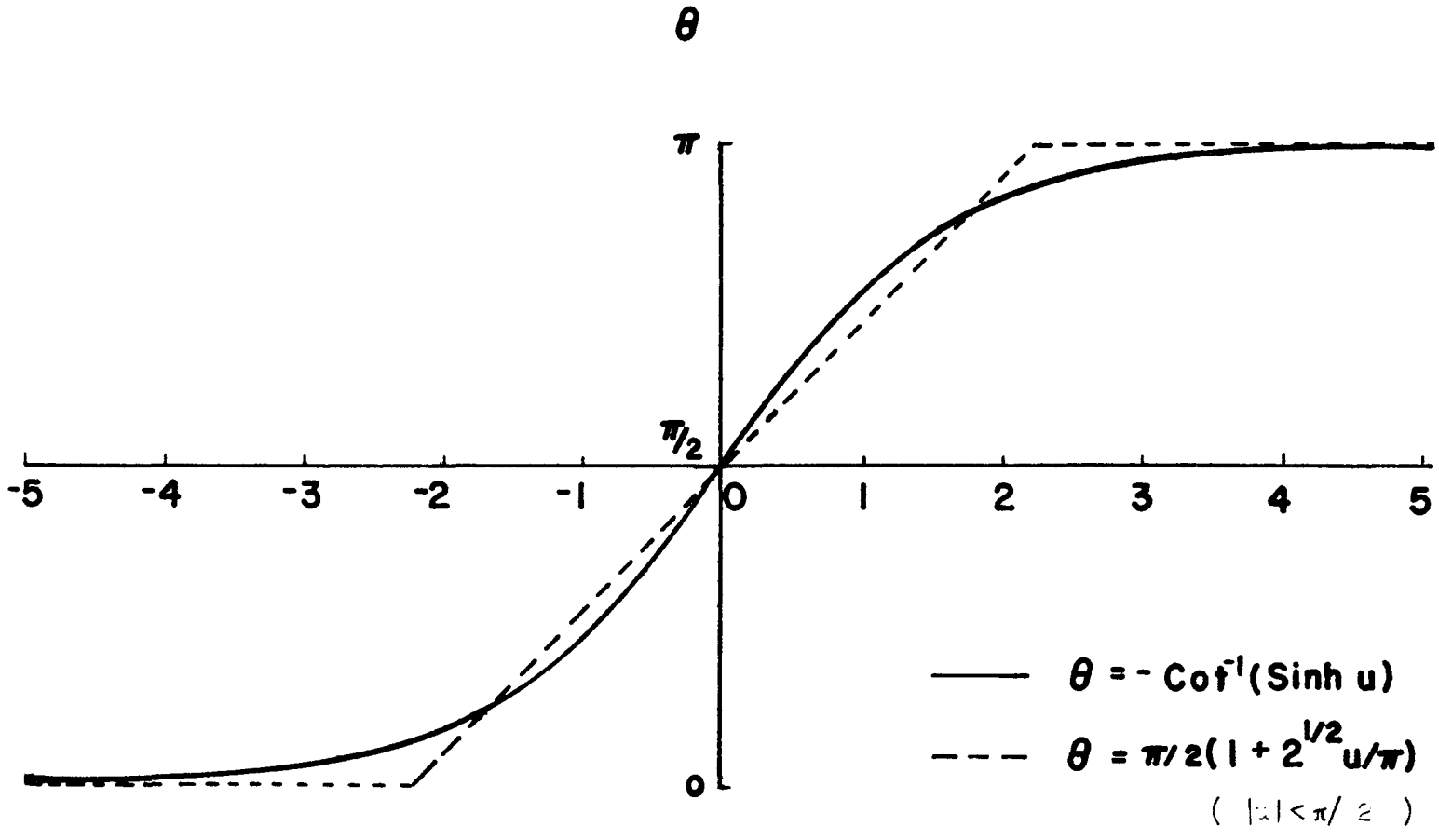

Fig.4-2(a) One dimensional magnetization rotation for a 180° wall.

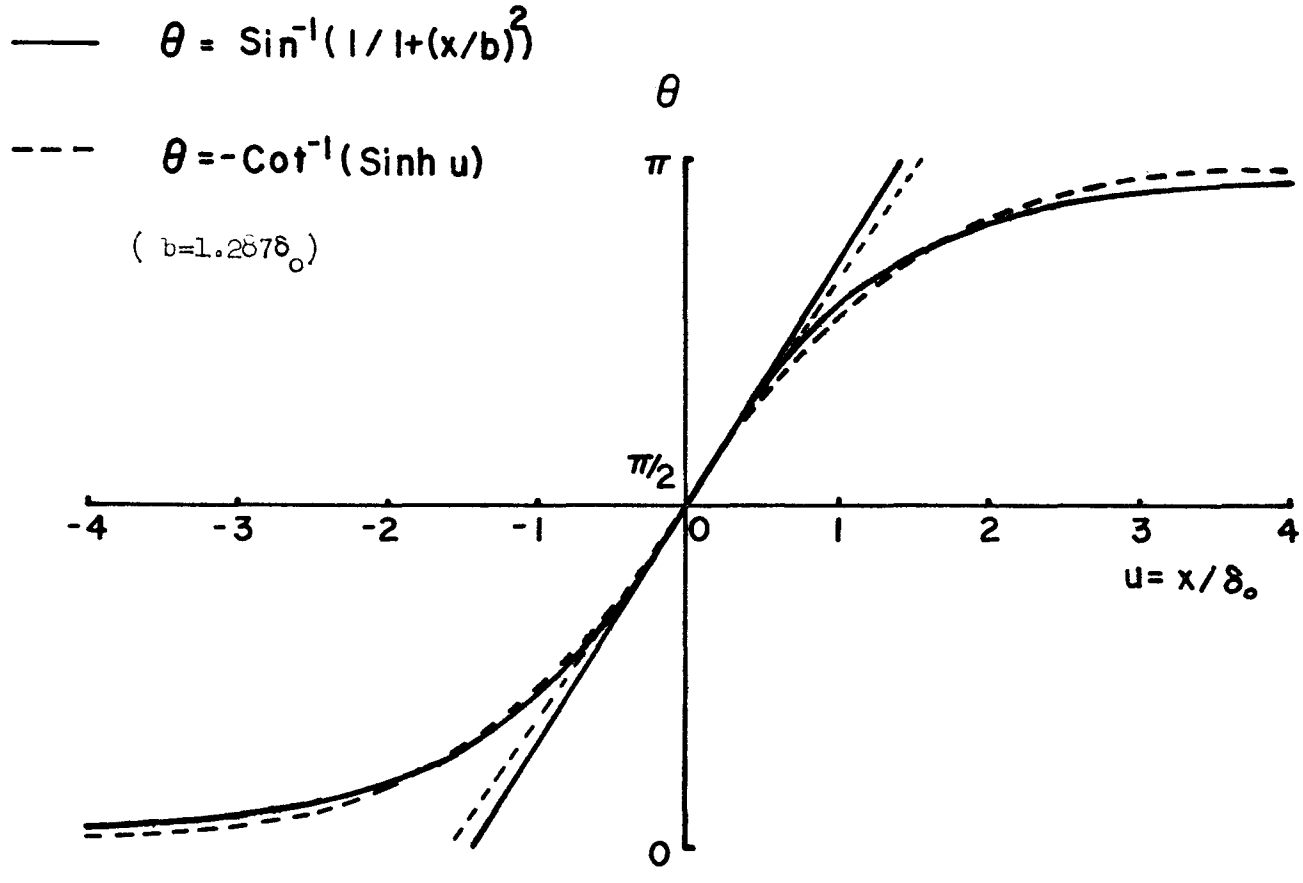

Fig.4-2(b) One dimensional magnetization rotation for a 180° wall for Dietz and Thomas model and the exact solution for zero or infinite film thickness, straight lines are extrapolation of slope at wall center.

these models can be used to give a good estimate of the actual wall size. In an effort to answer this question, Collette (1964), Brown and LaBonte (1965), and Kirchner and Döring (1968) have calculated wall shapes in more rigorous ways, but with one remaining important approximation -- that the wall has only one-dimensional variation.

Collette (1964) has calculated the wall energy and determined the wall shape for a one-dimensional 180° Néel wall. He solved the exact one-dimensional pair of simultaneous non-linear differential equations with two point boundary conditions by numerical integration. The calculations were made for films with thickness from 0 to 200 Å using magnetic parameters very close to those quoted earlier. The wall width and the wall energy as functions of film thickness are shown in Figs. 4-3 and 4-4(b) respectively.* In addition the calculated wall shapes are plotted for the thicknesses of 0, 50 and 200 Å in Fig. 4-5(a). His result is quite important since he demonstrated conclusively that the shapes assumed by others for the Néel wall were in very serious error for non-zero film thickness. In particular he showed that three regions in a Néel wall can be distinguished: a central region where the magnetization rotates rapidly, and two adjacent regions extending far into the neighboring domains where the magnetization rotation takes place slowly, as can be seen in Fig. 4-5(a). Indeed, it was found that the walls extend more than ten microns into each of the adjacent domains for film thickness of 200 Å. Because of difficulty in forcing convergence of the numerical integration, Collette

---

*The value of K_u used by Collette was K_u = 1,500 ergs/cc , 50% larger than that used in the other calculations. Corrections to his data have been estimated for the comparisons shown in these figures.

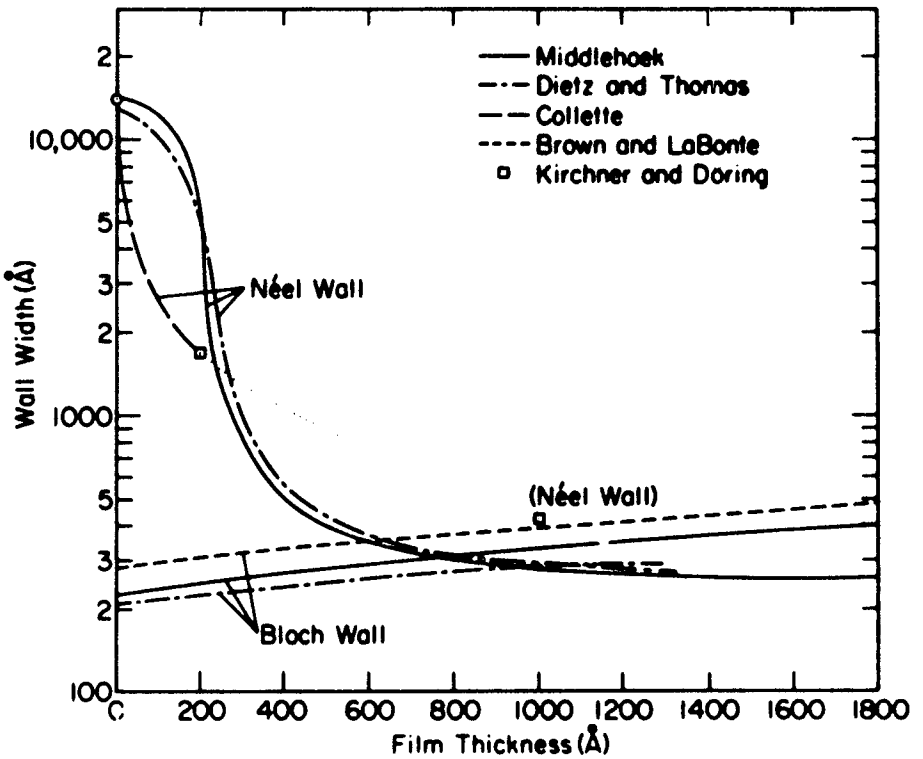

Fig. 4-3 Calculated wall width as a function of film thickness for a typical Permalloy film, on the basis of one dimensional wall models. ($A = 1 \cdot 10^{-6}$ erg/cm, $K_u = 1 \cdot 10^{3}$ erg/cc and $M_s = 800$ oe).

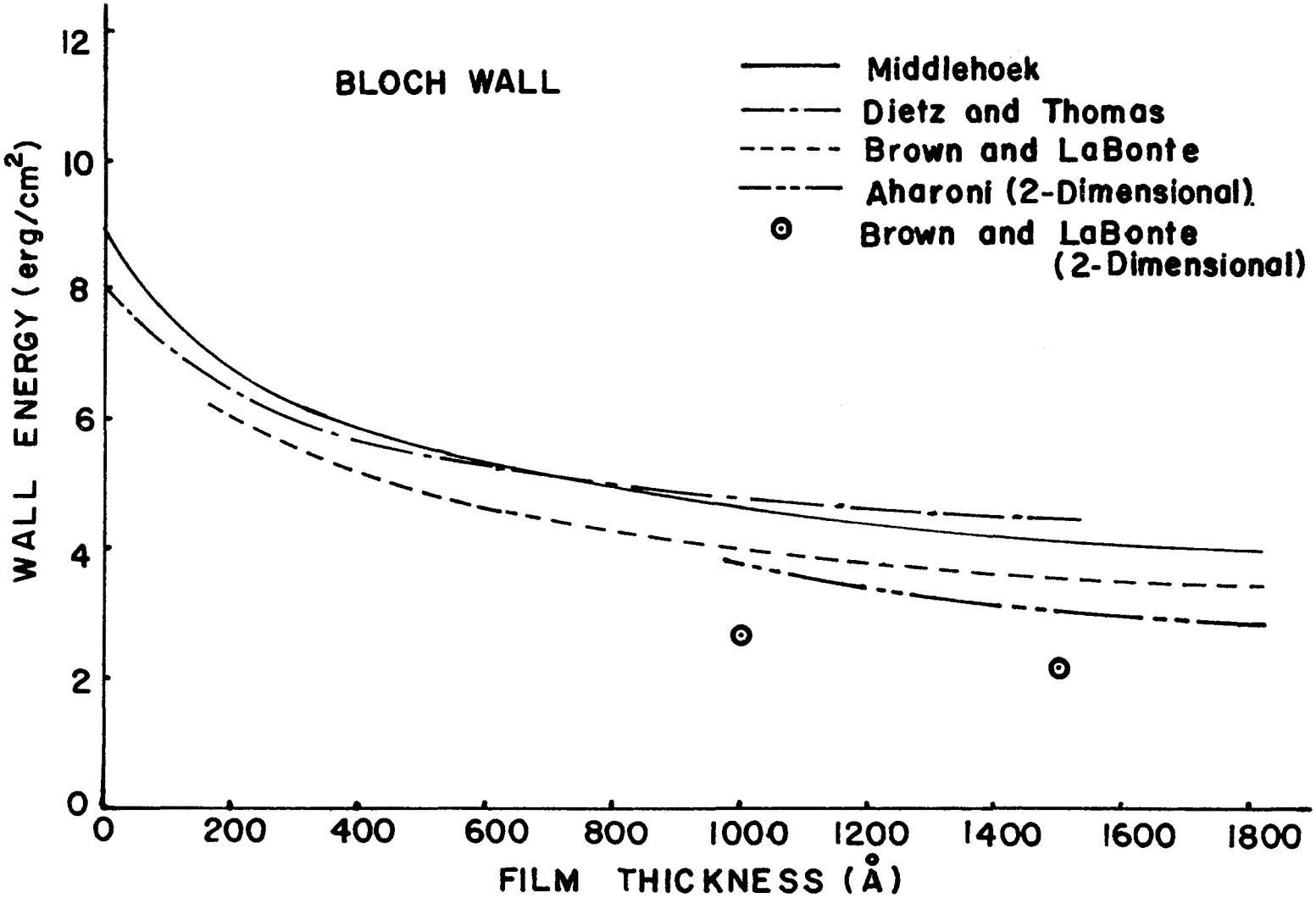

Fig.4-4(a) Calculated wall energy as a function of film thickness for a Bloch wall for a typical Permalloy film.

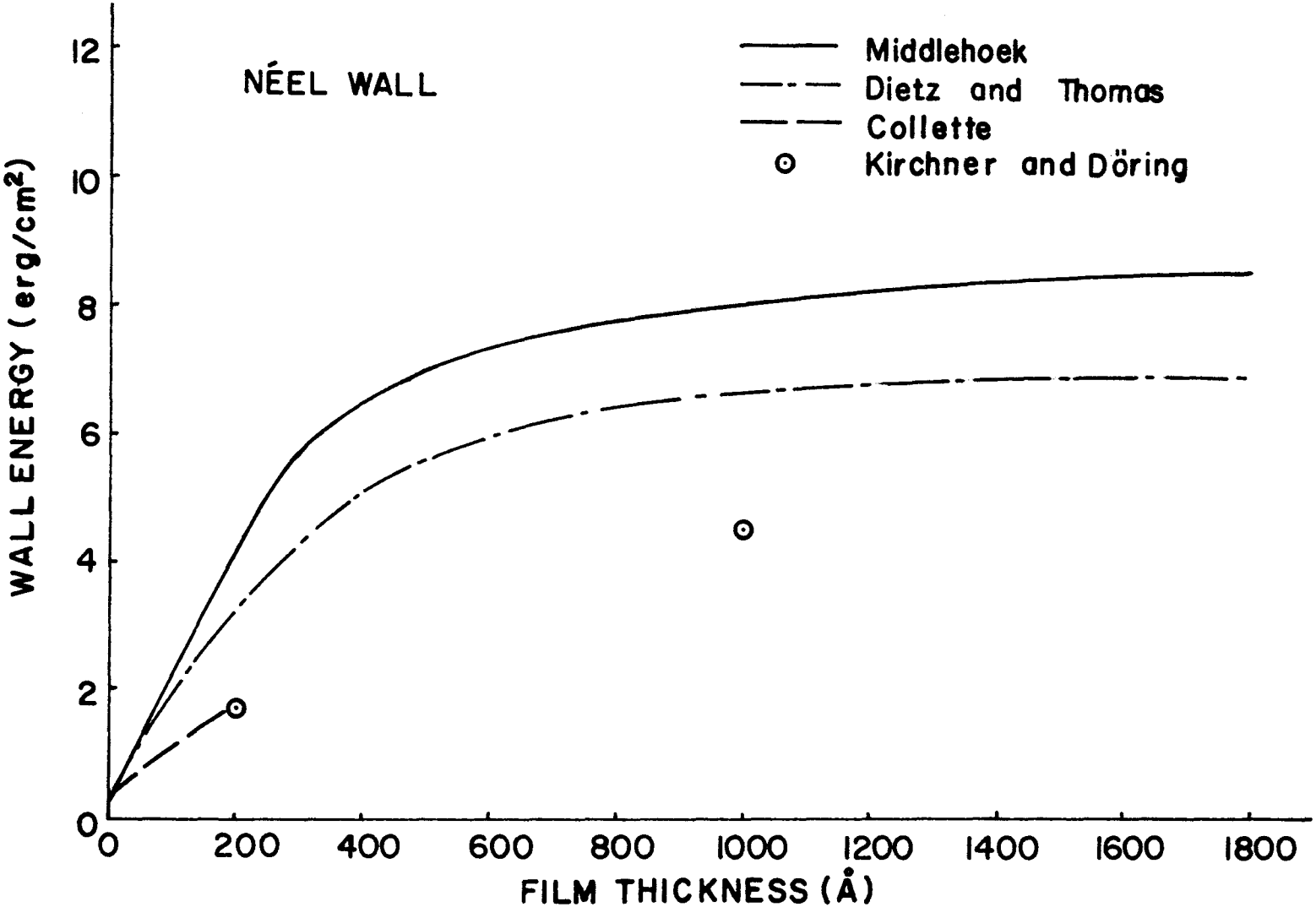

Fig.4-4(b) Calculated wall energy as a function of film thickness for a Neel wall for a typical Permalloy film.

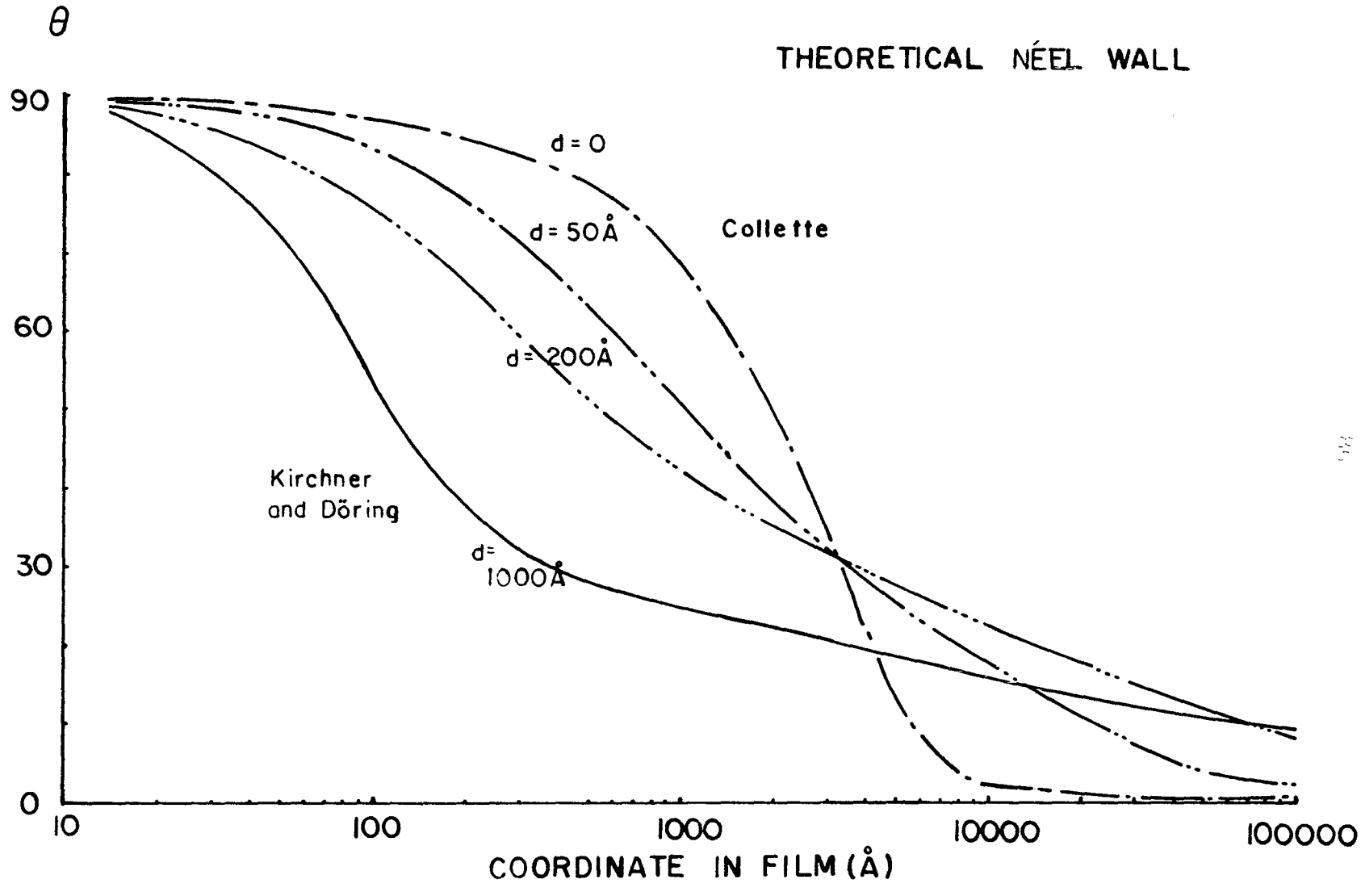

Fig. 4-5(a) Calculated Néel wall shape by Colltte, and Kirchner and Döring for film thicknesses of 0, 50, 200 and 1000Å. For Collette, $K_u = 1.5 \cdot 10^3$ erg/cc, and for Kirchner and Doring, $K_u = 1 \cdot 10^3$ erg/cc.

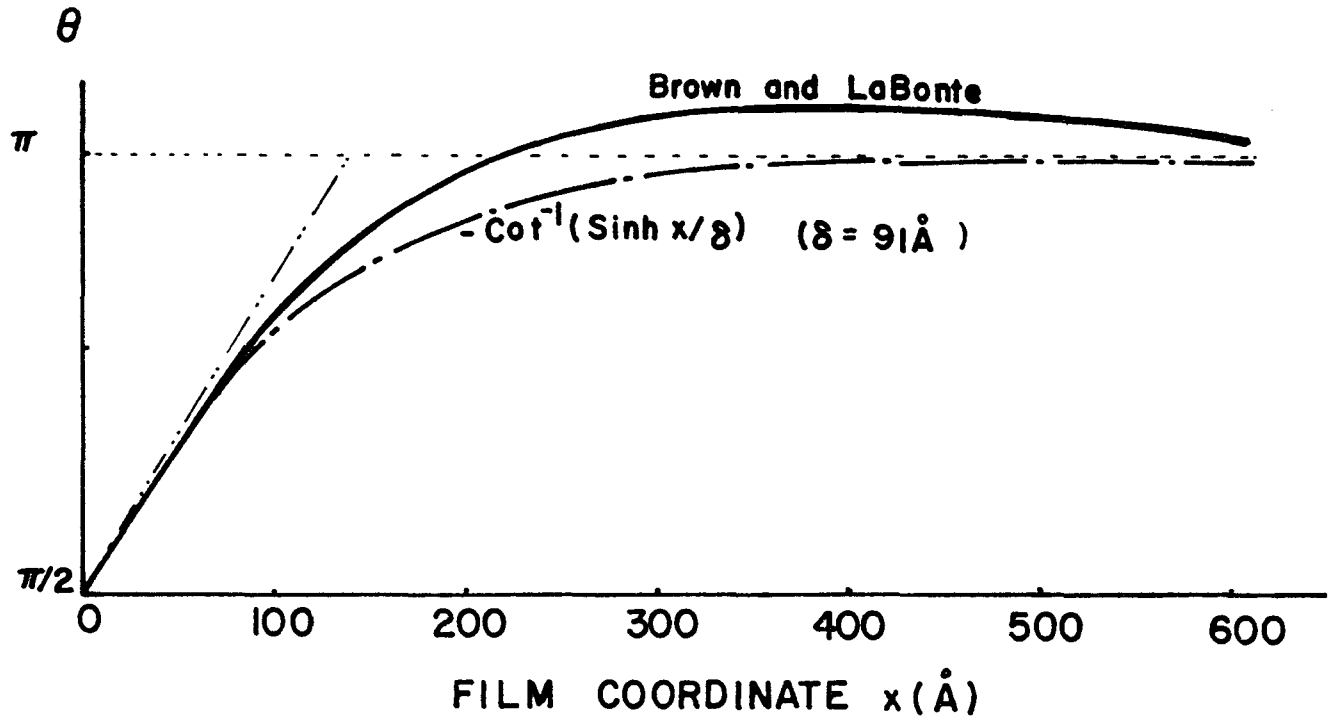

Fig.4-5(b) Calculated Bloch wall shape by Brown and LaBonte. Also shown is the model ($-\cot^{-1}(\sinh x/\delta)$) with δ=91Å. Film thickness is 1000A.

was not able to extend his calculations beyond a thickness of 200 Å.

Brown and LaBonte (1965) have carried out the numerical computation of Bloch wall shape and energy for a finite difference model, in which the wall is divided into a large number of prisms and the continuous magnetization distribution is approximated by a stepwise distribution of magnetization. For this model, the magnetostatic energy was calculated exactly, and the minimizing total wall energy was found by a variational method. Again, since they used still another definition of wall width, it is necessary to convert their results for comparison with the other calculations. The wall width obtained in this way is also shown in Fig. 4-3. The values of wall width do not differ greatly from those obtained by the other models, and the wall energy shown in Fig. 4-4(a) is only slightly lower. A similar calculation for a Néel wall could not be completed because the computer solution converged too slowly. The Bloch wall shape obtained for a film with 1000 Å thickness, having the same magnetic parameters mentioned above, is shown in Fig. 4-5(b). The figure also shows for comparison the wall shape expressed by $\theta = \cot^{-1}(\sinh(x/\delta))$ with the same slope $(d\theta/dx)_{x = o}$ as that for the Brown and LaBonte wall. One interesting feature in Brown and LaBonte's results is that on each side of the magnetization rotation, the magnetization tends to dip out of the plane of the film in the direction opposite to that in the central 180° transition region. This indicates that the magnetization is arranged so that some of the external stray field lines begin and terminate on the same side of the film. Stated in another way, the demagnetizing field due to the main reversal tends to magnetize the adjacent regions in the opposite direc-

tion. It should be noted further that in principle, the method by Brown and LaBonte like that of Collette should give an exact result for a one-dimensional wall as the number of prisms goes to infinity. The good agreement between the results by Brown and LaBonte and by the other approximations (Middlehoek, and Dietz and Thomas) shows that these crude models are quite good for the Bloch wall even though very poor for the case of the Néel wall.

Recently Kirchner and Döring (1968) reported results for Néel walls in thick films. They also made in principle an exact calculation of the wall shape and energy for a 180° one-dimensional Néel wall using a different scheme that avoids Collette's convergence difficulties. They obtained the value of 4.5 erg/cm^2 for a film with thickness 1000 Å. The wall energy is much smaller than that obtained by Middlehoek and Dietz and Thomas, but is quite consistent with Collette's result, as can be seen in Fig. 4-4(b). Furthermore, it should be noted that the wall shape shown in Fig. 4-5(a) has the same features of Collette's results. In fact Kirchner has also obtained unpublished results for a 200 Å wall that completely confirm Collette's work.

Very few attempts have been made to determine the effect of allowing two or three-dimensional variations in the magnetization through a wall. Aharoni (1967) calculated the Bloch wall energy for a two-dimensional variation of magnetization distribution, in which the magnetization direction varies through the film thickness as well as in the hard direction in the film plane. He obtained a wall energy which is again slightly smaller than that obtained by Brown and LaBonte, as shown in Fig. 4-4. For example, the energy calculated by Aharoni is

about 10% lower at film thickness 1000 Å.*

Since the Néel wall configuration is energetically more favorable in very thin films and the Bloch wall configuration is more favorable in very thick films, there must be a transition between Néel and Bloch walls at some intermediate film thickness. The one-dimensional models discussed above predict the transition thickness to be about 400 Å for a typical 80% Ni-Fe alloy film, as can be seen in Fig. 4-4(a) and (b). Huber, Smith and Goodenough (1958) first suggested that such a transition could be observed using the Bitter pattern technique. This technique consists of depositing a colloidal suspension of very fine magnetite (Fe_3O_4) particles on the surface of a specimen. Due to Brownian motion, the particles move about in the suspension until they are captured by the magnetic stray fields associated with the domain walls. With the domain boundaries indicated by the equilibrium positions of the magnetite particles, a visual picture of the domain configuration is obtained, which can be observed by dark field optical microscopy. It is found experimentally that the resulting contrast for Néel walls in a very thin film is much higher than that for Bloch walls in a thicker film, and the transition appears to occur at about 1000 Å film thickness for 80% Ni-Fe alloy films.

The observed transition thickness of about 1000 Å is much larger than the 400 Å predicted by the simple one-dimensional wall models. The cause of this discrepancy is not certain, but it is believed that

---

*Note: LaBonte also calculated a two-dimensional case (Ph.D. thesis, University of Minnesota, 1966, unpublished). He calculated just two points and obtained 2.7 erg/cm and 2.2 erg/cm^2 at 1000 and 1500 Å respectively for Bloch walls in a Permalloy film.

one of the reasons is due to the existence of the so-called "cross-tie walls", which are not considered in the simple one-dimensional wall models. The cross-tie walls are found in films of intermediate thickness. A typical Lorentz micrograph of the cross-tie walls for a 76% Ni-Fe alloy film with 615 Å film thickness is shown in Fig. 4-6. A schematic interpretation of cross-tie walls is given in Fig. 4-7. It can be seen that the main Néel wall* is cut at close intervals by short right angle "cross-ties". In addition, each cross-tie wall is associated with two structures called Bloch lines where the main Néel wall changes its polarity. The alternating polarity of the wall provides short flux closure paths outside the wall, so that the cross-tie wall structure serves to decrease the magnetostatic stray field energy and accordingly leads to larger wall widths than those calculated on the basis of one-dimensional wall models. Further detailed discussion of cross-tie walls will be given in later sections.

In 1965, Torok and co-workers showed theoretically that in addition to Néel and Bloch walls, there exist walls that have both Bloch and Néel components. For this type of walls, the magnetization rotates around an axis neither normal to a film plane nor normal to a wall plane, but roughly around an axis somewhere between them. It was shown that all 180° walls are either pure Néel or Bloch walls, depending on the film thickness. However, pure Bloch walls cannot exist unless the walls are 180° walls, and intermediate walls should exist for walls

---

*Based on experiments by Moon (1959) with Bitter powder pattern methods, there is strong evidence that both cross-tie and main walls are predominantly Néel in character.

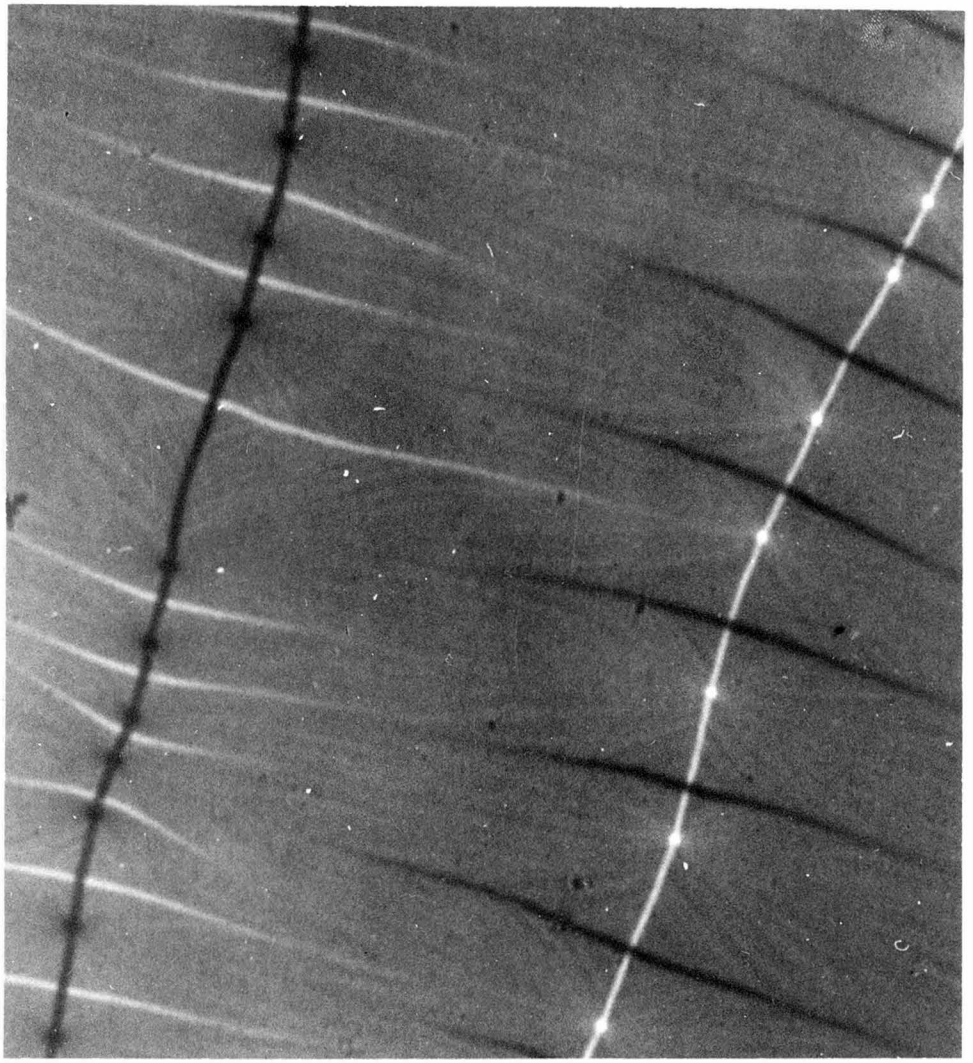

2.3 μ

Fig. 4-6. A typical Lorentz microscope photograph of the cross-tie walls associated with the Bloch lines for a 76%Ni-Fe alloy film with 615A film thickness, evaporated at room temperature. The cross-tie wall density will be given in Fig.4-19.

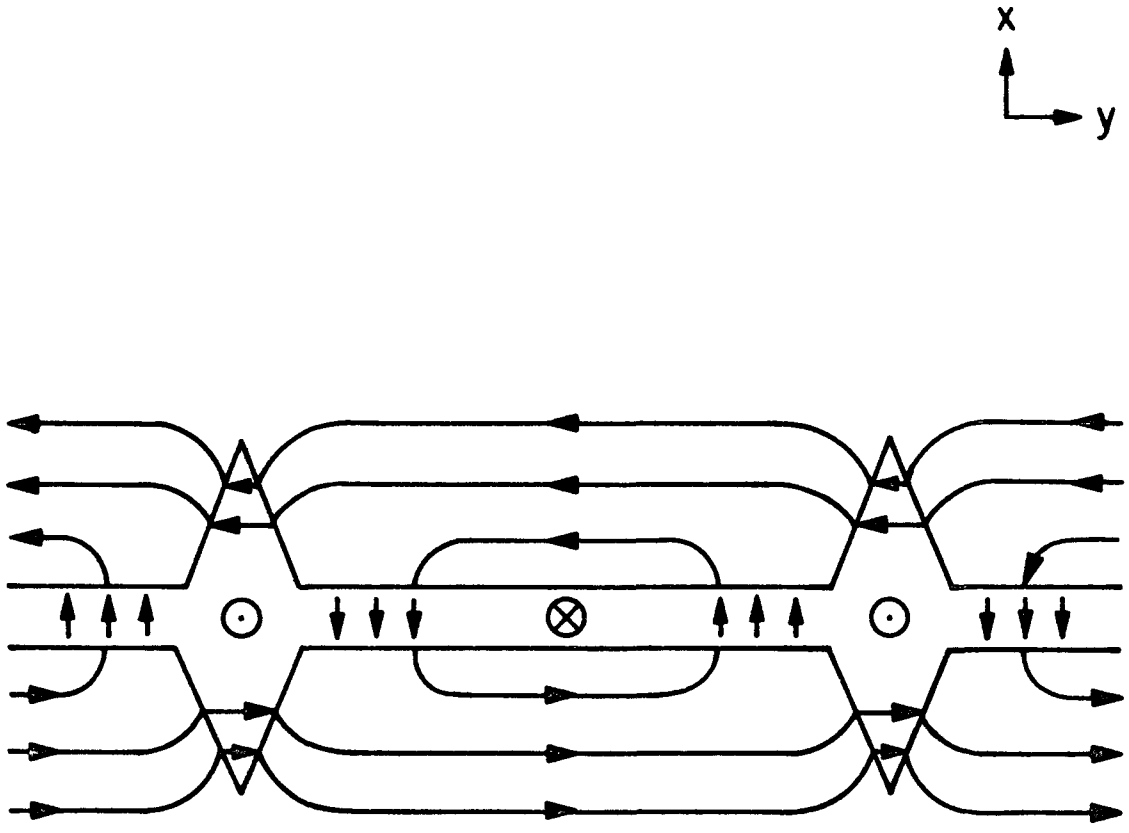

Fig.4-7 Schematical illustration of cross-tie walls and associated Bloch lines.

with angles smaller than 180° and larger than a critical angle which depends on film thickness. For walls with angles less than the critical angle, Néel walls exist. Thus the transition between Néel and Bloch walls as a function of wall angle was predicted to be gradual, rather than abrupt. Torok and coworkers further suggested that a 180° Bloch wall is probably energetically unstable, and tends to change its polarity by 180° along the wall, having cross-tie walls associated with transition regions, called Néel lines.* Janak (1966 and 1967) and others approximated the energy corresponding to such a configuration of a Bloch wall and showed that such division of Bloch walls is energetically favorable in materials with sufficiently small anisotropy, such as Ni-Fe alloys.

In summary, the general concept of the ferromagnetic domain structure in thin films has been briefly given in this section. The following points were emphasized: 1) The stray field energy associated with the magnetostatic charge distribution of the wall plays an important role in thin films in determining the wall structure, in contrast with bulk materials where the effect is believed to be negligible. 2) The influence of the stray field energy is to greatly reduce the wall width in thin films. 3) Cross-tie walls associated with Bloch lines can reduce the stray field energy of a wall, thus leading to larger wall width than that calculated from one dimensional wall models. 4) The transition between Néel and Bloch walls may not be abrupt but gradual, and an intermediate wall structure may exist. 5) Although accurate

---

*The name Néel line is due to the nature of the transition region, in which the magnetization lies in the film plane.

one-dimensional calculations have now been achieved for both Néel and Bloch walls, no conclusive calculation for two- or three-dimensional magnetization distribution has yet been made.

4.3 Survey of Earlier Experimental Investigations of Wall Structure and Width

A summary of theoretical work on wall structure in thin films was given in the previous section. It is worth presenting a brief survey of previous experimental investigations into wall structure, before discussing the present data of wall width in thin films. Up to the present time, no really systematic studies have been made, and thus the comparison of experimental data with theoretical predictions is of necessity incomplete. Most of the experimental measurements of wall width have been carried out by Lorentz microscopy. The description of this mode of operation of the electron microscope is given in Appendix 3. Lorentz microscopy has shown considerable advantage in resolution over the more conventional Bitter powder and magneto-optic methods. The contrast formation mechanism of this method was initially explained on the basis of geometric (classical) optics. However, it has been recently pointed out by Wohlleben (1966 and 1967) that an analysis of Lorentz microscopy on the basis of quantum mechanics or wave optics is often necessary. As discussed in Appendix 4 and later sections, the region of validity of geometric optics is $\Delta\Phi \gg h/2e$, where $\Delta\Phi$ is the minimum flux change in the sample which is to be detected, h is Planck's constant and e is the electronic charge. Outside of this region, wave optics must be considered. The quantity of magnetic flux, h/2e, appears to have a fundamental significance here. It is often called a fluxon.

Fuchs (1962) was the first to measure the wall width in a series of very thin films using Lorentz microscopy. He interpreted the Lorentz

microscope photographs in terms of geometric optics. Even though there is some question about the validity of his method of determining wall width in very thin films (100 Å film thickness), the results for thicker films are probably meaningful. The wall widths obtained for 80% Ni-Fe alloy film are shown in Fig. 4-8. In the thickness range 300 to 800 Å these widths are much larger than those calculated from the one-dimensional models. The discrepancy between the data and the theoretical values of Collette and Kirchner and Döring is about a factor of 3 over the entire thickness range.

In an earlier section, it was pointed out that Collette and others predicted long tails in the Neel wall shape. Fuchs experimentally measured such behavior in the Neel wall region, though not with sufficient accuracy to confirm the theoretical calculations. However, the qualitative agreement implies that it may not be meaningful to define wall width in terms of the slope of the magnetization at the center of a Neel wall. A detailed discussion of width and the intensity distribution for such wall shapes will be found in section (4.4.4).

Wade (1965) has also measured the wall width in thin films, but in a different way from that used by Fuchs, and with very different results. He used a very large out-of-focus distance in the range 20cm to 80cm. The measured wall width is essentially constant (about 2000 Å) for the film thickness range 125 Å to 260 Å. As shown in Fig. 4-8, the wall width measured is in agreement with that calculated by Collette and Kirchner and Döring. However, it is questionable whether

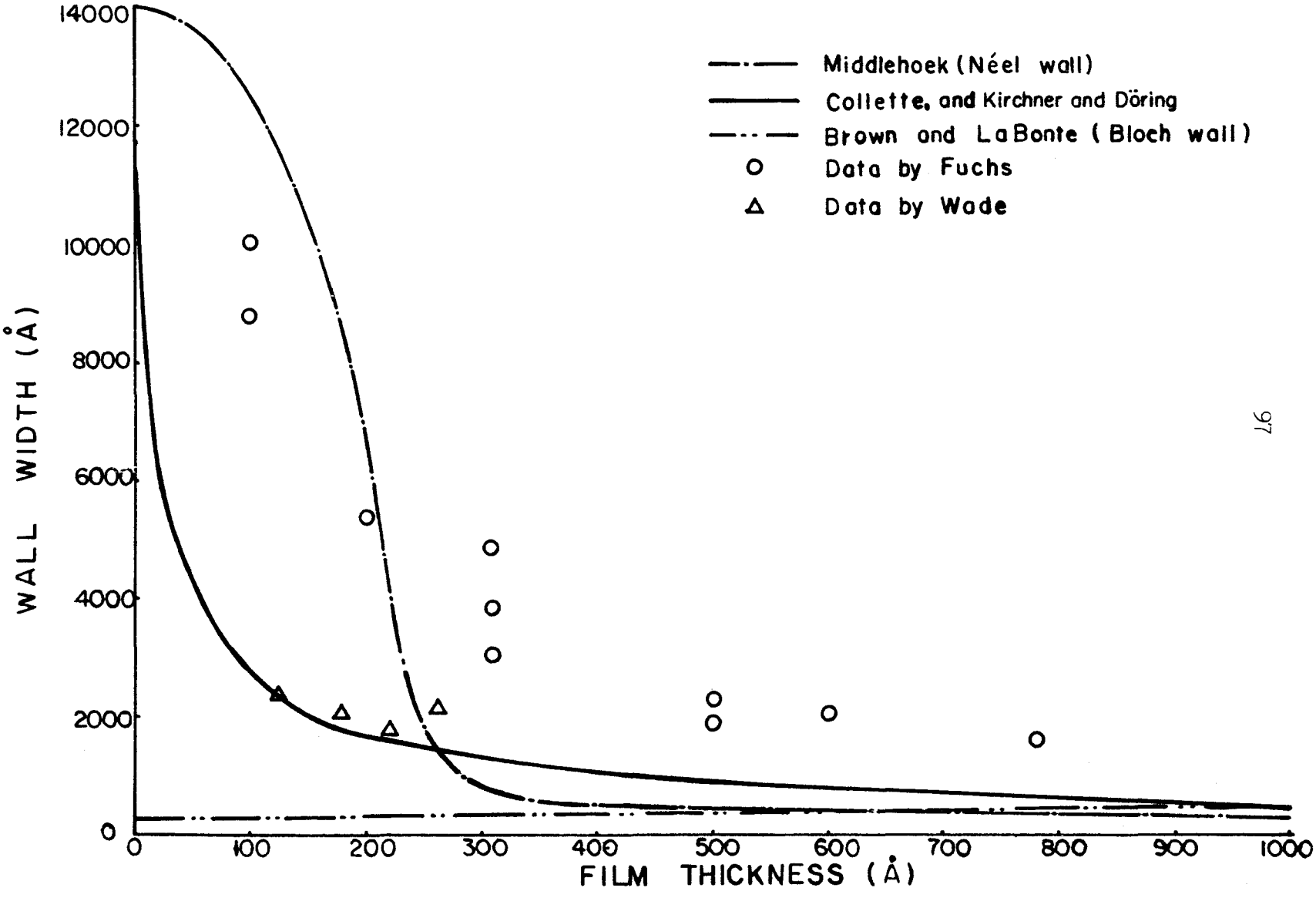

Fig.4-8 Wall width as a function of film thickness

his method of determining wall width is correct. In particular it should be mentioned that the flux change corresponding to the wall width 2000 Å inferred by Wade lies in the range 0.1 to 0.25 fluxons, and thus clearly this is beyond the classical limit. A more detailed criticism will be given in the section on wall width measurement (4.4.5). No attempt to determine wall width using a wave optical treatment in Lorentz microscopy has been made as yet, and no comparison with the results obtained classically is possible.

Patton and Humphrey (1966) have been able to indirectly estimate wall widths on the basis of their measurements of domain wall mobility. From such considerations they have suggested that the actual wall width for Néel walls is much greater than that calculated from simple one-dimensional wall models and completely consistent with the measurements of Fuchs. Furthermore mobility data for thicker films (presumably with Bloch walls) suggest wall widths even greater.

Before closing this section, notice should be taken of another experimental result which was obtained recently by Daughton, Keefe, Ahn and Cho (1967). They indirectly measured the wall energy in Permalloy films as a function of film thickness, and obtained values of energy which are smaller than those calculated by the simple wall models. The data of wall energy per unit area are shown in Fig. 4-9, which is reproduced from the paper by Daughton and coworkers. In the figure, the theoretical predictions by Middlehoek, Collette, Brown and LaBonte and Aharoni are shown for comparison. The measured wall energy per unit area is a maximum in the region 500 to 1400 Å film thickness, which corresponds roughly to the transition thickness between Néel

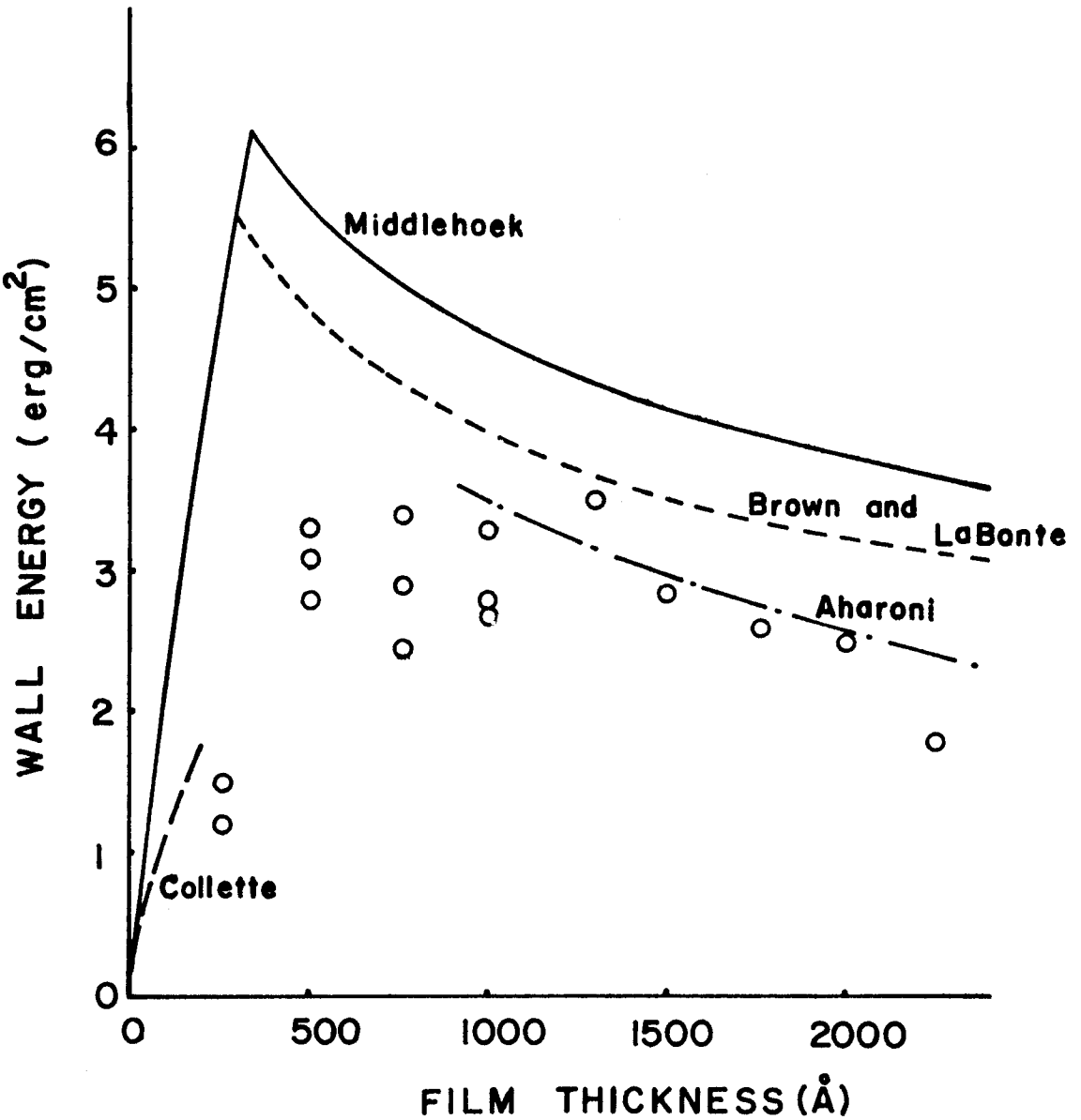

Fig.4-9 Experimental wall energy as a function of film thickness for Permalloy films. Also shown are the theoretical wall energies by Middlehoek, Brown and LaBonte, Collette and Aharoni.

and Bloch walls.

The energy per unit area of the wall in films with thickness above this transition decreases more rapidly with film thickness than is predicted by the one-dimensional simple models, but the data are in good agreement with the prediction by Aharoni on the basis of the two dimensional wall model. Furthermore, the theoretical prediction by Collette is in reasonable agreement at about 200 Å film thickness.

As the foregoing discussion has shown, experimental data for wall width have been given by only two experimenters for a single material and over a very limited thickness range, with results which disagree with each other and with the theoretical predictions based on the simple wall models. The reason for this discrepancy is still unknown. However, there may be real significance in the fact that for thick films, the measured wall energies are in better agreement with a preliminary calculation based on a two-dimensional model than with those using simple one-dimensional models. In this sense, a more rigorous calculation based on a model with three dimensional variation of magnetization is needed. On the other hand, for very thin films, the fact that wall energy measured at about 260 Å thickness is in reasonable agreement with that expected on the basis of the Collette's results implies that for this thickness range, the one-dimensional wall calculation may be adequate. The discrepancy between the measured wall widths and those calculated, however, is not understood and no convincing explanation has been offered. In any event, a more comprehensive experimental study of wall width in thin films is clearly needed.

4.4. Domain Wall Width Measurement in Thin Films

4.4.1 Introduction

The electron microscope has been found to be outstandingly successful for direct observations of magnetic domain walls in ferromagnetic materials. In one method the domain walls are revealed by covering the surface of the specimen with a fine ferromagnetic colloid, and surface replicas are taken to study these structures at high resolution (for review, see Craik and Tebble, 1961). However, it is questionable whether such replicas reveal the domain wall width in an accurate quantitative way. Another method, Lorentz microscopy, has been more commonly used to investigate the domain wall structure in a quantitative manner. In Lorentz microscopy, the domain walls are revealed directly as a result of the deflections of electrons caused by the magnetic induction of the sample. The beams from the two domains converge or diverge at the boundary, depending on the sense of the magnetization direction in the two domains. In principle the detailed structure of domain walls can be determined by measuring the intensity distribution across the image of the wall. However, in practice such determinations meet with difficulties, as will be discussed in later sections. The mechanism of contrast formation in this case is rather different from that leading to the observation of lattice defects, and special techniques are required. A detailed description of the image formation in Lorentz microscopy is given in Appendix 3.

4.4.2 Intensity distribution for walls on the basis of geometrical optics

The contrast formation mechanism in Lorentz microscopy may be discussed on the basis of either classical optics or wave optics. In the realization that a magnetic film is a phase object to an electron stream, the wave optical approach is more fundamental and basic. However, as will be discussed later, under certain conditions the classical optical approach is sufficiently accurate to obtain information on magnetic structure and this approach was used in the present study.

In order to calculate the intensity distribution of the wall image, one must know the magnetization distribution across the wall. However, since there is no valid information on the actual distribution, it is simplest to assume a class of distributions and seek a best fit. In practice the situation may be further complicated by the fact that films of different thickness may have different types of domain wall and, therefore, different magnetization distributions, which will in turn lead to different image profiles. If the observed image profile could be corrected for finite beam divergence and other errors and then processed by deconvolution, for example by using Fourier analysis, then the actual magnetization distribution would be obtained directly. Such an experiment has not yet been attempted since it is doubtful that the image intensity can be obtained with sufficient accuracy to give meaningful results.

As a first order approximation, one may assume a simple one-dimensional magnetization distribution for the calculation of the intensity profiles. In the present study the magnetization distribution was first assumed to have the same shape as that determined by exchange

and uniaxial anisotropy in the absence of demagnetizing fields. However, the scale of the wall or the wall width was allowed to vary in order to match the experimental intensity profile as closely as possible with a calculated profile. It is therefore necessary to know the calculated profile when the magnetization varies in the way described by Eq. (4.3).

In Section (4.1) it was shown that the magnetization variation desired here is given by

$$\theta = -\cot^{-1} (\sinh u) = -\cot^{-1} (\sinh x/\delta) \qquad (4.3)$$

giving a magnetization distribution

$$\overline{M} = + \vec{e}_x M_s \operatorname{sech} (x/\delta) - \vec{e}_y M_s \tanh (x/\delta) \qquad (4.12)$$

for a wall along the y-axis. A graph of this distribution has already been shown in Fig. 4-2(a). In the above expressions, θ is the angle between the magnetization and the easy axis direction at a distance x from the wall center in the hard axis or x-direction and $u = x/\delta$ is the normalized distance from the wall center in the film plane. The slope of the curve defined by Eq. (4.3) is $1/\delta$ at the wall center.

As discussed by Fuller and Hale (1960), the classical intenstiy distribution is given by the equation

$$I (U) / I_o = (1 + z \frac{\partial \psi_x}{\partial x})^{-1} \qquad (4.13a)$$

where I_o is the beam intensity far from the wall, z is the out-of-focus distance and ψ_x is a Lorentz deflection angle in the x direction after passing through the wall. For the present case, this becomes

$$I(U)/I_o = \{1 \pm R\,\mathrm{sech}^2(x/\delta)\}^{-1} \qquad (4.13b)$$

$$= \{1 \pm \frac{z\psi_o}{\delta}\,\mathrm{sech}^2(x/\delta)\}^{-1}$$

The variable $U = \xi / \delta$ is the normalized distance from the wall center in the focal plane, where ξ is the coordinate in the focal plane, parallel to the x-coordinate in the film plane. The Lorentz deflection is expressed in normalized form, $R = z\,\psi_o / \delta$, where z is the out-of-focus distance and ψ_o is the Lorentz deflection angle far from the wall. The positive and negative signs in Eq. (4.13b) refer to divergent and convergent walls respectively. The intensity distributions expressed by Eq. (4.13b) are shown graphically in the paper by Fuller and Hale (1960) and are reproduced here in Figs. 4-10 (a) and 4.10 (b). The curves indicate the intensity distributions as a function of R. One can see that the intensity at a wall center for the convergent wall case increases with R, and the divergent wall intensity decreases with increasing R. It should be emphasized that these intensity distributions are only valid for the shape given by Eq. (4.3). When it is necessary to calculate the distribution for a wall shape that cannot be expressed in simple functional form, it is necessary to determine $\frac{d\psi_x}{dx} = \psi_o \frac{d \cos\theta}{dx}$ from the wall shape $\theta(x)$.

4.4.3 Experimental Considerations.

In practice, the electron beam used to image the wall is not parallel and the beam divergence should be taken into account. The influence of beam divergence on the wall image was first discussed by Warrington in 1964. The resulting image may be considered as a series of parallel illumination images superposed with linear displacements

DIVERGENT WALL

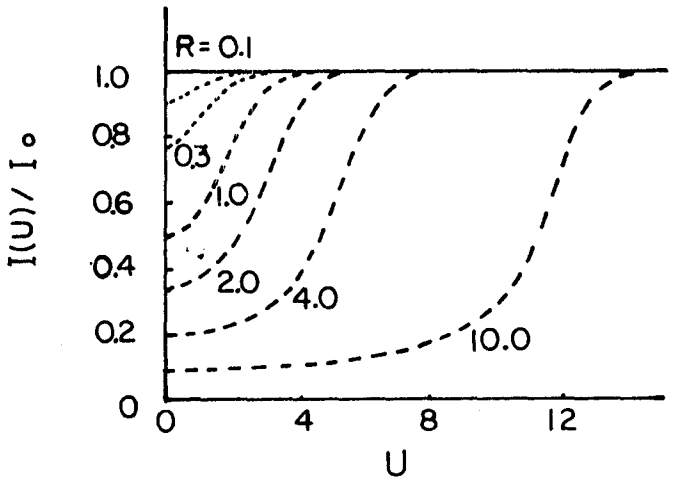

( )

CONVERGENT WALL

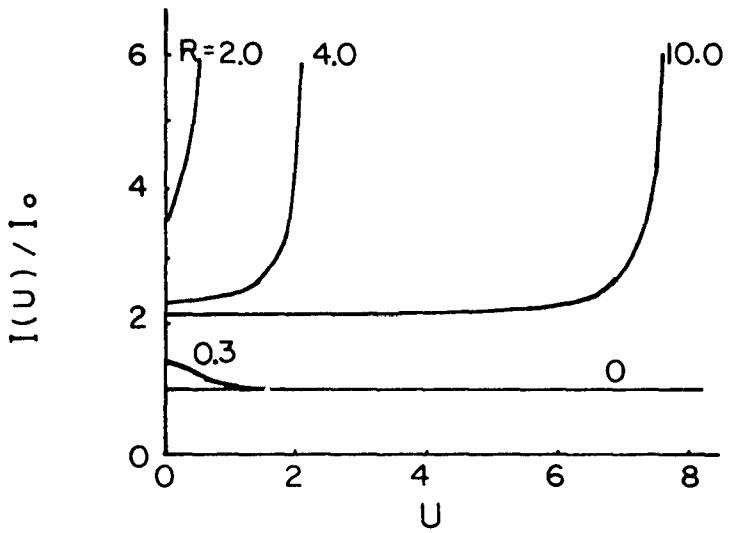

( )

Fig.4-10 Intensity distributions for a divergent wall image and for a convergent wall image, after Fuller and Hale (1960).

up to the limits of $\pm \beta z$ where β is the convergence angle of the incident beam. The presence of the condenser aperture ensures that, to a good approximation, the intensity per unit solid angle is reasonably constant over this angle. Using this assumption, the intensity of the wall image was calculated as a function of R for different values of the ratio of β/ψ_o. The results given in a paper by Warrington are reproduced in Fig. 4.11 (a) and (b) for both convergent and divergent walls respectively. The figures give results for the overfocused condition. The effects of a finite β is greater as R increases, especially for convergent walls. A typical value of β/ψ_o would be 0.6 and thus for a value of R = 0.8, one can see that the intensity ratio for a convergent wall is decreased from 5 to 2.2. On the other hand, for a divergent wall the effect is much smaller, with an increase in this case from 0.56 to 0.57. Therefore it is concluded that the Fuller and Hale result is applicable for the convergent wall case only if the ratio of the beam convergence angle β to the Lorentz deflection angle ψ_o is of the order of 10^{-1} or less. In the present situation, $\beta \approx \psi_o \approx 10^{-4}$ rad. and $\beta/\psi_o \approx 1$. For divergent wall images, on the other hand, the intensity profiles are very insensitive to beam divergence, and the Fuller and Hale result is applicable for β/ψ_o as large as unity.

To verify the influence of the finite beam divergence on the intensity maximum and minimum for both convergent and divergent wall cases respectively, a preliminary experiment was carried out. Using the methods described in Section 4.4.4, the intensity at the wall center for the convergent and divergent wall images was measured as a function of the out-of-focus distance for a 430 Å thick film made of 76% Ni-Fe alloy. The out-of-focus distance was varied from 1.1mm to

6.6mm. The results are shown in Figs. 4-12 (a) and (b) for the convergent and divergent walls respectively. The dotted lines in these figures are taken from Warrington's calculations (Fig. 4-11) using the approximate experimental values $\psi_o = 4\cdot(10^{-5})$, $\delta = 10^{-5}$cm, and assuming that $\beta/\psi_o \approx 1$. The agreement is very good except for the largest value of out-of-focus distance. As will be seen in later sections, the validity of this point is subject to question on two counts. First the basic validity of the classical calculation may be expected to fail for out-of-focus distances larger than about 3mm (see Sect. 4.4.7). Second the deviation caused by differences between the assumed shape and the true Néel wall shape is known to be small only for 1mm z-values. For values as large as 6mm it is very plausible that a large discrepancy would result (see Sect. 4.4.5). In the light of the general agreement shown by Fig. 4-12, it is concluded that Warrington's calculations are consistent with the experimental results. We therefore accept his conclusion that the intensity distribution for the divergent wall is not sensitive to β/ψ_o , and accordingly one does not have to determine β accurately to analyze an intensity distribution of a divergent wall image as long as β is roughly of the order of ψ_o or less. Furthermore, the source is so large that the images are free from a coherent interference fringe effect, as will be discussed in Sections 4.4.6 and 4.5.

The above discussion suggests two ways of determining the wall width from the intensity distribution on the Lorentz microscopy photograph. The intensity ratio at the center of the wall ($u = U = 0$) permits calculation of R from Eq. (4.13). The Lorentz deflection angle ψ_o can be calculated from known film and microscope data using Eq. (A-3.1) in Appendix 3. Thus wall width is obtained from $a = \sqrt{2}\,\pi\delta = \sqrt{2}\,\pi z\psi_o/R$.

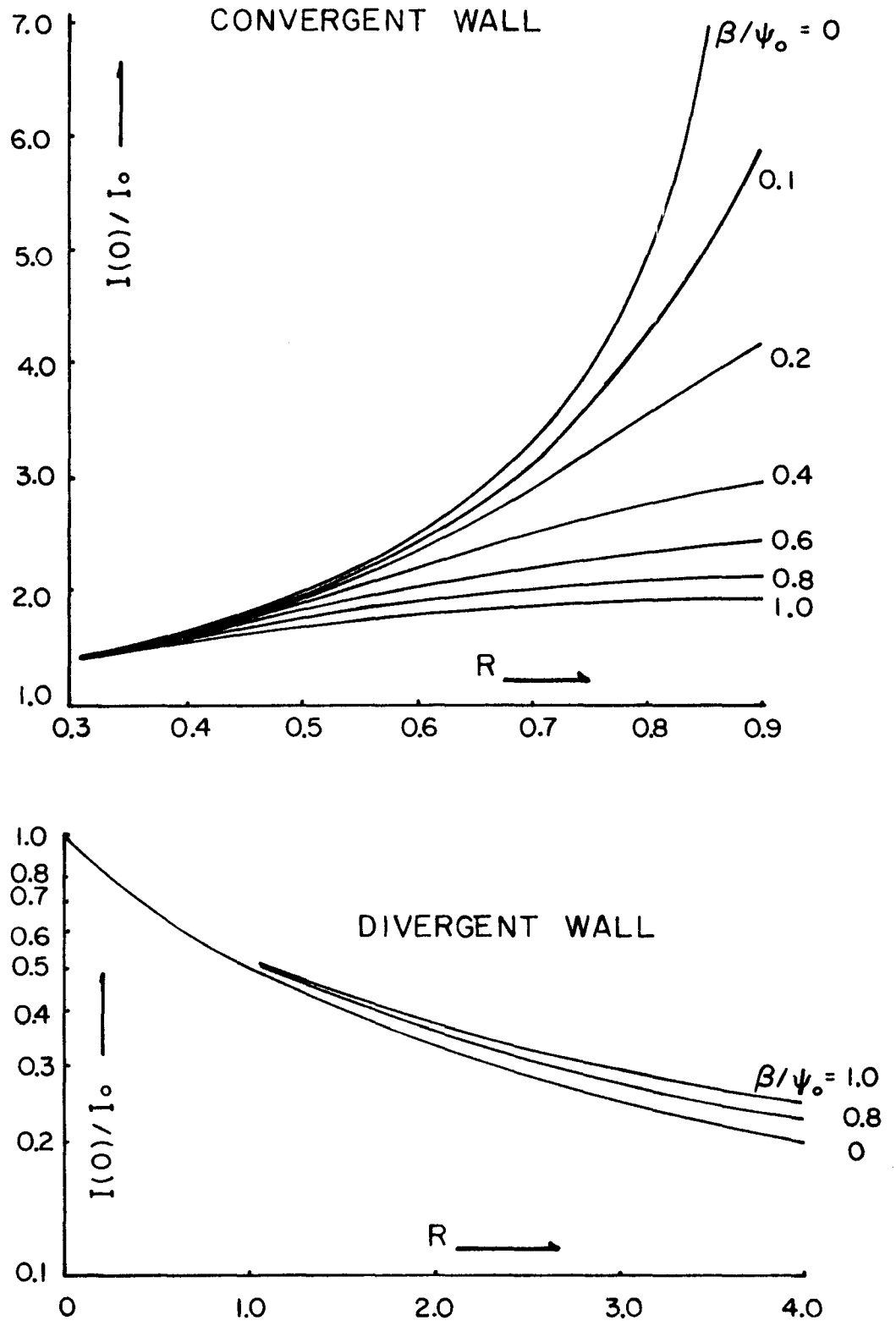

Fig.4-11 Intensities at the wall center as a function of R for a convergent wall and a divergent wall, after Warrington(1964).

(a)

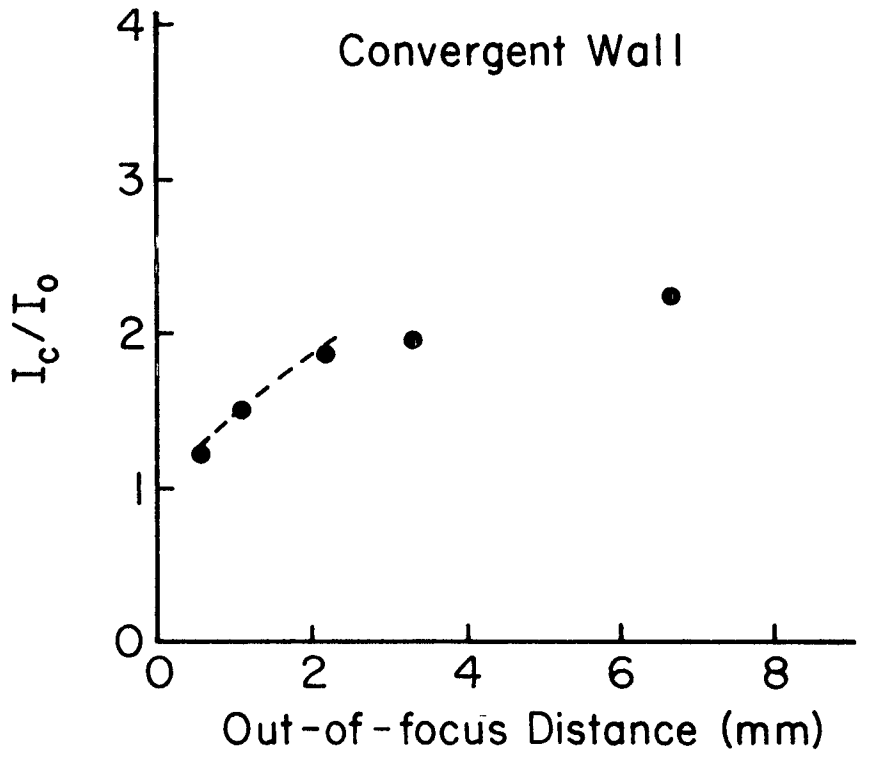

(b)

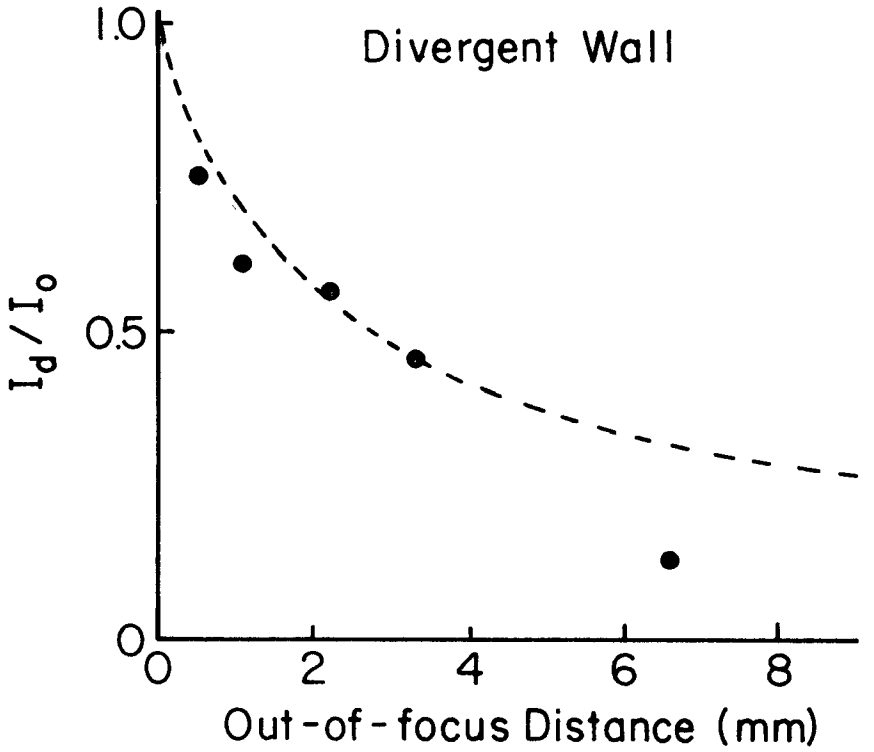

Fig.4-12 Experimental intensity values at the wall center as a function of out-of-focus distance for the 76%Ni-Fe alloy film with 430A film thickness.
The dotted lines are the predicted intensity values by Warrington for $\psi_o = 4 \cdot 10^{-5}$, $\delta = 10^{-5}$cm and $\beta/\psi_o = 1$.

However uncertainty in saturation magnetization and film thickness introduces substantial additional error into the wall width determination. Another method is to adjust δ in Eq. (4-13b) to match the experimental intensity distribution as closely as possible with the theoretical intensity profile. In order to use Eq. (4-13b) it is also necessary to know R. As discussed above this requires knowledge of $z\psi_o$ unless the value of R is obtained from the experiment. Since ψ_o is not known accurately, it seems more satisfactory to determine R experimentally from the intensity ratio at the wall center. Since this fixes the value of R independent of δ, only the normalized coordinates $u = x/\delta$ and $U = \xi/\delta$ should be changed in Eq. 4-13b in seeking a profile match.

On the basis of the foregoing discussion, the wall width determinations were made utilizing only the divergent wall images and by adjusting δ in Eq. 4-13b in order to get the best profile match with the experimental data.

4.4.4 Experimental Methods

Lorentz microscopy observations were made with an RCA EMU-3 microscope operated at 100 kV. Beam divergence was minimized by using a double condenser lens with the second lens overfocused beyond crossover as much as possible. The influence of the divergence angle on the intensity profile of the wall image was discussed in the previous section. The distance between the effective source and the sample plane in this case is about 20 cm. Condenser apertures were 250 microns in diameter, and a 20 micron objective aperture was used. Aperture angle β of the electron beam was of the order of 10^{-4} radians or less. It is important to know with reasonable accuracy the out-of-focus distance in Lorentz microscopy, since the distance influences the image profile in a signif-

icant way. The specimens were placed in an "over focussed" position by raising them above the focal plane of the objective lens mechanically by use of a special specimen holder. As discussed in the previous section, it is quite important to use a small out-of-focus distance, and thus for most measurements the out-of-focus distance was set at the small value of 0.55 mm. However, experimental difficulties made such measurements unreliable for thickness less than about 600 Å, and for these cases the out-of-focus distance was increased to 1.1 mm. Specimen preparation is discussed in Section 4.4.5 and Appendix 1.

The magnification of the microscope in the Lorentz mode was 1,600, and was measured by use of a carbon grating replica (E. F. Fullam, Inc., New York). For film thickness above 1,200 Å the illumination intensity on the observation screen was so weak that the exposure times of the photographic plates were longer than 10 minutes. Therefore, special precautions were taken to eliminate mechanical vibration of the microscope. The photographic plates used were Kodak High Contrast Projector Slide Plates. The photographic plates were analyzed by a scanning photodensitometer (Joyce, Loeble Co., England). The transmission data were converted to intensity using an experimental calibration curve for the emulsion. This calibration was made using 100 kV electrons, and established that the plate response was linear over the exposure range utilized. The magnification of the scanning photodensitometer was 50, and accordingly the total magnification of the trace curves was $8 \cdot 10^4$.

Determination of the intensity distribution and intensity ratio is complicated by the background intensity caused by electron scattering from the various microscope apertures and the sample itself. Accordingly the background intensity is variable, depending on exposure conditions

in the microscope. To correct for microscope scattering it is therefore necessary to determine the background intensity for each photographic plate. Fig. 4-13 (a) shows a Lorentz microscope photograph of domain walls for a 76% Ni-Fe alloy film with 220 Å thickness, taken at 100 kV. A schematic illustration of the densitometer trace for this photograph is shown in Fig. 4-13 (b). In this figure I_{00} is the intensity of regions unexposed to either direct or scattered electrons, I_b is the background density due to microscope (not sample) electron scattering, and $I_1(0)$ and $I_1(U)$ are the measured intensities far from the wall, and within the wall. If the emulsion response is linear, the intensities simply add, and the desired magnetic intensities far from the wall, and within the wall images become $I_0 = (I_1(0)-I_b)$ and $I(U) = (I_1(U)-I_b)$ respectively, providing that the background intensity I_b is uniform over the region under consideration. However, the correction for sample scattering is not achieved so simply. Discussion of this matter will be deferred to section 4.4.7.

4.4.5 Experimental values of domain wall width in 76% Ni-Fe alloy films

For quantitative comparison of theoretical models and experimental measurements, it is convenient to have a simply defined measure of the wall width. For a fixed shape of wall, there would be no problem, but in the real wall, the shape as well as the width varies with film thickness. As a result any definition must be arbitrary and approximate. For Néel walls of zero film thickness and Bloch walls of infinite thickness, the demagnetizing fields are zero and the theoretical wall shape is given in Eq. (4-4) and Fig 4-2 (a). For this shape, the wall width may be defined by extrapolating the central slope of the wall to the

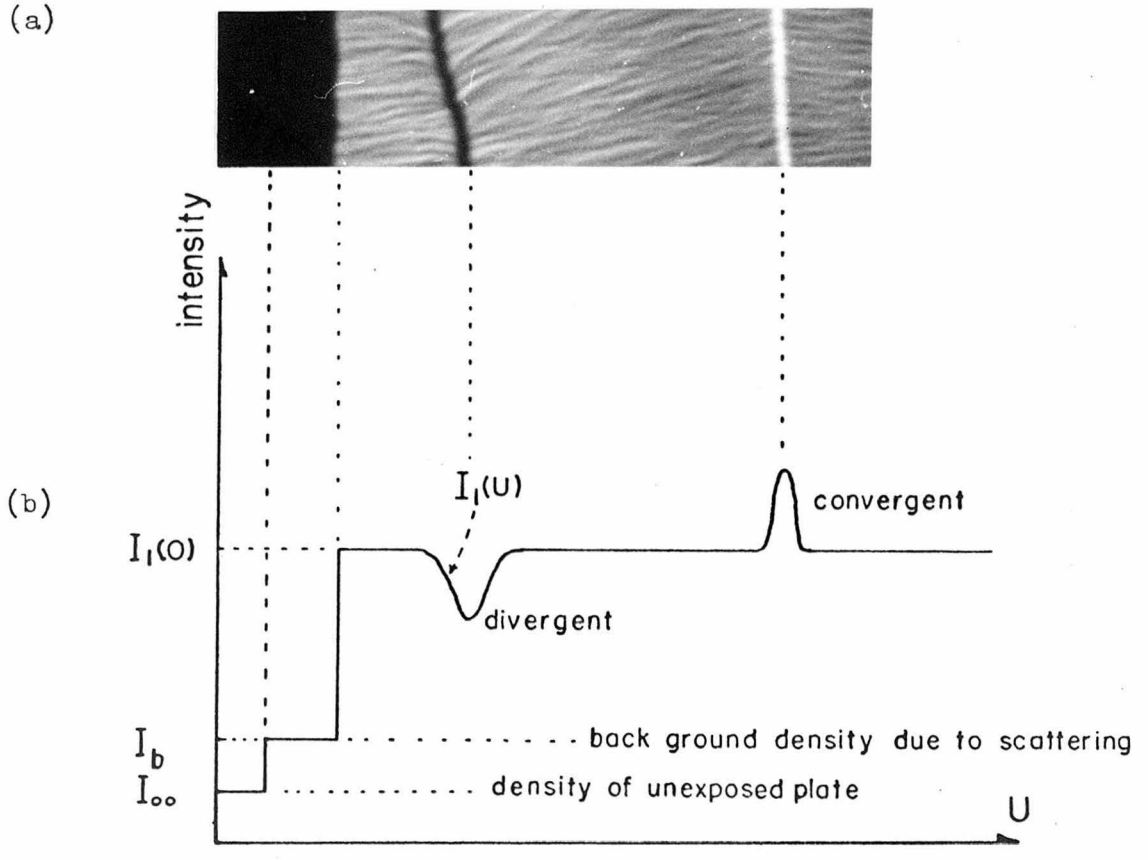

Fig.4-13 (a) A Lorentz micrograph showing the divergent and convergent wall images, the sample-mesh and the unexposed part of the photograph plate. (b) The schematical illustration of the intensity values.

extreme values of θ . This gives the value $\pi\delta$ for a 180° wall. In section (4.2), it was pointed out that the linear approximation model gives a value for slope which is smaller by a factor $(2)^{-1/2}$, and a wall width which is correspondingly larger, namely $(2)^{1/2}\pi\delta$. In order that the models will agree (at least in the absence of demagnetizing fields), the definition for wall width adopted in Sec. 4.2 was $(2)^{1/2}\pi\delta$. Specifically this means that the approximate calculation of Middlehoek including the demagnetizing field will agree with the wall width for the exact theoretical magnetization variation at the limits of zero and infinite thickness.

The 76% Ni-Fe alloy films used in the present study were vacuum evaporated from a melt of 80% Ni and 20% Fe onto glass or cleaved NaCl substrates at room temperature in a moderate vacuum of about 10^{-7} Torr. The detailed description of film preparation is given in Appendix 1. Electron diffraction analysis showed that the films were of f.c.c. polycrystalline structure. Film thickness and anisotropy energy K_u were determined magnetically, using a low frequency hysteresis loop tracer. The specimens for Lorentz microscopy were mounted on microscope grids after being floated off the NaCl substrates in water.

A typical example of the profile match method to experimentally determine the wall width is shown in Fig. 4-14 (a,b and c). The film thickness is 615 Å and the out-of-focus distance is 1.1 mm. In the figure, the solid dots indicate the experimental intensity distribution in the normalized coordinate ($U = \xi/1360$ Å). The solid curves (Fig. 4-14 (a, b and c)) correspond to the intensity distributions expressed by Eq. (4-13b) for δ of 300 Å, 600 Å, and 900 Å, respectively. It can be seen that the theoretical curve for δ = 600 Å most nearly matches

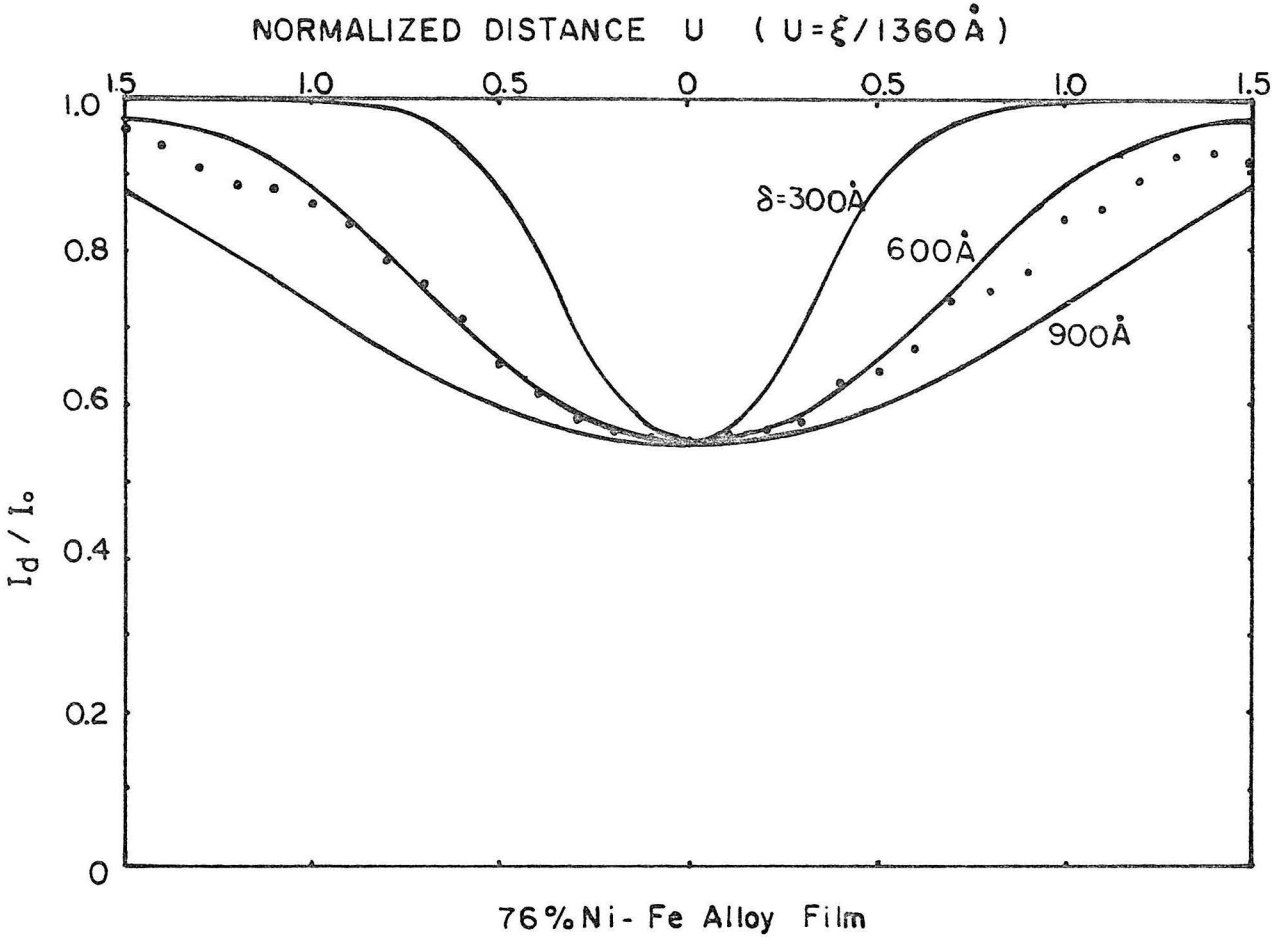

Fig.4-14 A typical example of the profile match method. The film thickness is 615A. The out-of-focus distance is 1.1mm. The solid dots are the intensity values obtained experimentally, and the solid lines are the theoretical profiles for δ=300, 600 and 900A.

the experimental intensity profile, giving an experimental wall width $a = \sqrt{2\pi} \cdot (600\ \text{Å}) = 2660\ \text{Å}$. For most of the measurements in the present thesis, the theoretical curves were plotted by computer in steps of 100 Å in δ to seek the best fit.

The measured wall width of 180° domain walls in 76% Ni-Fe alloy as a function of film thickness is shown in Fig. 4-15. Also shown are the theoretical curves based on one-dimensional wall models discussed in Sec. 4.2. It is tempting to regard the data between 200 and 800 Å as defining a trend lying above but roughly parallel to the theoretical curves for the Néel wall. However, this trend is largely determined by the point for 200 Å thickness, and it is for this thickness that the accuracy of the method is most uncertain. This matter will be discussed in detail in a later section. The other points for thickness between 350 Å and 800 Å show sufficient scatter that one cannot assert the trend to be well established. On the other hand, the data agree reasonably well with that obtained by Fuchs (Fig. 4-8), in which this trend is clearly seen. In any case, between 800 Å and 1800 Å thickness the measured wall width clearly increases nearly linearly from an apparent minimum of 2000 Å at 800 Å thickness to 9000 Å for the thickest film which could be measured with the 100 kilovolt microscope. As can be easily seen in the figure, all of these wall widths are in complete disagreement with calculations based on the simple wall models described previously.

4.4.6 Comparison with other experimental data

It is worth comparing the present experimental results of wall width with those obtained by others. Fuchs (1962) also used the simple geometric theory for calculating the experimental wall width. For suf-

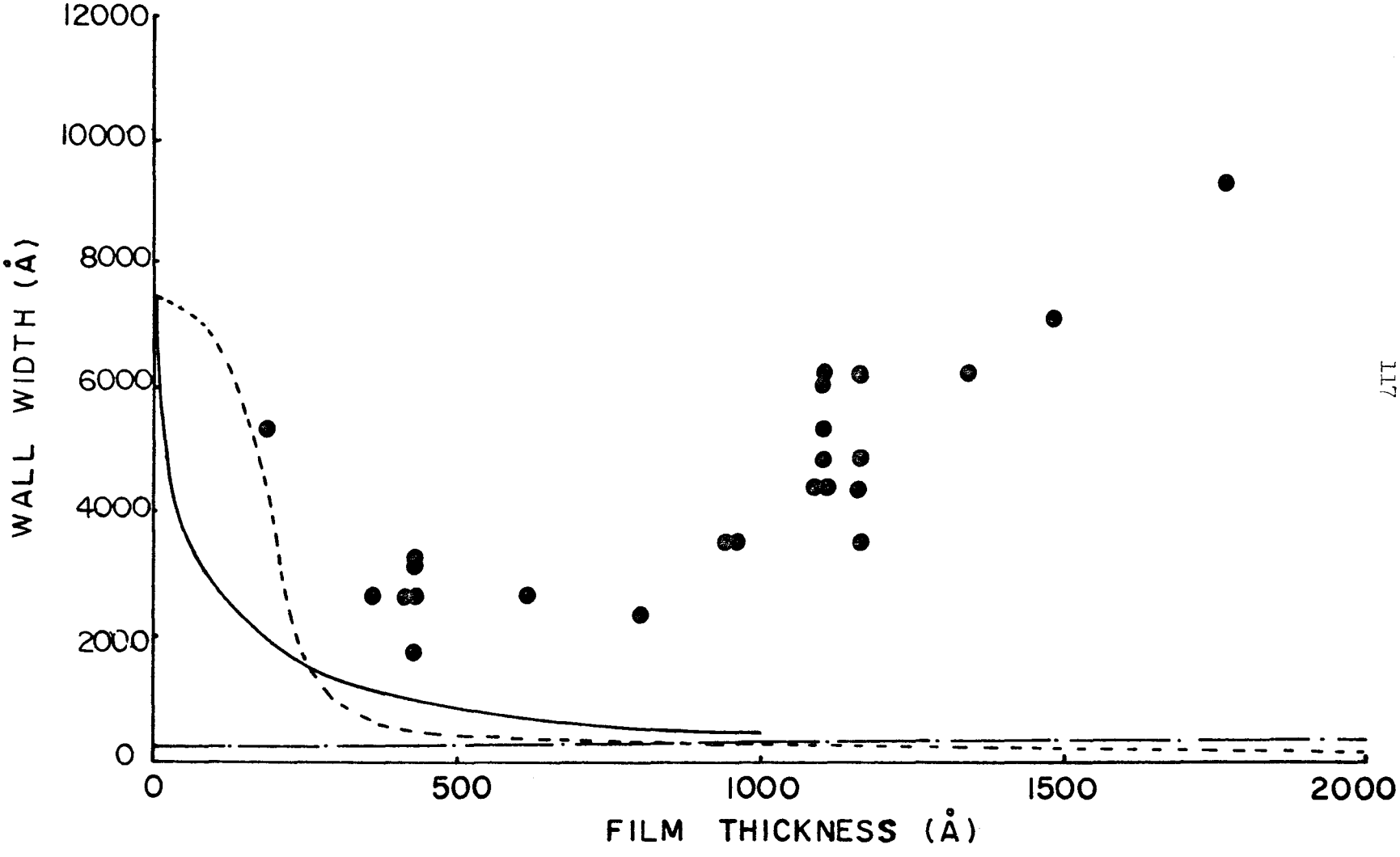

Fig.4-15 Experimental wall width as a function of film thickness for 76%Ni-Fe alloy films evaporated at room temperature. The solid line is the theoretical wall width by Collette, Kirchner and Doring. The dashed lines are the theoretical predictions by Middlehoek.

ficiently large out-of-focus distance, the convergent wall image contains two infinite peaks (see Fig. 4-10 (b)). Fuchs pointed out that the defocusing distance z_o at which the two peaks degenerate into one is simply related to the slope of $\theta(x)$ at $x = 0$, independent of the specific wall model. That is,

$$d\theta/dx\big|_{x=0} = 1/\psi_o z \quad .$$

Thus for a 180^o wall, the wall width as defined in this section may be determined to be

$$a = \sqrt{2\pi}(d\theta/dx\big|_{x=0} = \sqrt{2\pi} z_o \psi_o$$

Fuchs' wall width was obtained from this equation using the minimum out-of-focus distance z_o for which he could observe only one maximum.

According to Fuchs, the physical interpretation of z_o is complicated by diffraction and interference effects, and the experimental error in determing the value of z_o may be as large as 25%. If Fig. 4-8 is compared with Fig. 4-15 it is seen that Fuchs' data are in reasonable agreement with the present data in the range 200 to 800 Å.

Wade has also measured the domain wall widths in 80% Ni-Fe alloy films by Lorentz microscopy. He used a very large out-of-focus distance (8 cm to 80 cm) and measured the width of convergent and divergent domain wall images (W_c and W_d) which may be approximated by

$$W_c = 2z\psi_o - a$$

and

$$W_d = 2z\psi_o + a$$

Therefore, an approximate wall width may be experimentally determined by

$$a = (W_d - W_c)/2 = W/2$$

The result obtained by Wade is that the wall width in Ni-Fe films is about 2,000 Å ± 50%, independent of film thickness d, in the range between 125 and 260 Å. This result is quite different from those in the present study and by Fuchs. However, the experimental accuracy of Wade's work is very questionable for two reasons. First, the image widths he measured were of the order of 10 μ (100,000 Å) for a typical value of z = 50 cm and $\psi_o = 2 \cdot 10^{-5}$ rad., while the deduced value of wall width was about 2,000 Å which was thus extracted from the difference of two nearly equal quantities. Second, and more important, the edge of the wall image obtained at such large out-of-focus distance should be modulated by Fresnel fringes (Wade, private communication and

Wohlleben, private communication). On the basis of the foregoing arguments, the results obtained by Wade cannot be accepted as the actual wall widths in the samples.

4.4.7 Discussion on the discrepancy between the experimental and theoretical results.

As shown in Fig. 4-15, the discrepancy between the experimental and calculated wall widths is significant, particularly for thicker films. This section is concerned with the possible sources of the discrepancy. These sources can be grouped in the following categories, (1) sources due to experimental difficulties, (2) sources attributed to the limitation of classical optics, and finally (3) deficiencies in the models used for theoretical calculations.

(1) Experimental difficulties

The first thing one can consider on this matter is the effects of the finite beam divergence β of the illumination source in Lorentz microscopy. As discussed in detail in the previous section (4.4.3), the intensity of a convergent wall image is very sensitive to a finite β. Thus one has to accurately evaluate β, the width of the divergence cone as well as the electron intensity distribution within this cone in order to get meaningful intensity distribution of the wall. On the other hand, the effects of a finite β is much smaller in the case of a divergent wall image as long as $\beta/\psi_o \approx 1$. In view of this, only the intensity profile of the divergent wall image was considered. Accordingly, the influence of a finite β on the intensity profiles is not important.

Second, microscope scattering has been properly accounted for by the method of measuring intensity distribution on the photographic plates. Therefore, this should not contribute significantly to the discrepancy.

Third, it should be noted that the electron beam transmitted through a ferromagnetic film undergoes crystallographic scattering as well as magnetic deflection. The crystallographical scattering may be divided into two parts, (1) Bragg reflection (elastic scattering) in individual crystallites and (2) inelastic scattering. The contribution of the first is negligible because the diffracted beam of Bragg reflection (a Bragg angle of a low order diffraction beam is about 10^{-2} rad.) was cut out by the objective aperture (20 microns in diameter) which would correspond to a semi angular aperture of about $2 \cdot 10^{-3}$ rad. in the present microscope objective of focal length 4.7 mm. On the other hand, the contribution of the inelastic scattering is complicated, and the way in which this inelastic scattering smears the intensity profiles has not been worked out quantitatively. This effect is expected to be large for thicker films, and therefore it is possible that the discrepancy may be in part due to this effect. In the present work, the effect was minimized as much as possible by using small microscope lens apertures.

Finally, one should consider the assumed wall shape used in the present study. In order to determine the wall width experimentally, the wall shape expressed by Eq. (4.3) was used. However, as already mentioned in the previous section (4.2), there is a significant difference in wall shape between the finite thickness one-dimensional theoretical Néel wall and Eq. (4.3). For a Bloch wall, as shown in Fig. (4-5b), the theoretical wall shape determined by Brown and LaBonte is not significantly different from the present wall shape (Eq. 4.3). On the other hand, Collette, and Kirchner and Döring have shown (Fig. 4-5a) that the theoretical Néel wall shape is much different. Consequently

one would expect to get a better agreement for a Bloch wall than for a Néel wall, if this matter is mainly responsible for the discrepancy. However, experimentally this is not the case as shown in Fig. 4-15. The agreement between the experimental and calculated wall widths is better for Néel wall region ($d<900$ Å) than for the Bloch wall region ($d>900$ Å).

To clarify this point, the intensity distribution of a divergent wall image based on the wall shape by Collette has been calculated. Here, one is particularly interested in the case of thickness 200 Å. For this thickness, Collette obtained the slope $d\theta/dx|_{x=0} = 2.69 \cdot 10^5$ rad/cm . On the other hand, the zero thickness exact wall model has a slope $d\theta/dx|_{x=0} = 1/\delta$. The point in question is whether the two wall shapes will give similar intensity distribution if they have equal slope of the magnetization rotation at the wall center. For this value of slope in the zero thickness exact model, the value of δ must be $(2.69 \cdot 10^5)^{-1}$ cm or 372 Å. In Fig. 4-16 the cosine of the magnetization angle θ as a function of a normalized distance μ ($\mu = x/2580$ Å) in the film plane is shown for the two models (refer also to Fig. 4-5). The intensity distributions for the models were calculated using Eqs. 4.13a and 4.13b and the results are shown in Fig. 4-17. In the figure, the distance U in the focal plane is also normalized by the factor 2580 Å. Furthermore, in the figure, the value of $z\psi_o$ is taken to be 258 Å, which is close to the value used in the present experimental study. As can be seen in Fig. 4-17, the intensities for the two models are surprisingly similar though roughly 30% different in spread. This implies that the long tails in the Néel wall do not influence the inten-

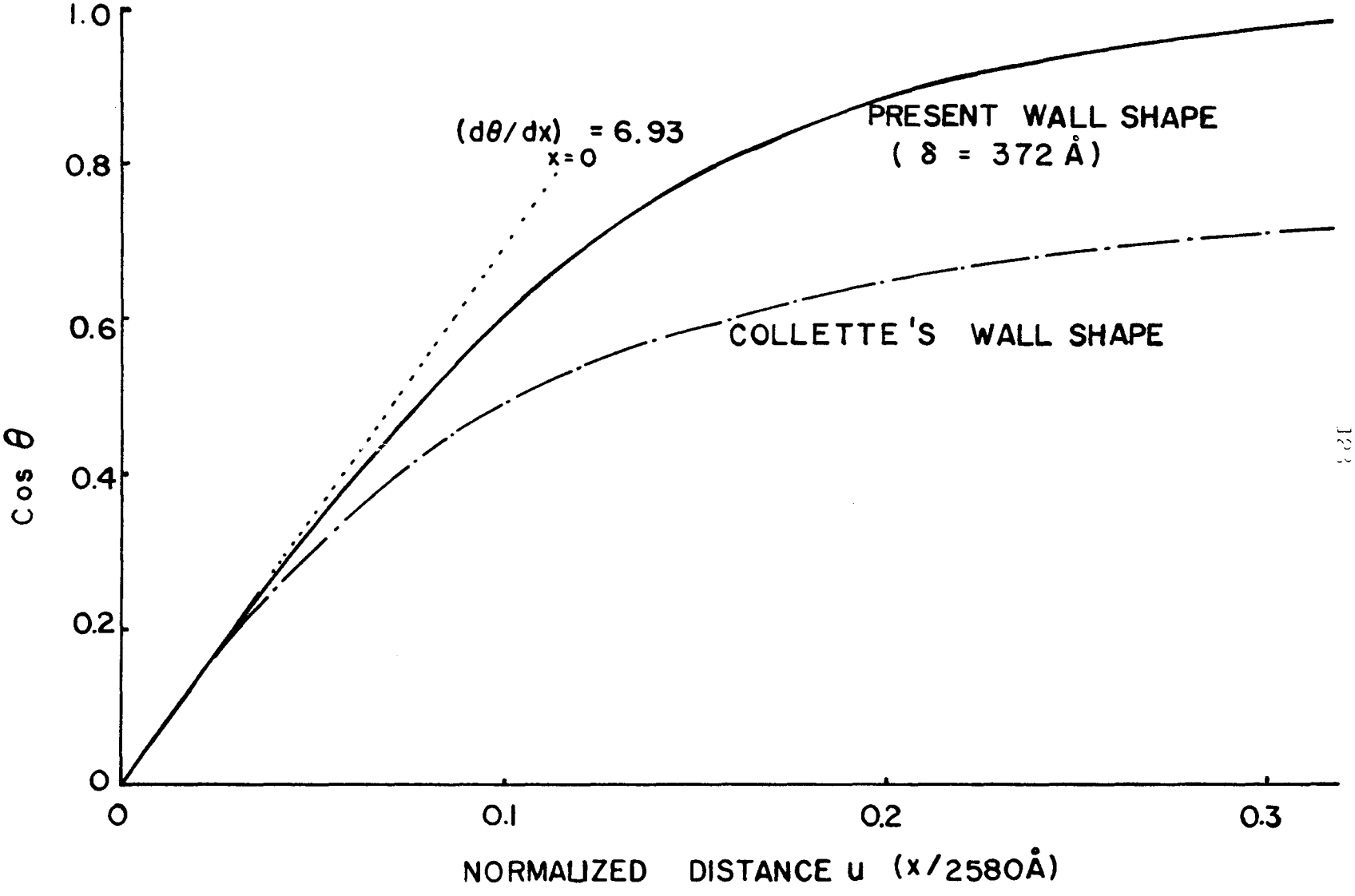

Fig.4-16 Comparison between the wall shape by Collette for 200A film thickness and the present wall model. The value of δ is chosen to be 372A so that the slope at the wall center is the same for that for Collette's model.

sity distribution in a significant way. Since the wall widths in the present work were determined on the basis of a profile match, Fig. 4-17 suggests that a 30% increase in experimental wall width would give a best fit for Collette's wall shape. Though the difference is not significant, it is distressing that the shift is in the wrong direction to reduce the large discrepancy between experimental and theoretical values at 200 Å film thickness.

(2) Classical limitation

The intensity distribution in the image plane given by Eq. 4.13 (a,b) was calculated on the basis of classical geometric optics, i.e., the electrons are incoherent and no interaction between them is considered. The most important question relating to the experimental measurement is the validity of this classical interpretation or calculation. The fundamental limitation of classical optics based on the uncertainty principle is discussed by Wohlleben (1967). This limitation sets the minimum amount of flux change which can be detected classically. That is, a change of magnetic field between two points (a magnetic inhomogenuity) can be resolved classically if the flux change due to the inhomogenuity is much larger than a fluxon, $h/2e$, where h is Planck's constant and e is the electronic charge (Appendix 4). For the measurements shown in Fig. 4-15, the number of fluxons is a minimum of about 5 for 160 Å film, increasing slowly to about 10 for 850 Å and then increasing rapidly to about 100 for the 1,800 Å film. This implies that as far as this criterion is concerned, the classical picture is quite adequate for films in excess of 1,000 Å, but may be somewhat inaccurate for films less than 500 Å thick.

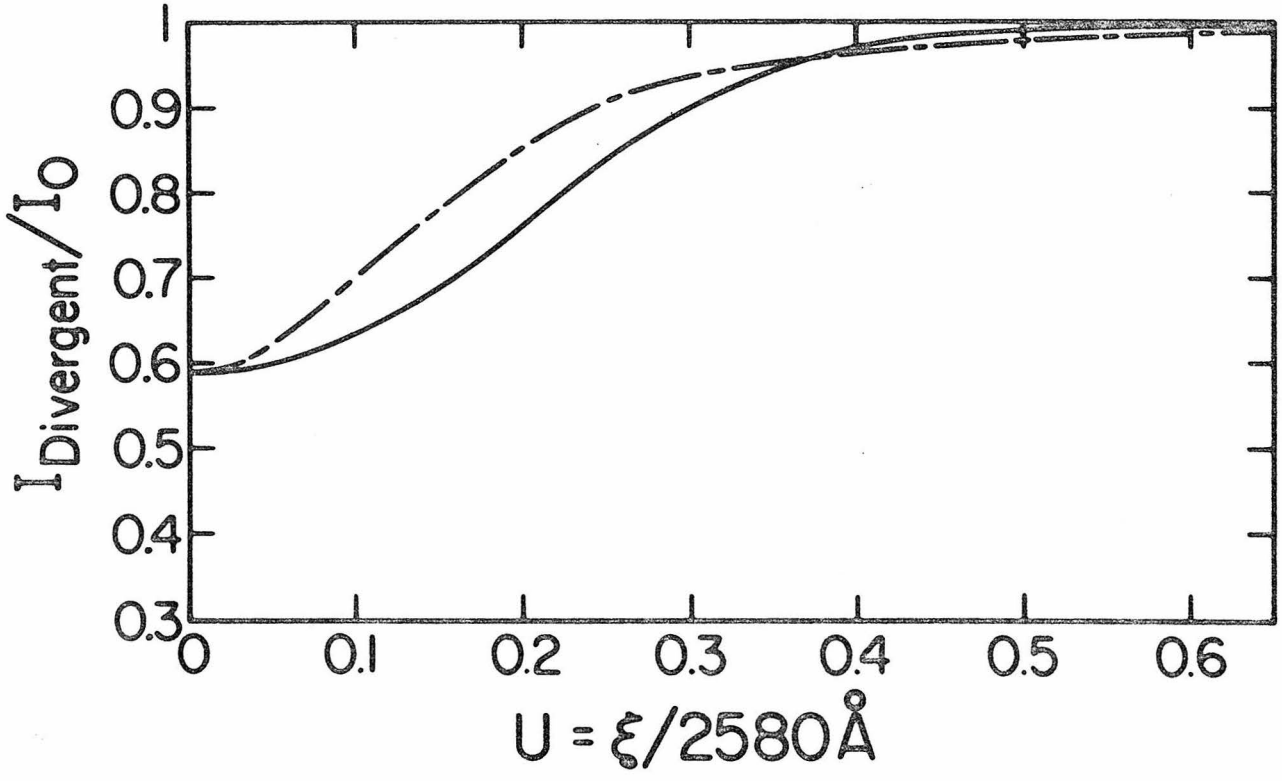

Fig.4-17 Intensity distributions of a divergent wall image for Collette's wall shape (dashed line) and for the present wall shape (solid line), using δ=372A.

A second criterion (Wohlleben, private communication) is that if $\Delta\Phi$ is not large compared to a fluxon, then the classical result is still similar to the wave-mechanical result provided the out-of-focus distance is small compared to the reciprocal of the gradient of the Lorentz deflection $(d\psi/dx)^{-1}$. In the region where the number of fluxons is small, the experimental value of $(d\psi/dx)^{-1}$ varied from about 2 cm for 160 Å thickness to about 2 mm for 600 Å thickness. This implies that if other things are equal the smallest z value possible (0.5 to 1 mm) should give more reliable results than larger values. In order to check this point, the out-of-focus distance was varied from 0.55 mm to 4.4 mm for two samples with thickness of about 1,000 Å, and from 1.1 mm to 6.6 mm for one sample with thickness of 430 Å. Wall widths deduced from both profile match and peak intensity ratio are shown in Fig. 4-18. The values of δ obtained from the profile match showed remarkably little scatter, typically ± 20%. The values obtained from the peak intensity ratio were in reasonable agreement with the other method at the smallest z value but were systematically high by a factor of about 1.7 for higher z values. In view of this result only wall widths obtained by a profile match were presented in the earlier sections.

Finally it is worth discussing the coherence condition of the electron beam. In the foregoing discussions, one assumed that an incoherent electron beam is deflected by the Lorentz force due to the internal flux of the film. According to Boersch, Hamisch, Wohlleben, and Grohmann (1960), non-classical diffraction effects occur if the electron beam satisfies the coherence condition,

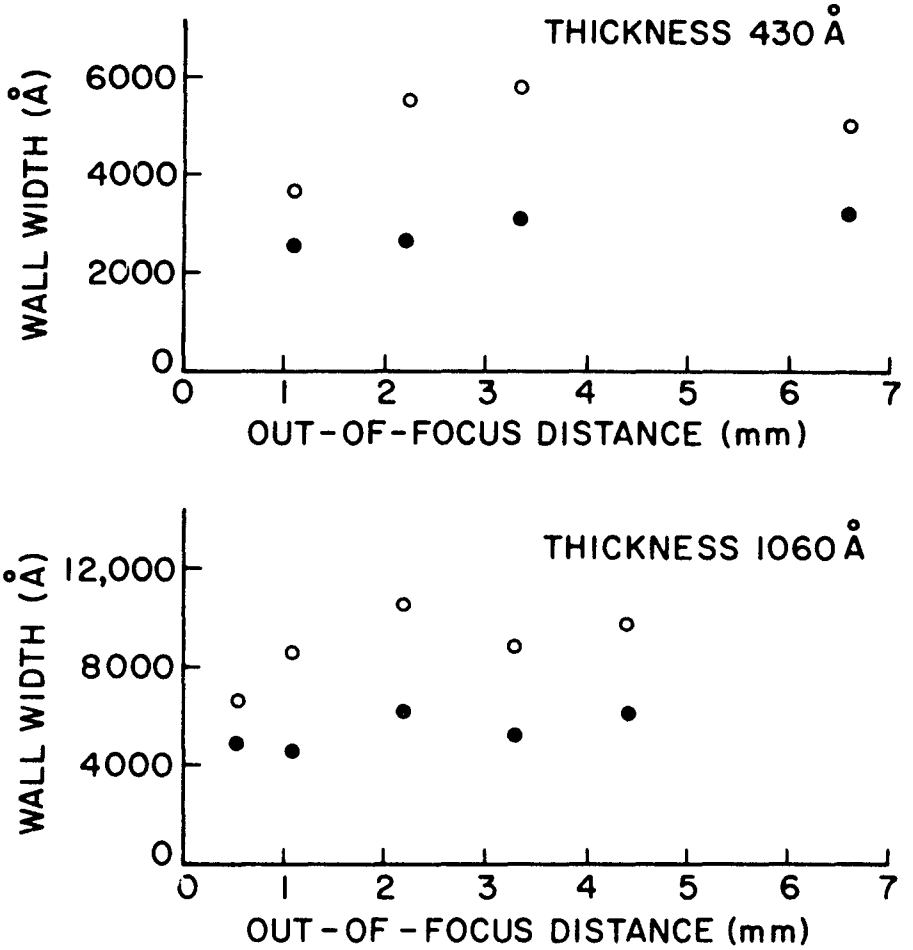

Fig.4-18 The experimental wall width as a function of out-of-focus distance for 430Å and 1060Å film thicknesses. The empty circles are the values by the intensity ratio at the wall center, and the solid dots are the values by profile match.

$$\lambda_e/4 > 2z\psi_o\beta \qquad (4.14)$$

where λ_e is the deBroglie wave length of the electrons, and $\epsilon \leq 1$. In the present case, $\lambda_e = 3.7 \cdot 10^{-10}$ cm, $z \approx 1$ mm and $\psi_o \approx 10^{-4}$ rad., thus the beam divergence angle β must be smaller than $5 \cdot 10^{-6}$ rad. for $\epsilon = 1$. Therefore the present experimental conditions ($\beta \approx 10^{-4}$ rad.) do not satisfy the coherence condition, and one may neglect the coherence effect of the electron beam. Furthermore, in the approximation that the domain wall represents an opaque region in the specimen, there may occur Fresnel diffraction fringes at the edges of the domain wall (Heidenreich, 1964). According to Heidenreich, if the $n^{\underline{th}}$ maximum in the fringes is just visible, the coherency condition requires that

$$[z(z+\ell)\cdot\lambda\cdot(2n-1)/\ell]^{\frac{1}{2}} \leq \lambda/2\beta$$

where ℓ is the distance between the effective source and the film plane. In the present case, $z \ll \ell$ ($\ell \approx 20$ cm), one can therefore obtain

$$n < 1/2$$

Under the present conditions even the first maximum is suppressed. Furthermore, a real wall presents a diffuse region rather than sharp edges, thereby restricting still further the visibility of the fringes. It follows that the observed images are negligibly modified by diffraction effects so that under the conditions described, geometrical optics can be expected to be valid. The detailed description of wave optics is given in section (4.5).

(3) Magnetic sources

Up to this point, possible sources for the discrepancy have been discussed from the experimental point of view. It is quite natural, however, to ask if the theoretical treatments discussed in the previous section, are reasonable or not. Further, it should be asked whether there is any significant change in magnetic parameters in films removed from substrate.

The data of Fig. 4-15 were obtained from films evaporated onto and stripped from NaCl substrates. In order for such data to be taken as representative for films evaporated on glass as well, it is necessary to determine whether the substrate or stripping procedure modified wall structure appreciably. A convenient wall structure parameter which can be easily measured for films on glass using the Bitter technique and films on microscope grids using Lorentz microscopy is the number of cross-tie structures per unit length of wall. These data are shown in Fig. 4-19. The cross-tie density is remarkably similar for both films on glass and stripped films mounted on copper grids. The cross-tie density increases with thickness to a maximum near 950 Å and decreases to zero for thicker films. Earlier data by Methfessel et al. (1960) using the Bitter technique are also shown. They are qualitatively similar but show a reduced maximum at about 750 Å instead of 950 Å. It is believed that the cross-tie configuration is a sensitive indicator of wall structure. The close agreement between cross-tie measurements on stripped films and films on glass strongly implies that the measurements of wall width of stripped films also are valid for films still adhering to the substrate.

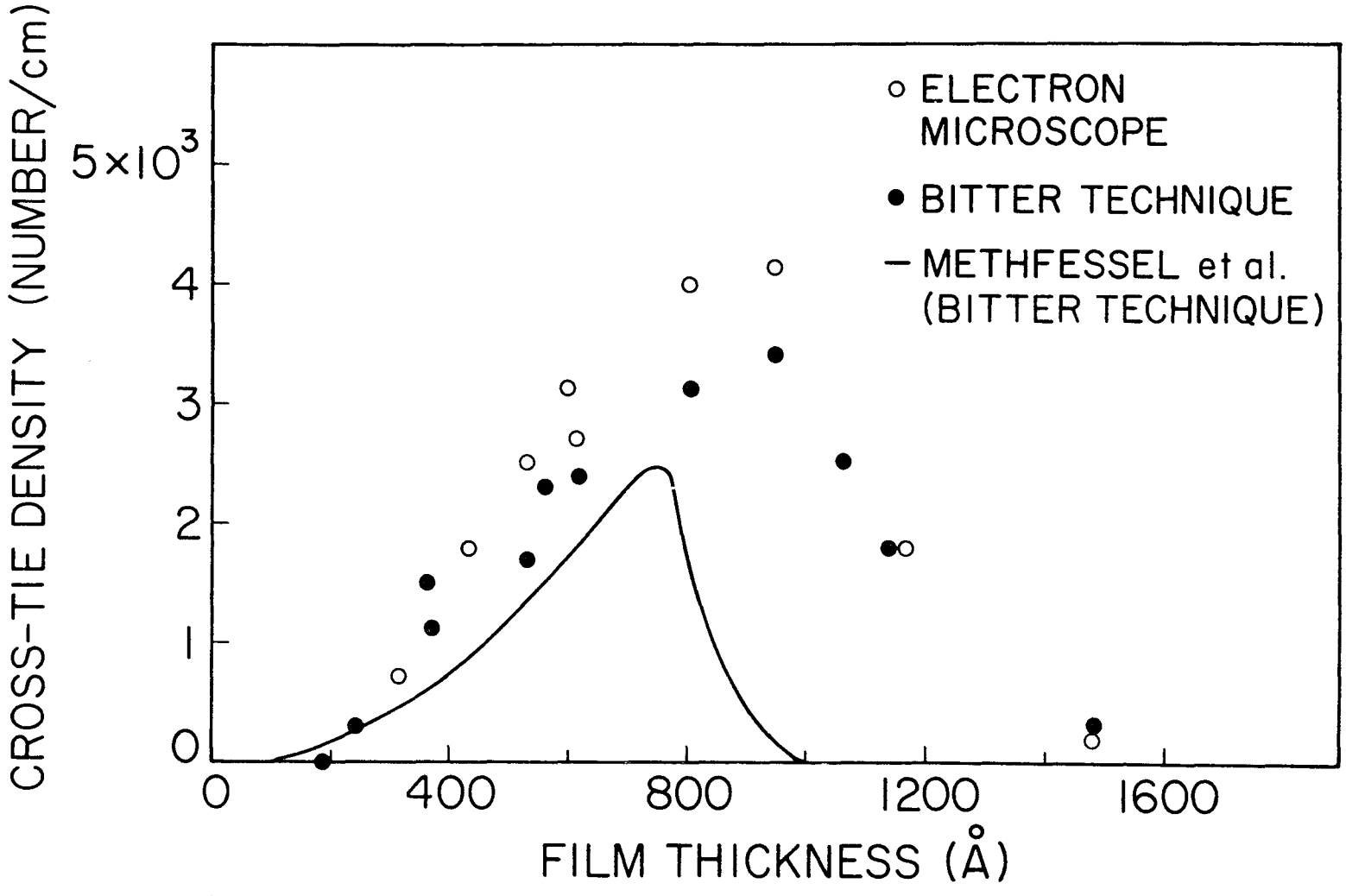

Fig.4-19 The cross-tie wall density measured as a function of film thickness for 76%Ni-Fe alloy films evaporated at room temperature.

The above measurements of cross-tie density lead to an interesting correlation, unrelated to the original purpose of the observations. It will be recalled that an apparent wall structure transition is observed at about 1000 Å thickness in Bitter patterns for domain walls in Permalloy films (see Sec. 4.2). There is also a distinct change observed at this thickness for both measured wall width (Fig. 4-15) and cross-tie density (Fig. 4-19). It is probable that all these phenomena are associated with the transition from a predominantly Néel to a predominantly Bloch wall.

As can be easily shown, the anisotropy energy of a wall for a finite film thickness is usually negligible in comparison with the exchange and magnetostatic stray field energies. In other words, there is very little change in wall width due to a change in the anisotropy constant, such as might occur upon removing the film from the substrate. However, it is still worthwhile noting that experimental measurements of uniaxial anisotropy of films deposited on glass and films deposited simultaneously on NaCl and subsequently stripped from the NaCl were in satisfactory agreement. In view of these observations, the discrepancy in wall width cannot be explained in terms of a change in anisotropy.

Sugita, Fujiwara, Saito and Taniguchi (1967) have shown that a large perpendicular anisotropy* $K_\perp$ will increase the width of a Bloch

---

*Note: It is known that films evaporated under certain conditions exhibit a uniaxial anisotropy called perpendicular anisotropy whose easy axis is normal to the film plane. The perpendicular anisotropy energy $E_\perp$ may be expressed by $E_\perp = K_\perp \cdot \cos^2\theta$ where θ is the angle between the magnetization out of the film plane and the easy axis in the film plane. This anisotropy is believed to be attributed to crystallographical structure in the film.

wall. For example, the wall width of the Bloch wall in a Permalloy film with $K_\perp/2\pi M_s^2 = 0.15$ becomes twice as large as that with zero perpendicular anisotropy. The value of $K_\perp/2\pi M_s^2 = 0.15$ was reported by Iwata, Prosen and Gran (1966) for an 81% Ni-Fe alloy film with thickness 1000 Å. However, Sugita, Fujiwara and Saito (1967) reported the value of $K_\perp/2\pi M_s^2$ to depend strongly on the degree of vacuum at deposition. The value of the anisotropy ratio was as large as 0.1 for vacuum of 5×10^{-5} Torr, but in the normal vacuum of 10^{-6} Torr, the ratio was less than 0.01, which is much too small to explain the discrepancy. The theories discussed previously (Sec. (4.2)) did not consider the effect of $K_\perp$ on wall structure in thin films, but in any event for normal fabrication procedures the effect should be negligible.

As discussed in Chapter 2, magnetostriction is one of the important factors which governs the state of magnetization. The calculations of theoretical shape based on one dimensional wall models have all avoided this problem. However, by use of 76% Ni-Fe alloy films the magnetostriction should not be important because of the small value of the magnetostriction constant at this composition. On the other hand, in the case of Co films, which will be discussed in a later section, magnetostriction might be an important factor in wall structure. In any case the effect of magnetostriction on wall structure is open to question at the present time.

Finally, it should be noted that the present consideration is restricted to one dimensional wall models. These models neglect any change in magnetization direction in a wall through the film thickness (z-axis) or along the wall direction (y-axis). In Section (4.3), it was pointed out that for thick films, the measured wall energies are

in better agreement with those based on a two dimensional wall model than with those using the simple one dimensional models. On the other hand, for very thin films the wall energy is in reasonable agreement with that expected on the basis of Collette's wall model.

For very thin films up to 300 Å, since the wall widths are much larger than film thickness, it is probable that the one dimensional wall model is adequate. However, as was seen earlier, cross-tie walls associated with Bloch lines appear for thickness above about 200 Å. For this situation the one dimensional wall picture is certainly no longer realistic (Fig. 4.6 and Fig. 4-19).

For thick films the calculated wall widths are much smaller than the film thickness, and the variation of demagnetization field along the z-direction (thickness direction) becomes significant. Accordingly, a two-dimensional wall model should be more realistic than a one-dimensional wall model. However, it should be emphasized that the experimental results indicate that the wall widths are in fact much larger than the film thickness and thus the argument that a one-dimensional wall picture is adequate would appear to be valid based on the experimental evidence. This matter remains unresolved.

As discussed in Section (4.2), the energy of the ordinary Bloch wall in a crystal has been calculated by neglecting the presence of the cross-tie walls associated with Bloch or Néel lines. The Bloch walls are subdivided by these cross-tie walls with alternation of their polarities. Such subdivisions of the Bloch wall into a periodic structure of right- and left-hand walls were first observed by Williams and Goertz (1952) and by DeBlois and Graham (1958) in bulk materials using

the Bitter technique. Shtrikmann and Treves (1960) have argued that the energy of the Bloch wall can be reduced if the wall is subdivided into segments of alternating polarity by a Néel line or region in which the magnetization rotates smoothly from one polarity to the other within the wall. They gave an approximate calculation to show that the periodic Bloch wall has a lower energy than the ordinary Bloch wall. Janak (1967) has also shown that the periodic Bloch wall is energetically more favorable than the ordinary Bloch wall in materials of sufficiently small anisotropy, such as Ni-Fe alloys. Thus, the present discrepancy could be in part due to the presence of the cross-tie walls, which is not taken into account in calculating the wall widths in thin films. However, it is doubtful that this detail provides the entire answer for the discrepancy since the cross-tie density is observed experimentally to be low for film thickness above 1200 Å, while the discrepancy is the greatest for thickness above this value.

4.4.8 Domain Wall Width in Co Films

The measured domain wall width of Ni-Fe alloy films from 200 Å to 1800 Å thick was found to be much wider than that predicted from one-dimensional Néel and Bloch wall models as discussed in the previous sections. In addition, the observation of a wall width minimum and cross-tie density maximum at about 1000 Å were ascribed to a wall structure transition in this region. The data suggested that theoretical calculations might be in error due to gross overestimation of the magnetostatic energy in the simple one-dimensional models. In order to obtain further information about this matter, domain wall width was measured for cobalt films with thickness from 200 Å to 1500 Å. The Co

films were evaporated onto glass or cleaved NaCl substrates at room temperature in a moderate vacuum of 10^{-6} Torr. The films, which were polycrystalline, showed H.C.P. structure by electron diffraction. As with Ni-Fe films, only the intensity profiles of the divergent wall image were taken into account in determining the wall width. The out-of-focus distance was 1.1 mm for the entire thickness range.

The measured domain wall width as a function of film thickness is shown in Fig. 4.20. Though the trend in wall width between 200 Å and 500 Å film thickness is not clearly established, there appears to be a slight decrease with increasing film thickness. In any case, the wall width for thicker films clearly increases from about 3000 Å at 500 Å thickness to about 6000 Å at 1500 Å thickness. This trend agrees with that found for Ni-Fe alloy films although the slope is smaller by a factor of two in the present case. By extrapolation, the wall width at zero film thickness is estimated to be about 4000 Å. Using the material in Sec. 4.2, it is possible to predict theoretically that at zero (and infinite) film thickness where the average stray field energy density is negligible the wall width should be $\sqrt{2\pi}(A/K_u)^{\frac{1}{2}}$. For such a calculation we take anisotropy constant $K_u = 2.0 \times 10^4$ erg/cc measured for Co films on glass substrates, and exchange constant $A = 1.3 \times 10^{-6}$ erg/cm measured by spin wave resonance. The predicted value is about 3600 Å in good agreement with the extrapolation. However, for the actual finite thickness films, the measured wall width is again much wider than that based on the simple one-dimensional models, and for thick films even exceeds the calculated value for infinite film thickness.

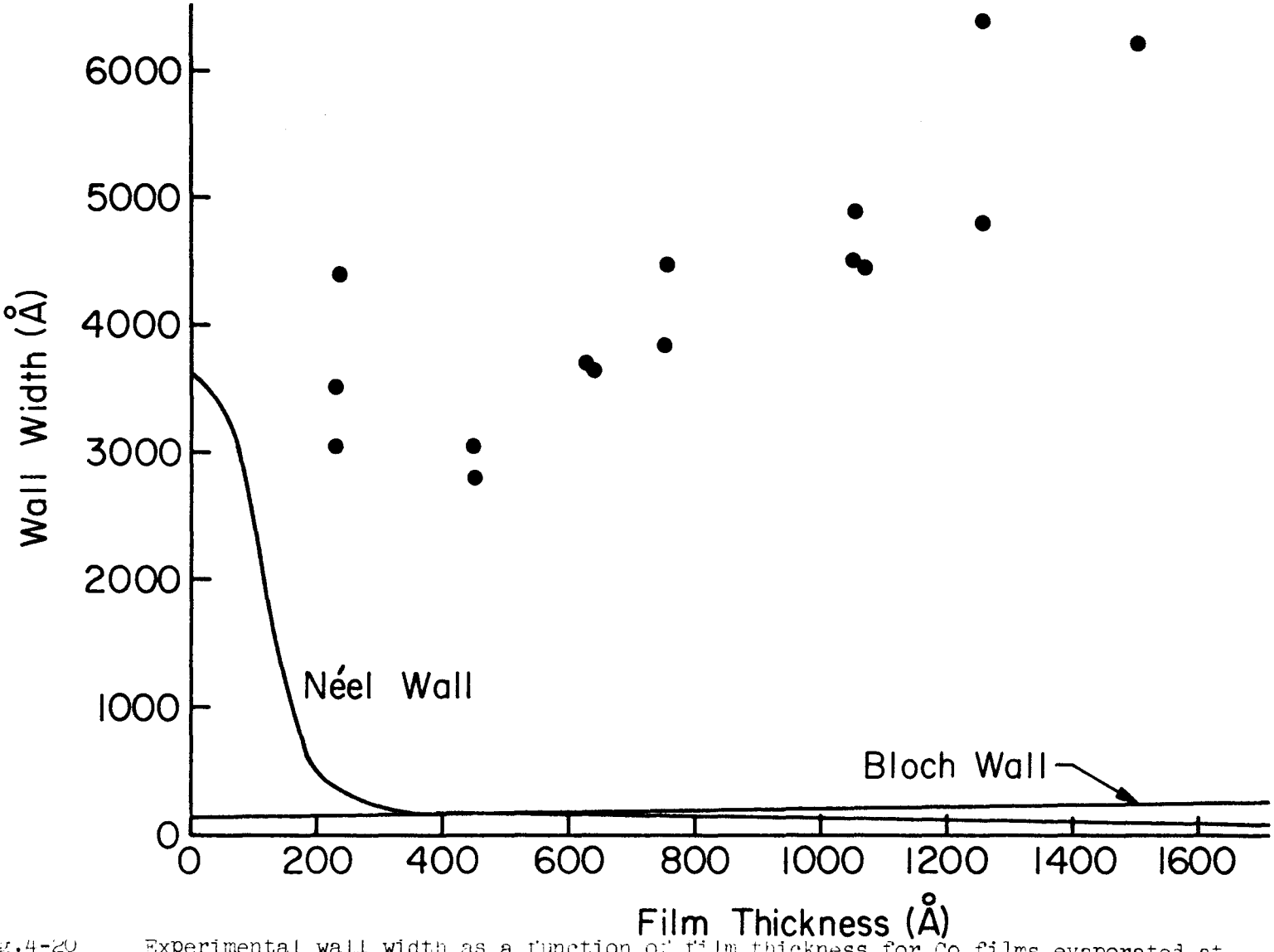

Fig.4-20 Experimental wall width as a function of film thickness for Co films evaporated at room temperature. Also shown is the theoretical prediction by Middlehoek for $K_u = 20 \cdot 10^3$ erg/cc, $A = 1.3 \cdot 10^{-6}$ erg/cm and $M_s = 1400$ oe.

As mentioned above, the discrepancy between the measured and calculated wall widths is quite large. It is necessary, therefore, to discuss possible sources for this discrepancy, as in the case of Ni-Fe alloy films. First of all, it should be emphasized that as with the case of Ni-Fe, the quantum mechanical limitations do not apply to this case either, because of the choice of divergent wall image, small out-of-focus distance, and the relatively large beam divergent angle. The discussion Sect. 4.4.7 certainly applies to this present case of Co, and thus it is not necessary to repeat here.

Second, the change of anisotropy on removing films from substrates as in the case of Ni-Fe films cannot be an important factor. Even though K_u is larger for Co films, by a factor of about 6, the effect on wall width is still very small except for very thin or extremely thick films. Furthermore it has been reported by Krukover (1967) and confirmed in this laboratory that the change in K_u for Co films is even less than for Permalloy films.

Third, as mentioned in Sect. 4.4.7 a probable source of discrepancy lies in the use of one-dimensional wall models to represent two or three-dimensional variation, but confirmation of this requires very difficult refinements of the computer programs used to make the theoretical predictions.

Regardless of the discrepancy with theoretical predictions, there is an interesting and significant difference between the experimental results for Ni-Fe alloy and Co films. This difference may be due to the larger magnetostriction in Co. In any case, there is a clear difference in cross-tie structure which implies a considerable difference in wall

structure. The cross-tie density for Co films was measured by Lorentz microscopy with the result shown in Fig. 4-21. This characteristic is very difficult to measure by the Bitter pattern technique because the cross-tie density is very large (about 4 times greater than for Ni-Fe films and the cross-tie length is very short compared to colloid size and minimum resolution of the optical microscope. As a result, clear identification of cross-tie in the micrograph is rather difficult. It should be mentioned, however, that the peak in the cross-tie density occurs at a lower value of thickness (500 to 800 Å) and the minimum in experimental wall width also occurs at a lower film thickness (about 500 Å) than is the case with Ni-Fe films.

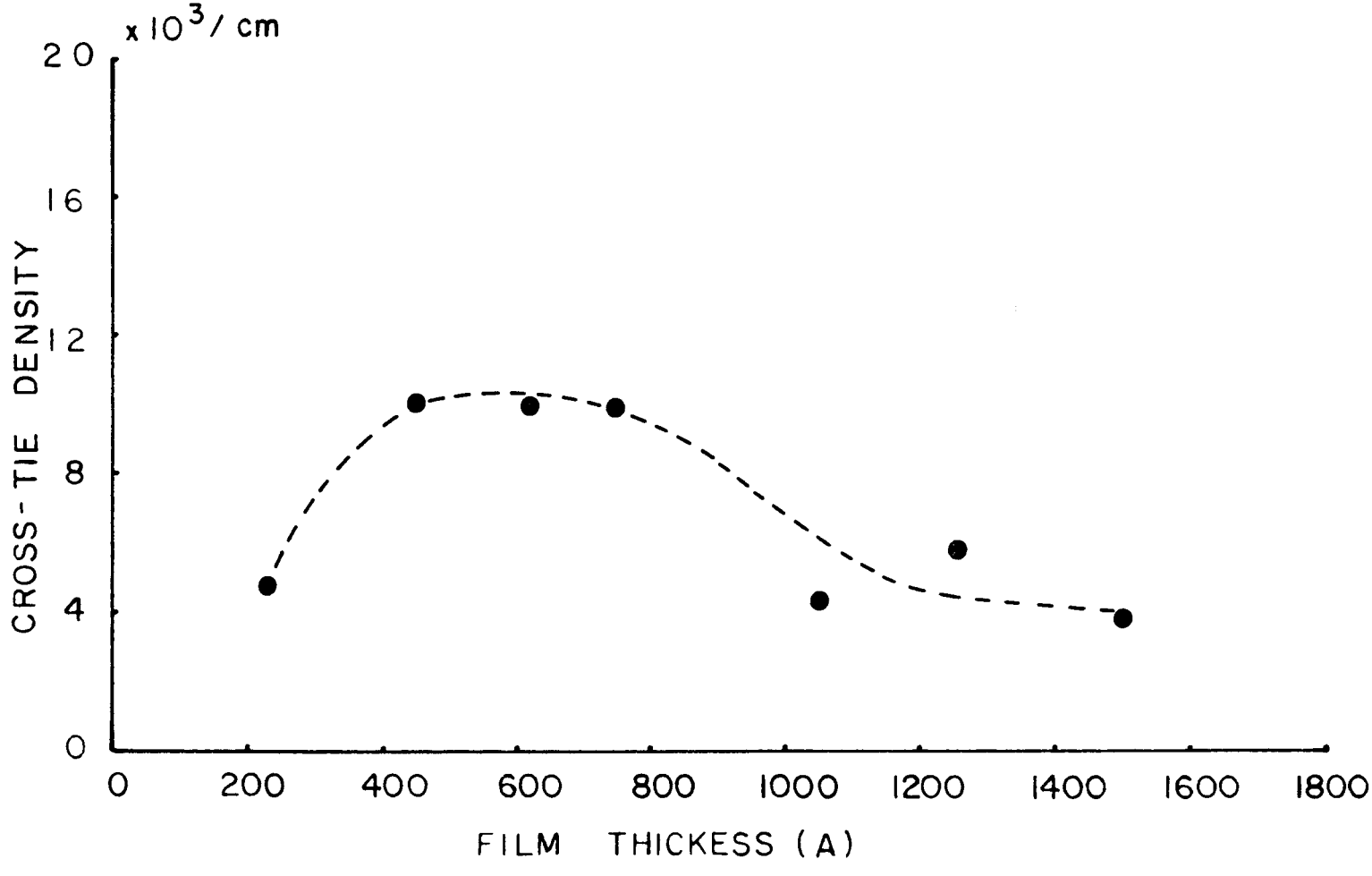

Fig. 4-21 The cross-tie wall density of Co films as a function of film thickness, obtained by Lorentz microscopy.

4.5. Wave Optics

The wave mechanical (diffraction) theory of Lorentz contrast formation has been given by Boersch, Hamisch, Wohlleben and Grohmann (1960). In the wave mechanical picture, magnetic structure in a sample presents a phase object to the electron beams, i.e. it changes the phase. It was shown by Aharonov and Bohm (1959) and Feinberg (1963) that the phase difference S between two points A and F along an electron ray is given by (Fig. 4-22)

$$S = - e/\hbar \int_F^A \vec{A} \cdot d\vec{\ell} \qquad (4.15)$$

where $\vec{A}$ is the vector potential. The two rays originate in the source point A and end in the same point F. It is evident that the interference of the two parts at F will depend on the phase difference $(S_1 - S_2)/\hbar = \Delta S$ between them. Thus there is a physical effect of the potentials even though no force is ever actually exerted on the electrons. The effect is evidently essentially quantum mechanical effect in nature because it comes in the phenomenon of interference.

The phase difference between the electrons traveling along the paths 1 and 2 at the point F is given by Eq. (4.15)

$$(S_1 - S_2)/\hbar = \Delta S = - \frac{e}{\hbar}\left[\int_{F,\,\text{path 1}}^{A} \vec{A}\, d\vec{\ell} - \int_{F,\,\text{path 2}}^{A} \vec{A} \cdot d\vec{\ell}\right] = - \frac{e}{\hbar} \oint \vec{A} \cdot d\vec{\ell} \qquad (4.16)$$

$$= - \frac{e}{\hbar} \Phi$$

where Φ is the total flux enclosed between the two paths. One assumes that there is a variation of the magnetization B in the x-direction in

Fig. 4-22. If one path goes through point x_1, while the other path goes through point x_2, one obtains

$$\Delta S = -\frac{e}{\hbar} d \int_{x_1}^{x_2} B(x)\, dx \tag{4.17}$$

Thus if the path Ax_1F is taken as the reference path, then Eq. (4.17) gives the phase shift for any arbitrary path Ax_2F. The object is thus a phase object, with the phase shift S given by Eq. (4.17). The phase difference given by Eq. (4.16) may be rewritten to be in the image plane

$$\Delta S = -\frac{2e}{\hbar} \, dB \, \frac{\ell}{\ell + z} \cdot \xi \tag{4.18}$$

Therefore, the phase shift is zero on the axis (ξ=0), and varies linearly with the coordinate ξ in the observation plane, that is, reinforcement and cancellation of the superimposed waves alternate, thus producing an interference fringe system. For the fringe separation, one can obtain from Eq. (4.18)

$$\Delta\xi = \left(\frac{\ell + z}{\ell}\right) (h/2edB) = \lambda(\ell + z)/2\ell\psi \tag{4.19}$$

The diffraction intensity distribution in the image plane has been also calculated on the basis of the Kirchoff theory (for reference, Born and Wolf, 1964; Wohlleben (1967) and Cohen, (1967). For the one-dimensional case described in Fig. 4.21, the intensity distribution is expressed by

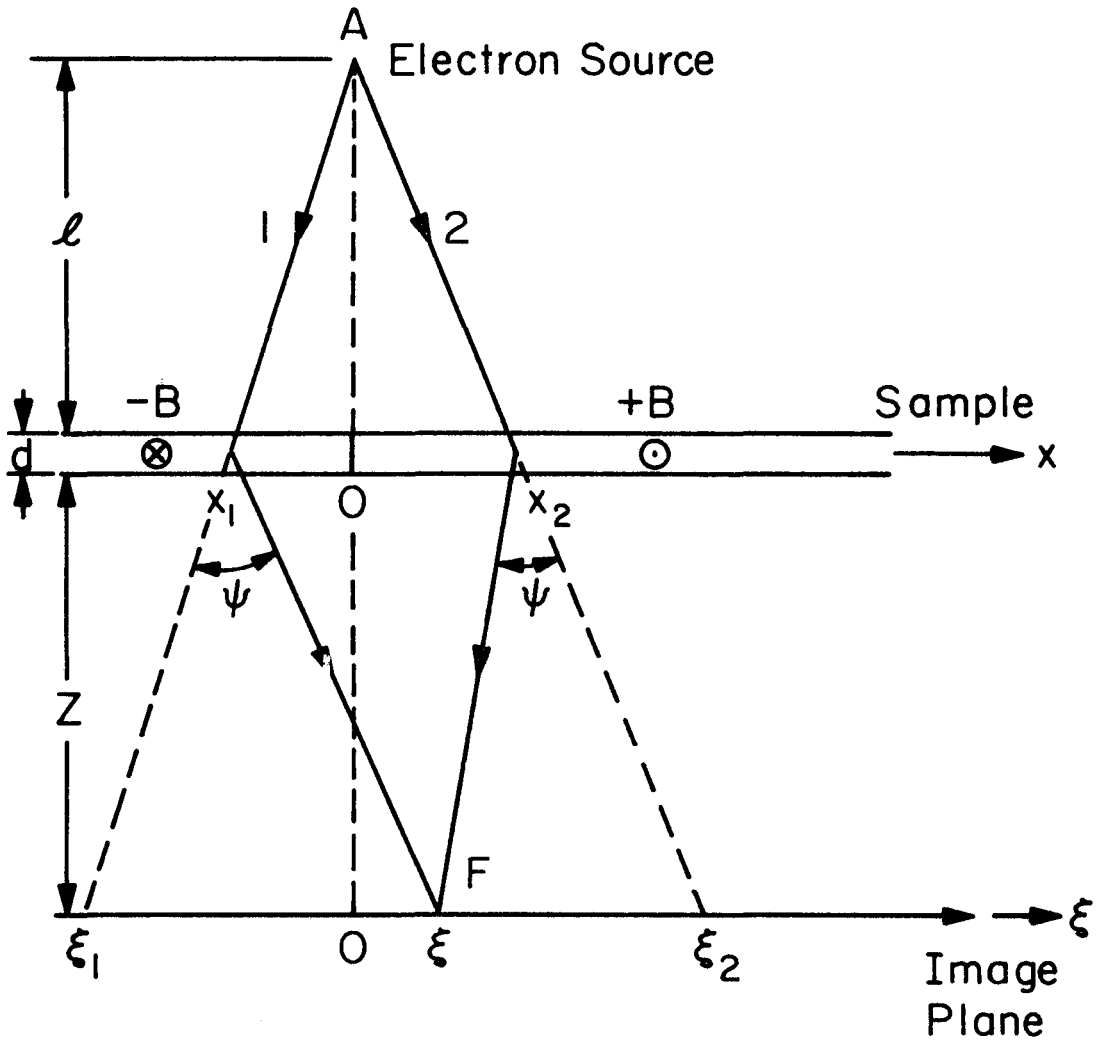

Fig.4-22 A schematical illustration of electron paths.

$$I(\xi)/I_o = \left| C' \int_{-\infty}^{\infty} dx \cdot \exp i\left\{ k\left[-\frac{x^2}{2}\left(\ell^{-1}+z^{-1}\right) + x\cdot\xi \cdot z^{-1}\right]\right\} - \right.$$

$$\left. - \frac{e}{\hbar}\Delta\Phi\right\}\Bigg|^2 \qquad (4.20)$$

where C' is a normalized constant.

A typical diffraction photograph taken at 50 kV behind the convergent wall in 79-21 Ni-Fe alloy film with 146 Å film thickness is shown in Fig. 4-23 (a). In an attempt to provide the coherent source of the electron beam, a special filament was made using one mil tungsten wire instead of the usual 4 mil wire. In addition, 100 microns condenser aperatures and 20 microns objective apertures were used. The exposure times of the photographic plate was about 20 minutes. The intensity distribution curve was obtained by the photodensitometer, as shown in Fig. 4-23 (b). The average fringe distance was measured to be about 1,500 Å in the image plane, while the expected value from Eq. (4.19) is 1,800 Å for $z \approx 3$ cm, $\ell \approx 20$ cm and $\psi_o \approx 1.6\cdot10^{-5}$ rad. These are in reasonable agreement with each other. The discrepancy probably due to uncertainties in the values of z and ℓ.

In order to obtain a perfect coherent source of electrons, there are some difficulties to be solved. The source may not be perfectly monochromatic, and has a finite width. Since the electrons leave the cathode surface uncorrelated in time, each point of the source produces its diffraction coherently, but in random phase in relation to the neighboring source points. Such a finite size of the source produces a finite illumination aperture β. In a commercial microscope, this angle cannot be decreased much below 10^{-6} rad. and one must consider the influence of illumination aperture on the diffraction profiles.

Another serious problem is that there is an inelastic scattering effect, which may disturb significantly the image profiles. In any event an attempt to apply the wave optics to study of magnetic inhomogeneities in thin films has not yet been systematically carried out.

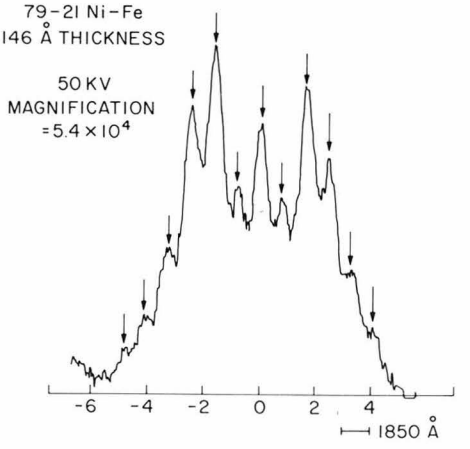

Fig. 4-23 (a) A Lorentz micrograph showing the interference fringes for 79%Ni-Fe alloy film with 146A thickness evaporated at room temperature. The photograph was taken at 50 kV using a 1-mil tungsten filament.
(b) Photodensitometer trace of the photograph shown in (a).

4.6 Summary

In this chapter, experimental measurements of the wall widths of Ni-Fe alloy and Co films have been presented. The experimental results were compared with the calculated results obtained by the simple domain wall models. The validity of the present technique to determine wall width has been also discussed on the basis of the criteria put forward by others.

Wall width was determined experimentally using the defocussed mode of Lorentz microscopy. It was found that the beam divergence must be considered for this technique, and only the divergent wall images were used to determine the wall widths. The profile match of the experimental intensity distribution of wall images with the theoretical intensity curves is believed to give more accurate measurement of wall width.

The 76% Ni-Fe alloy films in the thickness range between 200 Å and 1800 Å were examined. The results obtained are significantly different from those calculated with the simple one-dimensional wall models. The dependence of wall width on film thickness between 200 and 800 Å is not clear in the present study due to scatter in the data. Between 800 and 1800 Å film thickness the wall width increases nearly linearly from a minimum of about 2000 Å to 9000 Å. Such a rapid increase in wall width with thickness cannot be explained by the simple wall models.

The wall width of Co films as a function of film thickness from 200 Å to 1500 Å was also measured. It was found that (1) the wall widths are much wider than those expected from the one-dimensional

simple theories, as in the case of Ni-Fe alloy films, and (2) the change in wall width with thickness is more gradual than with Ni-Fe films.

At the present time, though the reason for the discrepancy between the experimental data and the theoretical predictions is not clear, it is possible that the calculations on the basis of the one-dimensional wall models may be in considerable error in overestimating the magnetostatic stray field energy of the wall. Whether this discrepancy can be explained or not is a question that can be only answered through careful and persevering studies of both experimentalists and theorists in the future.

Chapter 5

Ripple Structure

5.1 Introduction

In the previous sections, the magnetization within each domain was considered to be uniformly oriented along the easy axis. As will be discussed below, however, the local direction of magnetization in each domain is not uniform, but deviates in a quasi-periodic manner from the average direction of magnetization. This local variation in the magnetization direction gives rise to a fine structure evident in Lorentz microscopy photographs. Such a fine structure, called ripple structure, was first observed by Fuller and Hale, and by Boersch and coworkers, both in 1960. A photograph showing typical ripple structure in a 76% Ni-Fe alloy film evaporated at room temperature is shown in Fig. 5-1.

A polycrystalline thin film consists of randomly oriented crystallites. The individual crystallites have crystalline anisotropy energies, which depend on the magnetization direction with respect to the crystallographic axes of the crystallite, and therefore the crystalline anisotropy energy varies from crystallite to crystallite for a given direction of the magnetization. (Refer to Appendix 5.) It follows that the crystalline anisotropy is a variable local anisotropy in a polycrystalline film. In addition to the crystalline anisotropy, there are other sources which contribute to the total local anisotropy. For example, magnetostrictive anisotropy due to inhomogeneous stresses in a film may be one of these sources. Also, there may be a contribution to the local anisotropy from the crystallographical inhomogeneities, such as holes (porosities), impurities and dislocations.

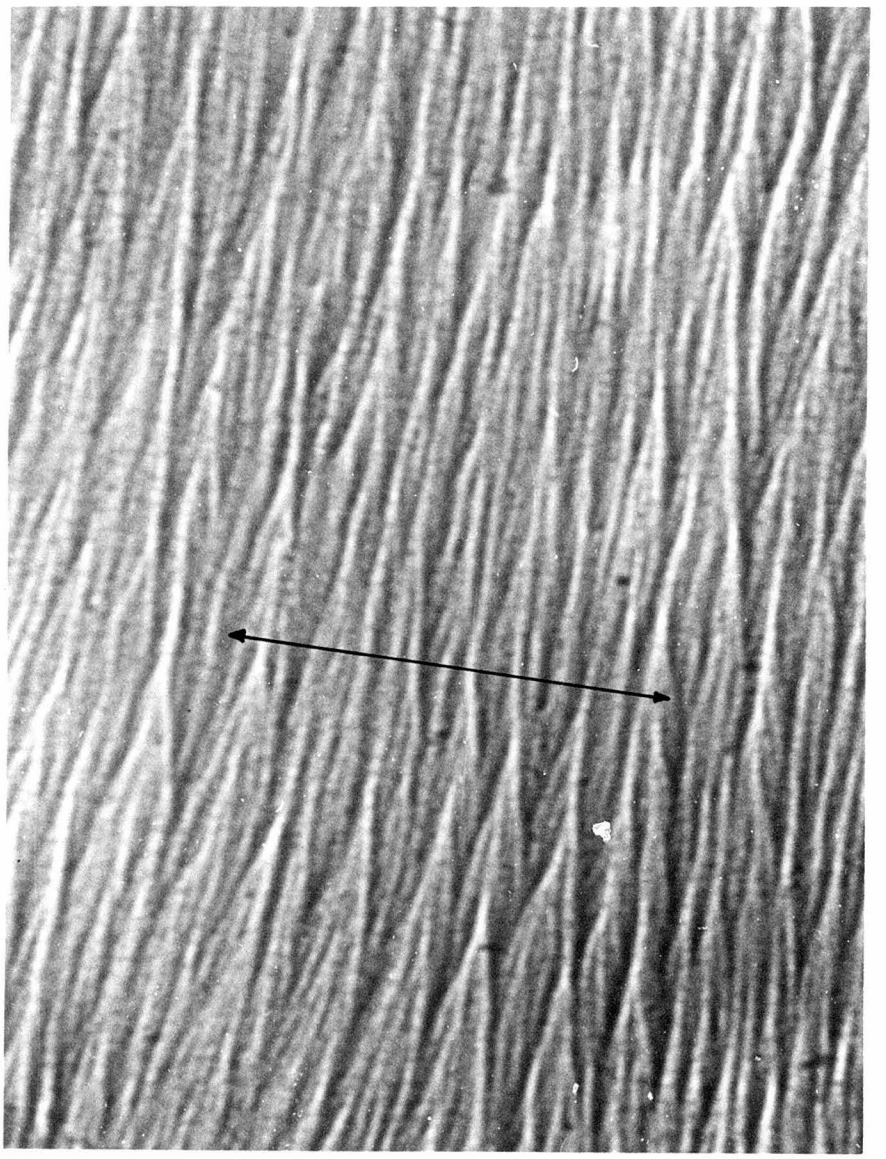

Fig. 5-1. A Lorentz microphotograph taken at 100 kV for a 76%Ni-Fe alloy film evaporated at room temperature.
(magnification, $2.5 \cdot 10^3$; the out-of-focus distance , about 3 cm).

It is easily seen that the magnetization does not completely follow these local wanderings of the direction of minimum local anisotropy energy. Instead, exchange coupling tends to straighten the course of the magnetization so that the magnetization nearly follows the mean easy axis. In addition, the magnetization dipoles are coupled by magnetostatic interactions which are of long range order and thus the ripple structure is not simply determined by the minimum local anisotropy energy condition.

There are two main questions concerning this ripple phenomenon, what is the origin, and how does it affect the macroscopic magnetic properties of a thin film? These questions are quite closely related. In fact, one of the means of studying the origin is to vary the film parameters in order to measure a macroscopic parameter which is related to the ripple via theory. In this chapter, it is intended to confine the discussion to topics which throw light on the origins of the ripple, and on the validity of the theories developed. First we shall discuss briefly some theoretical and experimental problems of magnetization ripple.

5.2 General considerations of ripple structure

5.2.1 Theoretical considerations

Lorentz microscopy reveals wavelike magnetic fine structure in a ferromagnetic polycrystalline film with uniaxial anisotropy, as shown in Fig. 5-1. To interpret the fine structure of ripple shown in the photograph, one can consider two possible kinds of ripple structure, a longitudinal ripple and a transverse ripple, as shown in Fig. 5-2. For a longitudinal ripple, the change in direction of the magnetization $\vec{M}$ is a function only of the coordinate along the direction parallel to the mean magnetization. Similarly, for a transverse ripple structure, the change in direction of the magnetization $\vec{M}$ is a function only of the coordinate normal to the mean magnetization direction. As a first approximation, for theoretical considerations, the change in $\vec{M}$ of the ripple structure may be considered as sinusoidal. If the wavelength λ and the maximum angular excursion θ_o are assumed to be equal for both longitudinal and transverse ripple, then the contribution of ripple to the total energy of the film from exchange and anisotropy is identical for both structures. This leaves only the magnetostatic stray field energy as that source which determines the configuration that is energetically more favorable.* From the assumed sinusoidal variation for the magnetization direction, one can find that the (hypothetical) volume density ρ_m is much smaller for longitudinal ripple ($\rho_m = -\nabla \cdot \vec{M}$ is proportional to θ^2) than for transverse ripple ($\rho_m = -\nabla \cdot \vec{M}$ is proportional to θ) as long as θ_c is small. Accordingly, the magnetostatic

*For simplicity of discussion here, one neglects other less important energy sources, such as magnetostrictive stress energy.

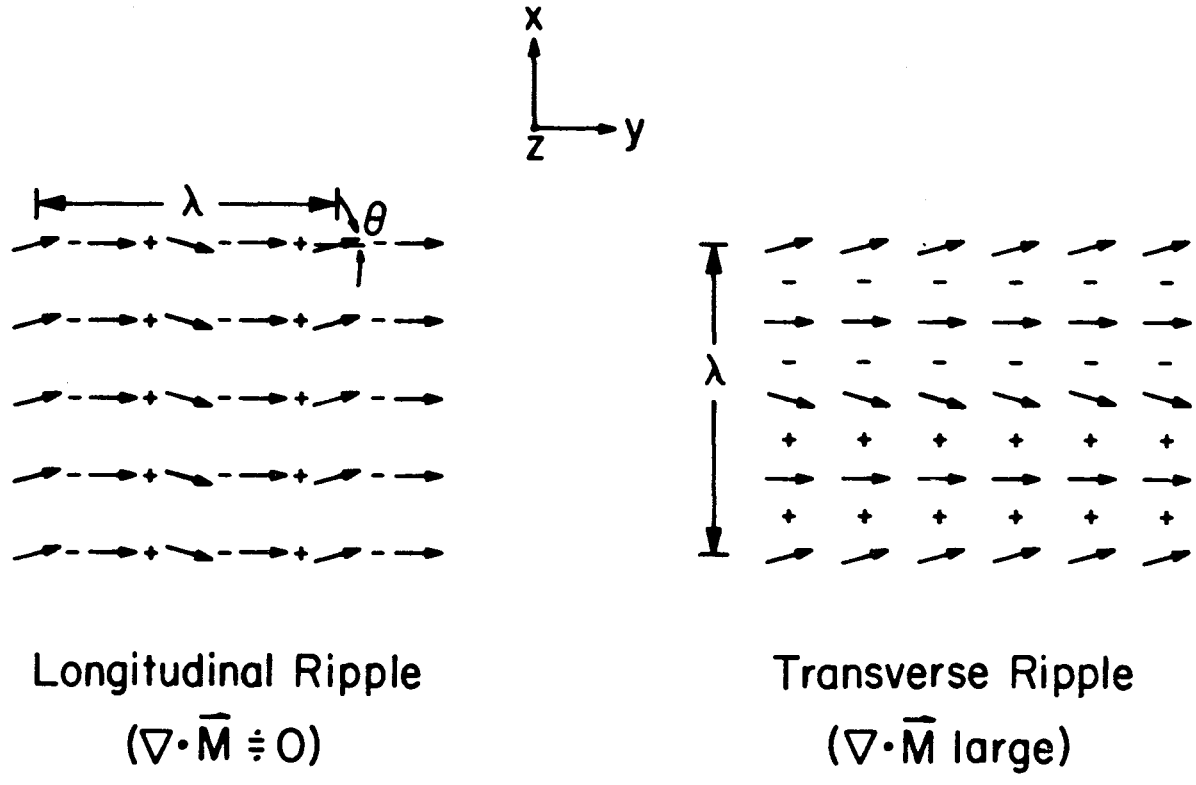

Fig. 5-2 Schematical illustration of longitudinal and transverse ripple configurations and their volume magnetic charge density.

stray field energy is much smaller for the longitudinal ripple than for the transverse ripple. Therefore, the main contribution to the magnetization ripple should be longitudinal, and the fine structure lines observed by Lorentz microscopy should be interpreted as loci of nearly constant magnetization direction. In the Lorentz microscopy photograph of the ripple shown in Fig. 5-1, the mean magnetization direction $\vec{M}_o$ is indicated by an arrow, which is normal to the stripes.

As discussed in the previous section, the source of the ripple structure must result from an inhomogeneous local anisotropy of some kind. Before summarizing the principle theoretical treatments of this problem, it is desirable to clearly state the difference between the homogeneous and the inhomogeneous local anisotropies. Consider the total anisotropy E_a which is a function of the coordinate $\bar{r}$ where the anisotropy is evaluated and of the angle Φ between $\vec{M}$ and the reference axis (Fig. 5-3).

We define the homogeneous and inhomogeneous anisotropy energies by the equation

$$E_a(\Phi, \bar{r}) = E_h(\Phi) + E_k(\Phi, \bar{r}) \tag{5.1}$$

where

$$E_h(\Phi) = \langle E_a(\Phi, \bar{r}) \rangle \quad \text{and} \quad \langle E_k(\Phi, \bar{r}) \rangle = 0$$

The average is taken over all values of $\bar{r}$ with Φ fixed, independent of $\bar{r}$. If we differentiate this with respect to Φ, we obtain the anisotropy torque

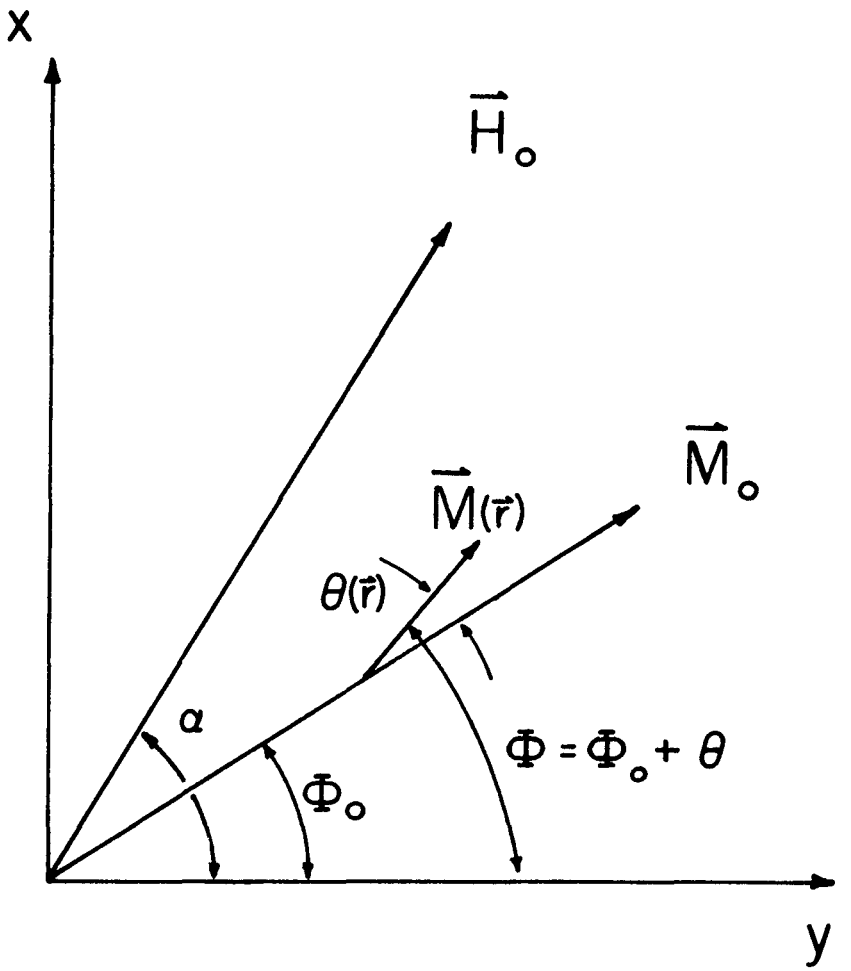

Fig.5-3 Schematical illustration of magnetization and field directions.

$$\frac{\partial E_a}{\partial \Phi}(\Phi, \bar{r}) = \frac{\partial E_h}{\partial \Phi}(\Phi) + \frac{\partial E_k}{\partial \Phi}(\Phi, \bar{r})$$

$$-T_a = -T_h - T_k$$

It is clear from the definition of E_h that

$$\langle T_k \rangle_{\substack{\text{over } \bar{r} \text{ with} \\ \Phi \text{ fixed}}} \equiv 0 \tag{5.2}$$

It is convenient to write $E_k = K \cdot f(\Phi, \bar{r})$ where K is the local anisotropy constant, and f is a trigonometric function of the angles between $\vec{M}$ and the reference axis, which is normalized so that its maximum absolute value is unity.

The first attempt to calculate the ripple wavelength and ripple amplitude was made by Rother in 1962. He formulated the variational problem of the total energy including only exchange and crystalline anisotropy, and neglecting other energy terms. The calculation was based on a model in which the thin film was assumed to consist of non-interacting linear chains of ideal, square, strain free, but randomly oriented crystallites. The mean wavelength was found to be a function of crystallite size D:

$$\lambda_{\text{Rother}} \approx 4D \tag{5.3}$$

The average maximum ripple angle was found to be

$$\theta_o \approx 6D^2K/A \tag{5.4}$$

where K is a local anisotropy constant, and A is the exchange constant.

The values of average wavelength and average ripple angle for a typical Permalloy film with exchange constant $A = 10^{-6}$ erg/cm, local anisotropy constant $K=10^{4}$ erg/cc, and crystallite size D= 200 Å, are about 800 Å, and 0.24 rad. respectively.

In 1964, he refined the calculation by allowing two-dimensional interactions and adding energy terms due to external and stray fields. In developing this theory, he found two distinctly different ripple components, i.e. short and long wavelength ripple. For the short wavelength ripple, the average ripple wavelength was found to be

$$\lambda_{short} \approx 4D \quad \text{for } D < D_g \tag{5.5a}$$

$$\lambda_{short} \approx 4D_g \quad \text{for } D > D_g \tag{5.5b}$$

where $D_g \approx (A/2M_sH)^{1/2}$. As before, M_s is the saturation magnetization and A is the exchange constant. The field H is the total effective field including both internal anisotropy field and applied field. The short wavelength ripple was found to have amplitude of the order of

$$\theta_{o_{short}} \approx 2^{1/4}\, \pi^{-1/4}\, d^{-1/4}\, KD^{7/4}\, A^{-3/4}\, M_s^{-1/2} \quad \text{for}$$

$$D < D_d \tag{5.6a}$$

$$\theta_{o_{short}} \approx 2^{3/4}\, \pi^{-1/4}\, d^{-1/4}\, KD^{3/4}\, A^{-1/4}\, M_s^{-1}\, H^{-1/2}$$

$$\text{for } D > D_g \tag{5.6b}$$

where d is the film thickness. It is instructive to evaluate Eqs. (5.6) for a typical permalloy film with $A = 10^{-6}$ erg/cm, $K = 10^{4}$ erg/cc,

$D = d = 200$ Å and $M_s = 800$:

$$\theta_{o_{short}} \approx .03 \text{ rad. for } D < D_g$$

$$\theta_{o_{short}} \approx 10^4 \, D^{3/4} \, H^{-1/2} \text{ for } D > D_g$$

It should be noted that for a normal field in the range of 1 oe. to 10 oe., the value of D_g is in the range of 2500 Å to 1000 Å and therefore only the approximations given by Eqs. (5.5a) and (5.6a) apply for the short wavelength ripple. In this case, the short wavelength ripple structure is independent of the field H and determined only by film parameters.

For the longer wavelength ripple, the average wavelength and the r.m.s. ripple angle were found to be

$$\lambda_{long} \approx 2^{5/4} \, \pi^{1/2} \, d^{1/2} \, A^{1/4} \, M_s^{1/4} \, H^{-3/4} \qquad (5.7a)$$

$$\theta_{o_{long}} \approx 2^{5/8} \, \pi^{-9/4} \, d^{-1/4} \, KD \, A^{-3/8} \, M^{-7/8} \, H^{-3/8} \qquad (5.8a)$$

Numerical values for a typical Permalloy film can be calculated using the same magnetic parameters:

$$\lambda_{long} \approx 10 \, H^{-3/4} \, (\mu) \qquad (5.7b)$$

$$\theta_{o_{long}} \approx 0.03 \, H^{-3/8} \text{ (rad.)} \qquad (5.8b)$$

It should be emphasized here that Rother predicted that the ripple could be regarded as a superposition of two ripple structures: one which has the short wavelength of about 800 Å and ripple angle of about

0.03 rad., and the other which has the long wavelength of about 1.8μ and ripple angle about .014 rad. at an effective field of 10 oe. for a typical Permalloy film.

Hoffmann (1964) also calculated the mean ripple wavelength and root-mean-square amplitude. The variational problem was considered for the total energy including exchange, uniaxial anisotropy, local anisotropy and magnetostatic energy resulting from both stray field and applied fields. His method of obtaining an approximate solution was completely different from that by Rother and led to a non-linear differential equation for the magnetization variation $\theta(\vec{r})$. As a first approximation, Hoffmann neglected the non-linear term in this differential equation, and found a solution which could be expressed in terms of modified Bessel functions. In obtaining this solution, he introduced a coupled region within which a given dipole is coupled to neighboring dipoles. This dipole is centered in the coupled region which is defined by an elliptical boundary. The major axis of the ellipse is normal to the mean magnetization direction. The ratio of the major and minor axes varies as the $(-1/4)$ power of the total homogeneous field H (α) defined below. Therefore, this ratio is insensitive to the value of the applied field over a wide range. In the absence of an external field, the ratio of the axes is about 30 for typical Permalloy films. Thus the coupled region is generally a narrow band normal to the mean magnetization direction. This implies that along the mean magnetization direction the magnetization variation takes place more rapidly than in the direction normal to the mean magnetization. Therefore, this theory also predicts that the ripple shown in

Fig. 5-1 is predominantly of the longitudinal type.

It was shown that the wavelength of the predominant ripple is related to the minor axis of a coupled region. The detailed calculation gave the value of the wavelength to be

$$\lambda_{\text{Hoffmann}} = 2\pi \left[2A/M_s H(\alpha)\right]^{1/2} \tag{5.9}$$

where

$$H(\alpha) = H_o \cos(\alpha - \Phi_o) + H_k \cos 2\Phi_o \tag{5.10}$$

In the above equations,

$\vec{H}_o$ is the applied field

$\vec{H}_k$ is the effective homogeneous anisotropy field

α is the angle between H_o and the easy axis

Φ_o is the angle between the mean magnetization direction and the easy axis.

The field $H(\alpha)$ is actually the component of the total homogeneous field $(\vec{H}_o+\vec{H}_k)$ in the direction of the mean magnetization M_o. Ripple components with shorter wavelengths than that expressed by Eq. (5.9) are suppressed by exchange coupling and thus are of small amplitude. Furthermore the components of longer wavelength are of lower amplitude because of the decreasing amplitude of their generating function. Therefore, he concluded that the wavelength λ of Eq. (5.9) is the mean wavelength which would be measured in a real film, essentially independent of the experimental parameters used in the microscopy. Since this conclusion is important in establishing an experimental verification of the theory, a detailed discussion of the matter will be given in a

later section dealing with the experimental measurements. For a typical Permalloy film with exchange constant $A = 10^{-6}$ erg/cm, and uniaxial anisotropy constant $K_u = 10^3$ erg/cc, the wavelength given by Eq. (5.9) is of the order of 1μ in the absence of an applied field (ie. $H(\alpha)=H_k$ and $\Phi_o=0$).

In Hoffmann's development it is necessary to evaluate the local torque at every point

$$T_k = -\frac{\partial}{\partial\Phi} E_k(\Phi,\bar{r}) = -\frac{\partial}{\partial\Phi}\left(Kf(\Phi,\bar{r})\right) \qquad (5.11)$$

In order to solve the differential equation for Φ, he found it convenient to use a Taylor expansion for the derivative of the anisotropy energy

$$-T_k = \frac{\partial}{\partial\Phi}\{Kf(\Phi,\bar{r})\Big|_{\Phi=\Phi_o} + (\Phi-\Phi_o)\frac{\partial^2 Kf(\Phi,\bar{r})}{\partial\Phi^2}\Big|_{\Phi=\Phi_o} + \text{higher order terms}\}$$

$$= K_s f_1(\Phi_o,\bar{r}) + (\Phi-\Phi_o)K_s f_2(\Phi_o,\bar{r}) + \text{higher order terms}$$

In the approximate solution of the differential equation, only the first term of the expansion was used. The torque function $f_1(\Phi_o,\bar{r})$ is basically a product of trigonometric function of the angles between the magnetization direction $\vec{M}$ and the crystallographic axes and has a value of the order of unity for random orientation of crystallites. As pointed out in Eq. 5.2, if this function is averaged over the entire film, it has a value of zero from its basic definition, ie., $\langle f_1\rangle_{\text{over the entire film}}=0$. Its root mean square value is therefore equal to its standard deviation $\sigma_1=\sqrt{\langle f_1^2\rangle}$. This parameter enters into Hoffmann's theory in a fundamental way. It should be emphasized that in the case

where local anisotropy contains only crystalline anisotropy, the standard deviation σ_1 characterizes the degree of epitaxy. For the case of completely random orientation of crystallites, σ_1 has a value which is independent of Φ_o and depends only on the particular form of local anisotropy, but its value is less than unity and in fact for the usual cubic anisotropies, it lies in the range $1/6 \leq \sigma_1 \leq 1/\sqrt{2}$. For partial epitaxial films, the value of σ_1 is reduced approximately by the factor $(1-\beta)$, where β is the fraction of the film which has preferred orientation.* For perfect epitaxy, $\sigma_1 = 0$.

With this background, it is possible to write Hoffmann's value for the r.m.s. ripple angle $\sqrt{\langle\theta^2\rangle} = \sqrt{\langle(\Phi-\Phi_o)^2\rangle}$ in the following form,

$$\theta_{rms} = \sqrt{\langle\theta^2\rangle} \approx 2^{-11/8}\ \pi^{-1/2}\ d^{-1/4}\ S\ A^{-3/8}\ M_s^{-7/8}\ H(\alpha)^{-3/8} \tag{5.12}$$

In this equation, S, called the structure factor, is a parameter which reflects the crystallographical structure of the film. It depends directly on the mean crystallite size D, local anisotropy constants K_s and σ_1, and inversely on the square root of n, the number of crystallites contained in the film thickness.

$$S = \sigma_1\ K_s\ D/\sqrt{n} \tag{5.13}$$

As can be seen in Eq. (5.12), the r.m.s. value of the ripple angle is sensitively dependent on the structure factor S. For typical films of Permalloy, the r.m.s. value of the ripple angle given by Eq. (5.12)

---

*Note: For the case where the non-epitaxial crystallites are completely random, the variation of σ_1 can be evaluated exactly: $\sigma_1 = \sigma_{1\ max}(1-\beta)(1+\beta)$.

becomes

$$\sqrt{\langle\theta^2\rangle} \approx 0.03\ [H(\alpha)/H_k]^{-3/8}\ (\text{rad.}) \approx 0.04\ (H(\alpha))^{-3/8} \qquad (5.14)$$

where we have taken the values $A = 10^{-6}$ erg/cm, $K_u = 10^3$ erg/cc, $M_s = 800$ gauss, $K_s = 10^4$ erg/cc, D=d= 200 Å, n=1 and $\sigma_1 = 1/\sqrt{2}$.

It should be emphasized that as far as the wavelength is concerned, the result obtained by Hoffmann is at variance with that by Rother since Rother predicted two different ripple components, neither of which varies with film parameters in the way predicted by Hoffmann. Nevertheless, for a normal Permalloy film, the average ripple wavelength of Hoffmann is about the same as that for the long wavelength of Rother (and is larger than the short wavelength of Rother by a factor of about 10). Also there is surprising agreement between the values of the ripple angle predicted by Hoffmann and Rother. Not only do they predict the same dependence on the magnetic parameters K,D,A,M_s, d and effective field H, but both have the same order of magnitude, 10^{-2} rad.

In summarizing the theory of Hoffmann, the important features are the introduction of the coupled region which essentially determines the average wavelength, and the prediction that the ripple results from the randomly oriented local anisotropy in a film. Since the average ripple angle strongly depends on the structure factor S, this is an important parameter through whose variation one can test the validity of the theory. It should be also noted that the average ripple angle is relatively insensitive to exchange, uniaxial anisotropy, applied field and film thickness.

In 1964, Harte made a detailed and more general calculation of the ripple structure in thin films. His calculation was based on local torque balance using the exchange, applied and stray fields, homogeneous anisotropy and inhomogeneous anisotropy terms. The predicted average spin coupling distance and the r.m.s. ripple angle are in excellent agreement with the mean wavelength and ripple angle obtained by Hoffmann, differing only slightly in the numerical factors (about 30% larger than that of Hoffmann for the case of $\sigma_1=1/\sqrt{2}$ and n=1).

5.2.2 Experimental situation of the ripple study

Limited experimental studies of the ripple structure in thin films have been carried out by several workers. Fuller and Hale (1960) and Boersch and coworkers (1960) were the first who showed the presence of the ripple structure in thin films by Lorentz microscopy. The mean wavelength observed by Fuller and Hale was of the order of 1μ in Permalloy films. This value is in reasonable agreement with that predicted by Hoffmann, and also with Rother's long wavelength prediction. Baltz and Doyle in 1964 reported an experimental confirmation of the short wavelength predicted by Rother, including the dependence of the shorter wavelength on crystallite size. They controlled the crystallite size D through recrystallization by annealing. In this way, they deduced a value of D_g of 2000 Å for Permalloy polycrystalline films.

Fuchs (1961), and Baltz (1964) studied the dependence of the ripple on alloy composition in Ni-Fe alloy films. They found that the ripple structure disappeared at the composition of about 74% Ni where the bulk crystalline anisotropy constant K_1 passes through zero (refer

to Appendix 5), and therefore suggested a correlation of the ripple structure with the crystalline anisotropy. Baltz further concluded that the origin of the ripple is in the random orientation of crystallites.

Puchalska in 1964 observed the temperature dependence of ripple in Ni-Fe alloy films (80% Ni melt composition) and found that the ripple disappeared partially or completely at about 300°C. For temperatures above this value, the ripple reappeared. It was suggested that the observed phenomenon of the ripple disappearance at 300°C was connected with the disappearance of either the crystalline anisotropy or the induced uniaxial anisotropy at this temperature.

In contrast to the conclusion mentioned above that the origin of the ripple structure is found in the crystalline anisotropy in polycrystalline films, Tsukahara and coworkers in 1963 concluded that local stresses are the main cause of ripple. This belief was primarily based on the observation of ripple in polished Ni-Fe alloy single crystals with relatively small crystalline anisotropy ($K_1 \leq 10^4$ erg/cc). They also observed the ripple structure in 75.8% Ni-Fe alloy films where the crystalline anisotropy constant K_1 is very small and where the magnetostriction constant is large ($\sim 10^{-5}$). Therefore, they concluded that the ripple was due to stresses in the films rather than to randomly oriented crystalline anisotropy. Even though their studies were carried out in a qualitative way, their result is at variance with that reported by Baltz and Fuchs.

From the above discussion, it is clear that no systematic experimental study of ripple has been made, and accordingly no meaning-

ful comparison between theoretical predictions and experimental results is possible. Therefore, it was felt that it was desirable to further examine experimentally the ripple structure in order to shed more light on the origin of ripple in thin films. In the next sections, the experimental method and results in Ni-Fe alloy films will be presented.

5.3 Experimental results and discussion of ripple in Ni-Fe alloy films

5.3.1 Ripple measurement

The present study of ripple structure has been performed by Lorentz microscopy. Since general considerations pertaining to Lorentz microscopy were presented in part in the previous chapter and are given in Appendix 3, we shall confine the discussion here to the more specific experimental details for ripple observation.

Since the large demagnetizing field through the film thickness direction constrains the magnetization to lie in the film plane, the magnetization distribution for ripple can be considered to be two-dimensional.*

$$\overline{M} = (\vec{e}_x \sin\theta + \vec{e}_y \cos\theta) M_s \qquad (5.15)$$

in which θ is the angle between the y-axis and the local magnetization direction, and $\vec{e}_x$ and $\vec{e}_y$ denote the unit vectors in the x- and y- direction in the film plane, respectively. We further assume that θ is a function of only x and y coordinates, ie. there is no variation of θ through the film thickness.

As discussed in section (5.2.1), the ripple structure is expected to be predominantly longitudinal, and it may be assumed to be sinusoidal as a first approximation.

---

*Note: As discussed in the previous section on domain wall structure, this approximation should be reconsidered if there is any perpendicular anisotropy which tends to pull the magnetization out of the film plane. Since this is believed to be negligible in the present study, we did not consider the case with magnetization component in the normal direction.

$$\theta = \theta_o \sin (2\pi y/\lambda) = \theta_o \sin ky \ . \qquad (5.16)$$

where θ_o is the maximum ripple angle, λ is the ripple wavelength and $k = 2\pi/\lambda$. The schematic description of the ripple was given in Fig. 5-2.

The present objective is to determine experimentally the predominant wavelength and the mean ripple amplitude in the magnetic film from the intensity distribution of the Lorentz micrograph. For the sinusoidal magnetization distribution expressed by Eqs. (5.15) and (5.16), the intensity distribution of ripple can be calculated on the basis of classical optics, in a similar way to that discussed in detail in Chapter 4 on domain wall structure. Substitution of Eq. (5.16) into the classical intensity distribution expressed by Eq. (A-3.1) in Appendix 3 yields

$$I(\eta) = I_o \ (1 + z\theta_o\psi_o k \cos ky)^{-1} \qquad (5.17)$$

$$\approx I_o \ (1 - z\theta_o\psi_o k \cos ky)$$

$$\eta = y + z\theta_o\psi_o \sin ky$$

provided

$$\theta_o \ll 1 \ , \text{ and } 2\pi z\theta_o\psi_o \ll \lambda$$

The derivation of Eq. (5.17) assumes zero-beam divergence in the microscope. The actual finite beam divergence sets a limit to the fineness of detail and therefore the minimum wavelength which can be observed. This limit is given approximately by

$$\lambda_{min} \approx z\beta \qquad (5.18)$$

In the present microscope, β has its minimum value if the double condenser lens is used with maximum over-focusing. In this case, β is about 5×10^{-5} rad, so λ_{min} is about 0.5μ for an out-of-focus distance $z = 1$ cm and 2μ for $z = 4$ cm. From the practical point of view, the out-of-focus distance must be greater than one cm, in order to obtain usable contrast in the photographs. Since the expected wavelength is about 2μ, the out-of-focus distance should not exceed 4 cm. Most of the measurements described in the following sections were made within these limits.

In the case of sinusoidal ripple with wavelength greater than λ_{min}, the wavelength can be simply obtained by direct measurement of the periodicity on the photomicrograph. The ripple angle θ_o can be determined from the intensity ratio $\tau = I_{min}/I_{max}$ where I_{min} and I_{max} are the minimum and maximum intensities. Using Eq. (5.17), the ripple angle θ_o is given by

$$\theta_o = [(1-\tau)/(1+\tau)]\,(zk\psi_o)^{-1} \tag{5.19}$$

As discussed in the previous section, a wide distribution of wavelengths is present in the case of actual ripple. For example, a typical photodensitometer trace is shown in Fig. 5-4. The problem then is to find an experimental method for determining the predominant wavelength predicted by the various theories. Several methods have been suggested for obtaining the main periodicity from measurements made on the photomicrographs. The two most obvious methods are: (1) counting the number of peaks per unit distance and (2) counting the number of times the intensity trace crosses the mean intensity per

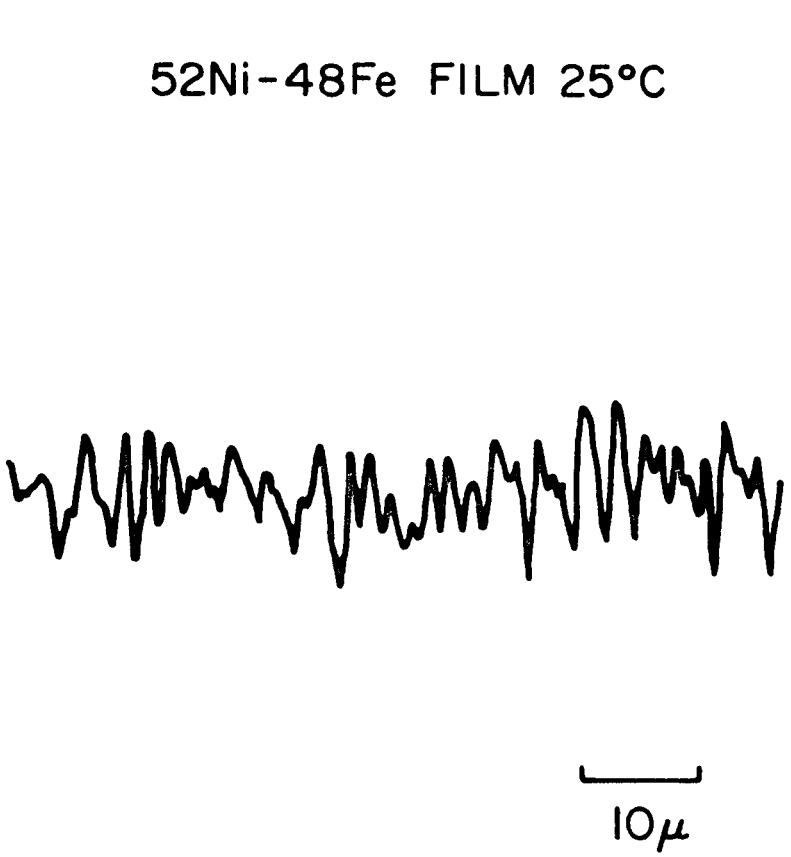

Fig. 5-4 A typical photodensitometer trace for a 52%Ni-Fe alloy film evaporated at room temperature.

unit distance (number of zero-crossings). Experimentally, it has been found that these criteria give very similar results for ripple photographs taken with out-of-focus distances varying from one to four cm. However, Harte has recently shown from a quantum mechanical treatment that the number of zero-crossings depends primarily on the microscope conditions and is almost independent of the actual ripple detail in the film, as long as the ripple spectrum covers a wide range of wavelength. His result is:

$$\lambda_{zero.} = 1.66\ (\pi z \lambda_e)^{\frac{1}{2}} \qquad (5.20)$$

where λ_e is the deBroglie wavelength of the electrons. Clearly, if this result is correct, the predominant wavelength in the actual film cannot be obtained by these methods.

A third method has been devised independently in the course of the present research and by Hoffmann. It is believed that a physically meaningful wavelength can be obtained by visually finding a well-defined predominant periodicity on the Lorentz photomicrograph which is independent of microscope conditions, particularly the out-of-focus distance. Up to date, no meaningful study of this matter has been reported in literature, and it is desirable and appropriate to investigate this problem systematically. In the present study, all three methods were explored for determining the wavelength. The measurements were carried out as a function of out-of-focus distance at 100 kV. The reasons for choosing z as a variable parameter are (1) the intensity should be directly dependent on out-of-focus distance, (2) the resolution of the microscope is dependent on out-of-focus distance as well as beam divergence, and (3) the most controversial point in this matter is whether

the average observed wavelength is changed by out-of-focus distance. Samples of 76% Ni-Fe and 81% Ni-Fe alloy films were chosen with thickness between 500 and 600 Å, evaporated at room temperature.

One sequence of photographs for a 76% Ni-Fe alloy film taken at several out-of-focus distances is shown in Fig. 5-5. All the photographs show the same region of the film. The following features are immediately evident: (1) the overall contrast of the ripple structure clearly increases with out-of-focus distance, (2) although the fineness of detail appears to decrease as the out-of-focus distance z increases, all the photographs exhibit essentially the same pattern of ripple lines. One can see a well defined ripple periodicity of about 2μ for all z values larger than one cm. It may be argued, however, that the definition of a well defined periodicity is subject to an individual person's choice. One might pick up each fine ripple line and call that the well defined ripple structure. However, the important thing is that within the network of fine ripple lines, one can recognize the presence of the main ripple by its higher contrast. It is probably easier to find such a well defined ripple periodicity if one looks at a photograph from some distance (about 1m) or at a glancing angle. The photographs shown later in Fig. 5-12 are other good examples in which the main ripple wavelength varies greatly with the applied field, even though z is held constant.

In order to determine the mean wavelengths by the three different methods described above, photodensitometer traces of the photographs were taken, and also the well defined ripple lines were counted visually on the photographs. The results are shown in Fig. 5-6. In the figure,

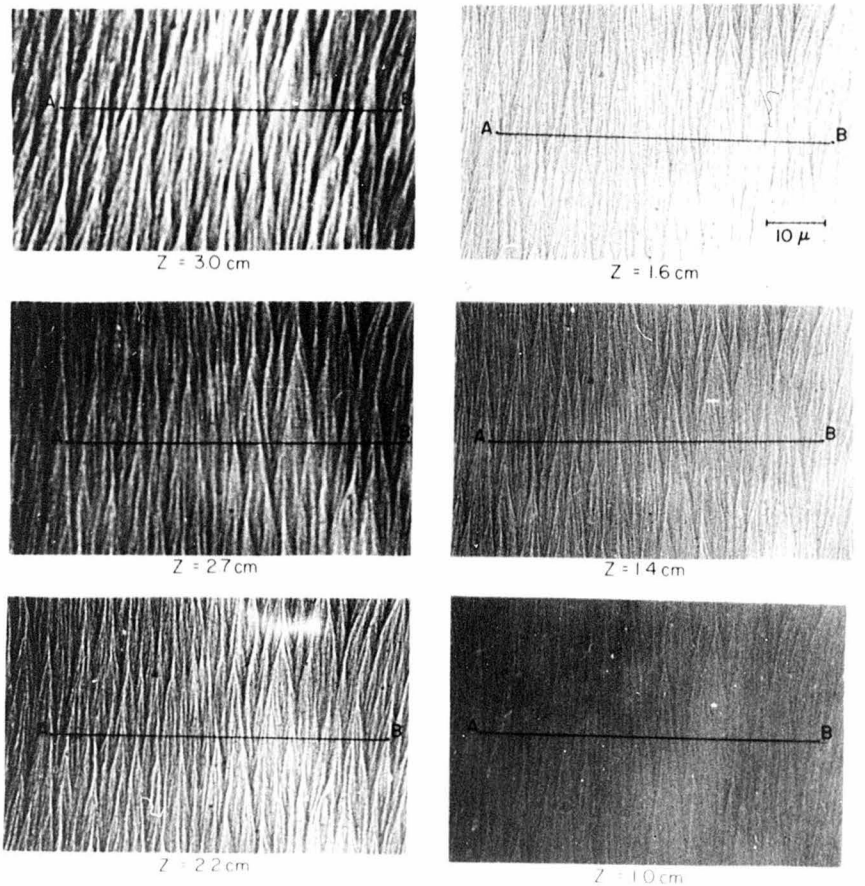

Fig.5-5 A sequence of ripple photographs for a 76%Ni-Fe alloy film with 560Å film thickness evaporated at room temperature.

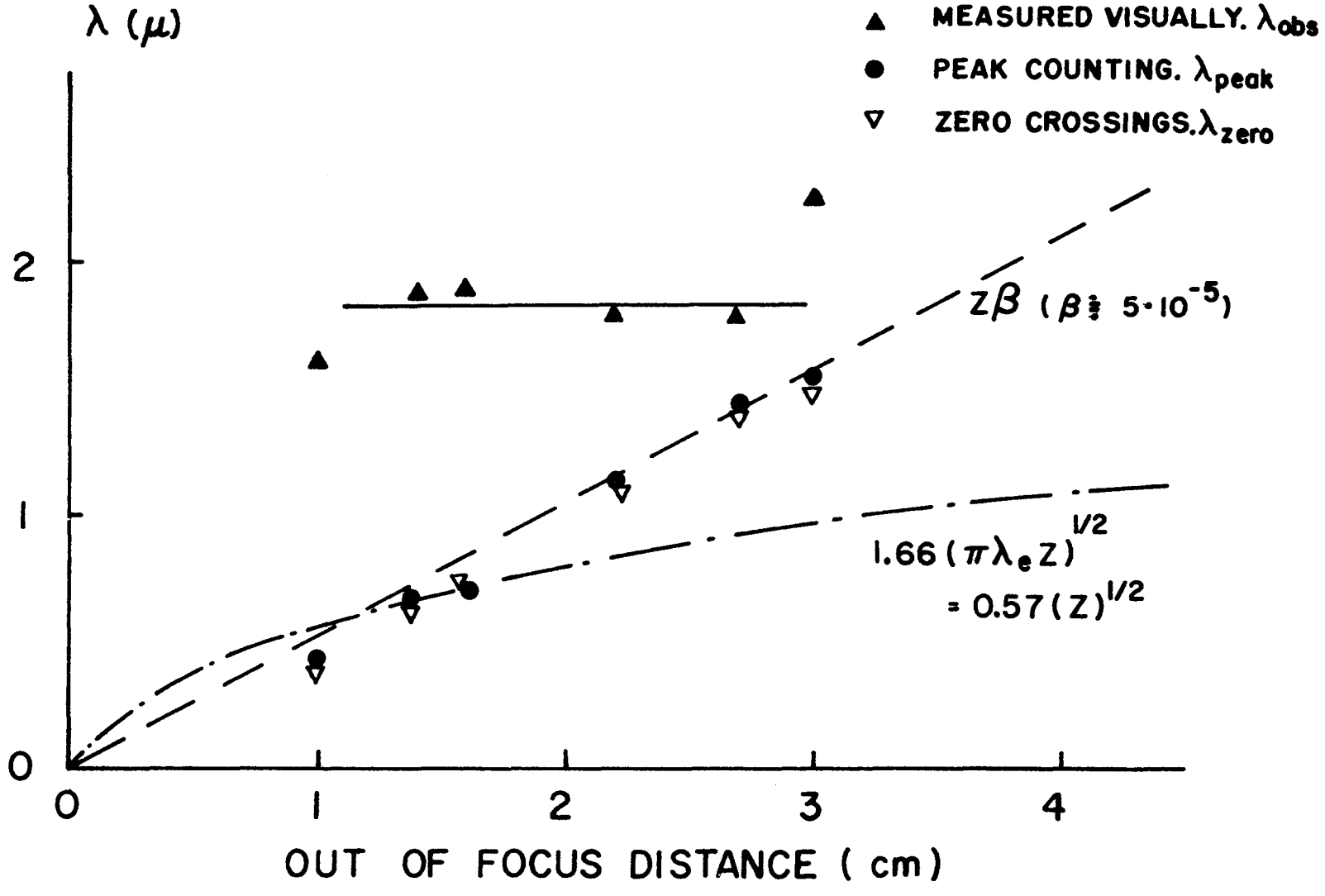

Fig.5-6 Observed mean wavelength by the three different methods as a function of out-of-focus distance for the 76%Ni-Fe alloy film. The ripple photographs were given in Fig.5-5. Also shown are the theoretical prediction by Harte and the resolution limit due to beam divergence.

λ_{peak} and λ_{zero} are the values of mean spacing of intensity peaks and mean spacing of zero-crossings respectively, and λ_{obs} corresponds to the value determined by choosing the well defined ripple periodicity. The following should be emphasized; (1) λ_{obs} remains essentially constant, until z exceeds 3 cm. and (2) λ_{zero} and λ_{peak} increase steadily with z. Similar results were obtained with four other samples. It is easily seen from the photographs given in Fig. 5-5, that the increase in λ_{zero} and λ_{peak} with z are due to the gradual disappearance of fine structure.

In order to compare this with theoretical predictions, the divergence cut-off Eq. (5.18), and Harte's results Eq. (5.20) have been plotted in Fig. 5-6. The agreement with the experimental values of λ_{zero} is quite satisfactory. However, it will be noted that since $z\beta$ and λ_{zero} are nearly equal for the smallest usable value of z, it is not possible to confirm Harte's calculation. In the present case, the effect of beam divergence dominates. In view of the above results, one may now conclude that the well defined ripple periodicity indicates something physically meaningful, e.g. the predominant wavelength predicted by Rother and Hoffmann, or the size of the coupled regions predicted by Harte. Furthermore, meaningful quantitative measurements with a photodensitometer are very difficult. It is somewhat ironic that with all of our well-developed instrumentation it may at times be easier to use one's qualitative judgement in making a physically meaningful measurement. It should be added that Hoffmann has independently put forth these same ideas.

The problem of ripple angle measurement is even more difficult.

In the case of sinusoidal ripple, Eq. (5.19) gives the peak ripple angle based on classical optics. In the case of actual ripple, the problem is complicated by the fact that a wide distribution of wavelengths is necessary for a Fourier representation of the magnetization variation. According to Harte, even though the microscope parameters are chosen so that the classical evaluation is valid for a single component, the same cannot be said for the Fourier representation. Since the intensity variation is not sinusoidal, Eq. (5.17) and (5.18) are not valid. It is possible, however, that use of equation (5.18) and the average minimum and maximum intensities of Fig. 5-4 will give an order of magnitude estimate of the ripple amplitude. This method has been used utilizing the techniques described in Chapter 4 for evaluating the background intensity. However, these measurements are not intended to represent an accurate value for the ripple amplitude. The accurate experimental determination of the ripple amplitude is an unsolved problem.

5.3.2 Dependence of ripple wavelength on applied magnetic field

The theories of Rother and Hoffmann predict slightly different dependence of ripple structure on magnetic field. It is important to study the field dependence of ripple if one wishes to establish the validity of one of the theories. The present section is concerned with such a study using an 81% Ni-Fe alloy film with 420 Å thickness evaporated at room temperature. The specimen was placed in a sample chamber which replaced the intermediate lens of the microscope. A uniform field was applied by a small Helmholtz coil with a compensation coil to minimize the net deflection of the electron beam. The microscope was

overfocused about 3.0 cm.

(1) The magnetic field along the easy axis:

In order to align the easy axis of the sample with the external magnetic field direction, the following procedure was used: (1) First the sample was placed so that its easy axis was roughly along the magnetic field. (2) If the axis was not accurately aligned, application of a magnetic field caused slight rotation of ripple lines. (3) The sample position was adjusted until the ripple lines did not change their direction. In this way the sample could be aligned with an accuracy of about two or three degrees.

After aligning the sample, a magnetic field of about 30 oe. was applied to saturate the magnetization along the easy axis. Lorentz micrographs were taken as the field was decreased to zero and increased in the opposite direction.

(2) The magnetic field along the hard axis:

In order to align the hard axis with the applied field, the following procedure was used: (1) The sample was placed so that the hard axis was roughly along the field direction. (2) A field was applied whose magnitude was large enough to saturate the film. (3) Then the field was decreased to zero, and the resulting domain splitting was observed. The sample was rotated until the splitting produced equal area of domains oppositely magnetized. The unequal splitting which results when a film is not in correct alignment is shown in Fig. 5-7. These figures are most easily interpreted if it is remembered that the mean magnetization is always perpendicular to the ripple lines. After aligning the film as accurately as possible, a hard axis field of about

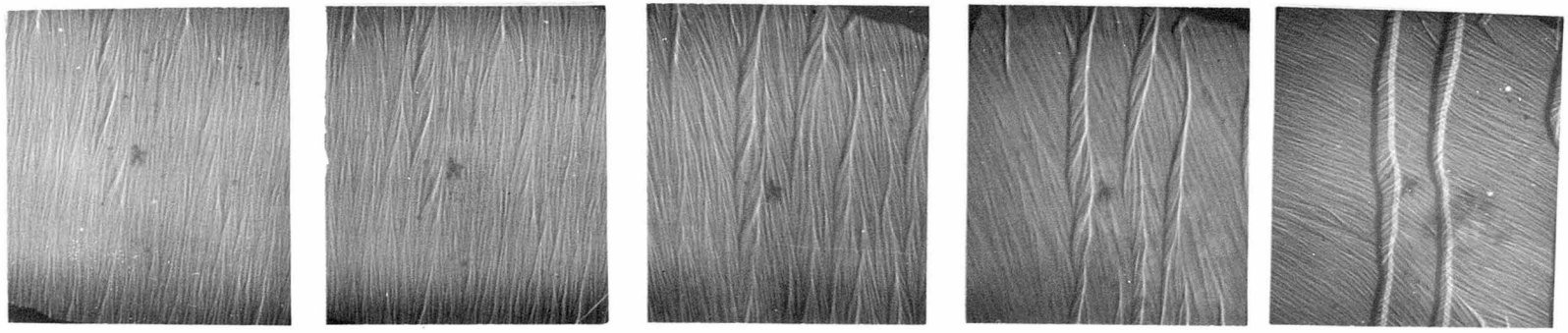

10.5 oe. 9.0 oe. 6.0 oe. 4.2 oe. 0

Fig. 5-7 Lorentz microphotographs showing the domain splitting for an 81%Ni-Fe with 420 Å thickness evaporated at room temperature. The field was decreased from 10.5 oe. to zero.

30 oe. was applied to saturate the film. As the field was lowered to the point where domain splitting took place, Lorentz photographs were taken.

(3) Results and discussion:

An example of ripple photographs as a function of applied field for the easy axis and hard axis directions is given in Fig. 5-8. In comparing these photographs it will be noted that the ripple lines are at right angles to each other in the two sets, and yet the ripple structure is remarkably similar in the two sets if the applied field in the easy direction is 18 oe. less than the corresponding value in the hard direction. The mean wavelength as a function of applied field was measured by visually counting the well defined periodicity of ripple rather than using a photo densitometer trace. As discussed in the previous section, the ripple wavelength was determined using the periodicity with high contrast. The data are plotted as a function of applied field in Fig. 5-9(a). In Hoffmann's theory, Eq. (5.9) shows that the ripple wavelength should vary inversely with $(H_a \pm H_k)^{1/2}$ where H_a is the applied field and H_k is the uniaxial anisotropy field. The plus and minus signs apply to the easy and hard axis cases respectively. Therefore, the two sets of experimental data should be separated horizontally by the amount $2H_k$ in Fig. 5-9(a). On the basis of this prediction, the anisotropy field H_k should be about 9 oe., which is in satisfactory agreement with the value $H_k = 8$ oe. measured by other methods for a film simultaneously evaporated onto a glass substrate.

The data have been normalized to the value $H_k = 9$ oe. and replotted in Fig. 5-9(b). The solid lines show the variation predicted by

Hard axis field

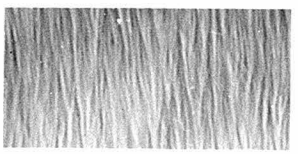

25.2 oe.

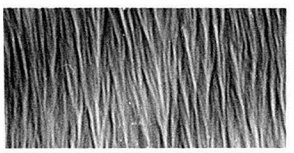

18.0 oe.

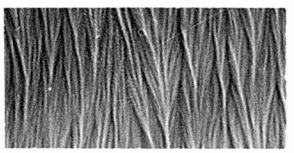

15.3 oe.

12.6 oe.

Easy axis field

7.2 oe.

0

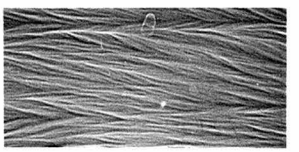

-2.7 oe.

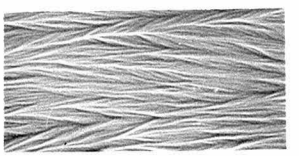

-5.4 oe.

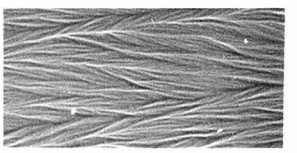

-7.6 oe.

Fig.5-8. Ripple photographs as a function of applied field for the easy and hard axis fields for an 81%Ni-Fe alloy film.

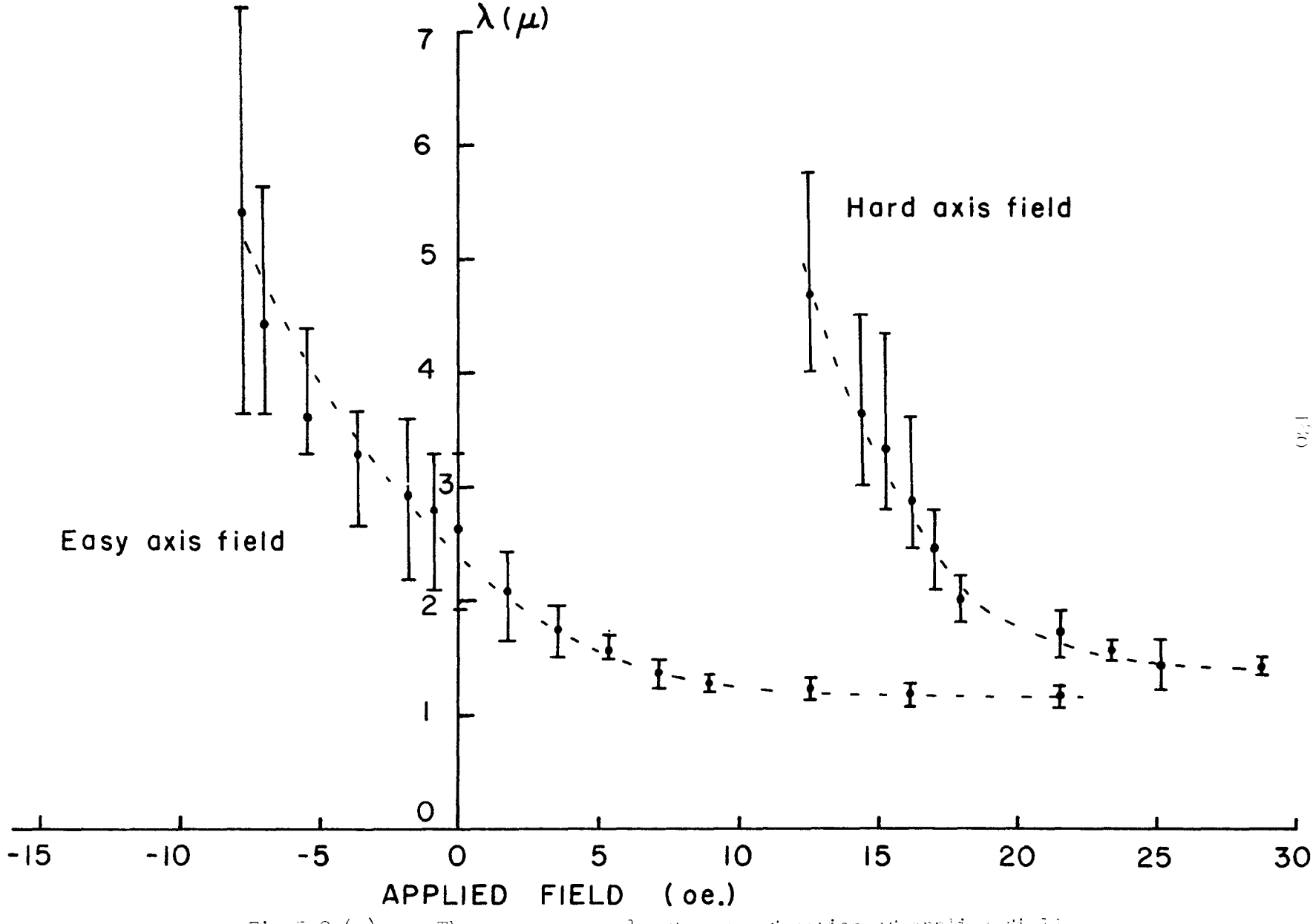

Fig.5-9 (a) The average wavelength as a function of applied field.

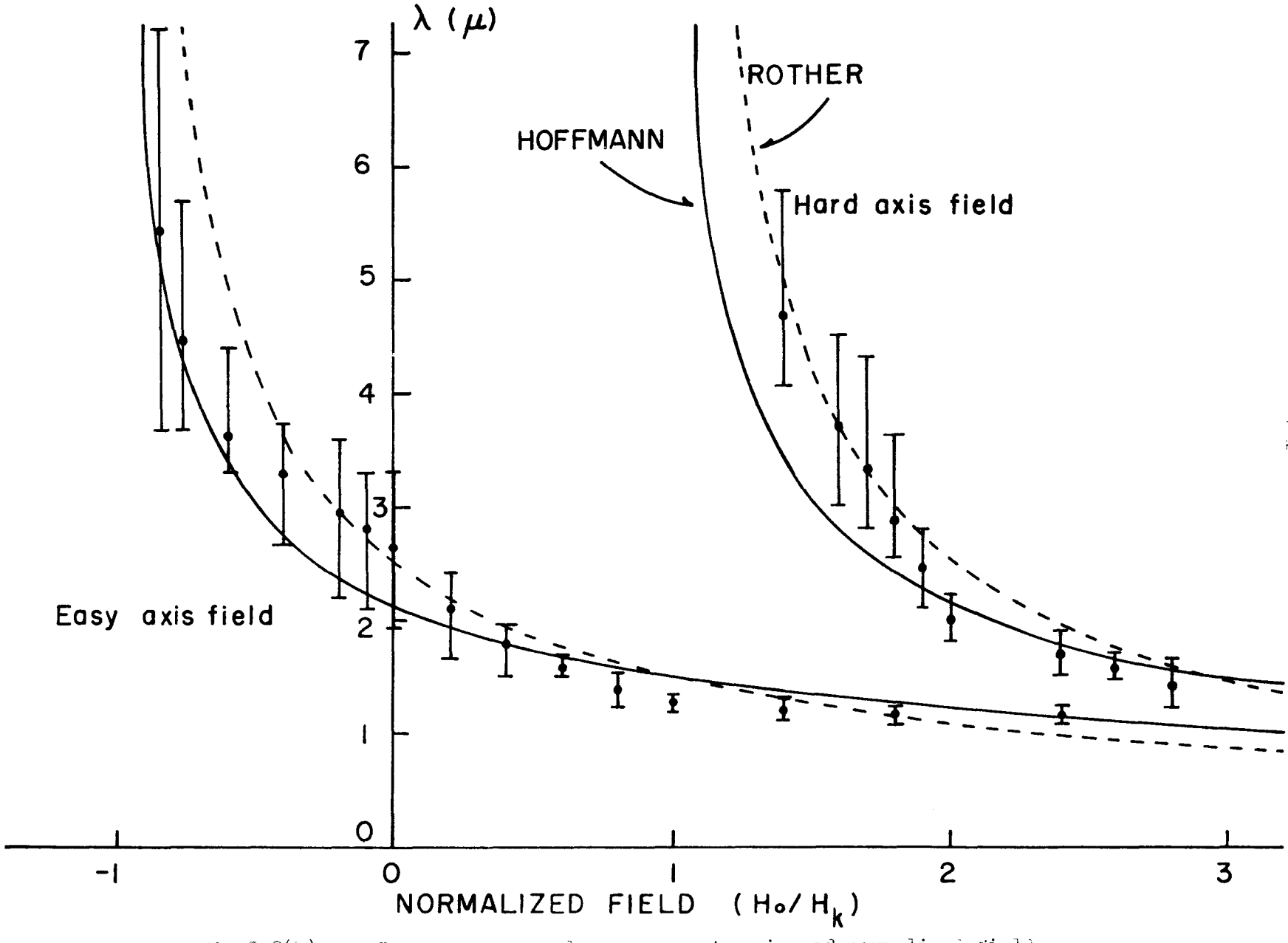

Fig.5-9(b) The average wavelength as a function of normalized field.

Hoffmann's theory if the value of λ is taken to be 1.5μ at an effective field of H/H_k=2.0. Also shown by dotted lines are the theoretical predictions of Eq. (5.7) for the long wavelength ripple component of Rother, $(H_a \pm H_k)^{-3/4}$. As can be seen, the agreement between both theoretical predictions, and the present data is reasonable. If these results are used with Rother's and Hoffmann's equations for the wavelength, one can estimate the value of the exchange constant A. Using the value M_s = 800 oe., such calculations give A = $0.7 \cdot 10^{-6}$ erg/cm for Rother, and A = $4 \cdot 10^{-6}$ erg/cm for Hoffmann. In view of the many approximations used in these theories, this is in reasonable agreement with the value A = 1.0 x 10^{-6} erg/cm obtained from ferromagnetic resonance experiments. In any case, the dependence of wavelength on field gives strong evidence supporting the basic hypotheses of the two theories. However the difference in dependence between the two theories is not great enough to give a clear choice of which gives better fit to the experimental data.

5.3.3 Dependence of the ripple structure on substrate deposition temperature

As the ripple structure is predicted by theories to depend on film parameters such as local anisotropy constant K, crystallite size D, exchange constant A, saturation magnetization M_s and induced uniaxial anisotropy K_u, one of the means of testing the validity of the theories is to vary these film parameters in order to see how the ripple is changed. The present section is concerned with the study of the ripple dependence on substrate deposition temperature for 76% Ni-Fe alloy films. Films about 300 Å thick were deposited in the temperature range -150 to

400°C onto freshly cleaved NaCl substrates. The method of measuring the average wavelength and ripple angle was described in the previous section. The samples were placed in the normal sample chamber in the microscope. The microscope was underfocused about 3 cm by decreasing the objective lens current the appropriate amount. Measurements were made at room temperature.

Epitaxy: A sequence of ripple photograph as a function of substrate deposition temperature is shown in Fig. 5-10. Also shown are the electron diffraction photographs as a function of substrate deposition temperature for each film. The ripple structure could be seen for films deposited at temperatures up to 350°C in which partial epitaxy is present. For the films deposited at 400°C, however, the ripple could not be observed. In this case, the films were found to be completely epitaxial. This finding is quite important. As discussed previously f_1 is zero over the entire film for the case of complete epitaxy, and therefore σ_1 becomes zero. Thus the present experimental evidence gives confirmation to the hypothesis that ripple is dependent on the random orientation of crystallites.

On the other hand, Tsukahara and coworkers reported that ripple was observed in a polished single crystal and concluded that the ripple resulted from local stresses rather than from random orientation of crystallites. No information regarding the sample preparation and measurement technique was published, and attempts to communicate with this laboratory by mail were unsuccessful. No other reports have been found in the literature in which ripple was observed in epitaxial films or single crystals. In any event, the present data are at variance with

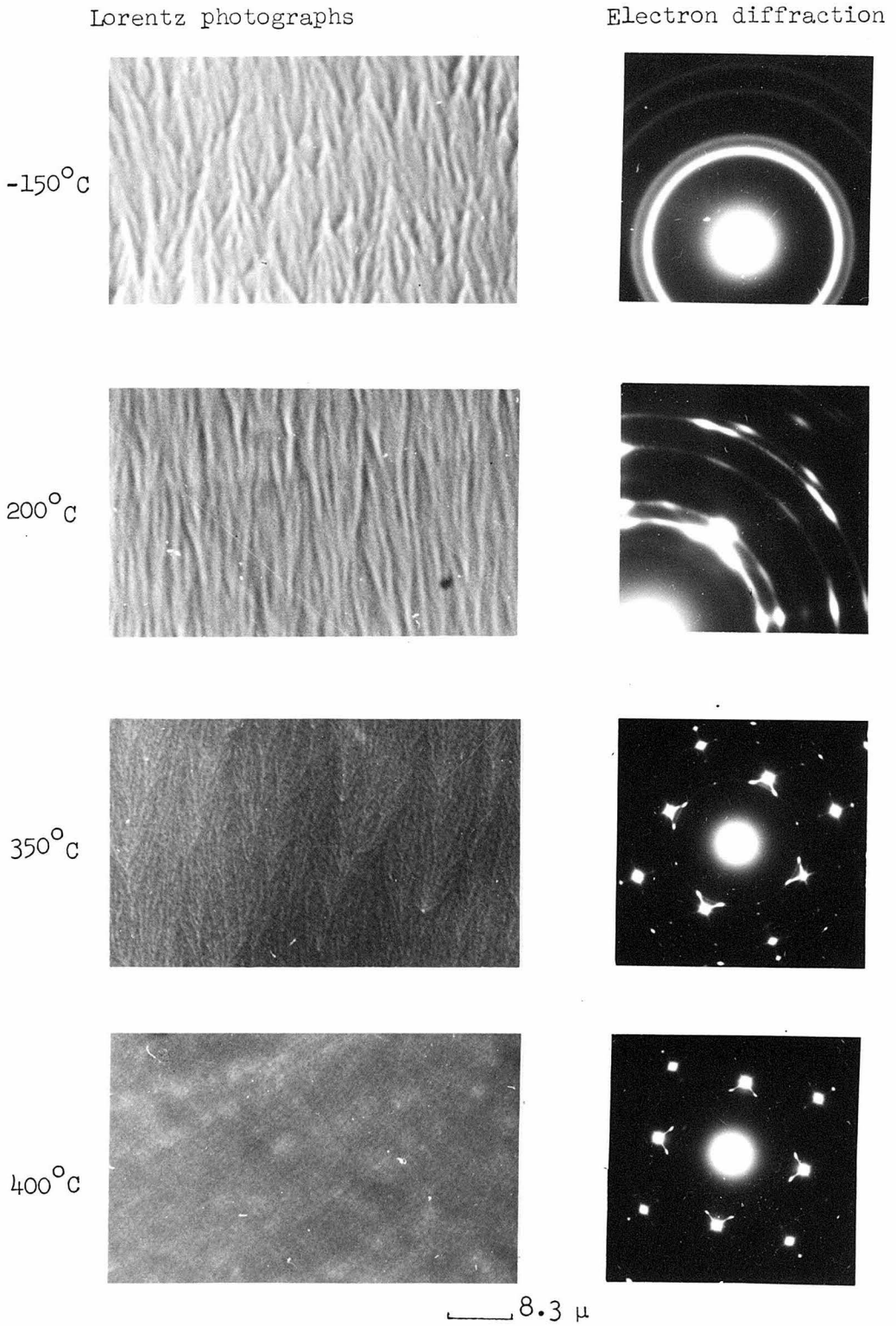

Fig.5-10. A sequence of ripple photographs for 76%Ni-Fe alloy films evaporated at -150°, 200°, 350° and 400° C. Also shown are the electron diffraction photographs for each film, taken at 100 kV.

their result.

Wavelength: The well defined ripple periodicity for films deposited in the temperature range -180°C to 200°C is given in Fig. 5-11. For the films deposited at 350°C, it is found that the ripple structure is not well defined and thus no meaningful measurement was possible. The figure also shows the theoretical predictions of Hoffmann and Rother (long wavelength ripple component) using $A = 1 \cdot 10^{-6}$ erg/cm, $M_s = 800$ oe. $d = 200$ Å and the values of K_u for each substrate deposition temperature as reported by Wilts (1966).* As can be seen the experimental mean wavelengths are larger by a factor of about 1.5 than those predicted by Hoffmann, and are in better agreement with those for the longwavelength component of Rother. However, in view of the approximate nature of the theories, it is not believed that these differences are significant. On the other hand, the slight dependence of the theoretical wavelength on substrate deposition temperature was not observed.

5.3.4 Ripple dependence on composition in Ni-Fe alloy films

In the previous section, we discussed the dependence of the ripple on substrate deposition temperature. Variation of temperature primarily affected crystallite size and the degree of epitaxy, both of which are important parameters in the structure factor S, and accordingly the ripple structure. Another parameter which enters into the structure factor S is the local anisotropy constant K. Since the local anisotropy constant is expected to depend strongly on alloy

---

*Note: For this film composition, the uniaxial anisotropy constant K_u for films removed from substrate is reported to be nearly same as that for films on glass, as mentioned in Chapter 2. (Krukover (1967)).

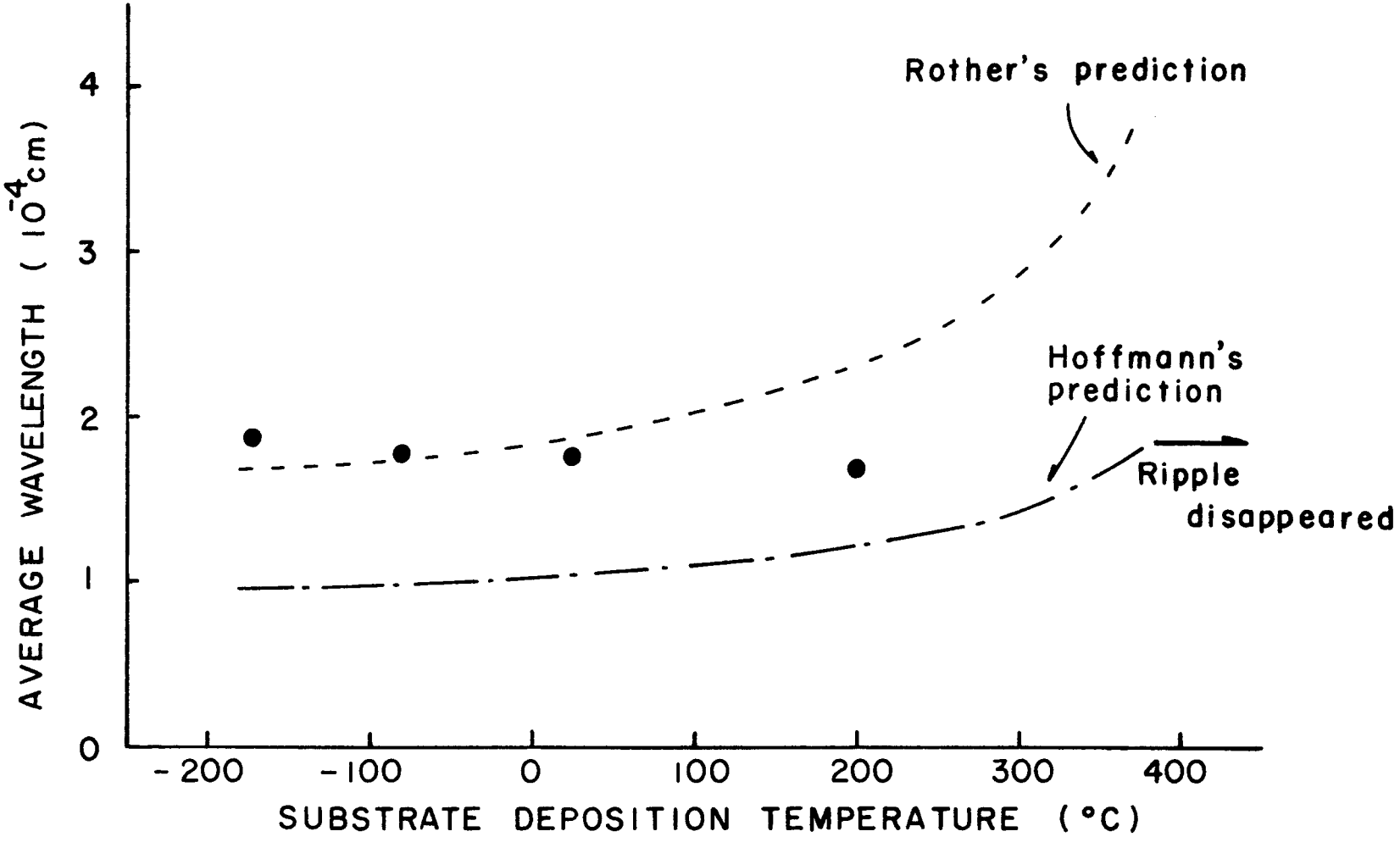

Fig.5-11 The average wavelength for 76%Ni-Fe alloy films as a function of substrate deposition temperature. Also shown are the theoretical predictions of Hoffmann and Rother (long wavelength ripple component).

composition, it was felt that varying the alloy composition would give additional information concerning the origin of ripple. In view of this, the study of the ripple dependence on alloy composition was carried out for Ni-Fe alloy films with composition varying between 50% and 90% Ni. All the films were deposited at room temperature and measurements were also made at room temperature. The electron microscope condition was the same as that described before.

Wavelength: It should be first noted and remembered as one of the important results in this study that in the range 71% to 75% Ni, no ripple structure could be seen except near the free edges where weak ripple was observed. A sequence of ripple structure photographs for 56%, 71.5% and 85% Ni is given in Fig. 5-12.

The average wavelength as a function of alloy composition is given in Fig. 5-13. Also shown are the theoretical prediction of Hoffmann and the long wavelength ripple component of Rother using the values of K_u reported by Wilts (1966). Furthermore, the values of K_u for films removed from the substrate have been reported to be different than for films on glass by an amount depending on composition. Therefore, the theoretical predictions using the changes of K_u reported by Krukover (1967) are also shown in the same figure. The measured wavelength remains essentially constant over the entire composition range (about 1.8μ), whereas the theoretical predictions show an increase with Ni composition. Even though the agreement between the data and the theoretical predictions is not unreasonable for the composition up to about 76% Ni, the discrepancy between the trends is obvious beyond this composition.

56%Ni

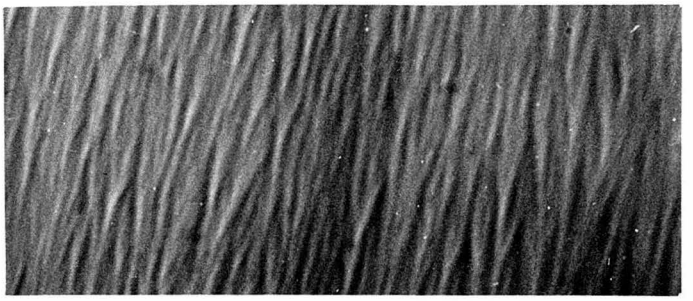

72%Ni

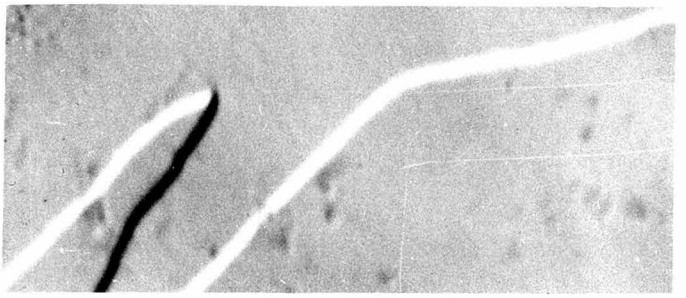

85%Ni

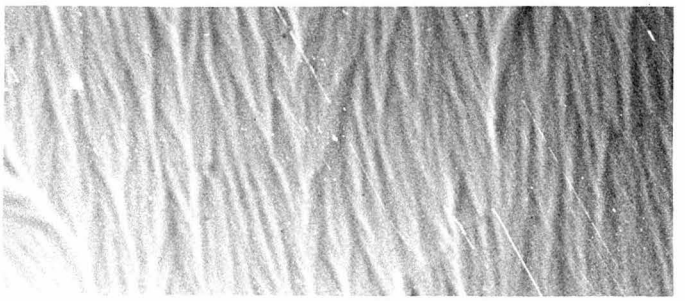

Fig. 5-12. Lorentz micrographs showing the presence and absence of ripple for films evaporated at room temperature. The photographs were taken at 100 kV.

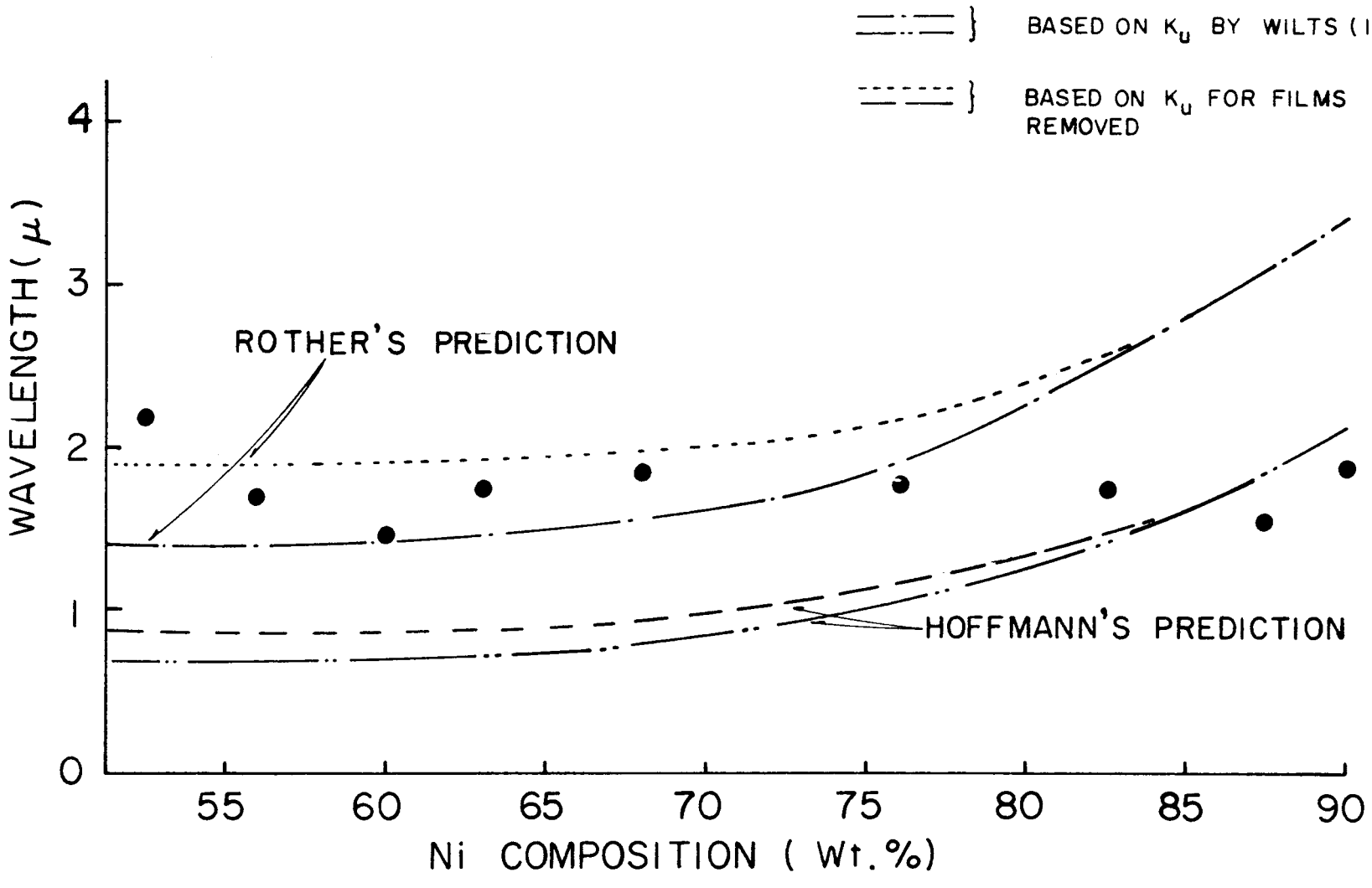

Fig.5-13 The average wavelength as a function of alloy composition for films evaporated at room temperature. The theoretical predictions of Hoffmann and Rother are also shown for the values of K_u by Wilts (1966) and using the changes of K_u reported by Krukover (1967).

It should be added that a recent unpublished report (Suhanova (1968)) indicates a definite direct correlation between the change in measured wavelength and the variation in longitudinal saturation magnetostriction constant λ_s as the composition is varied from 50% to 100% Ni. At the present time, no detailed information is available about the experimental technique or conditions, but in any event, the present data are in clear disagreement with this report.

5.3.5 Measurement of ripple angle

There is no generally accepted method of measuring the ripple angle. As pointed out in Sect. 5.3.1 the amplitude of a purely sinusoidal ripple can be obtained using Eq. 5.19, with a correction necessary for quantum mechanical reasons if the microscope parameters are not carefully chosen. However use of this equation cannot be justified theoretically when a wide spectrum of wavelengths is present. Nevertheless, it might be supposed that even in such a situation, Eq. 5.19 would at least give an order of magnitude measure of the ripple amplitude. Since the ripple angle is predicted to depend strongly on material composition and substrate temperature, this provides an experimental method for simultaneously testing the ripple theories and testing this method of measurement. Experimentally, the average intensity peak ratio was obtained from a photodensitometer trace. Measurements were made for both the variation of substrate deposition temperature and variation of composition discussed earlier in connection with wavelength measurements. Results are shown in Figs. 5-14 and 5-15. In most cases about 10 separate measurements were made for each sample. The points in the figures are the average value, with

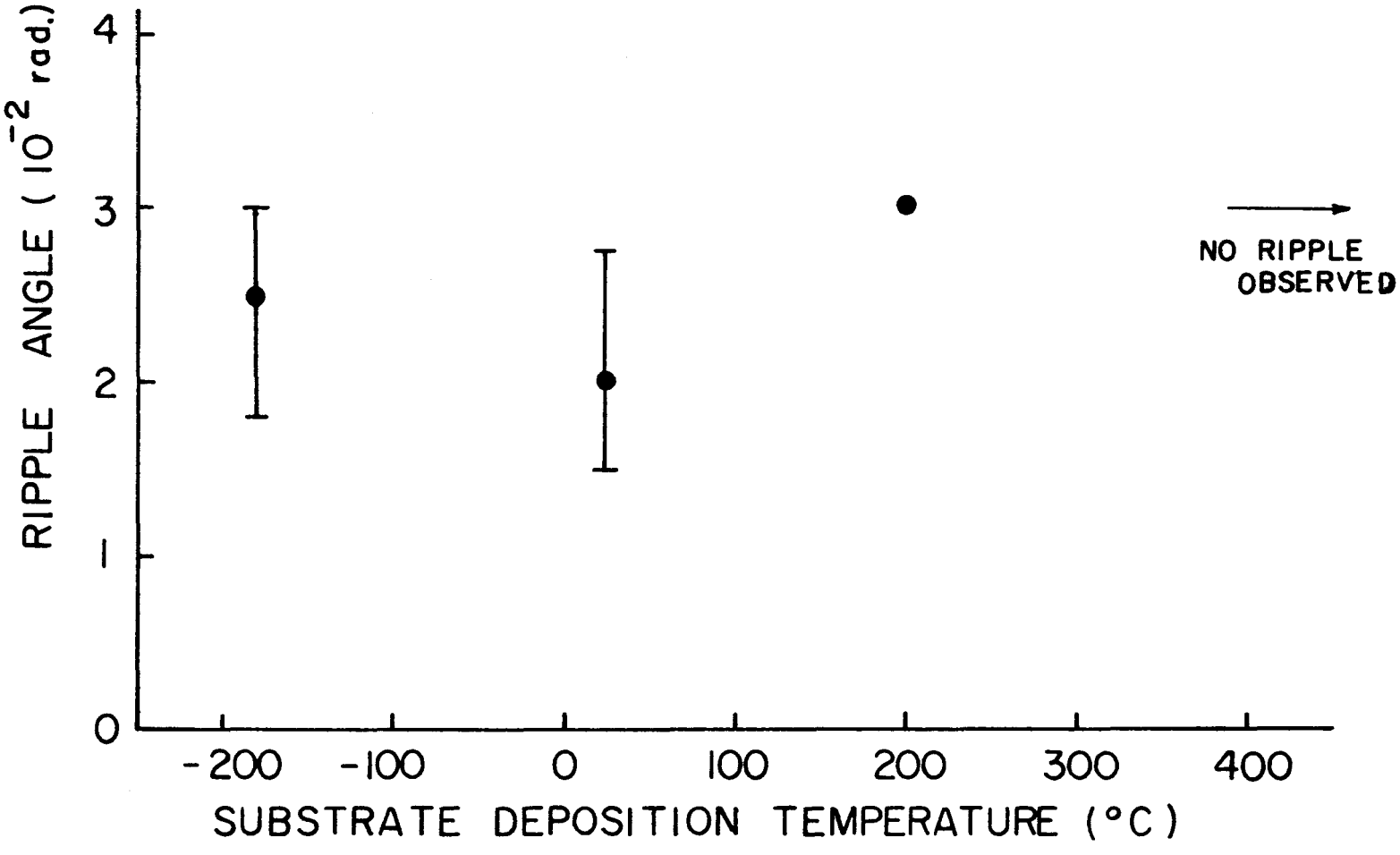

Fig. 5-14 Measured average ripple angle as a function of substrate deposition temperature for 76%Ni-Fe alloy films. The figure should be compared to Fig.5-10.

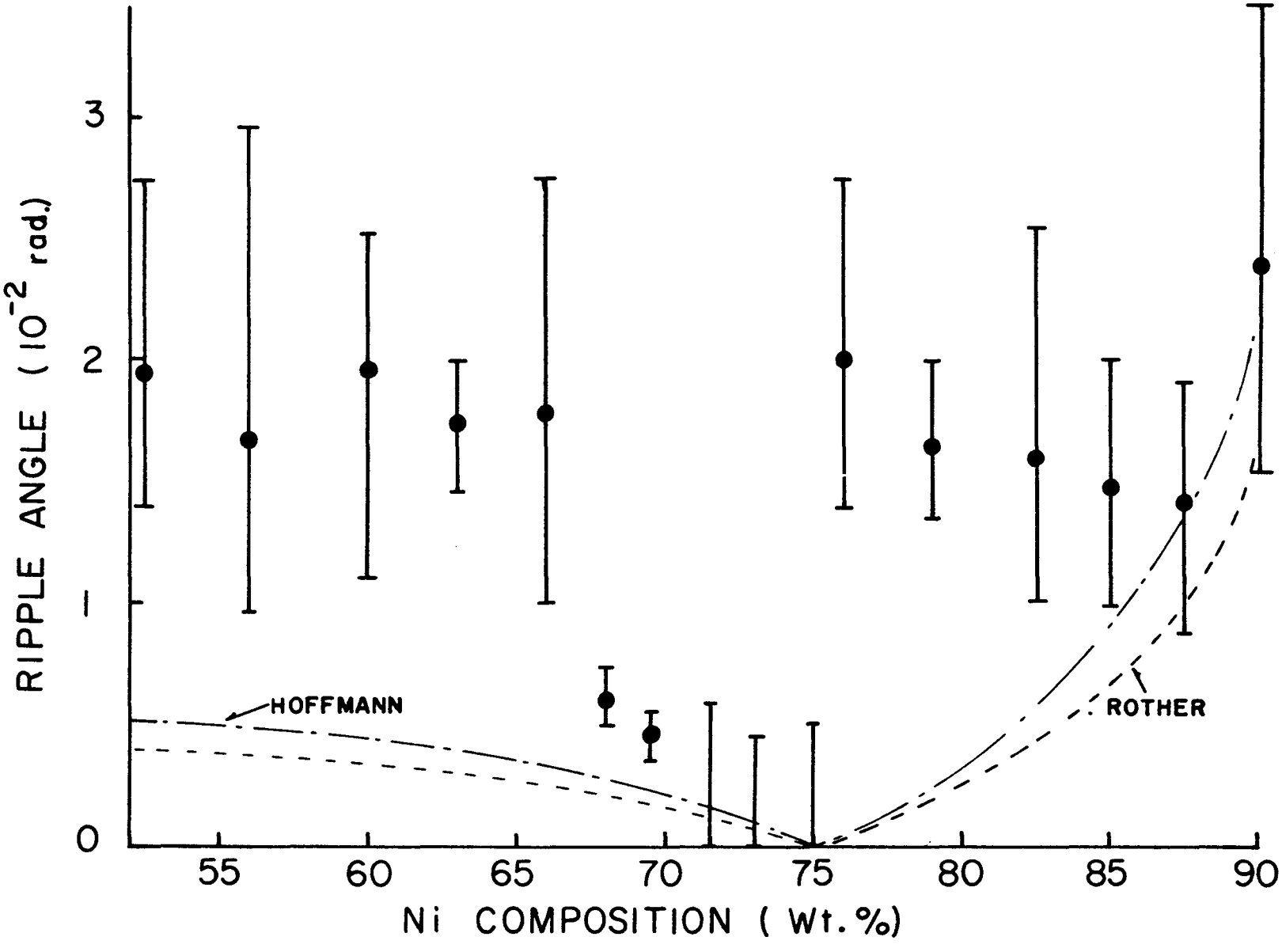

Fig.5-15 Ripple angle as a function of alloy composition for films deposited at room temperature. Also shown are the theoretical predictions of Hoffmann and Rother.

bars to indicate the range of the individual measurements.

Substrate temperature variation:

Although the point for 200°C indicates an increase in ripple angle, this represents a single measurement on a very poor photograph. If this point is discounted, the ripple angle shows little variation with temperature. In order to compare the present results with the theoretical predictions (section (5.2.1)), it should be recalled that the r.m.s. ripple angle is proportional to $KD\ d^{-1/4} M_s^{-1/2} A^{-3/8} K_u^{-3/8}$ in the theories of Hoffmann and Harte, and also the long wavelength ripple components of Rother's theory. In Hoffmann's theory, the additional term $\sigma_1 n^{-1/2}$ appears. In the present study, the composition is fixed. The film thickness for most of the films is about 300 Å to 500 Å and thus it may be considered to be constant in the theoretical predictions because of the 1/4th power variation. By changing substrate deposition temperature, one expects a change in the average crystallite size D, induced uniaxial anisotropy constant K_u, the standard deviation σ_1 and n, the number of crystallite through the film thickness. One would expect no change in the saturation magnetization M_s, exchange constant A and probably no change in local anisotropy constant K unless local anisotropic stresses are influenced by the deposition temperature.

Let us consider the parameters in more detail which depend on substrate deposition temperature. First of all, as discussed in Chapter 3, the average crystallite size D increases with substrate deposition temperature. The average crystallite size for the films deposited at -180°C was roughly estimated to be 50 Å. Since this value is close to the resolution limit of the present microscope (about 30 to

50 Å), an accurate measurement was not possible. However, the sharpness of the diffraction lines clearly requires the average crystallite size to be larger than 20 Å, (see Fig. 5-10), and direct observation in the microscope shows that they cannot be significantly larger than 50 Å. For higher temperatures, the crystallite size can be observed directly. The average size increases from 100 Å at 25°C to about 200 Å at 200°C (refer to Fig. 3-10). In summary, the average crystallite size D increases by a factor of about 4 from -180°C to 200°C.

Second, according to the work by Wilts (1966), the induced uniaxial anisotropy constant K_u for this alloy composition decreases by a factor of about 1.3 in this temperature range. Third, the films deposited at 400°C are completely epitaxial. Films evaporated at 350° and 200°C substrate deposition temperature are found to be partly epitaxial, possibly about 85% and 30% respectively. On the other hand, the films deposited between -180°C and 100°C show no significant epitaxy. Although the evaluation of σ_1 is difficult for the case of partial epitaxy, it was pointed out in section (5.2.1) that the value of σ_1 decreases approximately by that fraction of the film which is epitaxial. And finally, n , the number of crystallites through the film thickness, is a function of the average crystallite size and the shape of crystallite. Although there is no information available on the crystallite shape, one simple assumption is roughly spherical, in which case the value of n would be d/D. For this case, the value of n decreases by a factor of 4 from -180°C to 200°C. On the other hand, if the crystallite has the shape of a column, then the value of n is independent of the crystallite size. Therefore, the value of n changes

with temperature by a factor lying between 1 and 4, depending on the shape of crystallite.

With this background, one would expect the average ripple angle to increase with temperature by a factor of about 4.5 for Rother's and Harte's theories. It is difficult to estimate the expected change in Hoffmann's theory because of the uncertainty in the variation of σ_1 and n. The increase in the average ripple angle between -180° and 200°C could be as large as 10 and as small as 3. The roughly constant value of the experimental measurement appears to be in disagreement with both theories.

Composition variation: The measured average ripple angle as a function of Ni composition was presented in Fig. 5-15. As shown in this figure, the average ripple angle is about $2 \cdot 10^{-2}$ rad. except in the range 68 to 75% Ni and remains roughly constant within the scatter of the data. In the range 71% to 75% Ni, no ripple could be observed far from the free edges as mentioned before.

Let us consider in detail the comparison between the present data and the theoretical predictions. The additional term $\sigma_1 n^{-1/2}$ which appears in Hoffmann's theory is not significant. Since all the films in the present study were deposited at room temperature, the average crystallite size and the randomness of orientation should be constant. Since the thickness was also held constant, the factor n and σ_1 should not vary with composition. The dependence of exchange constant A on Ni composition in this alloy range is not available. However, since measured values of A for pure Ni, Fe and Co as well as 81% Ni-Fe alloy are all nearly equal and since exchange enters into the equation for

ripple angle as the 3/8 power, it is doubtful that variation in A is responsible for any variation in ripple angle.

The local anisotropy constant K, saturation magnetization M_s and induced uniaxial anisotropy constant K_u all change with composition: (1) The local anisotropy constant K may be one of the crystalline anisotropy constants, or may be a constant associated with magnetostriction, or a combination of these constants, depending on their relative size.

(a) It should be recalled that the crystalline anisotropy constants K_1 and K_2 appears in the energy expression for cubic symmetry, ie.,

$$E_{\text{cryst. aniso.}} = K_1 \left(\sum_{i>j}^{3} \alpha_i^2 \alpha_j^2\right) + K_2 \alpha_1^2 \alpha_2^2 \alpha_3^2$$

in which α_1, α_2, and α_3 are the directional cosines of $\vec{M}$ with respect to crystallographical axes. To discuss which term is most significant in the case of polycrystalline films, we will consider the average values of $\langle \Sigma \alpha_i \alpha_j \rangle$ and $\langle \alpha_1^2 \alpha_2^2 \alpha_3^2 \rangle$ over the all orientations of crystallites. It can be shown that

$$\langle \Sigma \alpha_i^2 \alpha_j^2 \rangle = 1/5$$

$$\langle \alpha_1^2 \alpha_2^2 \alpha_3^2 \rangle = 1/105$$

Therefore, the crystalline anisotropy constant K_1 can be considered as the major contribution to the crystalline anisotropy unless K_2 is greater than K_1 by a factor of more than 20. Now we consider the variation of K_1 and K_2 with composition in the range 50% Ni to 90% Ni. Data for bulk material taken from Bozorth and Walker (1953) and Bozorth (1951) are shown in Fig. 5-16(a), (b), and (c). As shown in Fig. 5-16

(a), the composition at which the anisotropy constant K_1 becomes zero depends on cooling rate and varies from 75% (quenched, cooling rate, 10^5 °C/hr) to 63% Ni (slow cooling, 2°C/hr). Bozorth and Walker stated further that alloys cooled at the intermediate rate of 50°C/hr have intermediate values of K_1 as shown by the broken line in Fig. 5-16(a). The alloy with 74% Ni was cooled at various rates, and the resultant anisotropy constants are shown in Fig. 5-16(b). In any event the composition where K_1 is zero is somewhat ambiguous unless the cooling rate is known. In the present case of thin films, the cooling rate is very high and therefore the data for rapid quenching in bulk material are probably representative for this case. It should be also noted from comparison of K_1 and K_2 (Fig. 5-16(a) and (c)), that the contribution of K_2 to the total crystalline anisotropy may be neglected in the entire range except within 1/2% of the zero crossing.

(b) Another possible factor is the magnetostriction. Even though it is very difficult to treat this problem in a quantitative way, the effect should depend on the longitudinal saturation magnetostriction constants. In this composition range, λ_{100}, λ_{111} and the polycrystalline λ_s all vary in approximately the same way. Data for λ_s are shown in Fig. 5-16(d) (Chikazumi, (1964)). As can be seen, the value of λ_s decreases with Ni content and passes through zero at about 83% Ni.

(2) The saturation magnetization M_s decreases almost linearly by a factor of about 2 from 50% to 90% Ni. (Bozorth (1951)).

(3) The induced uniaxial anisotropy constant K_u for films deposited onto glass at room temperature decreases uniformly by a factor of about 7 from 50% to 90% Ni (Wilts (1966)) (refer to Fig. 2-7).

Using the above data, one can now compare the measured data with the theoretical predictions. For simplicity, λ_s will be neglected initially so that we only consider the variation of K_1 (using the data for quenching), M_s and K_u. For this case, one can calculate the ripple dependence on composition from Eqs. (5.8) and (5.12) for Rother's and Hoffmann's theories respectively. The predicted r.m.s. ripple angles of Hoffmann and the longer wavelength components of Rother are plotted in Fig. 5-15. It can be seen that the present data agree with the theoretical prediction only in the existence of a minimum near 75% Ni. They are in disagreement with each other in the following points. (1) The minimum of the measured ripple angle is not as sharp as the theory predicts and is shifted about 2% to the lower Ni side. (2) The measured values of ripple angle are much larger than those predicted by theories. And (3) the experimental data appear to reach a saturation value within a few percent of the minimum, and remain constant outside this region. Concerning these discrepancies, it should be noted that the film composition was determined by x-ray fluorescence, and the accuracy of the film composition is believed to be better than 0.5%. Therefore, the shift of the minimum is not caused by error in film composition. It should be emphasized, however, that since the composition at which K_1 becomes zero depends on cooling rate, and since the accurate value of cooling rate is not known in the present case, the discrepancy stated in (1) may be due to this uncertainty. Furthermore, in the light of the recent work by Aubert (1968), earlier data of crystalline anisotropy constants are all suspect, and should be rechecked. Finally the crystalline anisotropy constant for

Fig.5-16(a)

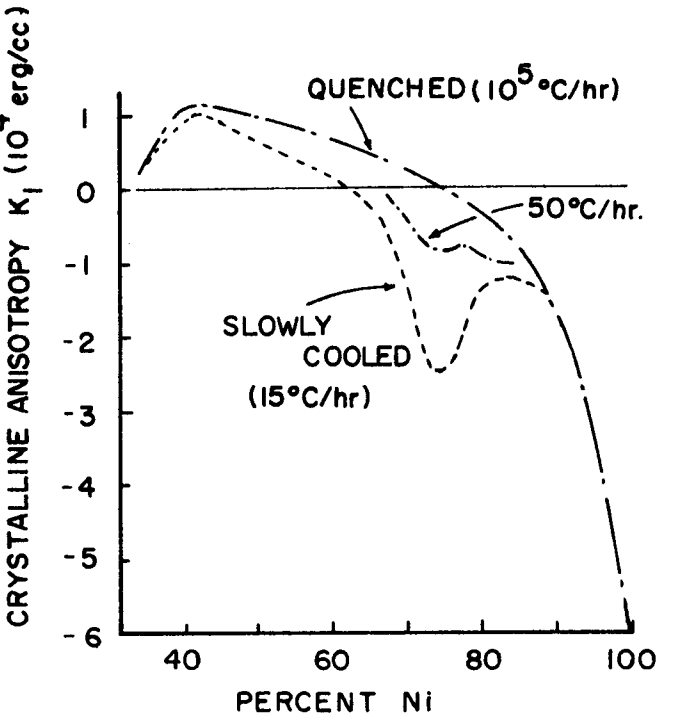

Fig.5-16(b)

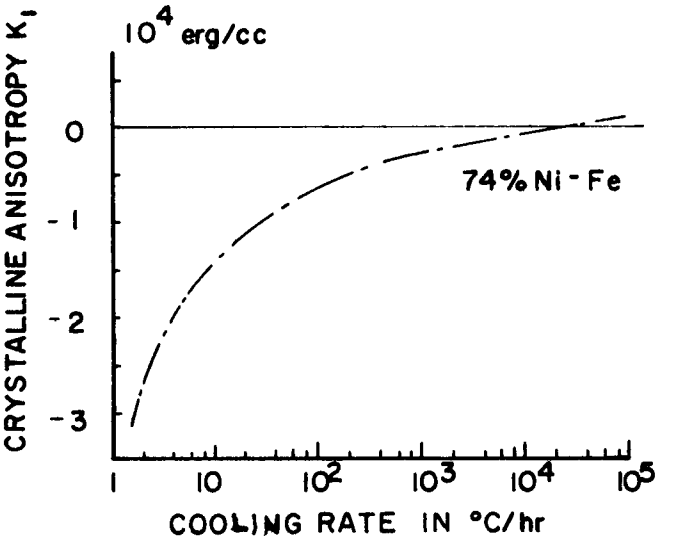

Fig.5-16 (a) Crystalline anisotropy constant K_1 as a function of alloy composition, after Bozorth (1951).
(b) Crystalline anisotropy constant K_1 of a 74%Ni-Fe alloy as a function of cooling rate, after Bozorth and Walker(1953).

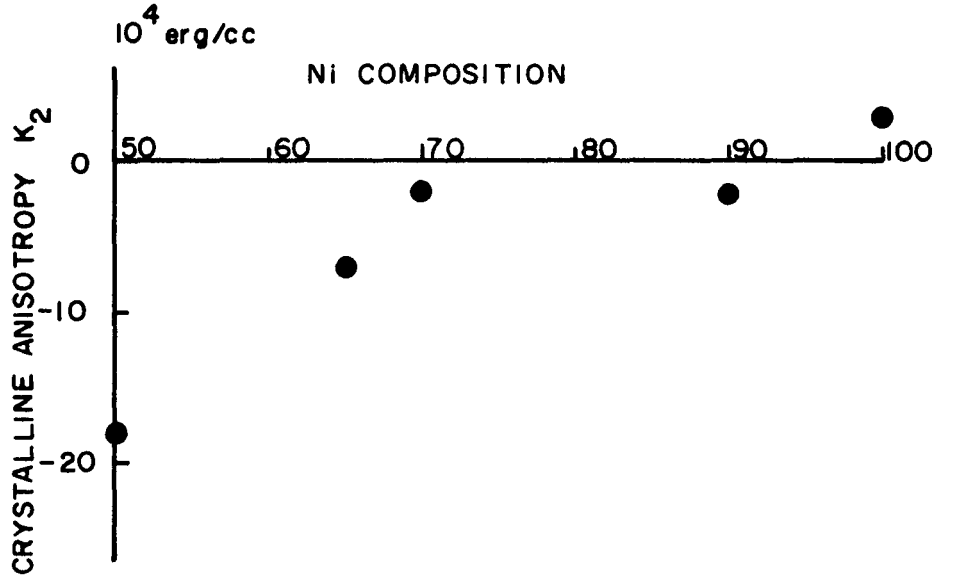

Fig.5-16(c) Crystalline anisotropy constant K_2 as a function of alloy composition, after Bozorth(1951).

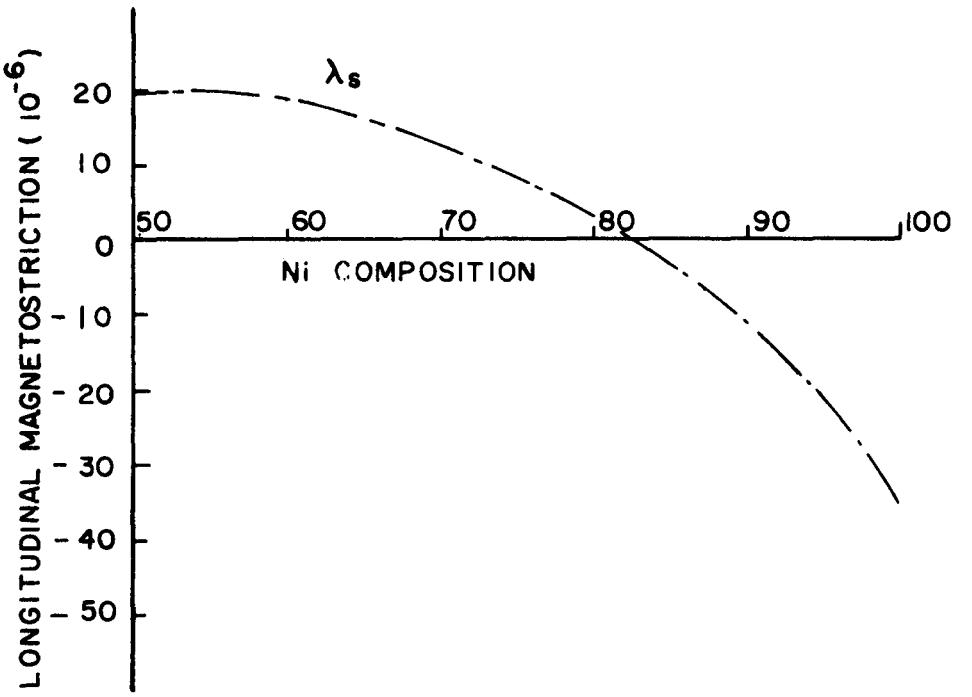

Fig.5-16(d) Longitudinal saturation magnetization as a function of alloy composition, after Chikazumi(1959).

a thin film may be significantly different than bulk material.

In the discussion given above, we only considered the crystalline anisotropy K_1. If the magnetostriction is the major part of K, then one would expect the ripple angle to have a minimum at around 83% Ni where the magnetostrictive constants becomes small (Fig. 5-16 (d)). As shown in Fig. 5-15 clearly this is not the case. Therefore, one can conclude from the absence of a minimum at 83% and from the observed minimum at about 75% Ni that the magnetostriction is not the major factor which is responsible for the origin of ripple, and that the experimental data support the hypothesis that the crystalline anisotropy is in large measure responsible for ripple. On the other hand, except for the range where the ripple vanished, all measured ripple angles in both Figs. 5-14 and 5-15 are nearly equal, with average value about 0.02 radius. In view of this and the great discrepancies with theory, it is difficult to argue that the experimental data are related in any significant way to the actual ripple angle in the magnetic film.

5.4 Summary

The experimental study of ripple by Lorentz microscopy in Ni-Fe alloy films was carried out, in order to test the validity of the theories developed by others. The following should be noted: (1) the only possible way to determine experimentally a meaningful wavelength is to find a well-defined ripple periodicity on a photomicrograph. (2) The average wavelength determined in this way is of the order of 1μ. This value is in reasonable agreement with the main wavelength predicted by the theories developed by others. However, the slight dependence of this observed wavelength on substrate deposition temperature and alloy composition were not observed. On the other hand, the strong dependence of the measured wavelength on the external magnetic field is in good agreement with that predicted theoretically. (3) The experimental fact that the ripple structure could not be observed in completely epitaxial films gives confirmation that the ripple results from the randomness of crystallite orientation. Furthermore, the experimental observation that the ripple disappeared in the range 71 and 75% Ni composition supports the possible correlation of the ripple origin with the crystalline anisotropy. Finally (4) the experimental problems of measuring the actual ripple angle were pointed out. An attempt to experimentally determine the order of magnitude of angle was carried out, using the average maximum and minimum intensities. The ripple angle was determined using the intensity formula based on the single frequency of a sinusoidal ripple component and based on classical optics. The ripple angles measured in this way are nearly equal (about 0.02 rad.) where the ripple was observed. The discrepancy

between the experimental data and the theoretical prediction is serious. The accurate experimental determination of the ripple angle is an unsolved problem.

Appendix 1 Film Preparation

All the samples used in the present study were fabricated by the vacuum-deposition method, first described by Blois in 1955. Nickel, iron and/or cobalt in the correct proportion were placed in a high purity alundum crucible (Van Waters and Rogers, Inc.), and melted by rf induction heating in vacuum of about 10^{-6} Torr. The total weighing of the melt was about 20 gr. Purity of the metals used was as follows: Ni - 99.98%, Fe - 99.99%, Co - 98%. The substrates were glass and NaCl single crystal. Glass plates were of 0.472" x 0.472" with 0.024" thickness (Corning #0211 microsheet). The glass substrates were cleaned carefully in benzine, acetone, chromic acid cleaner, methylalcohol and finally in distilled water, all with ultrasonic agitation for about 3 minutes in each cleaner. The NaCl single crystal substrates were prepared by cleaving a lump (Harshaw Chemical Company). The size and thickness were 1 cm x 1 cm, and about 0.7 mm, respectively. The substrates were baked in vacuum (10^{-6} Torr.) at about 350°C for 1 hour before bringing to deposition temperature. The substrates were located about 20 cm above the crucible, and the incident evaporation beam was normal to the substrate surface.

Substrates were mounted in a copper block and covered by two shutters, one of which was made of thick copper sheet fitting tightly against the holder. This in effect put the substrates in a "black body cavity," insuring an equilibrium substrate temperature equal to that of the block. Ordinary wire thermocouples attached to both

substrate holder and shutter were used to confirm that the shutter made good thermal contact and formed a real black body cavity. Usually, the temperature difference between these two varied from a few degrees to about 20°C, depending on the temperature of the body.

The deposition system is of conventional design using a liquid nitrogen filled Meissner trap in the vacuum deposition chamber in addition to the use of a liquid nitrogen trap above the oil diffusion pump. The vacuum was usually better than 1×10^{-6} Torr. during evaporation, measured by an ion gauge attached to the side of deposition chamber. (Fig.A-1).

The melt in the crucible was heated by high frequency induction (Lepel High Frequency Labs.). During the evaporation a magnetic field of 30 oe. was applied in the film plane by the pair of large diameter coils (about 10 in. diameter) placed outside of the vacuum. A copper mask with circular holes produced films 1 cm in diameter. The evaporation speed was in general about 10 Å/sec. and the film thickness ranged from 100 Å to 2000 Å. After evaporation, the films were cooled as rapidly as possible without admitting gas into the vacuum system. This corresponds to a rate of about 50°C/min. During cooling, the external magnetic field was left on.

In the earlier stages of the present research, film thickness was monitored during evaporation by measuring the resistance of a test strip of film and comparing the value obtained with a previous film thickness calibration. During the last stages of the research, a quartz crystal thickness monitor (sloan) was used.

The film thickness after evaporation could be determined directly

by the Tolansky multiple beam interference technique (S. Tolansky, "Multiple Beam Interferometry of Surface Films" (Oxford University Press (1948)), or indirectly from a flux measurement by the hysteresis loop tracer. Since the height of the hysteresis loop is proportional to the thickness of the film, the film thickness may be measured provided the instrument has been calibrated by comparison with the optical method. The hysteresis loop method permits the measurement of effective magnetic film thickness of as little as ten angstroms. In the present study, the film thickness was measured mainly by this hysteresis loop method.

For the purpose of examining the films in the electron microscope, it was necessary to remove the films from the substrates. In practice, it is very tedious to remove the films from glass substrates. Therefore, the films intended for electron microscope observation were evaporated onto NaCl single crystal substrates. Substrate surface was the (100) cleavage face of NaCl. The NaCl crystals were easily dissolved in water leaving the films on the surface. The films were placed on 3mm dia. microscope copper grids (150 mesh). The film thickness was considered to be the same as that for films deposited simultaneously onto glass. This is reasonable since experimentally there was little variation in thickness among the four films simultaneously deposited onto glass.

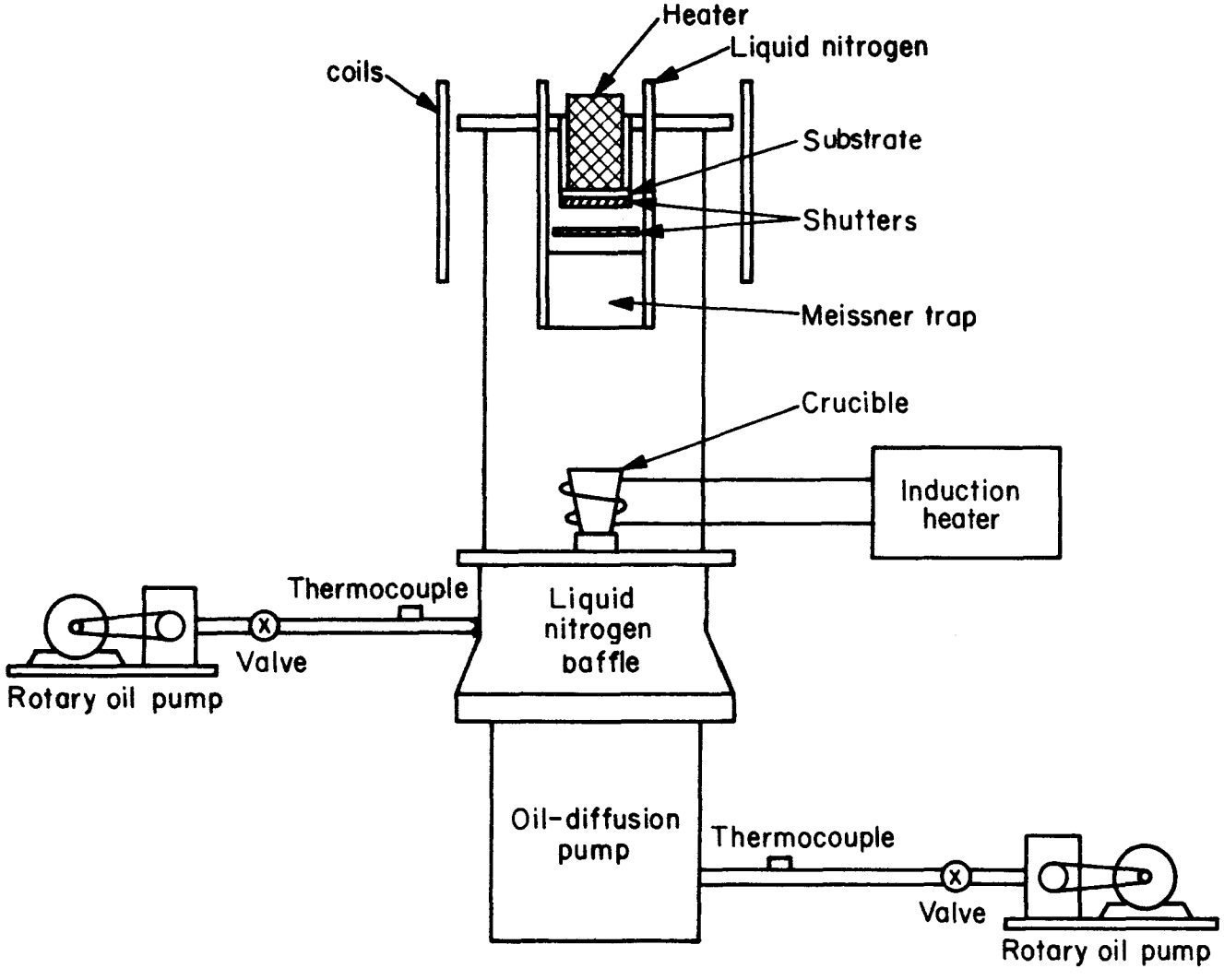

Fig.A-1 Vacuum system

Appendix 2 Uniaxial Anisotropy Measurement in Thin Ferromagnetic Films

(a) Hard Axis Loop.

The total energy per unit volume due to the external magnetic field energy and due to the uniaxial anisotropy energy for the single domain state is

$$E = - M_s H_x \cos\theta - M_s H_y \sin\theta + K_u \sin^2\theta \qquad \text{(A-2.1)}$$

where the component of the applied field in the easy axis direction is H_x, in the hard direction H_y and θ is the angle between the magnetization and the easy axis direction. When the field is in the hard direction only, one gets

$$E = - M_s H_y \sin\theta + K_u \sin^2\theta \qquad \text{(A-2.2)}$$

$$\delta E/\delta\theta = - M_s \cos\theta \, [H_y - H_k \sin\theta] \qquad \text{(A-2.3)}$$

$$\delta^2 E/\delta\theta^2 = M_s H_y \sin\theta + 2K_u(\cos^2\theta - \sin^2\theta) \qquad \text{(A-2.4)}$$

$$= M_s[H_y \sin\theta + H_k(\cos^2\theta - \sin^2\theta)]$$

where the usual notation $H_k = 2K_u/M_s$ is used. For a given H_y, the stable condition is given by that value of θ for which E is a minimum, ie., $\delta E/\delta\theta = 0$ and $\delta^2 E/\delta\theta^2 > 0$. The condition $\delta E/\delta\theta = 0$ allows two possible conditions on θ ,

$$H_y = H_k \sin\theta \qquad \text{(A-2.3a)}$$

or

$$\cos\theta = 0 \quad . \tag{A-2.3b}$$

If $|H_y| < H_k$, the second derivative given by Eq. (A-2.4) is positive in the first case (A-2.3a) and negative in the second (A-2.3b). Thus the stable state is given by the first, namely

$$\sin\theta = H_y/H_k \tag{A-2.5}$$

If $|H_y| > H_k$ the first condition is meaningless and the second derivative is positive in the second case provided θ is $\pi/2$ for positive H_y and $-\pi/2$ for negative H_y. Thus the stable conditions are that

$$\theta = \pi/2 \text{ for } H_y > H_k \tag{A-2.6a}$$

and

$$\theta = -\pi/2 \text{ for } H_y < H_k \quad . \tag{A-2.6b}$$

The component of the magnetization in the hard direction M_y is given by $M_y = M_s \text{Sin } \theta$.

Therefore,

$$M_y = M_s \text{Sin } \theta = M_s H_y/H_k \quad \text{unless } \theta = \pm \pi/2 \quad .$$

The hysteresis loop is a straight line below saturation and saturation takes place for $|H_y| = H_k$. Ideally the hard axis loop could be used to determine the uniaxia.. anisotropy field H_k by finding the field at which saturation occurs. In practice, however, the straight line usually exists only for $H_y < H_k$. At drive fields greater than H_k, the loop opens up so that the straight line can not be observed. Therefore, the conventional method of measurement is to extrapolate the slope at

low fields to the saturation value of magnetization and the field at the intersection is taken to be the experimental value of the anisotropy field H_k.

(b) Kobelev Method.

For films in which the straight line in the hard axis loop is not well defined, the hysteresis method is inaccurate to measure H_k. Several alternative methods have been developed. The method which is most convenient, uses the conventional hysteresis loop tracer in a different mode, first suggested by Kobelev (1962). This method requires a large a.c. field transverse to the axis of the pickup coil and 45^o to the axis of anisotropy. A d.c. field perpendicular to the a.c. field is then increased until a certain portion of the observed loop becomes flat, as shown in Fig. A-2. For ideal uniaxial anisotropy of the form given in Eq. A-2.1, this occurs when the d.c. field is equal to 0.5 H_k. The criterion of flatness is very sensitive allowing a very accurate measurement. In actual use, the measured values of H_k is quite independent of the magnitude of the a.c. field, and meaningful measurements can be made even on films which have an open loop characteristic with a hard axis field. For films in which the hard axis measurement is also possible, the values of H_k obtained by the two methods are almost always in agreement within 2 or 3 percent.

(c) Torque method.

Uniaxial anisotropy may be described by Eq. (2.1) in chapter 2. The effect of the anisotropy energy is that $\vec{M}$ is subject to a torque, tending to turn it into the easy direction, given by

(a)

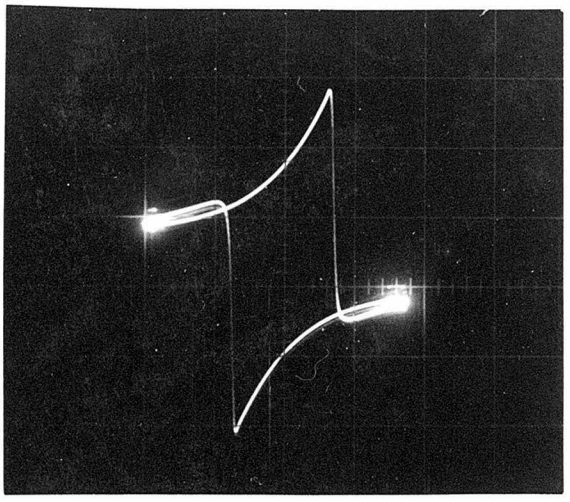

(b)

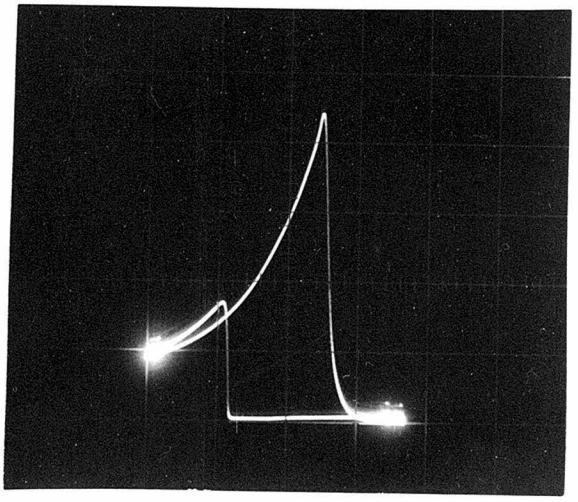

Fig.A-2 Kobelev method. (a) no d.c. field normal to drive field. (b) the d.c. field $H_k/2$ was applied.

$$L_u = dE_u/d\theta = K_u \sin 2\theta \ .$$

In the presence of an external field $\vec{H}$ applied in the plane of the film at angle α to the easy axis direction, the anisotropy torque is opposed by a magnetostatic torque $M \cdot H \sin(\alpha-\theta)$, so that $\vec{M}$ takes up an equilibrium position given by

$$K_u \sin 2\theta = M H \sin(\alpha - \theta).$$

If the field is large enough, say greater than $h = H/H_k = 1$, then the film remains a single domain and the maximum torque occurs when $\theta = 45^{\circ}$ Because the magnetization does not exactly follow the field, the plot of torque vs. α is not a pure sinusoidal wave, but the maximum torque is theoretically independent of H. The detailed descriptions of the torque magnetometer are given elsewhere (Humphrey and Johnston (1962) and Humphrey (1967)).

Appendix 3 Lorentz Microscopy

The electron microscope is now a well-established research tool both in the biological and physical-metallurgical domains, and there are several authoritative texts and review articles dealing with the special field of electron optics (Hall (1953), Heidenreich (1964), Hirsch and colleagues (1965) and Kay (1966)). The electron microscope used in the present study is an RCA EMU-3E equipped with the special double-condenser lens.

The Lorentz microscopy is based on the Lorentz deflection of electrons passing through a magnetic film. The mechanism of contrast formation in this use is rather different from that leading to the observation of lattice defects in transmission electron microscopy, and special techniques are required.

A magnetic flux $\vec{B}$ gives rise to the Lorentz force $\vec{F} = -e(\vec{v}x\vec{B})/c$. Hence the magnetic field curves the electron trajectory, but the energy of the electron remains constant. The trajectory geometry for calculation of electron intensity distribution in an observation plane is shown in Fig. A-3. In the figure, (x,y) are the coordinates in the magnetic sample with thickness d, $(\xi.\eta)$ are similar coordinates in the local plane, $\psi(x.y)$ is the Lorentz deflection angle and ℓ and z designate the distance from the electron source to the film plane A, and from the film plane to the local plane B.

Geometrical Optics:

The resulting intensity distribution in a plane B a distance z behind the plane A is

$$I(\xi\cdot\eta) = I_o\left[(1+z\frac{\partial\Phi_x}{\partial x})(1+z\frac{\partial\Phi_y}{\partial y}) - (z^2)\frac{\partial\Phi_x}{\partial y}\frac{\partial\Phi_y}{\partial x}\right]^{-1} \qquad \text{(A-3.1)}$$

$$\xi = x + z\Phi_x$$

$$\eta = y + z\Phi_y$$

$$\Phi_x = -\Phi My/Ms$$

$$\Phi_y = \Phi\ Mx/Ms\ ,$$

$$\Phi = (4\pi dMs/c)\ (e/2Vm)^{1/2}$$

where the symbols are defined in the table of notation. In the above derivation, the incoherence of electrons was assumed.

Wave Optics:

The wave mechanical theory of Lorentz contrast formation is based on the fact that the incoming electron wave experiences a phase shift S(x,y) in the object. The relative difference in magnetic phase shift between two points $\bar{r}_1$ and $\bar{r}_2$ in the plane A is calculated by the rule

$$\Delta S(\bar{r}_1,\bar{r}_2) = e/\hbar\Delta\varphi\ (\bar{r}_1,\bar{r}_2) \qquad \text{(A-3.2)}$$

where $\Delta\varphi\ (\bar{r}_1,\bar{r}_2)$ is the flux change through the area between the paths 1 and 2 and the planes z = 0 and z = d outlined in Fig. A-3. The Kirchoff diffraction theory is used to calculate the diffraction pattern in the local plane B from the incoming and phase-shifted wave in the plane A.

$$I(\xi\cdot\eta) = I_o\left|C'\int_{-\infty}^{\infty}\int_{-\infty}^{\infty} dxdy\right. \qquad \text{(A-3.3)}$$

$$\left.\exp i\{-1/2k_e(\frac{1}{\ell}+\frac{1}{z})\ (x^2+y^2) + \frac{ke}{z}\ (x\xi + y\eta) - \frac{e}{\hbar}\Delta\Phi(x\cdot y)\}\right|^2$$

where $k_e = 2\pi/\lambda_e$ and C' is a normalized constant.

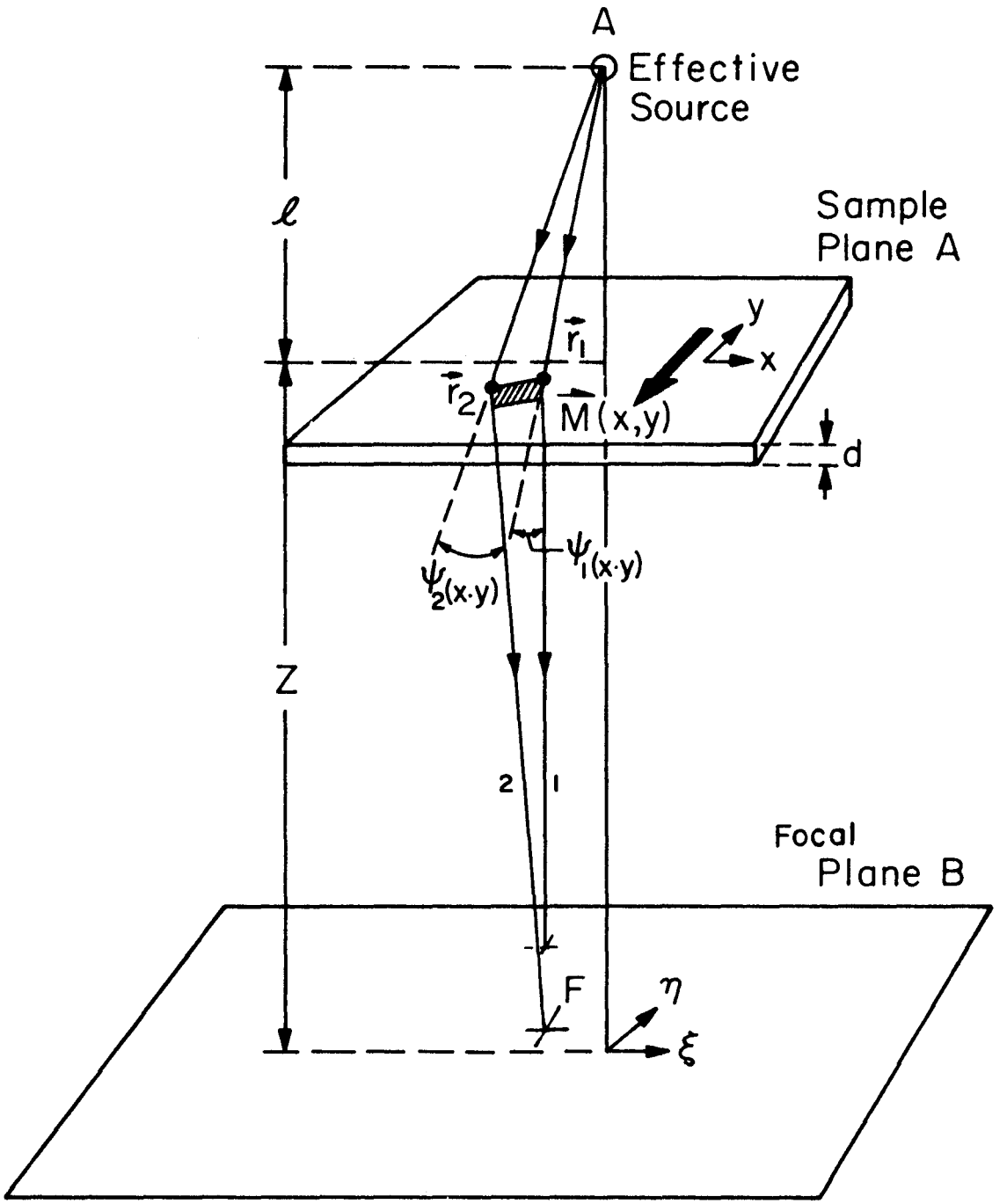

Fig.A-3 Lorentz microscopy.

Appendix 4 Flux Criterion

Consider the simple case sketched in Fig. A-4. The film plane is the x-y plane and the easy axis is along the y-direction. For simplicity, $B = B(x)$ and $dB/dy = dB/dz = 0$. Electrons with mass m and charge e travel in the negative z-direction with velocity v. In the field the electrons are deflected in the x-direction, i.e. they acquire momentum $P_x(x)$ depending on the field strength at the coordinates x of penetration,

$$P_x(x) = - e \int_{t_d}^{t_o} dt \cdot \upsilon \cdot B(x) = - e \int_{d}^{o} dz \cdot B(x) = e \cdot d \cdot B(x) \qquad (A\text{-}4.1)$$

Since the momentum $P_x(x)$ of one electron is canonically conjugate to its coordinate x, the uncertainty principle limits the exact knowledge of the coordinate

$$\Delta x \cdot \Delta P_x(x) = \Delta x \; e \cdot d \cdot \Delta B(x) > h \quad .$$

The quantity

$$d \int_{x_1}^{x_2} dx \; [B(x) - B(x_1)] = \Delta\varphi \qquad (A\text{-}4.2)$$

is the flux change through the area between the paths 1 and 2 and the planes $z = 0$ and $z = d$, due to the change in the magnetic field. In an approximation,

$$\Delta\varphi \approx \tfrac{1}{2} \cdot d \cdot \Delta x \cdot \Delta B \quad . \qquad (A\text{-}4.3)$$

Thus one may obtain from Eqs. (A4-1) and (A4-3)

$$\Delta\varphi > h/2e \qquad \text{(A-4.4)}$$

$$= 2.07 \times 10^{-15} \text{ weber} \qquad \text{(in M.K.S. unit).}$$

$$= 2.07 \times 10^{-7} \text{ gauss cm}^2 \qquad \text{(in C.G.S. units).}$$

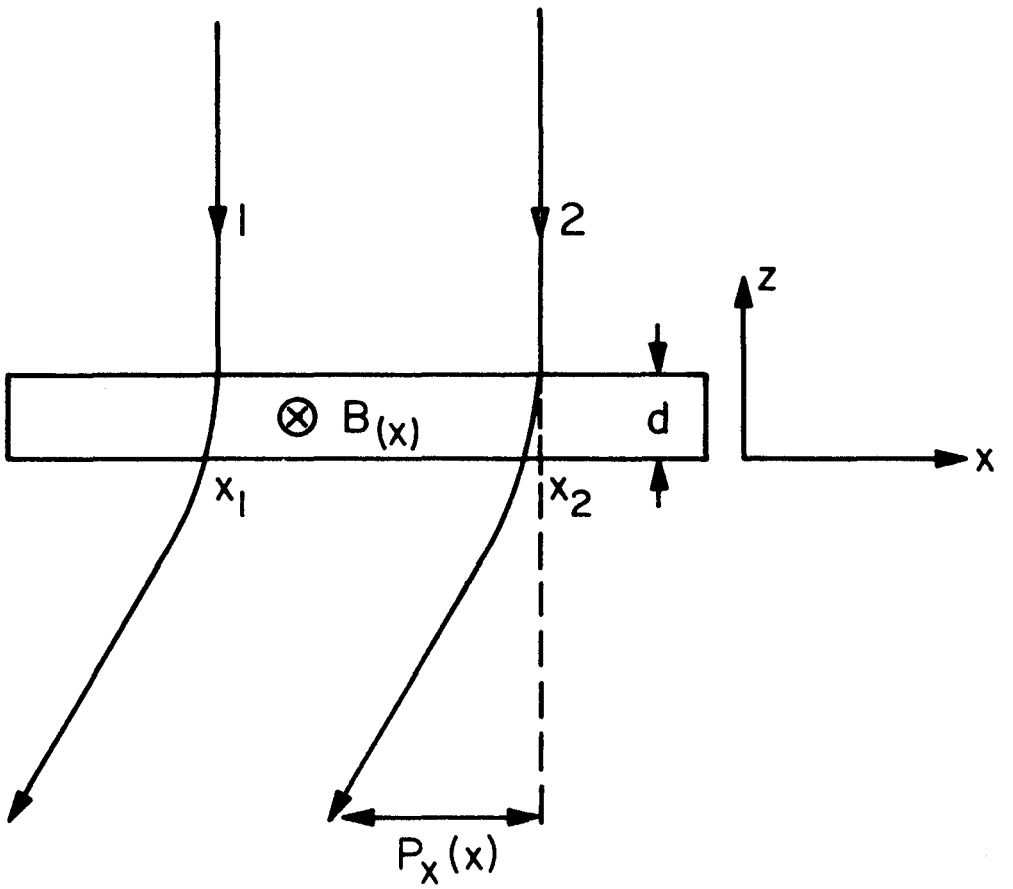

Fig.A-4 Schematical illustration of beam paths.

Appendix 5 Magnetocrystalline Anisotropy Energy

The magnetocrystalline anisotropy energy of a ferromagnetic single crystal acts in such a way that the magnetization tends to be directed along certain definite crystallographic axes which accordingly are called easy axes of magnetization. In the quantitative evaluation of magnetocrystalline anisotropy, the crystalline anisotropy energy may be expressed as a function of the direction cosines, α_1, α_2, α_3 of the magnetization vector with respect to the crystallographical axes.

In a cubic crystal, the expression, written in ascending powers of the α_i, is

$$E_k = K_1(\alpha_1^2\alpha_2^2 + \alpha_2^2\alpha_3^2 + \alpha_3^2\alpha_1^2) + K_2\alpha_1^2\alpha_2^2\alpha_3^2 + \quad \text{(A-5.1)}$$

$$+ \text{Higher order terms}$$

where K_1 and K_2 are the crystalline anisotropy constants.

For crystals of hexagonal symmetry, such as cobalt, it is more convenient to use the sine instead of the cosine of the angle between the magnetization and the hexagonal axis. Letting this angle be Φ, the energy may be expressed by

$$E_k = K_1\sin^2\Phi + K_2\sin^4\Phi + \text{Higher order terms} \quad \text{(A-5.2)}$$

Higher terms and terms depending on the orientation in the (00.1) plane have so far been found unnecessary.

Thesis Notations

A:	exchange constant
B:	magnetic flux density
C_a; C_b,	concentrations of A and B atoms respectively
C_{11}, C_{12}, C_{44} ...	standard elastic constants
D:	average grain size
E_e:	exchange energy density
E_s:	stray field energy density
E_h:	homogeneous anisotropy energy
E_k:	inhomogeneous local anisotropy energy
E_u:	uniaxial anisotropy energy density
$E_\perp$:	perpendicular anisotropy energy density
E_λ:	anisotropy energy density due to stress
E_p:	dipole-dipole interaction energy density
G:	Young's modulus
$\vec{H}_o$:	externally applied magnetic field
H_k:	anisotropy field
$H_{(\alpha)}$:	effective field component along the mean magnetization direction $H = H_o\cos(\alpha-\Phi_o) + H_k \cos 2\Phi_o$
I(U):	intensity distribution in the image plane by Lorentz microscopy
I_o:	incident beam intensity
I_b:	background intensity
K_u:	uniaxial anisotropy constant
$K_\perp$:	perpendicular-anisotropy constant

K_λ: anisotropy energy constant due to stress

K_p: anisotropy energy constant due to pair-ordering

$\vec{L}$: Torque = $\vec{M} \times \vec{H}$

M_a: magnetic moment of A atom

M_b: magnetic moment of B atom

M_s: saturation magnetization

$\vec{M}_o$: mean magnetization vector

$\vec{M}_{(\vec{r})}$: local magnetization

N: number of atoms per unit volume

N_{aa_i}, N_{bb_i} and N_{ab_i}: number of the A-A, B-B and A-B pairs directed parallel to the $i^{\underline{th}}$ direction

S: phase in electron waves

T: temperature where measurement is to be made

T': substrate deposition temperature, or annealing temperature

V: accelerating voltage

a: wall width

c: velocity of light

d: film thickness

e: electron charge

$\vec{e}_x$, $\vec{e}_y$: unit vectors along x - and y - directions respectively

h_o: applied field normalized to the anisotropy field $h_o = H_o/H_k$

h: effective field normalized to the anisotropy field $h = H/H_k$

ℓ: distance between the effective electron beam source and the film plane

$\ell_{ab(r)}$: dipole-dipole coupling constant between A and B atoms

ℓ_o: equivalent dipole-dipole coupling constant

ℓ_o: the value of ℓ_o at T'.

m: electron mass

n: number of the nearest neighboring atoms (Chapter 2)

number of crystallites through film thickness (Chapter 5)

z: out-of-focus distance

(x,y,z): rectangular (Cartesian) coordinates

x: coordinate along the hard axis in the film plane

y: coordinate along the easy axis in the film plane

$(\xi \cdot \eta \cdot \zeta)$: rectangular coordinates in the image plane

u: normalized x- coordinate

U: normalized ξ- coordinate

α: angle between $\vec{H}_o$ and the easy axis

$\alpha_1, \alpha_2, \alpha_3$ directional cosines of $\vec{M}$ to the crystallographical axes

β: beam divergence angle

γ_B: Bloch wall energy per unit area

γ_N: Néel wall energy per unit area

δ: wall width parameter

ψ_o: maximum Lorentz deflection angle

ψ_x: Lorentz deflection angle in the x-direction

ρ_m: (hypothetical) magnetic charge density

θ: angle between the mean magnetization $\vec{M}_o$ and the easy direction, (except Chapter 5), or angle between $\vec{M}$ and the mean magnetization direction (only in Chapter 5).

Φ_o: angle between $\vec{M}_o$ and the easy axis

Φ: angle between $\vec{M}$ and the easy axis

φ: angle between $\vec{M}$ and the line joining two atoms

φ_i: angle between $\vec{M}$ and the direction of an $i^{\underline{th}}$ pair

λ: ripple wavelength

λ_e: electron wavelength

λ_s: longitudinal saturation magnetostriction at T

λ_s': longitudinal saturation magnetostriction at T'

λ_{100}, λ_{111}: longitudinal magnetostriction constants along [100] and [111], respectively, at T

λ'_{100}, λ'_{111}: longitudinal magnetostriction constants along [100] and [111], respectively at T'

σ: stress magnitude

General References:

R. Becker and W. Döring, "Ferromagnetismus" (Springer, Berlin, 1939).

H. W. Wyckoff, "Crystal Structures" (Interscience Publishers, New York, 1948).

R. M. Bozorth, "Ferromagnetism" (D. van Nostland Co., 1951)

S. Chikazumi, "Ferromagnetism" (John Wiley, New York, 1964)

M. Born and E. Wolf, "Principles of Optics" (Pergamon Press, New York, 1959).

R. D. Heidenreich, "Fundamental Transmission Electron Microscopy" (Interscience Publishers, New York, 1964).

P. B. Hirsch, R. B. Nicholson, A. Howie, D. W. Pashley and M. J. Whelan, "Electron Microscopy of Thin Crystals" (Butterworths, London, 1965).

D. H. Kay, "Techniques for Electron Microscopy" (F. A. Davis Co., Philadelphia, 1965).

References:

A. Aharoni, J. Appl. Phys. 38, 3196 (1967).

Y. Aharonov and D. Bohm, Phys. Rev. 115, 485 (1959).

J. C. Anderson, Proc. Phys. Soc. 78, 25 (1961).

G. Aubert, J. Appl. Phys. 39, 504 (1968).

A. Baltz, Proc. Int. Conf. Magnetism (Nottingham), 845 (1964).

A. Baltz and W. D. Doyle (1964), J. Appl. Phys. 35, 1814 (1964).

F. Bitter, Phys. Rev. 38, 1903 (1931).

F. Bloch, Z. Physik 74, 295 (1932).

M. S. Blois, Jr., J. Appl. Phys. 26, 975 (1955).

H. Boersch, H. Hamisch, D. Wohlleben and K. Grohmann, Z. Physik, 159, 397 (1960).

R. M. Bozorth and J. G. Walker, Phys. Rev. 89, 624 (1953).

R. M. Bozorth, Conference on Magnetism and Magnetic Materials, Boston (1957).

W. Broniewski and W. Pietrik, Compt. rend. 201, 206, (1935).

W. F. Brown, Jr., and A. E. LaBonte, J. Appl. Phys. 36, 1380 (1965).

L. W. Brownlow and C. H. Wilts, Proc. International Colloq. on Physics, Mag. Films, Irkutsk, U.S.S.R. (1968).

R. D. Burbank and R. D. Heidenreich, Phil. Mag. 5, 373 (1960).

S. Chikazumi and T. Oomura, J. Phys. Soc. Japan 10, 842 (1955).

M. S. Cohen, Technical Note, Lincoln Lab, M.I.T. (May, 1967).

M. S. Cohen, J. Appl. Phys. 38, 4966 (1967).

R. Collette, J. Appl. Phys. 35, 3294 (1964).

D. J. Craik and R. S. Tebble, Rep. Prog. Phys. 24, 116 (1961)

J. M. Daughton, G. E. Keefe, K. Y. Ahn and C. C. Cho, IBM J. 555 (Sept.1967)

W. DeBlois and C. D. Graham, Jr., J. Appl. Phys. 29, 932 (1958)

H. D. Dietz and H. Thomas, Z. Physik 163, 523 (1961)

E. L. Feinberg, Soviet Phys. USPEKAI 5, 753 (1963)

E. T. Ferguson, J. Appl. Phys. 29, 252 (1958)

E. Fuchs, Z. Ang. Physik 13, 157 (1961)

E. Fuchs, Z. Ang. Physik 14, 203 (1962)

H. W. Fuller and M. H. Hale, J. Appl. Phys. 31, 308S (1960)

H. W. Fuller and M. H. Hale, J. Appl. Phys. 31, 238 (1960)

K. J. Harte, Tech. Rept. Lincoln Lab. M.I.T. (Aug. 1964)

K. J. Harte, J. Appl. Phys. 39, 1503 (1968)

U. Hashimoto, Nippon Kinzoku Gakkai-Shi, 1, 177 (1937)

W. Heisenberg, Z. Physik, 49, 619 (1928)

E. E. Huber, D. O. Smith and J. B. Goodenough, J. Appl. Phys. 29, 294 (1958)

H. Hoffmann, Phys. Kondens. Materie 2, 32 (1964)

H. Hoffmann, Phys. Stat. Sol. 5, 187 (1964)

H. Hoffmann, J. Appl. Phys. 35, 1790 (1964)

K. Hoselitz and W. Sucksmith, Proc. Roy. Soc. (London) A 181, 303 (1943)

F. B. Humphrey and A. R. Johnston, Tech. Rept. No. 32, J.P.L. (1962)

F. B. Humphrey, J. Appl. Phys. 38, 1520 (1967)

T. Iwata, P. J. Prosen and B. E. Gran, J. Appl. Phys. 37, 1285 (1966)

J. F. Janak, Appl. Phys. Letters 9, 225 (1966)

J. F. Janak, J. Appl. Phys., 38, 1789 (1967)

F. W. Jones and W. I. Pumphrey, J. Iron Steel Inst. 163, 121 (1949)

R. Kirchner and W. Döring, J. Appl. Phys. 39, 855 (1968)

V. V. Kobelev, Fitz. Metal Mettalloved. 13, 467 (1962)

W. Köster, Z. Metallk, 35, 194 (1943)

P. G. Krukover, Proc. Int. Colloq. Phys. Mag. Films, Irkutsk, U.S.S.R. (1968)

L. Landau and E. Lifshitz, Physik. Z. Sowjetunion 8, 153 (1935)

H. Masumoto, Sci. Repts. Tohoku Imp. Univ., 449 (1926)

S. Methfessel, S. Middlehoek and H. Thomas, IBM J. Res. Dev. 4, 96 (1960)

S. Methfessel, S. Middlehoek and H. Thomas, J. Appl. Phys. 31, 1959 (1961)

S. Middlehoek, Ph.D. Thesis, Univ. of Amsterdam (1961)

S. Middlehoek, J. Appl. Phys. 34, 1054 (1963)

R. M. Moon, J. Appl. Phys. 30S, 825 (1959)

S. Nagakura, M Kikuchi, Y. Kaneko and S. Oketani, Japan. J. Appl. Phys. 2, 201 (1963)

L. Neel, Compt. Rend. 237, 1468, 1613 (1953)

L. Neel, J. Phys. Radium 15, 225 (1954)

L. Neel, Compt. Rend. 241, 533 (1955)

S. Ogawa, D. Watanabe and T. Fujita, J. Phys. Soc. Japan. (1955)

H. N. Oredson and E. J. Torok, Rept. at Third Int. Colloq. (Boston, September (1967)) I.E.E.E. Trans. 4 (Mag.) 44 (1968)

A. Osawa, Sci. Repts. Tohoku Imp. Univ., 19, 235 (1930)

M.A. Otooni and R.W. Vook, J. Appl. Phys. 39, 2471 (1968)

E. A. Owen, E. L. Yates, A. H. Sully, Proc. Phys. Soc. (London) 49, 315 (1937)

E. A. Owen and A. H. Sully, Phil. Mag. 27, 614 (1939)

E. A. Owen and Y. H. Lin, J. Iron Steel Inst. 163, 132 (1949)

C. E. Patton and F. B. Humphrey, J. Appl. Phys. 37, 4269 (1966)

A. T. Pickles and W. Sucksmith, Proc. Roy. Soc. (London) 175, 331 (1940)

M. Purtton, Trans. Nineth Nat'l. Vacuum Symp. 59 (1963, New York, MacMillan)

I. B. Puchalska, Proc. Int. Conf. Mag. 870 (1964) (Nottingham)

E. W. Pugh, E. L. Boyd and J. F. Freedman, IBM J. 163 (1960)

G. W. Rathenau and J. L. Snoek, Physica 13, 555 (1941)

G. Robinson, Rept. Mullard Research Lab, No. 393 (1961), and J. Phys. Soc. Japan 17, 558 (1962)

H. Rother, Z. Physik, 168, 42 (1962)

H. Rother, Z. Physik, 168, 148 (1962)

H. Rother, Z. Physik, 179, 229 (1964)

S. Shtrikmann and D. Treves, J. Appl. Phys. 31, 147S (1960)

Y. Sugita, H. Fujiwara, N. Saito and T. Taniguchi, A Rept. At. Mag. Conf. (Japan, 1967)

Y. Sugita, H. Fujiwara and T. Sato, Appl. Phys. Letters, 10, 229 (1967)

T. Suzuki and C. H. Wilts, J. Appl. Phys. 38, 1356 (1967)

T. Suzuki and C. H. Wilts, J. Appl. Phys. 39, 1151 (1968)

T. Suzuki, C. H. Wilts and C. E. Patton, J. Appl. Phys. 39, 1983 (1968)

T. Suzuki and C. H. Wilts, J. Appl. Phys. 39, 6110 (1968)

T. Suzuki and C. H. Wilts, J. Appl. Phys. to be published, 40, (March, 1969)

M. Takahashi, J. Appl. Phys. 33, 1101 (1962)

S. Taniguchi, Sci. Repts. Res. Inst., Tohoku Univ. A7, 269 (1955)

S. Tsukahara, H. Kawakatsu and T. Nagashima, Rept. Electro-Technical Lab. Japan 27, No. 12 (1963)

R. H. Wade, J. Appl. Phys. 37, 366 (1966)

T. Wako, M. Saheki and T. Moriyama, Japan J. Appl. Phys. 2, 584 (1963)

D. H. Warrington, Phil. Mag. 9, 261 (1964)

P. Weiss, J. Phys. 6, 661 (1907)

F. G. West, J. Appl. Phys. 35, 1827 (1964)

H. Wiedenmann and H. Hoffmann, Z. Ang. Phys. 18, 502 (1964)

H. J. Williams and W. Shockley, Phys. Rev. 75, 178 (1949)

H. J. Williams and M. Goertz, J. Appl. Phys. 23, 316 (1952)

C. H. Wilts, Proc. Int'l. Symp. Thin Film Physics (Clausthal, Ctermany (1965)), and "Basic Problems in Thin Film Physics" 422 (Gottingen, Vandenhoek and Ruprecht (1966))

C. H. Wilts and F. B. Humphrey, J. Appl. Phys. 39, 1191 (1968)

D. Wohlleben, Phys. Letters, 22, 564 (1966)

D. Wohlleben, J. Appl. Phys. 38, 3341 (1967)